Mathematical Modelling of Lead-Acid Batteries

Valentin Sulzer
St Anne's College
University of Oxford

A thesis submitted for the degree of
Doctor of Philosophy

Trinity 2019

To my parents, Caroline and Pascal, for their dedication, selflessness and support

Abstract

Electrochemical and equivalent-circuit modelling are the two most popular approaches to battery simulation, but the former is computationally expensive and the latter provides limited physical insight. A theoretical middle ground would be useful to support battery management, online diagnostics, and cell design.

In this thesis, we present a porous-electrode model of a lead-acid battery, which includes an extension of concentrated-solution theory that accounts for excluded-volume effects, local pressure variation, and a detailed microscopic water balance.

Asymptotic analysis of the one-dimensional model in the limit of small discharge rate produces three reduced-order models, which relate the electrical behaviour to microscopic material properties, but simulate discharge at speeds approaching an equivalent circuit. A lumped-parameter model, which neglects spatial property variations, proves accurate for small discharge rates (below 0.1C), while a spatially resolved higher-order solution retains accuracy at higher discharge rates (up to 5C). The reduced-order models provide improved insight into the battery's behaviour. The models are fit to experimental data, showing good agreement.

We then consider the three-dimensional model and exploit the limit of small aspect ratio to decompose the through-cell and transverse dimensions. Further asymptotic analyses in the limit of high conductivity and/or small discharge rate give new simplified models that capture transverse non-uniformities at reduced computational cost. In the simplest case, the current collectors act as series resistors.

In order to explore the behaviour of a lead-acid battery during recharge, we return to a one-dimensional model and add an oxygen reaction to the model. We find that the oxygen recombination must be diffusion limited in the negative electrode, leading to non-monotonic voltage increase during constant-current recharge. Reduced-order models in the limit of slow recharge provide good approximations to the full charging model.

Acknowledgements

I was fortunate to be able to draw from the knowledge and experience of four academic supervisors, and my largest thanks must go to them. Colin Please was always available to answer all kinds of questions, both mathematical in nature and not, as well as transmit his contagious enthusiasm for "the pushing back of the frontiers". Jon Chapman brought exceptional mathematical ideas to the project, and always explained these very clearly. Charles Monroe demonstrated and ingrained an exemplary rigour and attention to detail. David Howey gave valuable advice on the more practical and applied considerations of the field. I am grateful for the freedom that they afforded me, which allowed me to grow as a researcher and as an individual.

Many breakthroughs and ideas came from interesting discussions with Scott Marquis, Robert Timms, Antti Aitio, and for this I am very grateful. Thanks also to Martin Robinson for help with and feedback on software development.

In addition to financial support, I am thankful to InFoMM for introducing me to a fantastic group of (sometimes knowledgeable) friends for breaks from work both near and far from the office. I would also like to thank BBOXX, and especially Chris Baker-Brian, for their keen interest in the project as well as financial support.

The last four years were not spent only in the office and thank you to friends at OUCC, OUTriC and OUL for making the remaining time very enjoyable. Thanks especially to Eddie, Florian, James, Matt K, Matt R, Ollie and Rowan for some great memories on bikes and in houses of questionable standard around Oxford, and to Sophia for excellent moral support in the final months.

Enfin, merci à ma famille, et surtout à mes parents, pour votre soutien inébranlable depuis toujours. Cette thèse est pour vous.

Contents

List of Figures

List of Tables

Glossary

DAE differential-algebraic equation.

FCI Fractional Charge Input.

FOQS first-order quasi-static.

LOQS leading-order quasi-static.

LPM lumped parameter model.

OCP open-circuit potential.

ODE ordinary differential equation.

PDE partial differential equation.

SoC State-of-Charge.

SoH State-of-Health.

SPM Single Particle Model.

SPMe Single Particle Model with electrolyte.

VRLA valve-regulated lead-acid.

Nomenclature

Accents

$\bar{}$	averaged in x-direction
$\breve{}$	averaged in y- and z-directions
$\hat{}$	dimensional
$\tilde{}$	microscale (in Appendix C)

Domains

Ω	domain
$\partial\Omega$	domain boundary

Superscripts

S	main reaction, (1.1)
O	oxygen reaction, (1.2)
H	hydrogen reaction, (1.3)
dl	double-layer
r	arbitrary reaction r
0	initial
max	maximum
(0)	leading order
(1)	first order
eff	effective

surf	surface	
$\square$	volume-averaged	

Subscripts

$+$	of cations	
$-$	of anions	
w	of solvent (water)	
e	of electrolyte	
s	of solid (electrodes)	
o	of oxygen	
k	of species k	
k,n	of k, in negative electrode	
k,s	of k, in separator	
k,p	of k, in positive electrode	

Variables

c	concentration	mol m^{-3}
ε	porosity	-
j	interfacial current density	A m^{-2}
$\mathbf{i}$	current density (3D)	A m^{-2}
i	current density in x-direction	A m^{-2}
$\mathbf{v}$	velocity (3D)	m s^{-1}
v	velocity in x-direction	m s^{-1}
$\mathbf{N}$	ion flux (3D)	mol m^{-2} s^{-1}
p	pressure	Pa
Φ	potential	V

ϕ	potential difference, $\Phi_s - \Phi_e$	V
a	reactive surface area	-
$\mathcal{U}$	electrode state of charge	-
q	electrolyte state of charge	-

Chapter 1

Introduction

As renewable energy sources become cheaper and more efficient, they are used increasingly to take over from fossil fuels in producing electricity. Since the sources are inherently fluctuating, the supply must be smoothed out by energy storage. Lead-acid batteries are the most widely used electrochemical storage technology, with applications including car batteries and off-grid energy supply. Due to their low cost, safety, reliability and recyclability, some have predicted that the market share of lead-acid batteries will only fall to 75% by 2025 [105], despite their relatively low energy and power density compared to other battery chemistries.

Mathematical modelling of batteries provides a mechanism to manage their charging and discharging regime efficiently and maximise their lifetime. Two important concepts in battery management are State-of-Charge (SoC) and State-of-Health (SoH) of a battery. SoC is a measure of the current capacity of the battery relative to a fully charged battery and can oscillate on a short time scale of minutes or hours as the battery charges and discharges, while SoH expresses the performance capabilities (capacity, maximum power, etc.) of the battery relative to its performance when new, and usually decreases monotonically over several years. A huge amount of data can be collected from batteries; for example, the energy company BBOXX records the current, voltage and temperature data from tens of thousands of batteries in the field in Sub-Saharan Africa. However, this information alone cannot directly be used to track the SoC and SoH. Instead, models must be developed that can take the raw voltage, current and temperature data and output estimates of the SoC and SoH.

Beyond state estimation, modelling can be useful to address a number of other challenges in battery management. One well-publicised challenge is optimisation of charging algorithms to reduce charge time while minimising the long-term degradation that can occur particularly as a result of overcharge. Another is designing battery recovery methodologies in order to repair degraded batteries and return them to the

field; several such techniques exist in industry, but are poorly understood. Finally, models can be used to optimise battery design, for example by maximising power capacity (the maximum power deliverable) while keeping energy capacity (the total charge available) above a certain threshold, or vice versa.

To manage batteries effectively in all of these areas, it is critical to have forward battery models that are both fast and accurate. There are two approaches to modelling batteries: equivalent-circuit and mechanistic. The popular equivalent-circuit approach [104] is efficient and well understood, but has limited physical meaning and performs poorly when extrapolated from its parametrisation. Mechanistic models, such as those developed by John Newman [86], include detailed descriptions of the physical, chemical and electrical processes occurring inside a battery, and hence have enhanced predictive capability. However, these mechanistic models require far more computational power. Battery management could be improved if there existed easily-solved models with greater mechanistic detail.

The objective of this thesis is to derive reduced-order models of lead-acid batteries, starting from a three-dimensional mechanistic model based on Newman porous-electrode theory. To do so, we use asymptotic analysis to systematically derive simplified models by exploiting the extremes of electrolyte diffusion, electrode conductivity and cell aspect ratio. Most of the work is performed in the context of a single discharge, but an extension to a model for recharge is also investigated. Models to account for degradation are not considered, but the framework created allows for such effects to be included.

In the remainder of this introductory chapter, we provide background for the operation of lead-acid batteries and an overview of the literature. We then summarise the key results and contributions and lay out the structure of this thesis.

1.1 Background and literature review

In this section, we start by providing an overview of lead-acid battery fundamentals in Section 1.1.1. Then, in Section 1.1.2, we consider the existing literature for battery models, from microscale models to macroscale models, and then models that include extensions to overcharge and degradation. Finally, in Section 1.1.3, we explore methods that are used to solve battery models, using either efficient numerical methods or simplified models.

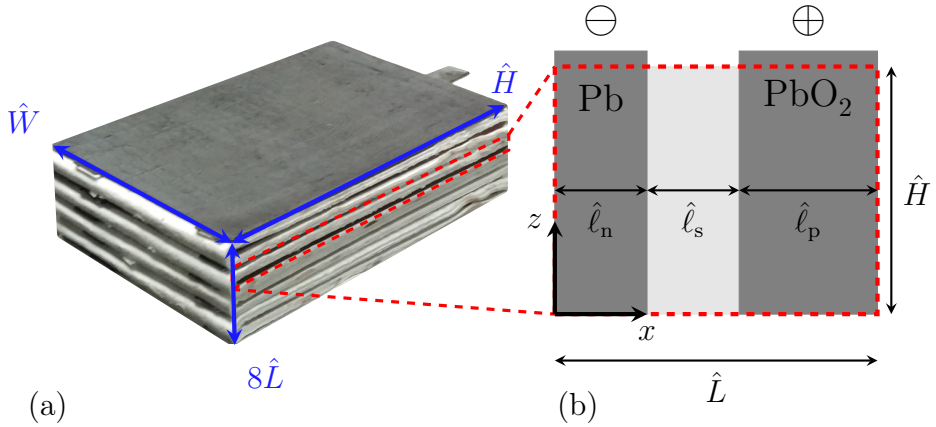

Figure 1.1: Geometry of a lead-acid battery. (a) A whole lead-acid pile (Photograph by Ashley Grealish, BBOXX). (b) A single cell. The y-axis is into the page.

1.1.1 Lead-acid battery fundamentals

Typically, a valve regulated lead-acid battery comprises six 2V piles wired in series. Figure 1.1 depicts one such pile, which consists of five lead (Pb) electrodes and four lead dioxide (PbO_2) electrodes, sandwiched alternatingly around a porous, electrically insulating separator to produce eight cells, wired in parallel at the top edge of the electrode pile. The pile has height $\hat{H}$, width $\hat{W}$, and cross-sectional area $A_{cs} = \hat{H}\hat{W}$. The negative (Pb) and positive (PbO_2) electrodes have half-thicknesses $\hat{\ell}_n$ and $\hat{\ell}_p$ respectively, and the separator has thickness $\hat{\ell}_s$, giving each internal cell total thickness $\hat{L} = \hat{\ell}_n + \hat{\ell}_s + \hat{\ell}_p$. The layers repeat periodically, and for the purpose of this thesis we will exploit this by assuming that the whole pile can be modelled via analysis of a single cell. Some thermal effects have been documented experimentally [28, 127] and considered theoretically [49, 114], but we assume an isothermal system for simplicity.

The electrodes are porous, permeated by an aqueous sulfuric acid (H_2SO_4) electrolyte that also permeates the separator. Half-reactions occur at the interface between electrode and electrolyte within each porous electrode. In the negative (lead) electrode,

$$\mathrm{Pb} + \mathrm{HSO_4^-} \underset{\text{charge}}{\overset{\text{discharge}}{\rightleftharpoons}} \mathrm{PbSO_4} + \mathrm{H^+} + 2\,\mathrm{e^-}, \tag{1.1a}$$

and in the positive (lead dioxide) electrode,

$$\mathrm{PbO_2} + \mathrm{HSO_4^-} + 3\,\mathrm{H^+} + 2\,\mathrm{e^-} \underset{\text{charge}}{\overset{\text{discharge}}{\rightleftharpoons}} \mathrm{PbSO_4} + 2\,\mathrm{H_2O}\cdot \tag{1.1b}$$

During a discharge, both the level and the concentration of the electrolyte drop, with the solution being more dilute at the positive electrode since water is created

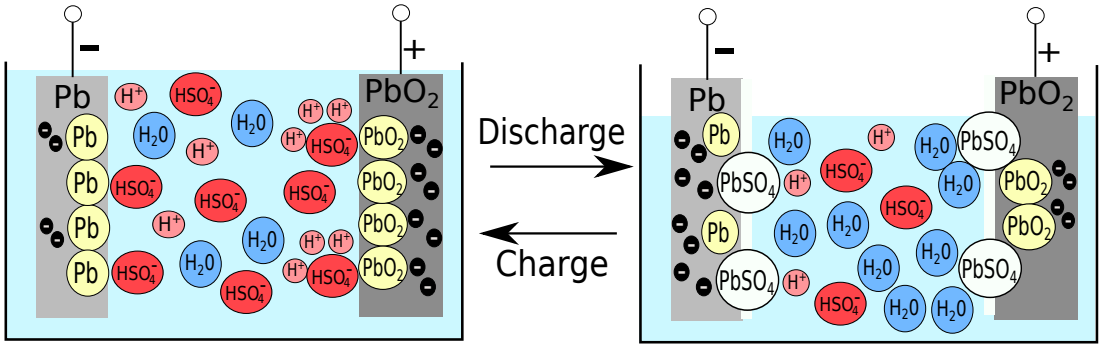

Figure 1.2: Reactions during charge and discharge in a single lead-acid cell. Solid reactants/products: lead (Pb), lead dioxide (PbO_2), lead sulfate ($PbSO_4$). Liquid reactants/products: water (H_2O), hydrogen ions (H^+), hydrogen sulfate ions (HSO_4^-).

there. Lead dioxide is used up in the positive electrode, lead is used up in the negative electrode, and a layer of solid lead sulfate builds up within the pores of both electrodes. During a charge, the opposite processes occur. In Figure 1.2, we show the elementary reactions in the simplified geometry of a planar cell – a cell with non-porous electrodes that are perfect conductors, so that the electrolyte-electrode interface acts as a current collector as well as a reaction surface.

Competitive reactions occur in addition to the main half-reactions (1.1), in particular during charging. The main side reactions are hydrolysis (evolution/recombination of oxygen, O_2),

$$\mathrm{O_2 + 4\,H^+ + 4\,e^-} \underset{\text{positive electrode}}{\overset{\text{negative electrode}}{\rightleftharpoons}} \mathrm{2\,H_2O}, \tag{1.2}$$

and to a lesser extent hydrogen (H_2) evolution and recombination,

$$\mathrm{2\,H^+ + 2\,e^-} \underset{\text{positive electrode}}{\overset{\text{negative electrode}}{\rightleftharpoons}} \mathrm{H_2}. \tag{1.3}$$

Additional side reactions occur to a much lesser extent, but can lead to degradation of the battery over many charge/discharge cycles.

While all lead-acid batteries follow the basic principles that we have described, it is important to distinguish between flooded batteries and valve-regulated lead-acid (VRLA) batteries. These two designs each have their own advantages and disadvantages [70]. Flooded lead-acid batteries are cheaper and better established, but require constant maintenance for optimal functioning. They have a 'free reservoir' region in which natural convection of the electrolyte may occur due to buoyancy induced by density changes. VRLA batteries require no maintenance and cannot be spilled, but are more expensive and raise their own challenges of overcharging and degradation. In this thesis, we will focus on VRLA batteries.

1.1.2 Battery modelling

We now focus our attention on mechanistic models for lead-acid batteries. Such models track the evolution in space and time of physical variables within the battery. To rigorously derive a physical model for lead-acid batteries, one must start with conservation laws and constitutive relations at the microscale for the electrolyte, electrode and interface between them, and then average the microscale model in some way to obtain the behaviour on the macroscale. In practice, most models in the literature are derived directly at the macroscale, but we are interested in the more systematic derivation of such models.

We now review the literature for microscale battery models, averaging techniques, resulting macroscale battery models and finally extensions relating to overcharge and degradation.

Microscale models. Different models of the electrolyte can be derived depending on whether the electrolyte is assumed to be 'dilute' or 'concentrated'. Dilute models (e.g. [100]), developed by Planck, are simpler and are often appropriate for lithium-ion chemistries. However, for lead-acid batteries, with a 6 Molar electrolyte, concentrated theory should be used. The theory of transport in a concentrated electrolyte (e.g. [55]) is applied to electrochemical systems by Newman and Chapman [85].

Liu and Monroe [71] extend Newman's model to ensure thermodynamic consistency. Bizeray et al. [11] point out a discrepancy between dilute and concentrated theory (which is also noted by [100]) and show how it can be resolved. Goyal and Monroe [45] further extend the model to include pressure variations in the system.

The electrodes are usually modelled as obeying Ohm's law. The reactions (1.1) occurring at the interface between electrolyte and electrode are usually captured by a kinetic law such as Butler-Volmer or Tafel. Richardson et al. [101] have shown that the Butler-Volmer reaction accounts for most of the physical effects in the double layer between the electrode and the electrolyte. The interface between electrolyte and electrode moves as the reaction proceeds due to the deposition of the lead sulfate discharge product.

Averaging. Once a microscale model has been obtained, it must be applied to the porous electrode. One option is to determine the exact electrode geometry and solve the full model in 3D. However, this approach is very time consuming, and requires explicit knowledge of the microstructure, which will vary from battery to battery in the field. Instead, Newman and Tiedemann [87] define 'average' quantities, which

are continuous functions of space and time over the whole porous electrodes. The justification for these arguments can be found in [124], and more recently in [129]. A more systematic approach is to use homogenisation techniques such as the method of multiple scales [96, 97]. For example, this is applied to an electrochemical system by Richardson, Denuault and Please [100], and Arunachalam et al. [3, 4].

The method of multiple scales provides a unit cell problem at the microscale that can be solved in order to obtain effective properties at the macroscale. However, to solve the unit cell problem, one must make assumptions about the representative microscale geometry [16]. In practice, effective diffusion coefficients are based on experimental results, with the most notable being Bruggeman's (e.g. [72]). Chung et al. [24] find that this is a good approximation, but Pharoah et al. [93] argue that it is a poor representation as it does not take the anisotropy of the material into account. In the context of battery models, Arunachalam et al. [4] show that the Bruggeman relation is only accurate at relatively low currents. After averaging, interfacial effects appear in the model through a changing porosity and reactive surface area per volume.

Macroscale lead-acid battery models. Almost all mechanistic models are derived directly at the macroscale, with homogenisation from the microscale implied. Many such models are based on the seminal work by John Newman, summarised in [86].

In lead-acid batteries, there is no intercalation from electrolyte to electrode. Therefore, most of the modelling effort focusses on the behaviour of the electrolyte, and the interface between electrolyte and electrodes. Lead-acid battery models are often reported to be based on a study of lead-acid battery modelling presented by Tiedemann and Newman [122]. Following on from this, several authors extend Newman's work to include behaviour during charge and rest [47] and two-dimensional effects [1, 7, 48]. However, these works focus on effects that are specific to flooded batteries, such as buoyancy. To model VRLA more specifically, one must take into account overcharge and degradation.

Overcharge. When lead-acid batteries are charged at too high a voltage (overcharged), significant side reactions occur in which hydrogen and oxygen are produced by electrolysis in the positive electrode, and recombine in the negative electrode.

These reactions can lead to a significantly different voltage curve than would be predicted by a simple model. The overcharging process is studied experimentally by several authors.

Li et al. [68] explore the effect of several factors such as electrolyte concentration and temperature, finding saturation level of the negative electrode to be the most important factor. Guo et al. [50] study different pathways that the oxygen can travel along between the two electrodes. Pavlov et al. [91] investigate the oxygen cycle in the negative plate experimentally and propose a mechanism for it, but do not include it into a complete model. Mahato et al. [74] and Berndt [8] study the recombination mechanism, and show that it must be diffusion-limited.

A full model for overcharge is proposed by Bernardi et al. [6], who include hydrolysis as a side reaction in the model but only provide a qualitative fit with experimental data. Several authors extend this model. Newman and Tiedemann [88] improve the model to obtain better quantitative fit with the experiments. Gu et al. [49] manage even better fit with data, by incorporating temperature effects as well as overcharge. Cugnet et al. [26] highlight that the charging response depends on how the battery was discharged, and also find good agreement with experimental data.

Degradation. The models discussed so far only estimate SoC. To model SoH, degradation effects must be included. The main mechanisms for degradation of VRLA batteries, given by Bindner et al. [9], are corrosion, irreversible sulfation, shedding and degradation of active material, water loss and electrolyte stratification. Bindner et al. study all of these processes experimentally, which might be useful for model validation. The majority of research is done on corrosion and irreversible sulfation.

Corrosion is the process by which a layer builds up between the lead oxide electrode and the lead sulfate layer. Corrosion is studied experimentally by Berndt [8] and is modelled by several authors. Tenno [119] models the process with an additional side reaction, while Cugnet et al. [27] simulate corrosion by including an additional resistance in the system. Boovaragavan et al. [14] assess three different models for corrosion and conclude that a side reaction is intuitively the best model. Bindner et al. argue that high temperatures are a very important driver of corrosion, but none of the above models include temperature effects.

Irreversible sulfation occurs when the the battery remains at low SoC for a long time, so the layer of lead sulfate that builds up on the pore surfaces during discharge crystallizes and cannot be removed by charging. Irreversible sulfation is modelled as a reduction in the available active surface area by Cugnet et al. [14]. Shi [111] and Jense

van Rensburg [57] both use empirical, data-driven approaches to model irreversible sulfation, rather than including it in their models. A model would need to take into account the time between full charges, to capture the crystallisation process.

A few additional processes have been explored experimentally, but are not usually included in modelling. For example, Gandhi et al. [41] consider the changes in electrode conductivity and active surface area that occur during a discharge, as well as resistance across the insulating lead sulfate layer. Liu et al. [72] show that, for a different chemistry of lithium-air, these effects are very important and can provide better fit with experimental data. Alternatively, Bensmann et al. [5] show that proton incorporation into the positive electrode is chemically possible and has some influence on the transient behaviour of the system.

In this thesis, we will focus on a single discharge or recharge of a battery, and hence do not include any degradation effects. However, the framework that we develop could be extended to models that consider such effects.

1.1.3 Solutions of battery models

Efficient numerical solutions. A major focus of recent lead-acid modelling has been to apply fast numerical methods to Newman's model for a single discharge [35, 36]. As explained by [120], one can trade off between accuracy and speed by solving the model with various degrees of implicitness. For example, one approach that has been taken to simplify the model is proper orthogonal decomposition, by Ansari et al. [2] and Esfahanian et al. [34]. Alternatively, Bizeray et al. have shown that fast and accurate numerical solutions can be obtained using Chebyshev orthogonal collocation [12]. In this thesis, we use standard numerical methods and focus our attention on developing reduced-order models analytically. We anticipate that some of the gains from developing faster numerical methods could be transferred to these reduced-order models.

Simplified one-dimensional models. Some efforts have been made to analytically reduce the complexity of the lead-acid models so that they can be solved more efficiently. Newman and Tiedemann [88] recognise that, for charges or discharges at low current, a lumped parameter model (LPM) can be used in which spatial concentration gradients are ignored. However, the link between the LPM and the full model is not explicitly stated, and so the range of validity of the LPM, and extensions to it, cannot be easily assessed. Gandhi et al. [42] also use a LPM and provide an analytical expression for the voltage in terms of current.

For lithium-ion batteries, a larger number of simplified models have been developed. The Single Particle Model (SPM) [32, 33, 80, 106, 130] is similar to Newman and Tiedemann's LPM, but includes additional physical processes that are specific to lithium-ion. The SPM can be extended to the Single Particle Model with electrolyte (SPMe) [51, 59, 81, 95, 98, 118] which takes into account concentration gradients in the electrolyte.

Recently, methods from asymptotic analysis have been used to derive reduced-order models more systematically. Richardson et al. [100, 102] use the limit of small thermal voltage relative to characteristic change in overpotential to derive an alternative SPM. Moyles et al. [82, 83] consider the limit of fast transport in the particles, and derive a 'Single Particle Model-Electrode Averaged Model' consisting of two coupled ordinary differential equations (ODEs).

Outside asymptotic analysis, some alternative approaches to model order reduction have been used, such as balanced truncation [84], proper orthogonal decomposition [18, 19, 73, 113], Padé approximation [38, 76, 125], and reduced basis method [89]. The first three of these approaches are reviewed and compared by Fan et al. [37]. An advantage of asymptotic analysis over balanced truncation, proper orthogonal decomposition and reduced basis method is that, when using asymptotic analysis, the physical parameters in the reduced-order models are the same as the physical parameters in the full model. Hence asymptotic analysis can more readily be used for parameter estimation, and give more insight into the physical behaviour of the full model. Padé approximation also preserves physical parameters and hence could be combined with asymptotic analysis to exploit the advantages of both methods. In addition to this, asymptotic analysis provides relatively simple estimates for the error in the approximation.

Three-dimensional models. Many of the models discussed so far consider a one-dimensional system in which the key direction is the through-cell direction (the x-direction in Figure 1.1) and the battery behaves uniformly in transverse directions. This is justifiable in the limit of infinite current-collector conductivity, since the voltage supplied at the tabs is applied uniformly to all points in the current collector. However, in real-life batteries with finite current-collector conductivity, non-uniform current distributions in the current collectors can lead to accelerated degradation [63, 103].

For lead-acid batteries, Bernardi et al. [7] develop a two-dimensional model that captures effects in the vertical direction. However, solving the full three-dimensional

system is computationally expensive. One common approach to simplify the system is to model the current collector as a network of nonlinear resistors, with the through-cell system acting as a nonlinear resistor [43, 60, 67]. However, these models are usually derived in an ad-hoc manner, which gives limited confidence in their validity relative to the full three-dimensional porous-electrode model.

1.2 Aims and structure of this thesis

We begin, in Chapter 2, by deriving a complete macroscale model for charge/discharge of a VRLA battery that takes into account all of the relevant physics. To do this, we first develop, from first principles, a microscale, thermodynamically consistent model for a general battery with a concentrated electrolyte, and an arbitrary number of additional species in dilute concentration. This model augments the standard porous electrode model, firstly by extending solute-volume theory to include additional species in dilute concentration, secondly by including pressure-diffusion effects, and finally by including Faradaic convection, the convective effects driven by volume changes that occur as a result of the electrochemical reactions.

We then nondimensionalise this model in order to identify the dominant physical effects, and those that can be neglected to reduce the model complexity. With this approach, we gain confidence that neglected physical effects would not significantly change the results of our model. Further, we use this insight to highlight effects that may be important in other battery chemistries. Finally, we use the method of multiple scales to derive a model on the macroscale that is based systematically on the microscale.

In Chapters 3-5, we use perturbation methods and asymptotic analysis to derive a hierarchy of reduced-order models that retain the physical insights and accuracy of the full mechanistic model but are easier to solve. First, in Chapter 3, we consider a one-dimensional model and simplify it in the limit where the timescale for diffusion is much shorter than the timescale for a full charge/discharge. This approach yields similar results to Newman and Tiedemann's approach [88], or to the SPM and SPMe for lithium-ion batteries, but in a much more systematic manner. At leading order we reduce the model to a nonlinear system of ODEs (Section 3.3.2), with spatially homogeneous behaviour. At first order, we capture spatial inhomogeneities quasi-statically, and hence require only an additional linear system of ODEs (Section 3.3.3). Finally, we extend the first-order model to a composite solution that captures diffusional transients, with only a single additional linear partial differential equation (PDE) per

species. In all cases, the complexity of the system is reduced from the original full mechanistic model.

Second, in Chapter 4, we simplify the full three-dimensional model in the physically-relevant limit in which the aspect ratio (ratio of thickness to height) of the battery is small. In this limit, we decompose the through-electrode dimension from the transverse dimensions. Hence we reduce the system of three-dimensional PDEs (hyperbolic and elliptic) to a system of one-dimensional hyperbolic PDEs coupled with two two-dimensional elliptic equations, one for each electrode. In the remainder of Chapter 4, we examine further simplifications that can be made in the limit where the timescale for diffusion is much shorter than the timescale for a full charge/discharge; here the details depend on the size of the electrode conductivity, and we explore various limits.

Third, in Chapter 5, we extend the results of Chapter 3 to a toy model for recharge in which oxygen evolution and recombination occur in addition to the main reactions. We show that the oxygen recombination reaction in the negative electrode must be diffusion limited, and explore the modelling consequences of this observation. We then extend the reduced-order models from Chapter 3 to the recharge case, and compare them to the full one-dimensional system.

In summary, the key contributions of this thesis are as follows:

- augmentation of the standard porous electrode model to include additional species, pressure-diffusion and convection;
- nondimensionalisation of the model to identify key dimensionless parameters;
- derivation of a hierarchy of reduced-order models, using asymptotic analysis, which approximate the one-dimensional model for a slow discharge;
- decomposition of three-dimensional model into through-cell and transverse directions, and further asymptotic analysis for slow discharge;
- development of a one-dimensional model for recharge with diffusion-limited oxygen kinetics, and further simplifications thereof for slow charge.

We give more detail on these contributions, draw conclusions and consider future perspectives in Chapter 6.

Chapter 2

Model

In this chapter, we begin by extending concentrated-electrolyte theory to develop an isothermal model that includes excluded-volume effects, local pressure variation, and a detailed microscopic water balance. We then perform a novel nondimensionalisation of the model to reveal a set of fundamental dimensionless parameters that control the battery's response. We use the method of multiple scales to homogenise the microscale model and obtain a macroscale porous-electrode model for a single cell in a lead-acid battery. The resulting model is similar to the standard porous-electrode model, but includes additional physics due to excluded-volume changes, pressure-diffusion and Faradaic convection. This chapter is an extension of work that has been published in [116].

2.1 Three-dimensional microscale model

To develop a battery model at the microscale, we separately consider the electrolyte (liquid) region (Sections 2.1.1 to 2.1.3), the electrode (solid) region (Section 2.1.4), and the interface between them (Section 2.1.5). Of the two bulk regions, the electrolyte is significantly more complex; we organise our development of the model in this region into three further subsections, progressing from the basic laws of thermodynamics (Section 2.1.1), through physical balances (Section 2.1.2) to experimentally-motivated constitutive laws (Section 2.1.3). We conclude by giving relevant boundary and initial conditions in Section 2.1.6.

2.1.1 Liquid electrolyte thermodynamics

In water (H_2O), sulfuric acid (H_2SO_4) dissociates mainly to hydrogen cations (H^+) and hydrogen sulfate anions ($HSO_4{}^-$); in keeping with prior models [6, 7, 47, 48], we

neglect speciation to sulfate (SO_4^{2-}). Thus the pore-filling liquid mainly comprises H_2O, HSO_4^- and H^+ with partial molar volumes $\bar{V}_\mathrm{w}$, $\bar{V}_-$ and $\bar{V}_+$, molar masses M_w, M_- and M_+, and equivalent charges 0, -1 and $+1$ respectively. Dimensional (and unscaled) variables are denoted with a hat: the species molarities are $\hat{c}_\mathrm{w}$, $\hat{c}_-$, and $\hat{c}_+$.

In addition to these three species, an arbitrary number of additional reacting species (such as dissolved oxygen or hydrogen) can be present (in dilute concentration), with concentration $\hat{c}_k$, partial molar volume $\bar{V}_k$, molar mass M_k and equivalent charge 0.

The sulfuric acid ion concentrations are related to the electric potential in the liquid, $\hat{\Phi}_\mathrm{e}$, by Gauss's law for electric fields [86],

$$-\varepsilon_0 \hat{\nabla}^2 \hat{\Phi}_\mathrm{e} = F\left(\hat{c}_+ - \hat{c}_-\right), \tag{2.1}$$

where ε_0 is the permittivity of free space and F is the Faraday constant.

Equation (2.1) introduces a characteristic length scale, known as the Debye length, on which there is diffuse charge (non-electroneutral behaviour):

$$l_\mathrm{Debye} = \sqrt{\frac{\varepsilon_0[\Phi_\mathrm{e}]}{F[c_\mathrm{e}]}}, \tag{2.2}$$

where $[\Phi_\mathrm{e}]$ and $[c_\mathrm{e}]$ are typical potential and concentration scales respectively. Typically, the Debye length is of the order of nanometres, which is much smaller than the cell length scale (millimetres) or even the pore scale (micrometres). Hence the bulk of the electrolyte is electroneutral ($\hat{c}_+ = \hat{c}_-$), with boundary layers of diffuse charge at electrode-electrolyte interfaces (called double layers). We take the electrolyte to be electroneutral everywhere, and in Section 2.1.5 incorporate the effect of the double-layer via, firstly, interfacial constitutive laws [101], and secondly capacitance in the charge-transfer at the solid-electrolyte interface.

By electroneutrality, the sulfuric acid ion concentrations relate to the sulfuric acid concentration, $\hat{c}_\mathrm{e}$, through

$$\hat{c}_\mathrm{e} = \hat{c}_+ = \hat{c}_-. \tag{2.3}$$

In the following model derivation, we define:

- $\mathcal{S}^\mathrm{all}$ to be the set of all species present in the liquid (for example, in a five-species system with oxygen and hydrogen, $\mathcal{S}^\mathrm{all} = \{\mathrm{w}, -, +, \mathrm{o}, \mathrm{h}\}$);
- $\mathcal{S}^\mathrm{other}$ to be the set of additional species (e.g. $\mathcal{S}^\mathrm{other} = \{\mathrm{o}, \mathrm{h}\}$);
- $\mathcal{S}$ to be the set of species that we will solve for in our final model (e.g. $\mathcal{S} = \{\mathrm{e}, \mathrm{o}, \mathrm{h}\}$).

If there are no additional reaction species, $\mathcal{S}$ consists only of the electrolyte. In all cases, we use subscript k to denote either individual species (such as w, +, -) or aggregations (such as 'e', for 'electrolyte').

In an isothermal state, thermodynamic consistency of the liquid volume requires that $\hat{c}_{\mathrm{w}}$ depends on $\hat{c}_k$, $k \in \mathcal{S}$ if the bulk modulus of the liquid is very large [46], through

$$\hat{c}_{\mathrm{w}} = \frac{1 - \sum_{k\in\mathcal{S}} \bar{V}_k \hat{c}_k}{\bar{V}_{\mathrm{w}}}, \tag{2.4}$$

where $\bar{V}_{\mathrm{e}} = \bar{V}_+ + \bar{V}_-$ is the partial molar volume of the acid. Consequently the total liquid molarity

$$\hat{c}_{\mathrm{T}} = 2\hat{c}_{\mathrm{e}} + \hat{c}_{\mathrm{w}} + \sum_{k\in\mathcal{S}^{\mathrm{other}}} \hat{c}_k = \frac{1 + (2\bar{V}_{\mathrm{w}} - \bar{V}_{\mathrm{e}})\hat{c}_{\mathrm{e}} + \sum_{k\in\mathcal{S}^{\mathrm{other}}} (\bar{V}_{\mathrm{w}} - \bar{V}_k)\hat{c}_k}{\bar{V}_{\mathrm{w}}} \tag{2.5}$$

also depends only on $\{\hat{c}_k\}$, $k \in \mathcal{S}$. Acid molarity further determines the mass density $\hat{\rho}$ of the liquid, because

$$\hat{\rho} = \hat{c}_{\mathrm{w}} M_{\mathrm{w}} + \sum_{k\in\mathcal{S}} \hat{c}_k M_k = \frac{M_{\mathrm{w}}}{\bar{V}_{\mathrm{w}}} + \sum_{k\in\mathcal{S}} \left[\left(\frac{M_k}{\bar{V}_k} - \frac{M_{\mathrm{w}}}{\bar{V}_{\mathrm{w}}} \right) \bar{V}_k \hat{c}_k \right], \tag{2.6}$$

in which $M_{\mathrm{e}} = M_+ + M_-$ stands for the acid's molar mass. In practice, the concentrations of species other than electrolyte are much smaller than $\hat{c}_{\mathrm{e}}$, and so the electrolyte concentration determines the density. Further, experiments show that $\hat{\rho}$ varies almost linearly with $\hat{c}_{\mathrm{e}}$ [22], so the partial molar volumes of electrolyte ions and water can be assumed to be constant [86]. We further assume that the partial molar volumes of all other species in the liquid are constant.

2.1.2 Balances in the electrolyte

The region where there is electrolyte can be divided into three subdomains: within the pores of the negative electrode, Ω_{n}, within the pores of the separator, Ω_{s}, and within the pores of the positive electrode, Ω_{p}. The model structure is identical in each subdomain. Parameters describing the electrolyte are similar everywhere, while those describing pore geometry generally differ among subdomains. Quantities that parametrize reactions differ in the negative- and positive-electrode subdomains, and vanish in the separator.

The local mass balance of species $k \in \mathcal{S}^{\mathrm{all}}$ in the liquid phase implies that

$$\frac{\partial \hat{c}_k}{\partial \hat{t}} = -\hat{\nabla} \cdot \hat{\mathbf{N}}_k, \tag{2.7}$$

where $\hat{\mathbf{N}}_k$ represents the molar flux of k. With electroneutrality condition (2.3) and equation of state (2.4), all balances (2.7) combine to show liquid-volume continuity,

$$\hat{\nabla} \cdot \hat{\mathbf{v}}^{\square} = 0, \tag{2.8}$$

in which $\hat{\mathbf{v}}^{\square} = \sum_{k \in \mathcal{S}^{\mathrm{all}}} \bar{V}_k \hat{\mathbf{N}}_k$ signifies the volume-averaged liquid velocity.

The liquid-phase current density is $\hat{\mathbf{i}}_{\mathrm{e}} = F(\hat{\mathbf{N}}_+ - \hat{\mathbf{N}}_-)$. Under Faraday's law, ion balances (2.7) combine to demonstrate charge continuity in the liquid,

$$\hat{\nabla} \cdot \hat{\mathbf{i}}_{\mathrm{e}} = 0. \tag{2.9}$$

In practice, we solve (2.7) for $k \in \mathcal{S}$ (with $\hat{c}_{\mathrm{e}} = \hat{c}_+$), and replace (2.7) for $k \in \{\mathrm{w}, -\}$ with (2.8) and (2.9).

In a general isothermal setting, liquid convection is determined by a momentum balance, such as Cauchy's equation [46, 71]. This governs the distribution of momentum density $\hat{\rho}\hat{\mathbf{v}}$, naturally expressed in terms of the mass-averaged velocity $\hat{\mathbf{v}} = \left(\sum_{k \in \mathcal{S}^{\mathrm{all}}} M_k \hat{\mathbf{N}}_k\right) / \hat{\rho}$. The kinematic relation

$$\hat{\mathbf{v}} - \hat{\mathbf{v}}^{\square} = \sum_{k \in \mathcal{S}} \left[\frac{\bar{V}_k}{\hat{\rho}} \left(\frac{M_k}{\bar{V}_k} - \frac{M_{\mathrm{w}}}{\bar{V}_{\mathrm{w}}} \right) \left(\hat{\mathbf{N}}_k - \hat{c}_k \hat{\mathbf{v}}^{\square} \right) \right] + \frac{\bar{V}_-}{\hat{\rho}} \left(\frac{M_{\mathrm{w}}}{\bar{V}_{\mathrm{w}}} - \frac{M_-}{\bar{V}_-} \right) \frac{\hat{\mathbf{i}}_{\mathrm{e}}}{F} \tag{2.10}$$

specifies how $\hat{\mathbf{v}}$ must relate to $\hat{\mathbf{v}}^{\square}$. (Note that, for convenience, we abuse notation in (2.10) by using $\mathbf{N}_{\mathrm{e}}$ to refer to $\mathbf{N}_+$).

2.1.3 Flux constitutive laws

Transport in the liquid phase is governed by $n-1$ Onsager-Stefan-Maxwell flux laws, where n is the number of species. The law for the thermodynamic force on water [46] can be inverted [71, 79, 85] to give

$$\hat{\mathbf{N}}_+ = -\hat{D}_{\mathrm{e}} \left(\hat{\nabla} \hat{c}_{\mathrm{e}} - \frac{\hat{\psi}_{\mathrm{e}} \hat{\nabla} \hat{p}}{RT} \right) + \frac{t_+^{\mathrm{w}} \hat{\mathbf{i}}_{\mathrm{e}}}{F} + \hat{c}_{\mathrm{e}} \hat{\mathbf{v}}^{\square}, \tag{2.11}$$

where R is the gas constant, T is the absolute temperature, t_+^{w} is the cation transference number relative to the water velocity, $\hat{D}_{\mathrm{e}}$ is the (concentration-dependent) diffusivity of acid in water and $\hat{p}$ is the pressure in the liquid. For $k \in \mathcal{S}$, the electrolyte pressure-diffusion factor $\hat{\psi}_k$ depends on species concentrations through

$$\hat{\psi}_k = \frac{\bar{V}_{\mathrm{w}} \hat{c}_{\mathrm{T}} M_{\mathrm{w}} \hat{c}_{\mathrm{w}} M_k \hat{c}_k}{2 \hat{\rho} \hat{\chi}_k} \left(\frac{\bar{V}_{\mathrm{w}}}{M_{\mathrm{w}}} - \frac{\bar{V}_k}{M_k} \right). \tag{2.12}$$

To put equation (2.11) in the form given, one must have that $\bar{V}_+ = (1 - t_+^{\mathrm{w}})\bar{V}_{\mathrm{e}}$ and $\bar{V}_- = t_+^{\mathrm{w}}\bar{V}_{\mathrm{e}}$ [85].

The laws for the thermodynamic force on additional species can be inverted to give equations in Nernst-Planck form that describe the excess fluxes of additional species molecules [78, 79]. These relations involve new migration coefficients and cross-diffusivities whose values are not known in practice. However, in the limit in which cross-species interactions vanish (that is, the Stefan-Maxwell diffusivity of each species through any other tends to infinity), all migration coefficients and cross-diffusivities tend to zero [78], and we retrieve Fick's law with a correction term for pressure,

$$\mathbf{N}_k = -\hat{D}_k \left(\hat{\nabla} \hat{c}_k - \frac{\hat{\psi}_k \hat{\nabla} \hat{p}}{RT} \right) + \hat{c}_k \hat{\mathbf{v}}^{\square}, \quad k \in \mathcal{S}^{\mathrm{other}}. \tag{2.13}$$

Finally, the law for the thermodynamic force on cations can be linearly transformed to produce a current/voltage relation. In the limit in which ion/oxygen, ion/hydrogen and oxygen/hydrogen interactions vanish [78], the relation is

$$\hat{\mathbf{i}}_{\mathrm{e}} = -\hat{\kappa} \hat{\nabla} \hat{\Phi}_{\mathrm{e}} + \frac{2RT\hat{\chi}_{\mathrm{e}}(1 - t_+^{\mathrm{w}})\hat{\kappa}}{F\bar{V}_{\mathrm{w}}\hat{c}_{\mathrm{T}}} \left(\hat{\nabla} \ln \hat{c}_{\mathrm{e}} - \frac{\hat{\psi}_{\mathrm{e}} \hat{\nabla} \hat{p}}{RT\hat{c}_{\mathrm{e}}} \right) + \frac{\hat{\kappa} M_+ \hat{\nabla} \hat{p}}{F\hat{\rho}}. \tag{2.14}$$

Here $\hat{\kappa}$ is the conductivity of sulfuric acid, $\hat{\Phi}_{\mathrm{e}}$ is the potential measured by a reversible hydrogen electrode at $\hat{p}$ [11], and $\hat{\chi}_{\mathrm{e}}(\hat{c}_{\mathrm{e}})$ is the thermodynamic Darken factor ([31], reported by [71]), which describes the mixing free energy of the electrolyte.

A momentum balance closes the model [71]; for example, the Cauchy equation

$$\hat{\rho} \left(\frac{\partial \hat{\mathbf{v}}}{\partial \hat{t}} + \hat{\mathbf{v}} \cdot \hat{\nabla} \hat{\mathbf{v}} \right) = -\hat{\nabla} \hat{p} + \hat{\nabla} \cdot \hat{\tau}, \tag{2.15a}$$

where the deviatoric stress tensor $\hat{\tau}$ is given by Newton's law of viscosity,

$$\hat{\tau} = \lambda \left(\hat{\nabla} \cdot \hat{\mathbf{v}} \right) + \mu \left(\hat{\nabla} \hat{\mathbf{v}} + \left(\hat{\nabla} \hat{\mathbf{v}} \right)^T \right), \tag{2.15b}$$

where λ is the bulk viscosity and μ is the shear viscosity. The mass-averaged velocity, $\hat{\mathbf{v}}$, is used in (2.15) because (2.15) is derived by combining the momentum balances for individual species [46]. There is debate over what the exact form of the advection term on the left-hand side of (2.15a) should be [46]. However, this is not important for our present study, since we will show below that terms involving momentum are negligible in the first approximation.

2.1.4 Balance and constitutive law in the solid electrode

In the electrodes, conservation of current implies

$$\hat{\nabla} \cdot \hat{\mathbf{i}}_{\mathrm{s}} = 0, \tag{2.16}$$

where $\hat{\mathbf{i}}_{\mathrm{s}}$ is the solid-phase current density. The solid phase is electronically but not ionically conductive. Thus the current density there relates to the solid-phase potential, $\hat{\Phi}_{\mathrm{s}}$, through Ohm's law,

$$\hat{\mathbf{i}}_{\mathrm{s}} = -\hat{\sigma}\hat{\nabla}\hat{\Phi}_{\mathrm{s}}, \tag{2.17}$$

where $\hat{\sigma}$ is the electrode conductivity.

2.1.5 Interfacial constitutive laws

To link the electrolyte model with the electrode model, we must derive equations describing behaviour at the interface between the two. However, there are several interfaces to consider: a 'solid-electrolyte' interface between the electrolyte and the conductive electrode (lead or lead dioxide), but also an 'electrolyte-discharge-product' interface between the electrolyte and the discharge-product layer of lead sulfate, and similarly a 'solid-discharge-product' interface.

For simplicity, we would like to consider a single interface. We assume that the creation of lead sulfate reduces the porosity, and induces a flow in the electrolyte. Hence we choose the 'electrolyte-discharge-product' layer to be our single interface, denoted by $\hat{\mathbf{x}} = \mathbf{S}$. Since the reaction must occur at the 'solid-electrolyte' interface, we assume that transport of electrolyte is instantaneous from the 'electrolyte-discharge-product' interface, across the porous discharge-product layer, to the 'solid-electrolyte' interface.

Electrons are the only solid-phase charge carrier in the scheme consisting of reactions (1.1), (1.2) and (1.3), making interfacial current densities a proxy for the half-reaction rates. We denote the interfacial current density due to the main reactions (1.1) by $\hat{j}^{\mathrm{S}}$, and additional reactions (such as for example (1.2) or (1.3), or reactions that lead to degradation) by $\hat{j}^{r}$. The set of all kinetic reactions, including the main reaction, is denoted by $\mathcal{R}$. Continuity of current requires that

$$\hat{\mathbf{i}}_{\mathrm{s}} \cdot \mathbf{n} = \hat{j}^{\mathrm{dl}} + \sum_{r \in \mathcal{R}} \hat{j}^{r} = \hat{\mathbf{i}}_{\mathrm{e}} \cdot \mathbf{n} \quad \text{on } \hat{\mathbf{x}} = \mathbf{S}, \tag{2.18}$$

where $\mathbf{n}$ is the unit normal to $\mathbf{S}$, pointing out of the electrode (into the electrolyte), and $\hat{j}^{\mathrm{dl}}$ is the double-layer interfacial current density due to charge stored in the

double layer. We assume that the double-layer interfacial current density takes the form

$$\hat{j}^{\mathrm{dl}} = \hat{C}^{\mathrm{dl}} \frac{\partial}{\partial \hat{t}} \left(\hat{\Phi}_{\mathrm{s}} - \hat{\Phi}_{\mathrm{e}} \right), \tag{2.19}$$

where $\hat{C}^{\mathrm{dl}}$ is the double-layer capacitance [40, 90, 115]. We define $\mathcal{R}^{\mathrm{dl}}$ to be the set of all interfacial current densities including the double-layer interfacial current density.

As reactions (1.1) occur, deposition (removal) of solid $PbSO_4$ on pore surfaces is accompanied by removal (deposition) of solid Pb or PbO_2, and so the electrode surface itself moves. This deposition/removal process is significant enough to halve the electrode porosities over a full discharge, and so should be included in the model. We define $\hat{v}^{\mathrm{surf}}_{\mathrm{normal}}$ to be the normal velocity of the interface due to the creation of lead sulfate. Accounting for this electrode surface normal velocity and using Faraday's law of electrolysis, the molar flux of species $k \in \mathcal{S}^{\mathrm{all}}$ normal to the surface is [61, 71, 124]

$$\hat{\mathbf{N}}_k \cdot \mathbf{n} = \hat{c}_k \hat{v}^{\mathrm{surf}}_{\mathrm{normal}} - \sum_{r \in \mathcal{R}} \frac{\hat{s}^r_k \hat{j}^r}{F n^r_{\mathrm{e}^-}} \quad \text{on } \hat{\mathbf{x}} = \mathbf{S}, \tag{2.20}$$

where $\hat{s}^r_k$ is the signed stoichiometric coefficient of species k in the half-reaction r, and $n^r_{\mathrm{e}^-}$ is the number of electrons transferred in the reaction. (For a reduction half-reaction, s_k is positive for a product and negative for a reactant. For example, $\hat{s}^{\mathrm{S}}_{\mathrm{e,n}} = -3$, by (1.1a), and $\hat{s}^{\mathrm{H}}_{\mathrm{h}} = 2$, by (1.3)). Note that terms due to the normal velocity of the moving boundary, $\hat{v}^{\mathrm{surf}}_{\mathrm{normal}}$, did not appear in (2.18), because of the definition of liquid-phase current density ($\hat{\mathbf{i}}_{\mathrm{e}} = F(\hat{\mathbf{N}}_+ - \hat{\mathbf{N}}_-)$) and electroneutrality (2.3).

By considering conservation of mass of solid species, electrode surface normal velocity is given by

$$\hat{v}^{\mathrm{surf}}_{\mathrm{normal}} = -\frac{\hat{s}_{\mathrm{Pb}} \bar{V}_{\mathrm{Pb}} + \hat{s}_{\mathrm{PbO_2}} \bar{V}_{\mathrm{PbO_2}} + \hat{s}_{\mathrm{PbSO_4}} \bar{V}_{\mathrm{PbSO_4}}}{F n^{\mathrm{S}}_{\mathrm{e}^-}} \hat{j}^{\mathrm{S}}. \tag{2.21}$$

Note that $\hat{v}^{\mathrm{surf}}_{\mathrm{normal}}$ depends only on the interfacial current density due to main half-reactions (1.1), j^{S}, since these are the only reactions that act on solid species. Multiplying each interfacial flux condition (2.20) by $\bar{V}_k$, summing over all species, using (2.4), and requiring that no electrolyte pass through the interface, we obtain an interfacial condition for $\hat{\mathbf{v}}^{\square}$ [71]

$$\hat{\mathbf{v}}^{\square} \cdot \mathbf{n} = \hat{v}^{\mathrm{surf}}_{\mathrm{normal}} - \sum_{r \in \mathcal{R}} \sum_{k \in \mathcal{S}^{\mathrm{all}}} \frac{\hat{s}^r_k \bar{V}_k \hat{j}^r}{F n^r_{\mathrm{e}^-}} \quad \text{on } \hat{\mathbf{x}} = \mathbf{S}. \tag{2.22}$$

Equation (2.22) can be interpreted as conservation of volume in the liquid. Due to the viscous terms in (2.15b), we require an additional boundary condition for $\hat{\mathbf{v}}$ at the electrode-electrolyte interface, and we take this to be no-slip so that

$$\hat{\mathbf{v}} \cdot \mathbf{t} = \mathbf{0} \quad \text{on } \hat{\mathbf{x}} = \mathbf{S}, \tag{2.23}$$

where $\mathbf{t}$ is the unit tangent vector to $\hat{\mathbf{x}} = \mathbf{S}$. Note that individual species can still move tangentially to the boundary.

To complete the model, we specify a form for the interfacial current densities, $\hat{j}^r$. No interfacial reactions occur in the separator domain, so $\hat{j}^r = 0$ uniformly there. In the electrode domains, $\hat{j}^r$ is governed by a chemical-kinetic constitutive law. Generally such laws involve the voltage difference between the liquid and solid, the equilibrium potential of the half-reaction, and the chemical activities of the reactants. We assume the half-reactions in (1.1), (1.2) and (1.3) are elementary, following Butler-Volmer kinetics,

$$\hat{j}^r = \hat{j}^r_{0\mathrm{a}} \exp\left(\frac{n^r_{\mathrm{e}^-}\alpha^r F\hat{\eta}^r}{RT}\right) - \hat{j}^r_{0\mathrm{c}} \exp\left(-\frac{n^r_{\mathrm{e}^-}\left(1-\alpha^r\right)F\hat{\eta}^r}{RT}\right), \quad r \in \mathcal{R}, \tag{2.24}$$

where $\hat{j}_{0\mathrm{a}}$ and $\hat{j}_{0\mathrm{c}}$ are the concentration-dependent exchange-current densities (forward and backwards respectively), $\alpha^r \in (0,1)$ are Butler-Volmer symmetry factors, and $\hat{\eta}^r$ are the surface overpotentials

$$\hat{\eta}^r = \hat{\Phi}_{\mathrm{s}} - \hat{\Phi}_{\mathrm{e}} - \hat{U}^r\left(\hat{c}_{\mathrm{e}}\right), \quad r \in \mathcal{R}. \tag{2.25}$$

Here $\hat{U}^r\left(\hat{c}_{\mathrm{e}}\right)$ stands for the half-reaction's open-circuit potential (OCP) relative to a reversible hydrogen electrode. We summarise typical forms of $\hat{j}^r_0$ in Table B.3. It can be shown that the Butler-Volmer reaction accounts for behaviour in the Debye layers [101].

2.1.6 Boundary and initial conditions

Boundary conditions. Equations (2.3) to (2.25) comprise a three-dimensional model with closure at every interior point in a cell.

Symmetry and no-flux boundary conditions demand that no species in the liquid phase flows through the sides, front, back, and bottom of the cell (the external boundaries, denoted by $\partial\hat{\Omega}_{\mathrm{ext}}$), so

$$\hat{\mathbf{N}}_k \cdot \mathbf{n} = \hat{\mathbf{i}}_{\mathrm{e}} \cdot \mathbf{n} = \hat{\mathbf{v}} \cdot \mathbf{n} = 0 \quad \text{on } \partial\hat{\Omega}_{\mathrm{ext}}, \tag{2.26}$$

for $k \in \mathcal{S}$ (with $\hat{c}_\mathrm{e} = \hat{c}_+$), and the no-slip condition at these boundaries further requires

$$\hat{\mathbf{v}} = \mathbf{0} \quad \text{on } \partial\hat{\Omega}_\mathrm{ext}. \tag{2.27}$$

The kinematic relation (2.10) shows that $\hat{\mathbf{v}}^\square \cdot \mathbf{n} = 0$ at these boundaries too, and the flux laws (2.11), (2.14), and (2.15) further require the surface-normal gradients $\partial\hat{c}_k/\partial\mathrm{n}$, $\partial\hat{p}/\partial\mathrm{n}$ and $\partial\hat{\Phi}_\mathrm{e}/\partial\mathrm{n}$ to vanish at these boundaries.

Above the electrodes, there is a head region of free electrolyte. For simplicity, we assume that the electrolyte region is well-mixed, so that species concentrations are spatially uniform, denoted by $\hat{c}_k^\mathrm{head}(t)$, and the flow is dominated by gravity, so that the surface has uniform height $\hat{h}\left(\hat{t}\right)$. At the interface between porous cell and free electrolyte, the concentration of all species is continuous,

$$\hat{c}_k = \hat{c}_k^\mathrm{head} \quad \text{on } \hat{z} = \hat{H}. \tag{2.28}$$

By conservation of mass, the head concentration of each species is determined by its average flux at the interface,

$$\frac{\mathrm{d}}{\mathrm{d}\hat{t}}\left(\hat{h}\hat{c}_k^\mathrm{head}\right) = \frac{1}{\hat{L}\hat{W}}\int_0^{\hat{L}}\int_0^{\hat{W}} \hat{\mathbf{N}}_k \cdot \mathbf{n}\Big|_{\hat{z}=\hat{H}} \,\mathrm{d}\hat{x}\,\mathrm{d}\hat{y} \quad \text{for } k \in \mathcal{S}^\mathrm{all}. \tag{2.29}$$

It is worth noting that multiplying each condition (2.29) by z_k and summing over all k gives a boundary condition for the current,

$$\mathbf{i}_\mathrm{e} \cdot \mathbf{n} = 0 \quad \text{at } \hat{z} = \hat{H}, \tag{2.30}$$

and similarly multiplying each condition (2.29) by $\bar{V}_k$ and summing over all k determines the head height $\hat{h}\left(\hat{t}\right)$:

$$\frac{\mathrm{d}\hat{h}}{\mathrm{d}\hat{t}} = \frac{1}{\hat{L}\hat{W}}\int_0^{\hat{L}}\int_0^{\hat{W}} \hat{\mathbf{v}}^\square \cdot \mathbf{n}\big|_{\hat{z}=\hat{H}} \,\mathrm{d}\hat{x}\,\mathrm{d}\hat{y}. \tag{2.31}$$

In subsequent work we will use (2.30) and (2.31) rather than the complete set (2.29). Finally, we assume that the pressure at the cell/free region interface is purely hydrostatic,

$$\hat{p} = p_\mathrm{ext} + \hat{\rho}g\hat{h} \quad \text{at } \hat{z} = \hat{H}, \tag{2.32}$$

where p_ext is an external pressure, which could be measured directly or assumed to be atmospheric pressure, and g is gravitational acceleration. We could model the head region more carefully by considering flow and the spatial distribution of electrolyte within this region, but this is beyond the scope of this thesis.

We choose the negative electrode tab to be at the ground state,

$$\hat{\Phi}_{\mathrm{s}} = 0 \quad \text{on } \partial\hat{\Omega}_{\mathrm{tab,n}}. \tag{2.33}$$

For the positive electrode tab, we can either control the voltage,

$$\hat{\Phi}_{\mathrm{s}} = \hat{V}\left(\hat{t}\right) \quad \text{on } \partial\hat{\Omega}_{\mathrm{tab,p}}, \tag{2.34a}$$

or control the current. In the latter case, we can either impose an integral for the current and uniform potential across the tab,

$$\iint_{\partial\hat{\Omega}_{\mathrm{tab,p}}} \hat{\mathbf{i}}_{\mathrm{s}} \cdot \mathbf{n} \mathrm{d}S = \hat{\mathrm{I}}\left(\hat{t}\right), \tag{2.34b}$$

$$\Phi_{\mathrm{s}} \text{ uniform on } \partial\hat{\Omega}_{\mathrm{tab,p}}, \tag{2.34c}$$

where the current drawn from the cell, $\hat{\mathrm{I}}$, is positive for a discharge, or impose a uniform current on the tab,

$$A_{\mathrm{tab,p}}\hat{\mathbf{i}}_{\mathrm{s}} \cdot \mathbf{n} = \hat{\mathrm{I}}\left(\hat{t}\right), \tag{2.34d}$$

where $A_{\mathrm{tab,p}}$ is the cross-sectional area of the tab. We choose the latter since it is easier to implement numerically, but in practice there is little difference between the two since the solid potential is usually uniform over short distances (such as the tab width) anyway. Note that we define the cell interfacial current density to be

$$\hat{\mathcal{I}}\left(\hat{t}\right) = \hat{\mathrm{I}}\left(\hat{t}\right)/A_{\mathrm{cs}}. \tag{2.34e}$$

Third and fourth alternatives are to control the power or resistance, in which case we apply both (2.34a) and (2.34b), but leave $\hat{V}$ and $\hat{\mathrm{I}}$ as free variables, and add an algebraic equation

$$\hat{V}\hat{\mathrm{I}} = \hat{P}\left(\hat{t}\right) \text{ (for power control)}, \quad \text{or} \quad \hat{V}/\hat{\mathrm{I}} = \hat{R}\left(\hat{t}\right) \text{ (for resistance control)}, \tag{2.34f}$$

where the power $\hat{P}$ or resistance $\hat{R}$ are known functions of time.

In this thesis, we will mainly consider experiments under 'galvanic control' following condition (2.34b), which allows $\hat{\mathrm{I}}\left(\hat{t}\right)$ to be any function of time.

Relationships between subdomains. The liquid phase permeates all three subdomains. Therefore scalar variables $\hat{c}_{\mathrm{e}}$, $\hat{p}$, and $\hat{\Phi}_{\mathrm{e}}$, as well as normal components of all flux vectors, are all continuous across electrode/separator boundaries.

There is no solid-phase current at either edge of the separator subdomain or pore-surface charge exchange within it, so $\hat{\mathbf{i}}_{\mathrm{s}} \cdot \mathbf{n}$ vanishes uniformly there. Since the separator subdomain electronically isolates the positive and negative electrodes, $\hat{\Phi}_{\mathrm{s}}$ need not be defined across it.

Initial conditions. The initial concentrations and potential difference are spatially uniform. To allow a simple interpretation for a typical battery, we relate the initial electrolyte concentration to the state of charge, q, which we define as

$$q = q^0 - \frac{1}{A_{\mathrm{cs}}\hat{L}\hat{\mathcal{Q}}_{\mathrm{e}}^{\max}} \int_0^{\hat{t}} \hat{\mathrm{I}}(s)\,\mathrm{d}s, \tag{2.35}$$

where $\hat{\mathcal{Q}}_{\mathrm{e}}^{\max}$ is the volumetric capacity of the battery, in $\mathrm{C/m^3}$. We calculate $\hat{\mathcal{Q}}_{\mathrm{e}}^{\max}$ in Appendix B. Note that this definition of q means that $q = 0$ and $q = 1$ does not necessarily correspond to the min/max voltage on the manufacturer's spec sheet.

In a lead-acid battery, the state of charge is closely linked to the concentration of the electrolyte. Hence we would like q to be unity when the concentration of the electrolyte is at its maximum value, $c_{\mathrm{e}}^{\max}$, and zero when the concentration of the electrolyte is zero, so that the initial condition for the concentration is taken as

$$\hat{c}_{\mathrm{e}}\left(\hat{\mathbf{x}}, 0\right) = \hat{c}_{\mathrm{e}}^0 = c_{\mathrm{e}}^{\max} q^0. \tag{2.36}$$

We take the initial concentration of any additional dissolved species to be zero,

$$\hat{c}_k\left(\hat{\mathbf{x}}, 0\right) = 0, \quad k \in \mathcal{S}^{\mathrm{other}}. \tag{2.37}$$

Because of double-layer capacitance effects, we also require initial conditions for the potential difference, $\Phi_{\mathrm{s}} - \Phi_{\mathrm{e}}$. We choose spatially homogeneous values such that the interfacial current density given by (2.24) is zero at $\hat{t} = 0$ for the main reactions ($r = S$):

$$\hat{\Phi}_{\mathrm{s}}\left(\hat{\mathbf{x}}, 0\right) - \hat{\Phi}_{\mathrm{e}}\left(\hat{\mathbf{x}}, 0\right) = \hat{U}^{\mathrm{S}}\left(\hat{c}_{\mathrm{e}}^0\right). \tag{2.38}$$

Finally, we must also provide initial conditions for the species concentrations in the head, $\hat{c}_k^{\mathrm{head}}$, and head height, $\hat{h}$. For the former, we assume that the initial concentrations are the same as in the bulk. For the latter, we impose some initial head height $\hat{h}^0$, which should be on the order of a few millimetres. The exact value of $\hat{h}^0$ does not matter for the purposes of this thesis, but we simply note that $\hat{h}^0$ must be positive so that the electrodes are immersed in electrolyte.

2.2 Dimensionless model

We now nondimensionalise the system presented in Section 2.1 with the aim of determining the dominant effects in the system.

We begin by introducing dimensionless variables

$$\mathbf{x} = \hat{\mathbf{x}}/\hat{L}, \quad (\mathbf{i}_{\mathrm{e}}, \mathbf{i}_{\mathrm{s}}, \mathcal{I}) = (\hat{\mathbf{i}}_{\mathrm{e}}, \hat{\mathbf{i}}_{\mathrm{s}}, \hat{\mathcal{I}})/\bar{\imath}, \quad c_k = \hat{c}_k/c_{\mathrm{e}}^{\max}, \tag{2.39}$$

for $k \in \mathcal{S}$, where $\bar{i} = \max_{\hat{t}} \left(\hat{\mathcal{I}}(\hat{t}) \right)$. We also scale subdomain thicknesses $\hat{\ell}_i$, $i \in \{\mathrm{n}, \mathrm{s}, \mathrm{p}\}$, and macroscale dimensions $\hat{L}$, $\hat{W}$ and $\hat{H}$, with $\hat{L}$ (so the dimensionless battery thickness is equal to one).

We scale time with the discharge time-scale, $c_{\mathrm{e}}^{\max} F \hat{L} / \bar{i}$:

$$t = \hat{t} \Bigg/ \frac{c_{\mathrm{e}}^{\max} F \hat{L}}{\bar{i}} \,. \tag{2.40}$$

To nondimensionalise the interfacial current, we consider a representative material volume in the porous electrode, Ω_{ref}, within which the electrode-electrolyte interface is represented by $\partial\Omega_{\mathrm{ref}}$. Integrating (2.18) over $\partial\Omega_{\mathrm{ref}}$, and applying the divergence theorem, we find that

$$\int_{\Omega_{\mathrm{ref}}} \hat{\nabla} \cdot \hat{\mathbf{i}}_{\mathrm{e}} \, \mathrm{d}V = \int_{\partial\Omega_{\mathrm{ref}}} \sum_{r \in \mathcal{R}^{\mathrm{dl}}} \hat{j}^r \, \mathrm{d}S. \tag{2.41}$$

Applying the current scaling in (2.39) appropriately to (2.41) gives

$$\frac{\bar{i}}{\hat{L}} \sim \mathcal{A}[j], \tag{2.42}$$

where $\mathcal{A}$ is the reactive interfacial surface area per unit volume, which is in general different in the negative and positive electrodes. Hence the scale for the interfacial current density is

$$[j] = \frac{\bar{i}}{\mathcal{A}\hat{L}} =: \delta_{\mathrm{p}} \bar{i}, \tag{2.43}$$

We nondimensionalise the interfacial current densities, $\hat{j}^r$, the exchange-current densities, $\hat{j}^r_{0\mathrm{a}}$ and $\hat{j}^r_{0\mathrm{c}}$, and the double-layer current density, $\hat{j}^{\mathrm{dl}}$, with the scale (2.43) (with appropriate choice of $\mathcal{A}$ depending on the domain). After nondimensionalisation, $j^{\mathrm{S}}_{0\mathrm{a}}$ and $j^{\mathrm{S}}_{0\mathrm{c}}$ are $\mathcal{O}(1)$ functions of c_{e}.

To nondimensionalise the potentials, we note that the dominant exponents in (2.24) should be $\mathcal{O}(1)$, since the terms multiplying the exponential functions are all $\mathcal{O}(1)$. We make use of (B.1) to define the dimensionless open-circuit potentials

$$U^r\left(c_{\mathrm{e}}\right) = \begin{cases} \frac{F}{RT}\left(\hat{U}^r\left(\hat{c}_{\mathrm{e}}\right) - U_{\mathrm{n}}^{\mathrm{S},\ominus} \right), & x \in \Omega_{\mathrm{n}}, \\ \frac{F}{RT}\left(\hat{U}^r\left(\hat{c}_{\mathrm{e}}\right) - U_{\mathrm{p}}^{\mathrm{S},\ominus} \right), & x \in \Omega_{\mathrm{p}}. \end{cases} \tag{2.44a}$$

Then, to ensure that the exponents in (2.24) are $\mathcal{O}(1)$ and noting that $\hat{\Phi}_{\mathrm{s}} = 0$ at $\hat{x} = 0$, we introduce the dimensionless potentials

$$\Phi_{\mathrm{e}} = \frac{F}{RT}\left(\hat{\Phi}_{\mathrm{e}} + U_{\mathrm{n}}^{\mathrm{S},\ominus} \right), \tag{2.45a}$$

$$\Phi_{\mathrm{s}} = \begin{cases} \frac{F}{RT}\hat{\Phi}_{\mathrm{s}}, & x \in \Omega_{\mathrm{n}}, \\ \frac{F}{RT}\left(\hat{\Phi}_{\mathrm{s}} - U_{\mathrm{n}}^{\mathrm{S},\ominus} + U_{\mathrm{p}}^{\mathrm{S},\ominus} \right), & x \in \Omega_{\mathrm{p}}. \end{cases} \tag{2.45b}$$

We scale $\hat{D}_\mathrm{e}$ and $\hat{c}_\mathrm{w}$ with their values at $c_\mathrm{e} = c_\mathrm{e}^{\max}$. However, we need to be slightly more careful when nondimensionalising the MacInnes equation, (2.14). When deriving the MacInnes equation, we can show that $\hat{\kappa}\left(\hat{c}_\mathrm{e}\right) \sim F^2 \hat{D}_\mathrm{e} \hat{c}_\mathrm{e} / RT$ [11, 71]. Hence we introduce the dimensionless conductivity

$$\kappa\left(c_\mathrm{e}\right) = \hat{\kappa}\left(\hat{c}_\mathrm{e}\right) \Big/ \frac{F^2 D_\mathrm{e}^{\max} c_\mathrm{e}^{\max}}{RT} \,. \tag{2.46}$$

Then, substituting the nondimensionalisations (2.39), (2.45a) and (2.46) into (2.14), we find

$$\begin{aligned} \mathbf{i}_\mathrm{e} = {} & \frac{c_\mathrm{e}^{\max} D_\mathrm{e}^{\max} F}{\hat{L}\bar{i}} \kappa\left(c_\mathrm{e}\right) \\ & \times \left(\frac{2(1-t_+^\mathrm{w}) \hat{\chi}_\mathrm{e}\left(\hat{c}_\mathrm{e}\right)}{\hat{c}_T\left(\{c_k\}\right)} \left(\nabla \ln\left(c_\mathrm{e}\right) - \pi_\mathrm{os} \frac{\psi_\mathrm{e}}{c_\mathrm{e}} \nabla p \right) - \nabla \Phi_\mathrm{e} + \pi_\mathrm{os} \frac{M_+ c_\mathrm{e}^{\max}}{\rho^{\max} \rho} \nabla p \right). \end{aligned} \tag{2.47}$$

We can simplify (2.47) in two ways. Firstly, we identify the leading fraction on the right-hand side to be the inverse of the diffusional C-rate,

$$\mathcal{C}_\mathrm{e} = \frac{\hat{L}\bar{i}}{c_\mathrm{e}^{\max} D_\mathrm{e}^{\max} F} = \frac{\hat{L}^2}{D_\mathrm{e}^{\max}} \times \frac{Q}{8 A_\mathrm{cs} c_\mathrm{e}^{\max} F \hat{L}} \times \frac{8 A_\mathrm{cs} \bar{i}}{Q}, \tag{2.48}$$

where Q is the capacity of the battery (in Ah), $8 A_\mathrm{cs} c_\mathrm{e}^{\max} F \hat{L}$ is the volumetric capacity of the battery (in Ah), and $\mathcal{C} = 8 A_\mathrm{cs} \bar{i} / Q$ is the C-rate of operation, which is defined as the current through the battery divided by the current under which the battery would deliver its nominal rated capacity in one hour and is usually specified by the manufacturer. Alternatively, we can identify $\mathcal{C}_\mathrm{e}$ to be the ratio between the applied current scale, $\bar{i}$, and the limiting current, $i_\mathrm{L} = c_\mathrm{e}^{\max} D_\mathrm{e}^{\max} F / \hat{L}$.

Secondly, we use the form (2.5) of $\hat{c}_T$ to define

$$\chi_\mathrm{e}\left(\{c_k\}\right) = \frac{2(1-t_+^\mathrm{w}) \hat{\chi}_\mathrm{e}\left(\hat{c}_\mathrm{e}\right)}{1 + (2\bar{V}_\mathrm{w} - \bar{V}_\mathrm{e}) c_\mathrm{e}^{\max} c_\mathrm{e} + (\bar{V}_\mathrm{w} - \bar{V}_\mathrm{o}) c_\mathrm{o}^{\max} c_\mathrm{o} + (\bar{V}_\mathrm{w} - \bar{V}_\mathrm{h}) c_\mathrm{h}^{\max} c_\mathrm{h}}, \tag{2.49}$$

which is $\mathcal{O}(1)$. (The factor '$-(2\bar{V}_\mathrm{w} - \bar{V}_\mathrm{e}) c_\mathrm{e}^{\max}$' is defined by Liu and Monroe [71] as the excluded-volume number.)

We scale all the fluxes, $\hat{\mathbf{N}}_k$, with the diffusive flux scale $D_\mathrm{e}^{\max} c_\mathrm{e}^{\max} / \hat{L}$. To scale the velocity equations (2.8), (2.15) and (2.10), we scale $\hat{\rho}$ and $\hat{\mu}$ with their values at $c_\mathrm{e}^{\max}$ and choose the reaction velocity scale $v^\mathrm{rxn} = \bar{i} / c_\mathrm{e}^{\max} F$ and Stokes flow pressure scale $\mu^{\max} v^\mathrm{rxn} / \hat{L}^2$, so that

$$\mathbf{N}_k = \hat{\mathbf{N}}_k \Big/ \frac{D_\mathrm{e}^{\max} c_\mathrm{e}^{\max}}{\hat{L}} \,, \quad \left(\mathbf{v}^\square, \mathbf{v}\right) = \left(\hat{\mathbf{v}}^\square, \hat{\mathbf{v}}\right) \Big/ \frac{\bar{i}}{c_\mathrm{e}^{\max} F} \,, \quad p = p^\mathrm{ref} + \hat{p} \Big/ \frac{\mu^{\max} v^\mathrm{rxn}}{\hat{L}^2} \,, \tag{2.50}$$

for $k \in \mathcal{S}$, where p^{ref} is a reference pressure (e.g. atmospheric). We scale the deviatoric stress tensor $\hat{\tau}$ with $v^{\mathrm{rxn}}/\hat{L}^2$.

The pressure-diffusion factors $\hat{\psi}_k$ are already dimensionless and $\mathcal{O}(1)$, so we define

$$\psi_k\left(\{c_j\}\right) = \hat{\psi}_k\left(\{c_{\mathrm{e}}^{\max} c_j\}\right). \tag{2.51}$$

With these choices of scaling, the dimensionless model at the microscale is, in the electrolyte domain,

$$\frac{\partial c_k}{\partial t} = -\frac{1}{\mathcal{C}_{\mathrm{e}}} \nabla \cdot \mathbf{N}_k, \tag{2.52a}$$

$$\mathbf{N}_k = -\left(\mathcal{D}_k D_k \left(\nabla c_k - \pi_{\mathrm{os}} \psi_k \nabla p\right)\right) + \mathcal{C}_{\mathrm{e}} t_k^{\mathrm{w}} \mathbf{i}_{\mathrm{e}} + \mathcal{C}_{\mathrm{e}} c_k \mathbf{v}^{\square}, \tag{2.52b}$$

$$\nabla \cdot \mathbf{i}_{\mathrm{e}} = 0, \tag{2.52c}$$

$$\mathcal{C}_{\mathrm{e}}\, \mathbf{i}_{\mathrm{e}} = \kappa \left(\chi_{\mathrm{e}} \nabla \ln\left(c_{\mathrm{e}}\right) - \nabla \Phi_{\mathrm{e}} + \pi_{\mathrm{os}} \left(\frac{M_+ c_{\mathrm{e}}^{\max}}{\rho^{\max} \rho} - \frac{\chi_{\mathrm{e}} \psi_{\mathrm{e}}}{c_{\mathrm{e}}} \right) \nabla p \right), \tag{2.52d}$$

$$\nabla \cdot \mathbf{v}^{\square} = 0, \tag{2.52e}$$

$$\rho\left(\mathbf{v} - \mathbf{v}^{\square}\right) = \sum_{k \in \mathcal{S}} \left[\frac{\omega_{c,k} \mathcal{D}_k D_k}{\mathcal{C}_{\mathrm{e}}} \left(\nabla c_k - \pi_{\mathrm{os}} \psi_k \nabla p\right) \right] + \omega_i \mathbf{i}_{\mathrm{e}}, \tag{2.52f}$$

$$\mathrm{Re}\, \rho \left(\frac{\partial \mathbf{v}}{\partial t} + \mathbf{v} \cdot \nabla \mathbf{v} \right) = -\nabla p + \mu \nabla^2 \mathbf{v}; \tag{2.52g}$$

in the electrode domain,

$$\nabla \cdot \mathbf{i}_{\mathrm{s}} = 0, \tag{2.52h}$$

$$\mathbf{i}_{\mathrm{s}} = -\sigma \nabla \Phi_{\mathrm{s}}; \tag{2.52i}$$

and at the electrolyte-electrode interface,

$$\mathbf{N}_k \cdot \mathbf{n} = \delta_{\mathrm{p}} \mathcal{C}_{\mathrm{e}} \left(\beta^{\mathrm{surf}} c_k j^S - \sum_{r \in \mathcal{R}} s_k^r j^r \right), \tag{2.52j}$$

$$\mathbf{i}_{\mathrm{e}} \cdot \mathbf{n} = \delta_{\mathrm{p}} \sum_{r \in \mathcal{R}^{\mathrm{dl}}} j^r, \tag{2.52k}$$

$$\mathbf{v}^{\square} \cdot \mathbf{n} = \delta_{\mathrm{p}} \sum_{r \in \mathcal{R}} \beta^r j^r, \tag{2.52l}$$

$$\mathbf{i}_{\mathrm{s}} \cdot \mathbf{n} = \delta_{\mathrm{p}} \sum_{r \in \mathcal{R}^{\mathrm{dl}}} j^r, \tag{2.52m}$$

$$j^r = j^r\left(\{c_k\}, \Phi_{\mathrm{s}} - \Phi_{\mathrm{e}}\right), \tag{2.52n}$$

$$j^{\mathrm{dl}} = C^{\mathrm{dl}} \frac{\partial}{\partial t} \left(\Phi_{\mathrm{s}} - \Phi_{\mathrm{e}}\right). \tag{2.52o}$$

In (2.52b), we have defined $t_{\mathrm{e}}^{\mathrm{w}} = t_+^{\mathrm{w}}$, and $t_k^{\mathrm{w}} = 0$ otherwise.

The dimensionless parameters $\mathcal{C}_{\mathrm{e}}$, $\mathcal{D}_k$, π_{os}, $\omega_{c,k}$, ω_i, Re, σ, β^{surf}, β^r, δ_{p} and C^{dl} are summarised in Table 2.1, and we define $s_k^r = \hat{s}_k^r / n_{\mathrm{e}^-}^r$.

Parameter	Definition	Interpretation	Value		
			n	sep	p
$\mathcal{C}_\mathrm{e}$	$\dfrac{\bar{i}}{c_\mathrm{e}^\mathrm{max} D_\mathrm{e}^\mathrm{max} F/\hat{L}}$	$\dfrac{\text{applied current density}}{\text{limiting current density}}$	$0.60\mathcal{C}$		
$\mathcal{D}_k$	$\dfrac{D_k^\mathrm{max}}{D_\mathrm{e}^\mathrm{max}}$	$\dfrac{\text{species diffusivity scale}}{\text{electrolyte diffusivity scale}}$	o: 0.65 h: 1.4		
π_os	$\dfrac{\mu^\mathrm{max} v^\mathrm{rxn} \hat{L}/d^2}{RT c_\mathrm{e}^\mathrm{max}}$	$\dfrac{\text{viscous pressure scale}}{\text{osmotic pressure scale}}$	$3.6 \times 10^{-5}\mathcal{C}$		
$\omega_{c,k}$	$\dfrac{c_\mathrm{e}^\mathrm{max} M_k}{\rho^\mathrm{max}} \left(1 - \dfrac{M_\mathrm{w} \bar{V}_k}{M_k \bar{V}_\mathrm{w}}\right)$	Diffusive kinematic relationship coefficient	e: 0.43 o: 0.13 h: 0.008		
ω_i	$\dfrac{c_\mathrm{e}^\mathrm{max} M_\mathrm{e}}{\rho^\mathrm{max}} \left(t_+^\mathrm{w} + \dfrac{M_-}{M_\mathrm{e}}\right)$	Migrative kinematic relationship coefficient	0.71		
Re	$\dfrac{\rho^\mathrm{max} v^\mathrm{rxn} \hat{L}}{\mu^\mathrm{max}}$	Reynolds number	$1.0 \times 10^{-3}\mathcal{C}$		
σ	$\dfrac{\hat{\sigma}^\mathrm{eff} RT/F\hat{L}}{\bar{i}}$	$\dfrac{\text{Ohmic current scale}}{\text{applied current density}}$	$3.8 \times 10^4/\mathcal{C}$	-	$55/\mathcal{C}$
β^surf	$-\dfrac{c_\mathrm{e}^\mathrm{max}}{n_{\mathrm{e}^-}} \sum_{p \in \{\mathrm{PbO_2}, \mathrm{Pb}, \mathrm{PbSO_4}\}} s_p \bar{V}_p$	Change in porosity associated with local half-reaction going to completion	0.085	-	-0.064
β^r	$-c_\mathrm{e}^\mathrm{max} \sum_{k \in \mathcal{S}^\mathrm{all} \cup \{\mathrm{Pb}, \mathrm{PbSO_4}, \mathrm{PbO_2}\}} s_k^r \bar{V}_k$	Change in acid volume fraction associated with local half-reaction going to completion	S: 0.033 O: 0.097 H: 0.011	- - -	0.040 0.097 0.011
δ_p	$\dfrac{1}{\mathcal{A}\hat{L}}$	$\dfrac{\text{micro length scale}}{\text{macro length scale}}$	1.2×10^{-4}	-	1.2×10^{-5}
C^dl	$\dfrac{\hat{C}^\mathrm{dl} RT \mathcal{A}\hat{L}/F\bar{i}}{c_\mathrm{e}^\mathrm{max} F\hat{L}/\bar{i}}$	$\dfrac{\text{capacitance time-scale}}{\text{discharge time-scale}}$	2.1×10^{-5}	-	2.1×10^{-4}
$\mathcal{Q}^\mathrm{max}$	$\dfrac{\hat{\mathcal{Q}}^\mathrm{max}}{c_\mathrm{e}^\mathrm{max} F}$	Dimensionless electrode theoretical capacity	6.37	-	5.03

Table 2.1: Dimensionless parameters, evaluated using parameter values in Table B.1, relative to the C-rate, $\mathcal{C} = 8A_\mathrm{cs}\bar{i}/Q$. $\mathcal{C}_\mathrm{e}$ is the diffusional C-rate.

2.3 Homogenisation and three-dimensional porous-electrode model

The model that we have developed so far, (2.52), holds on the microscale. That is, each point in space is either liquid electrolyte, solid electrode, or on the clearly defined interface between the two. In theory, we could now solve the system in 3D on the exact electrode geometry. However, both determining the electrode geometry and solving a 3D model on such a complex geometry is impractical. Instead, we derive a macroscale model that holds everywhere in an 'averaged' sense: each point in space has simultaneously liquid electrolyte and solid electrode. All of the variables in the system (2.52) will then exist continuously across each of the subdomains (negative electrode, separator and positive electrode).

2.3.1 Homogenisation

There are two separate length scales in the system (2.52): the 'macroscale', battery length scale, $\hat{L}$, and the 'microscale', pore length scale, which we call r_p. The pore length scale is much smaller than the battery length scale; this allows us to use the method of multiple scales to derive a macroscale model that depends systematically on the microscale. The ratio between the microscale and macroscale length scales is of a similar order of magnitude to δ_p as defined in (2.43). For simplicity, we let $\delta_\mathrm{p} = r_\mathrm{p}/L$.

We now investigate the system in the limit where $\delta_\mathrm{p} \to 0$, letting all other parameters in the model be $\mathcal{O}(1)$ for full generality. To do this, we assume that the structure is locally periodic inside a completely periodic array of boxes, each denoted by $\tilde{\Omega}_\mathrm{e} \cup \tilde{\Omega}_\mathrm{s}$, where $\tilde{\Omega}_\mathrm{e}$ represents the liquid domain of the box and $\tilde{\Omega}_\mathrm{s}$ the solid domain of the box, with $\partial\tilde{\Omega}$ the interface between them. In particular, $\tilde{\Omega}_\mathrm{e}$ (and hence $\tilde{\Omega}_\mathrm{s}$ and $\partial\tilde{\Omega}$) can depend on the large scale variable $\mathbf{x}$, and time t.

Most of the equations in (2.52) are approximately of the form of a conservation equation

$$k\frac{\partial f}{\partial t} = -\nabla \cdot \mathbf{q} \qquad \text{in } \tilde{\Omega}_\mathrm{e}, \tag{2.53a}$$

coupled with a flux equation

$$\mathbf{q} = -D\nabla f \qquad \text{in } \tilde{\Omega}_\mathrm{e}, \tag{2.53b}$$

and an interface condition

$$\mathbf{q} \cdot \mathbf{n} = \delta_\mathrm{p}(k\beta^\mathrm{surf} f + Q)j \quad \text{ on } \partial\tilde{\Omega}, \tag{2.53c}$$

with $k = 1$ ((2.52a), (2.52b) and (2.52j)) or $k = 0$ ((2.52c), (2.52d) and (2.52k); (2.52h), (2.52i) and (2.52m)). In Appendix C, we outline the homogenisation of the system (2.53), using the method of multiple scales. This is identical to the method used by Richardson et al. [100], but with the addition of a moving interface. The resulting general 'averaged' system is

$$k\frac{\partial}{\partial t}(\varepsilon f) = -\nabla \cdot \mathbf{q} + Qaj, \tag{2.54a}$$

$$\mathbf{q} = -D\mathcal{B}\nabla f. \tag{2.54b}$$

where the porosity, ε, and reactive interfacial surface area, a, are defined in (C.20), and the diffusivity tensor, $\mathcal{B}$, is defined in (C.28).

For equations that represent the solid domain ((2.52h), (2.52i) and (2.52m)), the sign of the term pre-multiplying the source term Qa is switched (since the unit normal points in the opposite direction relative to the domain), and the porosity, ε_{s} and diffusivity tensor, $\mathcal{B}_{\mathrm{s}}$, are defined in (C.29).

Finally, the Navier-Stokes equation (2.52g) is not in the general conservation form of (2.53a). However, since the Reynolds number, Re, is small, we can use the method of multiple scales to derive Darcy's law relating the mass-averaged velocity to the pressure, [39, 66],

$$\mathbf{v} = -\frac{\mathcal{K}}{\mu}\nabla p, \tag{2.55}$$

where $\mathcal{K}$ is the permeability tensor. Note that, since we use Darcy's law, we only need to specify the normal velocity at the boundary, and we no longer need the macroscale no-slip boundary condition (2.27).

2.3.2 Three-dimensional porous-electrode model

To write the full homogenised model in closed form, we must specify how the porosities, diffusivity and permeability tensor, and interfacial surface area relate to the other variables in the model.

Porosity. We obtain an equation for the electrolyte porosity, ε, by applying the Reynolds Transport Theorem (C.8) with $f = 1$:

$$\frac{\partial \varepsilon}{\partial t} = -\beta^{\mathrm{surf}} a^{\mathrm{S}} j^{\mathrm{S}}. \tag{2.56}$$

The differential equation for porosity requires an initial condition for ε. We ensure that (2.35) and (2.36) are consistent with (2.56) and (2.65a) (see Appendix B for details) by setting

$$\varepsilon\left(\mathbf{x}, 0\right) = \varepsilon^0 = \varepsilon^{\max} - \frac{\left|\beta^{\mathrm{surf}}\right| \mathcal{Q}_{\mathrm{e}}^{\max}(1 - q^0)}{\ell}, \tag{2.57}$$

where

$$\mathcal{Q}_{\mathrm{e}}^{\max} = \frac{\ell_{\mathrm{n}}\varepsilon_{\mathrm{n}}^{\max} + \ell_{\mathrm{s}}\varepsilon_{\mathrm{s}}^{\max} + \ell_{\mathrm{p}}\varepsilon_{\mathrm{p}}^{\max}}{s_{\mathrm{p}} - s_{\mathrm{n}}}. \tag{2.58}$$

Diffusivity and permeability tensors. For the diffusivity tensor, the most common form in electrochemical modelling, and the one that we will use in this thesis, is the Bruggeman tortuosity correlation,

$$\mathcal{B}_{ij} = \varepsilon^{1.5}\delta_{ij}, \tag{2.59}$$

where δ_{ij} is the Kronecker delta, and similarly $B_{\mathrm{s},ij} = \varepsilon_\mathrm{s}^{1.5}\delta_{ij}$ [7, 47, 48]. Some alternatives are summarised by van Brakel and Heertjes [128]; a more systematic approach is to directly solve the cell problem (C.25a) for $\mathcal{B}$, assuming a certain geometry for the pores (e.g. spherical, square or hexagonal) [16].

We define effective diffusivities and conductivities $D_k^\mathrm{eff} = D_k\mathcal{B}$, $\kappa^\mathrm{eff} = \kappa\mathcal{B}$ in the electrolyte and $\sigma^\mathrm{eff} = \sigma\mathcal{B}_\mathrm{s}^0$ in the solid. Here σ^eff is taken to depend only on the initial solid volume fraction, ε_s^0, since the volume fraction of conductive lead bounded within electron-exchange surface $\mathcal{A}$, does not vary as porous lead-sulfate is created (i.e. as ε_s changes).

The permeability tensor is usually taken to be a function of both porosity and the pore size, for example via the Kozeny-Carman equation [48]

$$\mathcal{K}_{ij} = \frac{d^2}{180}\frac{\varepsilon^3}{(1-\varepsilon)^2}\delta_{ij}, \tag{2.60}$$

where d is the dimensionless pore size relative to r_p. Costa [25] suggests a similar formula based on a fractal pore space geometry assumption. Lee et al. [66] describe numerical solutions of the underlying cell problem, but do not suggest an explicit formula for $\mathcal{K}$.

Reactive surface area. Solid $PbSO_4$ does not tend to deposit as a compact thin film, so in general each of the reactive surface areas per volume, a^r ($r \in \mathcal{R}$), changes as the battery is charged and discharged. Although we will assume constant reactive surface areas in this thesis for simplicity, we briefly discuss here how the changing surface areas could be modelled.

The reactive surface areas depend on the electrode utilisation, $\mathcal{U}$ [6, 7, 47, 48, 88], which represents how much of the electrode's maximum theoretical volumetric capacity has been used, and hence *increases* as battery SoC decreases. The electrode utilisation depends only on the interfacial current density from the main reactions, j^S, via differential equations

$$\frac{\partial\mathcal{U}}{\partial t} = \beta^U a^\mathrm{S} j^\mathrm{S}, \tag{2.61}$$

where

$$\beta^U = \frac{1}{|\mathcal{Q}^\mathrm{max}|} = \begin{cases} 1/\mathcal{Q}_\mathrm{n}^\mathrm{max}, & \mathbf{x} \in \Omega_\mathrm{n}, \\ -1/\mathcal{Q}_\mathrm{p}^\mathrm{max}, & \mathbf{x} \in \Omega_\mathrm{p}, \end{cases} \tag{2.62}$$

and $\mathcal{Q}^\mathrm{max}$ is the dimensionless maximum theoretical volumetric capacity of the electrodes (given in Table 2.1). Note that the maximum theoretical volumetric capacity of each electrode is higher than the volumetric capacity of the battery as given by

total number of moles of electrolyte, so $\mathcal{U}$ is always smaller than one. For the initial conditions, we should ensure that (2.35) and (2.36) are consistent with (2.61) (see Appendix B for details) by setting

$$\mathcal{U}(\mathbf{x}, 0) = \frac{\mathcal{Q}_{\mathrm{e}}^{\max}(1 - q^0)}{\mathcal{Q}^{\max}\ell}. \tag{2.63}$$

The reactive surface areas per volume are different for the different reactions. For the side reactions (1.2) and (1.3), the reactive surface area is the amount of electrode not covered by lead sulfate, while for the main reactions (1.1), the reactive surface area is, during discharge, the amount of electrode not covered by lead sulfate and, during charge, the amount of electrode covered by lead sulfate. The relationship between area covered by lead sulfate and electrode SoC depends on the electrode morphology. If the lead sulfate deposits as a compact film, then the area covered by lead sulfate is zero at full charge ($\mathcal{U} = 0$), and one otherwise. At the other end of the scale, if lead sulfate nucleates in small islands at the electrode surface, then the area covered by lead sulfate depends linearly on electrode SoC.

Motivated by these observations, we suggest that the most appropriate form for the reactive surface area per volume is the one used by Gu et al. [49] and Srinivasan et al. [115]:

$$a^r(\mathcal{U}) = (1 - \mathcal{U}^\xi), \quad r \in \mathcal{R}/\{\mathrm{S}\}, \tag{2.64a}$$

$$a^{\mathrm{S}}(\mathcal{U}) = \begin{cases} (1 - \mathcal{U}^\xi) & \text{for a discharge,} \\ \mathcal{U}^\xi & \text{for a charge,} \end{cases} \tag{2.64b}$$

where $\mathcal{U}^\xi$ is the proportion of surface area covered by sulfate, and the morphological parameter ξ is the same for all reactions. We illustrate this dependence for various values of ξ in Figure 2.1. The case where ξ is very small (but non-zero) corresponds to a compact film, while the case where ξ is one corresponds to nucleation. Understanding the exact relationship between a^r and $\mathcal{U}$ would require a detailed model of nucleation at the microscale.

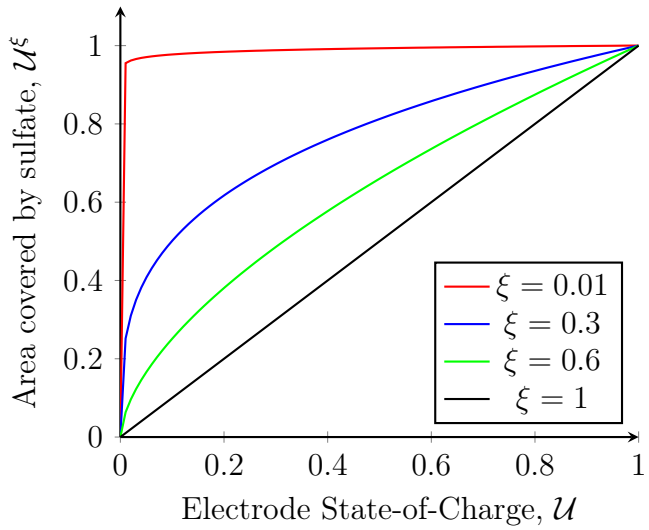

Figure 2.1: Dependence of reactive surface area for the main reactions (1.1) on electrode state-of-charge, for different values of ξ.

Summary. After homogenisation, the general, dimensionless model is

$$\frac{\partial}{\partial t}(\varepsilon c_k) = -\frac{1}{\mathcal{C}_\mathrm{e}}\nabla\cdot\mathbf{N}_k - \sum_{r\in\mathcal{R}} s_k^r a^r j^r, \tag{2.65a}$$

$$\mathbf{N}_k = -\mathcal{D}_k D_k^\mathrm{eff}\left(\nabla c_k - \pi_\mathrm{os}\psi_k\nabla p\right) + \mathcal{C}_\mathrm{e} t_k^\mathrm{w}\mathbf{i}_\mathrm{e} + \mathcal{C}_\mathrm{e} c_k \mathbf{v}^\square, \tag{2.65b}$$

$$\frac{\partial\varepsilon}{\partial t} = -\beta^\mathrm{surf} a^\mathrm{S} j^\mathrm{S}, \tag{2.65c}$$

$$\nabla\cdot\mathbf{i}_\mathrm{e} = \sum_{r\in\mathcal{R}} a^r j^r + a^\mathrm{dl} C^\mathrm{dl}\frac{\partial}{\partial t}\left(\Phi_\mathrm{s} - \Phi_\mathrm{e}\right), \tag{2.65d}$$

$$\mathcal{C}_\mathrm{e}\,\mathbf{i}_\mathrm{e} = \kappa^\mathrm{eff}\left(\chi_\mathrm{e}\nabla\ln\left(c_\mathrm{e}\right) - \nabla\Phi_\mathrm{e} + \pi_\mathrm{os}\left(\frac{M_+ c_\mathrm{e}^\mathrm{max}}{\rho^\mathrm{max}\rho} - \frac{\chi_\mathrm{e}\psi_\mathrm{e}}{c_\mathrm{e}}\right)\nabla p\right), \tag{2.65e}$$

$$\nabla\cdot\mathbf{v}^\square = \sum_{r\in\mathcal{R}} \beta^r a^r j^r, \tag{2.65f}$$

$$\mathbf{v} = -\frac{\mathcal{K}}{\mu}\nabla p, \tag{2.65g}$$

$$\rho\left(\mathbf{v} - \mathbf{v}^\square\right) = \frac{\omega_c D_\mathrm{e}^\mathrm{eff}}{\mathcal{C}_\mathrm{e}}\left(\nabla c_\mathrm{e} - \pi_\mathrm{os}\psi_\mathrm{e}\nabla p\right) + \omega_i\mathbf{i}_\mathrm{e}, \tag{2.65h}$$

$$\nabla\cdot\mathbf{i}_\mathrm{s} = -\sum_{r\in\mathcal{R}} a^r j^r - a^\mathrm{dl} C^\mathrm{dl}\frac{\partial}{\partial t}\left(\Phi_\mathrm{s} - \Phi_\mathrm{e}\right), \tag{2.65i}$$

$$\mathbf{i}_\mathrm{s} = -\sigma^\mathrm{eff}\nabla\Phi_\mathrm{s}, \tag{2.65j}$$

$$j^r = j^r\left(\{c_k\}, \Phi_\mathrm{s} - \Phi_\mathrm{e}\right), \tag{2.65k}$$

$$\frac{\partial\mathcal{U}}{\partial t} = \beta^U a^\mathrm{S} j^\mathrm{S}, \tag{2.65l}$$

$$a^r = a^r\left(\mathcal{U}\right), \tag{2.65m}$$

for $k \in \mathcal{S}$. The dimensionless boundary conditions are, assuming galvanic control,

$$\frac{\partial c_k}{\partial \mathrm{n}} = \frac{\partial \Phi_\mathrm{e}}{\partial \mathrm{n}} = \frac{\partial p}{\partial \mathrm{n}} = 0 \quad \text{on } \partial\Omega_\mathrm{ext}, \tag{2.66a}$$

$$\frac{\partial \Phi_\mathrm{s}}{\partial \mathrm{n}} = 0 \quad \text{on } \partial\Omega_\mathrm{ext} / \partial\Omega_\mathrm{tab}\ , \tag{2.66b}$$

$$c_k = c_k^\mathrm{head}, \quad \mathbf{i}_\mathrm{e} \cdot \mathbf{n} = 0, \quad p = \rho g h \quad \text{on } z = H, \tag{2.66c}$$

$$\Phi_\mathrm{s} = 0 \quad \text{on } \partial\Omega_\mathrm{tab,n}, \tag{2.66d}$$

$$A_\mathrm{tab,p}\sigma^\mathrm{eff}\frac{\partial \Phi_\mathrm{s}}{\partial z} = A_\mathrm{cs}\mathcal{I}\left(t\right) \quad \text{on } \partial\Omega_\mathrm{tab,p}, \tag{2.66e}$$

for $k \in \mathcal{S}$, where

$$\frac{\mathrm{d}}{\mathrm{d}t}\left(h c_k^\mathrm{head}\right) = \frac{1}{\mathcal{C}_\mathrm{e} W}\int_0^1\int_0^W \mathbf{N}_k \cdot \mathbf{n}\big|_{z=H}\ \mathrm{d}x\,\mathrm{d}y \tag{2.67a}$$

and

$$\frac{\mathrm{d}h}{\mathrm{d}t} = \frac{1}{W}\int_0^1\int_0^W \mathbf{v}^\square \cdot \mathbf{n}\big|_{z=H}\ \mathrm{d}x\,\mathrm{d}y. \tag{2.67b}$$

For other types of operation, (2.66e) can be replaced by another option from (2.34).

All scalar variables and the normal components of vector variables are continuous at the electrode-separator interfaces. The dimensionless initial conditions are

$$c_k\left(\mathbf{x},0\right) = c_k^0, \quad \varepsilon\left(\mathbf{x},0\right) = \varepsilon^0, \quad \mathcal{U}\left(\mathbf{x},0\right) = \mathcal{U}^0, \tag{2.68a}$$

$$\Phi_\mathrm{s}\left(\mathbf{x},0\right) - \Phi_\mathrm{e}\left(\mathbf{x},0\right) = U^\mathrm{S}\left(c_\mathrm{e}^0\right), \quad c_k^\mathrm{head}(0) = c_k^0, \quad h(0) = h^0. \tag{2.68b}$$

Several aspects of the model (2.65) are new. Firstly, a pressure-diffusion term appears in (2.65b), (2.65e) and (2.65h) because the flux laws are based on thermodynamic forces. Secondly, changes in volume due to the interfacial reactions induce a flow in the cell via (2.65f). Thirdly, the difference between the mass-averaged velocity, $\mathbf{v}$, and volume-average velocity, $\mathbf{v}^\square$, is captured by the kinematic relation (2.65h). Finally, the free surface above the cell is modelled via the boundary condition (2.66c).

In the remainder of this thesis, we will take the limit in which π_os tends to zero, thus ignoring any pressure-diffusion effects. However, in different chemistries or operating regimes, π_os may be large, and these pressure effects may be significant [44].

2.4 Classification

We rewrite the system (2.65)-(2.68) in terms of scalar variables c_k, Φ_e, Φ_s, p, ε and $\mathcal{U}$ only, in order to classify the equations. For simplicity, we present the system here

in the limit in which π_{os}, ω_c and ω_i are zero, but the classification of the equations is unchanged if those parameters are non-zero.

Note that, since the dimensionless double-layer capacitance C^{dl} is small (Table 2.1), we can consider the limit in which C^{dl} tends to 0, so that j^{dl} is identically zero everywhere. The classification of the system is different depending on whether we include the capacitance interfacial current, j^{dl}, or set it to be identically zero everywhere.

2.4.1 System without capacitance

Setting j^{dl} to be zero, the system (2.65)-(2.68) consists of one parabolic PDE for each c_k,

$$\frac{\partial}{\partial t}(\varepsilon c_k) = \nabla \cdot \left[\frac{\mathcal{D}_k D_k^{\text{eff}}}{\mathcal{C}_{\text{e}}} \nabla c_k + c_k \left(\frac{\mathcal{K}}{\mu} \nabla p \right) \right] - \sum_{r \in \mathcal{R}} \left(s_k^r + t_k^{\text{w}} \right) a^r j^r, \tag{2.69a}$$

three elliptic PDEs for Φ_{e}, Φ_{s} and p,

$$\sum_{r \in \mathcal{R}} a^r j^r = \frac{1}{\mathcal{C}_{\text{e}}} \nabla \cdot \left[\kappa^{\text{eff}} \left(\chi_{\text{e}} \nabla \ln (c_{\text{e}}) - \nabla \Phi_{\text{e}} \right) \right], \tag{2.69b}$$

$$\sum_{r \in \mathcal{R}} a^r j^r = \nabla \cdot \left[\sigma^{\text{eff}} \nabla \Phi_{\text{s}} \right], \tag{2.69c}$$

$$\sum_{r \in \mathcal{R}} \beta^r a^r j^r = -\nabla \cdot \left[\frac{\mathcal{K}}{\mu} \nabla p \right], \tag{2.69d}$$

and two hyperbolic equations for ε and $\mathcal{U}$ (which could be interpreted as ODEs in time parametrised in space),

$$\frac{\partial \varepsilon}{\partial t} = -\beta^{\text{surf}} a^{\text{S}} j^{\text{S}}, \tag{2.69e}$$

$$\frac{\partial \mathcal{U}}{\partial t} = \beta^U a^{\text{S}} j^{\text{S}}, \tag{2.69f}$$

with

$$j^r = j^r \left(\{c_k\}, \Phi_{\text{s}} - \Phi_{\text{e}} \right), \tag{2.69g}$$

$$a^r = a^r \left(\mathcal{U} \right). \tag{2.69h}$$

The boundary conditions and initial conditions are unchanged from (2.66) and (2.68), except we no longer need an initial condition for the potential difference, $\Phi_{\text{s}} - \Phi_{\text{e}}$, since we ignore capacitance effects.

2.4.2 System with capacitance

If we include capacitance effects, then we can reorganise the system (2.65) into a form that is easier to classify. To do this, we define the potential difference

$$\phi = \Phi_{\mathrm{s}} - \Phi_{\mathrm{e}}, \tag{2.70}$$

and substitute Φ_{s} with $\phi + \Phi_{\mathrm{e}}$ in each electrode. Then (2.69a) and (2.69d)-(2.69h) remain unchanged, and we simply convert (2.69c) into a parabolic equation, and manipulate (2.69b) to eliminate the capacitance terms so that it remains an elliptic equation:

$$a^{\mathrm{dl}} C^{\mathrm{dl}} \frac{\partial \phi}{\partial t} = \nabla \cdot \left[\sigma^{\mathrm{eff}} \nabla \left(\phi + \Phi_{\mathrm{e}} \right) \right], \tag{2.71a}$$

$$0 = \nabla \cdot \left[\frac{\kappa^{\mathrm{eff}}}{\mathcal{C}_{\mathrm{e}}} \left(\chi_{\mathrm{e}} \nabla \ln \left(c_{\mathrm{e}} \right) - \nabla \Phi_{\mathrm{e}} \right) - \sigma^{\mathrm{eff}} \nabla \left(\phi + \Phi_{\mathrm{e}} \right) \right]. \tag{2.71b}$$

We also substitute Φ_{s} with $\phi + \Phi_{\mathrm{e}}$ in the boundary conditions (2.66a), (2.66b) and (2.66e) to give

$$\frac{\partial \phi}{\partial \mathrm{n}} = 0 \quad \text{on } \partial\Omega_{\mathrm{ext}} / \partial\Omega_{\mathrm{tab}}\,, \tag{2.72a}$$

$$\phi + \Phi_{\mathrm{e}} = 0 \quad \text{on } \partial\Omega_{\mathrm{tab,n}}, \tag{2.72b}$$

$$A_{\mathrm{tab,p}} \sigma^{\mathrm{eff}} \frac{\partial \phi}{\partial \mathrm{n}} = A_{\mathrm{cs}} \mathcal{I}\left(t\right) \quad \text{on } \partial\Omega_{\mathrm{tab,p}}. \tag{2.72c}$$

The other boundary conditions are unchanged from (2.66):

$$\frac{\partial c_k}{\partial \mathrm{n}} = \frac{\partial \Phi_{\mathrm{e}}}{\partial \mathrm{n}} = \frac{\partial p}{\partial \mathrm{n}} = 0 \quad \text{on } \partial\Omega_{\mathrm{ext}}, \tag{2.73a}$$

$$c_k = c_k^{\mathrm{head}}, \quad \mathbf{i}_{\mathrm{e}} \cdot \mathbf{n} = 0, \quad p = \rho g h \quad \text{on } z = H, \tag{2.73b}$$

and the initial conditions (2.68) become

$$c_k\left(\mathbf{x}, 0\right) = c_k^0, \quad \varepsilon\left(\mathbf{x}, 0\right) = \varepsilon^0, \quad \mathcal{U}\left(\mathbf{x}, 0\right) = \mathcal{U}^0, \tag{2.74a}$$

$$\phi_{\mathrm{e}}\left(\mathbf{x}, 0\right) = U^{\mathrm{S}}\left(c_{\mathrm{e}}^0\right), \quad c_k^{\mathrm{head}}(0) = c_k^0, \quad h(0) = h^0. \tag{2.74b}$$

Since we have replaced an elliptic equation (2.69c) with a parabolic one (2.71a), we expect the system with capacitance to be more amenable to solution using the Method of Lines. We compare the solutions with and without capacitance in a one-dimensional setting in Chapter 3. As we will show in Chapter 3, for the problem in one-dimension, (2.71) can be further reduced to a single PDE for ϕ, by using the fact that $\nabla \cdot (\mathbf{i}_{\mathrm{e}} + \mathbf{i}_{\mathrm{s}}) = 0$ to eliminate $\nabla \Phi_{\mathrm{e}}$.

Chapter 3

Simplified models for slow discharge

In this chapter, we consider a simplified one-dimensional model in which we assume uniformity in the plane normal to x. Such behaviour would be expected in the limit where the electrode conductivity is very large (we will derive the one-dimensional model from the three-dimensional model more systematically in Chapter 4). In Section 3.1, we write down the one-dimensional form of the model developed in Chapter 2, accounting in particular for non-symmetric volume changes. We discuss methods for numerical solutions of this one-dimensional model, and investigate the effect of capacitance and Faradaic convection, in Section 3.2.

Then, in Section 3.3, we perform an asymptotic analysis in the limit in which the *diffusional C-rate*, $\mathcal{C}_\mathrm{e}$ – the C-rate scaled with the diffusion time-scale – is small, to derive a hierarchy of reduced-order models that approximate the full model, as shown in Section 3.4. The small-$\mathcal{C}_\mathrm{e}$ limit is a physically relevant limit in most cases of VRLA battery usage, when discharge takes place over the course of several hours. This chapter is an extension of work that has been published in [117].

3.1 One-dimensional battery model

We start with the full one-dimensional version of the model derived in Chapter 2, (2.65). From a high-level perspective, we can obtain the one-dimensional model from the three-dimensional model by assuming that all variables are uniform in the directions normal to the x-axis, setting y- and z-components of fluxes to zero (hence replacing three-dimensional gradient and divergence operators with the one-dimensional derivative, $\partial/\partial x$), and applying boundary conditions at $x = 0$ and $x = 1$ instead of on $\mathbf{x} \in \partial\Omega_{\mathrm{tab,n}}$ and $\mathbf{x} \in \partial\Omega_{\mathrm{tab,p}}$ respectively.

However, this naive approach leads to an inconsistency in the equation for conservation of velocity, (2.65f), since the volumetric change parameters β^r are different

in the negative and positive electrodes (Table 2.1). This means that there must be a velocity in the y- and/or z-directions in order for the no-flux conditions (2.66a) for $\mathbf{v}^{\square}$ to be satisfied at both $x = 0$ and $x = 1$. To understand the flow in one dimension, we systematically consider the limit in which the aspect ratio of the cell is small, the conductivity of the current collectors is very large, and the permeability of the separator is much larger than the permeability of the electrodes. Details of this approach are given in Chapter 4; here, we simply state the resulting one-dimensional model.

For the sake of simplicity, we take the reactive surface areas $a(\mathcal{U})$ to be constant, and so equal to one. We then do not need to keep track of the varying electrode surface area. Hence we no longer need to solve for the electrode utilisation, $\mathcal{U}$. Extending to the case of varying surface area is straightforward if algebraically tedious.

For the remainder of this thesis, unless stated otherwise, equations involving subscripts k hold for $k \in \mathcal{S}$, and equations involving superscripts r hold for $r \in \mathcal{R}$. We also denote the x-component of any flux $\mathbf{f}$ by f (for example, $i_e = \mathbf{i}_e \cdot \mathbf{e}_x$).

The resulting one-dimensional model is

$$\frac{\partial}{\partial t}(\varepsilon c_k) + \frac{\partial}{\partial x}\left(c_k v^{\square}\right) + c_k V_z^{\square} = \frac{\mathcal{D}_k}{\mathcal{C}_{\mathrm{e}}}\frac{\partial}{\partial x}\left(D_k^{\mathrm{eff}}\frac{\partial c_k}{\partial x}\right) - \sum_{r\in\mathcal{R}} s_k^r j^r, \tag{3.1a}$$

$$\frac{\partial \varepsilon}{\partial t} = -\beta^{\mathrm{surf}} j^{\mathrm{S}}, \tag{3.1b}$$

$$\frac{\partial i_{\mathrm{e}}}{\partial x} = \sum_{r\in\mathcal{R}} j^r + C^{\mathrm{dl}}\frac{\partial}{\partial t}\left(\Phi_{\mathrm{s}} - \Phi_{\mathrm{e}}\right), \tag{3.1c}$$

$$\mathcal{C}_{\mathrm{e}}\, i_{\mathrm{e}} = \kappa^{\mathrm{eff}}\left(\chi_{\mathrm{e}}\frac{\partial \ln\left(c_{\mathrm{e}}\right)}{\partial x} - \frac{\partial \Phi_{\mathrm{e}}}{\partial x}\right), \tag{3.1d}$$

$$\frac{\partial v^{\square}}{\partial x} = \sum_{r\in\mathcal{R}} \beta^r j^r - V_z^{\square}, \tag{3.1e}$$

$$\frac{\partial i_{\mathrm{s}}}{\partial x} = -\sum_{r\in\mathcal{R}} j^r - C^{\mathrm{dl}}\frac{\partial}{\partial t}\left(\Phi_{\mathrm{s}} - \Phi_{\mathrm{e}}\right), \tag{3.1f}$$

$$i_{\mathrm{s}} = -\sigma^{\mathrm{eff}}\frac{\partial \Phi_{\mathrm{s}}}{\partial x}, \tag{3.1g}$$

$$j^r = j^r\left(\{c_k\}, \Phi_{\mathrm{s}} - \Phi_{\mathrm{e}}\right), \tag{3.1h}$$

where $V_z^{\square}$ represents the transverse contribution to the dilation $\nabla \cdot \mathbf{v}^{\square}$, and is given by

$$V_z^{\square} = \begin{cases} 0, & x \in \Omega_{\mathrm{n}}, \\ -\frac{1}{\ell_{\mathrm{s}}}\sum_{r\in\mathcal{R}} \int_0^1 \beta^r j^r \,\mathrm{d}x, & x \in \Omega_{\mathrm{s}}, \\ 0, & x \in \Omega_{\mathrm{p}}. \end{cases} \tag{3.1i}$$

Note that we do not write the equation for pressure, since it decouples entirely from the rest of the system in 1D.

In the limit of infinitely conductive current collectors, the boundary conditions (2.66) become

$$\frac{\partial c_k}{\partial x} = i_\mathrm{e} = v^\square = \Phi_\mathrm{s} = 0 \quad \text{at } x = 0, \tag{3.2a}$$

$$i_\mathrm{s} = 0 \quad \text{at } x = \ell_\mathrm{n}, 1 - \ell_\mathrm{p}, \tag{3.2b}$$

$$\frac{\partial c_k}{\partial x} = i_\mathrm{e} = 0, \quad i_\mathrm{s} = \mathcal{I}, \quad \Phi_\mathrm{s} = V \quad \text{at } x = 1. \tag{3.2c}$$

(Recall that either $\mathcal{I}(t)$ or $V(t)$ is given, and the other calculated by the model.) All variables are continuous at the electrode-separator interfaces. The initial conditions are unchanged from (2.68):

$$c_k(\mathbf{x}, 0) = c_k^0, \quad \varepsilon(\mathbf{x}, 0) = \varepsilon^0, \quad \Phi_\mathrm{s}(\mathbf{x}, 0) - \Phi_\mathrm{e}(\mathbf{x}, 0) = U^\mathrm{S}\left(c_\mathrm{e}^0\right). \tag{3.3a}$$

3.2 Numerical solutions

When solving the model numerically, it is useful to consider the different methods that might be used depending on whether we include or do not include capacitance in the model.

Solution without capacitance. The more direct approach to solving (3.1)-(3.3) is to take the limit in which C^dl tends to 0, so that j^dl is identically zero everywhere. Then the system (3.1) consists of one-dimensional parabolic, hyperbolic and elliptic equations. We can solve this using the Method of Lines, and here we first discretise spatially, using the Finite Volume method, with a grid chosen such that cell edges are at $x = 0$ and $x = 1$ (since the system has Neumann boundary conditions). This gives a differential-algebraic equation (DAE) system for the variables at each point in discretised space. We solve this DAE system using the IDA solver in SUNDIALS [53, 54, 75].

Solution with capacitance. As discussed in Section 2.4, when capacitance is included in the system (3.1)-(3.3), we first manipulate it into a form suitable for the Method of Lines by defining

$$\phi = \Phi_\mathrm{s} - \Phi_\mathrm{e}. \tag{3.4}$$

In a one-dimensional setting, we note that $i_\mathrm{s} = \mathcal{I} - i_\mathrm{e}$, and replace (3.1d) to (3.1g) with

$$\mathcal{C}_\mathrm{e}\, i_\mathrm{e} = \kappa^\mathrm{eff}\left(\chi\frac{\partial \ln(c_\mathrm{e})}{\partial x} - \frac{\partial \Phi_\mathrm{e}}{\partial x}\right), \tag{3.5a}$$

$$\mathcal{I} - i_\mathrm{e} = -\sigma^\mathrm{eff}\frac{\partial}{\partial x}(\phi + \Phi_\mathrm{e}). \tag{3.5b}$$

This allows us to eliminate $\partial\Phi_\mathrm{e}/\partial x$ from (3.5), and hence find i_e as a functional of c_e and ϕ:

$$i_\mathrm{e} = \kappa^\mathrm{eff}\frac{\chi_\mathrm{e}\frac{\partial \ln(c_\mathrm{e})}{\partial x} + \frac{\partial \phi}{\partial x} + \mathcal{I}/\sigma^\mathrm{eff}}{\mathcal{C}_\mathrm{e} + \kappa^\mathrm{eff}/\sigma^\mathrm{eff}}. \tag{3.6a}$$

Note that in the limit of very large conductivity ($\sigma^\mathrm{eff} \to \infty$) (3.6a) is identical to (3.1d), since $\partial\Phi_\mathrm{s}/\partial x$ is zero in that limit.

We then have a closed system of equations for c_k, ε, $v^\square$, and ϕ:

$$\frac{\partial}{\partial t}(\varepsilon c_k) + \frac{\partial}{\partial x}\left(c_k v^\square\right) + c_k V_z^\square = \frac{\mathcal{D}_k}{\mathcal{C}_\mathrm{e}}\frac{\partial}{\partial x}\left(D_k^\mathrm{eff}\frac{\partial c_k}{\partial x}\right) - \sum_{r\in\mathcal{R}}\left(s_k^r + t_k^\mathrm{w}\right) j^r, \tag{3.6b}$$

$$\frac{\partial \varepsilon}{\partial t} = -\beta^\mathrm{surf} j^\mathrm{S}, \tag{3.6c}$$

$$\frac{\partial v^\square}{\partial x} = \sum_{r\in\mathcal{R}}\beta^r j^r - V_z^\square, \tag{3.6d}$$

$$\frac{\partial \phi}{\partial t} = \frac{1}{C^\mathrm{dl}}\left(\frac{\partial i_\mathrm{e}}{\partial x} - \sum_{r\in\mathcal{R}} j^r\right), \tag{3.6e}$$

where i_e is given by (3.6a), $V_z^\square$ is given by (3.1i), and each j^r is given by a Butler-Volmer equation

$$j^r = j_{0\mathrm{a}}^r \exp\left(n_{\mathrm{e}^-}^r \alpha^r \left(\phi - U^r\left(c_\mathrm{e}\right)\right)\right) - j_{0\mathrm{c}}^r \exp\left(-n_{\mathrm{e}^-}^r \left(1-\alpha^r\right)\left(\phi - U^r\left(c_\mathrm{e}\right)\right)\right), \tag{3.6f}$$

in each electrode, and is zero in the separator. The boundary and initial conditions are unchanged from (3.2) and (3.3).

As before, we discretise the system (3.6) using Finite Volumes and solve the resulting DAE system using SUNDIALS. We then calculate Φ_e by integrating (3.1d),

$$\Phi_\mathrm{e} = \int_0^x \left(\chi_\mathrm{e}\frac{\partial \ln(c_\mathrm{e})}{\partial x} - \mathcal{C}_\mathrm{e}\frac{i}{\kappa^\mathrm{eff}}\right)\mathrm{d}x - \phi|_{x=0}\,, \tag{3.7}$$

where the final term comes from the fact that $\Phi_\mathrm{e} = -\phi$ at $x = 0$. Finally, the solid potential Φ_s can be calculated using (3.4), and the voltage drop across the cell is computed with

$$V = \Phi_\mathrm{s}|_{x=1} = (\phi + \Phi_\mathrm{e})|_{x=1}\,. \tag{3.8}$$

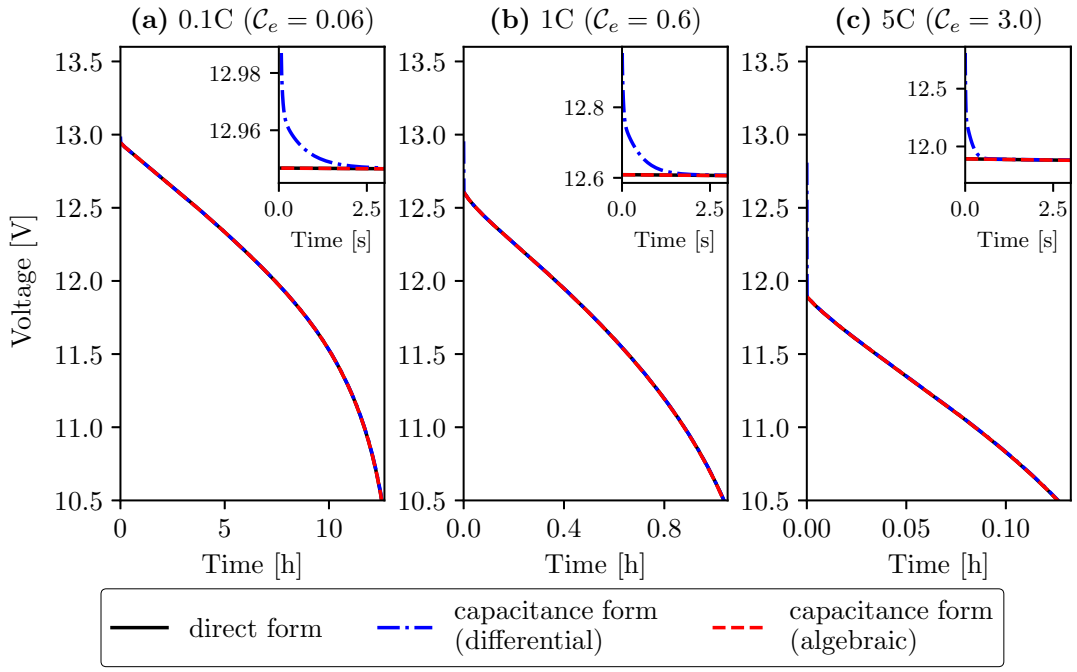

Figure 3.1: Comparing voltages for a constant-current discharge for the three formulations of the model (3.1)-(3.3), for a range of C-rates. In the insets, we show the initial discrepancy due to capacitance effects. Capacitance effects are included in the second case, but not in the first and third cases.

3.2.1 Results

3.2.1.1 Effect of capacitance

We compare the results from solving the model (3.1)-(3.3) in three different ways:

(i) Directly solving (3.1)-(3.3), as a DAE system, taking the limit $C^{\mathrm{dl}} \to 0$ to remove the double-layer capacitance term

(ii) Rearranging to the form (3.6), with C^{dl} as in Table 2.1

(iii) Rearranging to the form (3.6), taking the limit $C^{\mathrm{dl}} \to 0$ so that (3.6e) becomes algebraic in time

In Figure 3.1, we compare the voltage curves from the three solution methods (i)-(iii), for a range of C-rates. We see that the direct and algebraic forms give identical answers, but the differential form differs during a very short initial transient due to capacitance effects. The dimensional capacitance timescale is given by

$$\tau_{\mathrm{cap}} = \frac{\hat{C}^{\mathrm{dl}} RT \mathcal{A} \hat{L}}{F \bar{i}}, \tag{3.9}$$

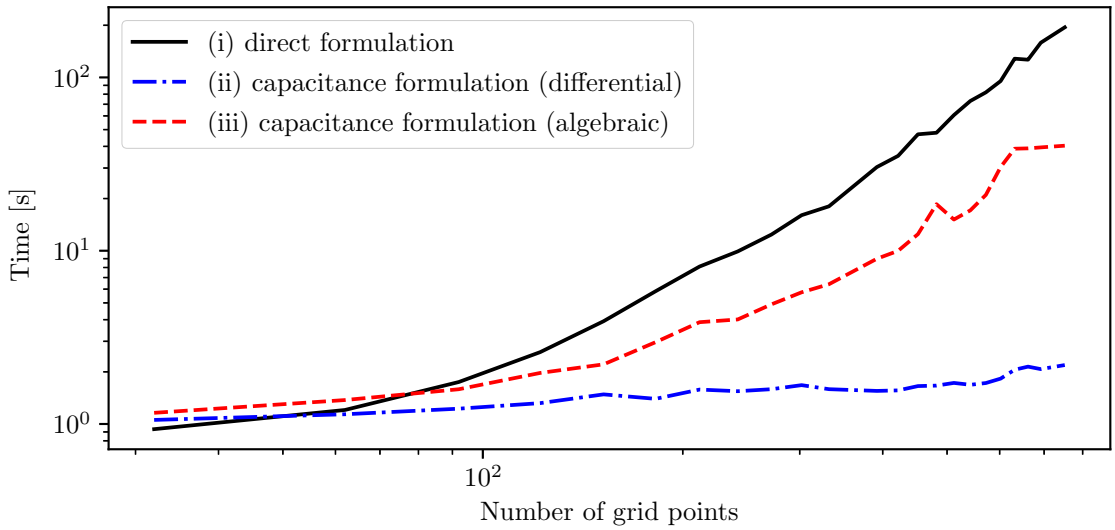

Figure 3.2: CPU time taken in seconds, obtained on an Intel(R) Core(TM) i5-8500T CPU, to solve the three different formulations of the problem in one dimension.

and hence is inversely proportional to the current scale $\bar{i}$. This explains why the timescale for capacitance effects (Figure 3.1, inset) decreases as we increase the C-rate.

The advantage of the capacitance reformulation can be seen in Figure 3.2, where we show the time taken to solve the three formulations of the model, at a C-rate of 1C, as a function of the number of grid points.

In conclusion, capacitance terms are useful to include in the model for faster and more robust numerical solutions, but make negligible difference to the final result outside of very short transients following jumps in the current. For the remainder of this chapter, we use the algebraic capacitance formulation to compare the full model with reduced-order models.

3.2.1.2 Effect of Faradaic convection

We can investigate the effect of including Faradaic convection (equation (3.1e), which is coupled to the rest of the model through (3.1a)) by comparing the solution of the system (3.1)-(3.3) when convection is included (all β^r non-zero in (3.1e) and (3.1i)) against the solution when convection is not included (all β^r set to zero in (3.1e) and (3.1i), so that $v^{\square} = 0$).

In Figure 3.3, we show that the Faradaic convection has minimal effect on the voltage when the system is solved for a constant-current discharge using the parameters and C-rates considered in this thesis. As expected, the dimensional volume-averaged

velocity increases proportionally to the C-rate (Figure 3.4), since the velocity scale (2.50) is proportional to the current scale. However, in all cases, the velocity is small, even by comparison with the battery length scale. The velocity in the separator is not uniform in x, due to the difference in volume changes in the negative and positive electrodes (3.1i). This is linked with the non-zero transverse velocity in the separator, represented by $V_z^{\square}$.

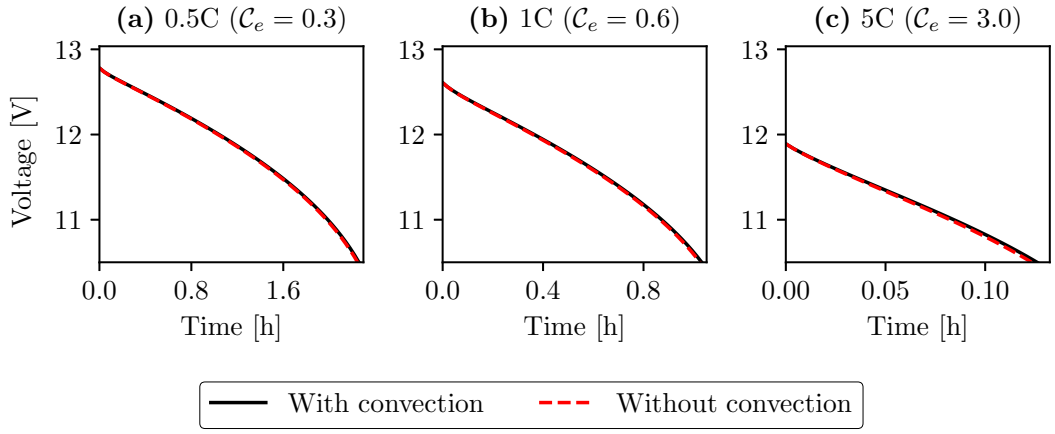

Figure 3.3: Comparing the voltages obtained by solving the system (3.1)-(3.3) with and without convection terms, for a constant-current discharge at a range of C-rates.

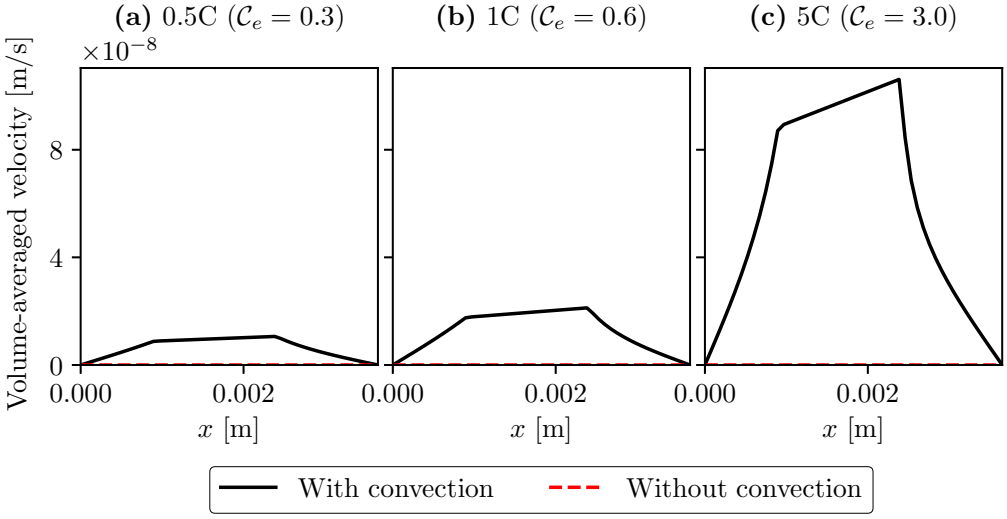

Figure 3.4: Volume-averaged velocity, $v^{\square}$ (in m/s), at 75% SoC, during a constant-current discharge at a range of C-rates.

However, the concentration profiles are slightly different when convection is included (Figure 3.5). The volume-averaged velocity is positive everywhere, and so

induces a flow from the negative electrode to the positive electrode, which flattens out concentration gradients. The effect of convection becomes greater with increasing C-rate, since $\mathcal{C}_e$ acts as a Péclet number.

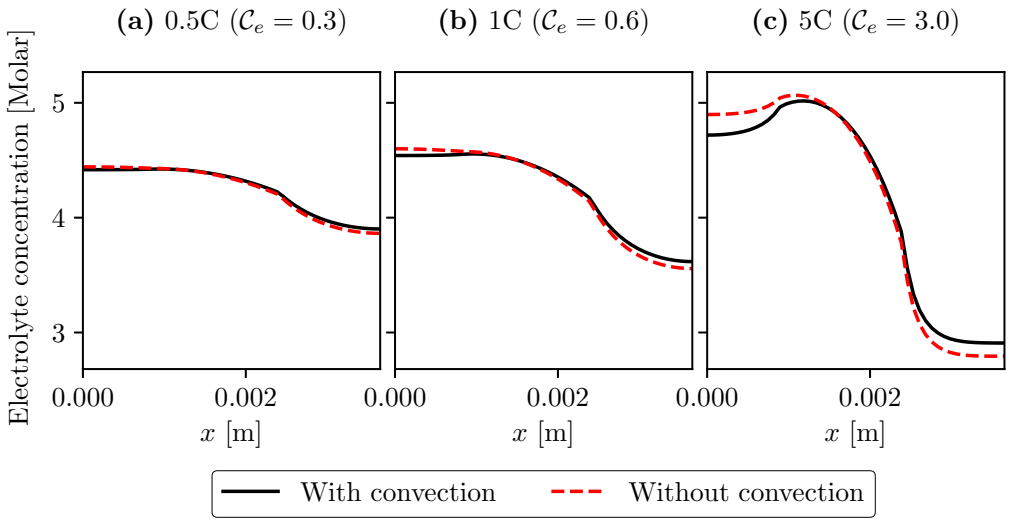

Figure 3.5: Comparing electrolyte concentrations, c_e (in mol/L), at 75% SoC, obtained by solving the system (3.1)-(3.3) with and without convection terms, during a constant-current discharge at a range of C-rates.

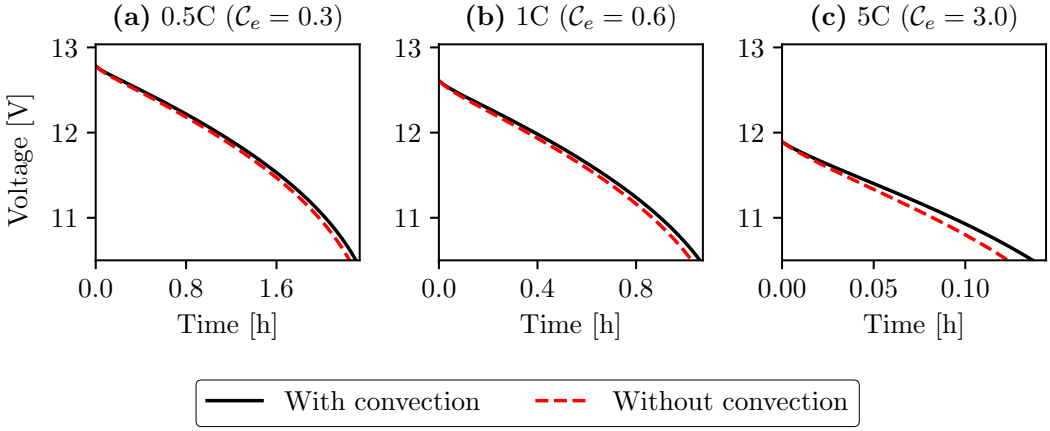

Figure 3.6: Comparing the voltages obtained by solving the system (3.1)-(3.3) with and without convection terms, for a constant-current discharge at a range of C-rates, with volume changes increased by a factor of 5.

To highlight the impact of including Faradaic convection, we solve the model again with volume-change effects (the dimensionless parameters β^r in (3.1i)) artificially increased by a factor of 5. This demonstrates how the solution might change in cases

where there are significant volume changes in the electrodes during charge and discharge, such as in silicon anodes for lithium-ion batteries [15, 23, 108, 109, 110, 107]. In Figure 3.6, we see that the impact of convection on the voltage becomes significant at higher C-rates, with convection raising the voltage (since the concentrations are more uniform) and hence increasing the effective capacity of the battery at that C-rate. The volume-averaged velocities (not shown) have the same profile but are five times larger, and there are significantly greater differences in the concentration profiles (Figure 3.7).

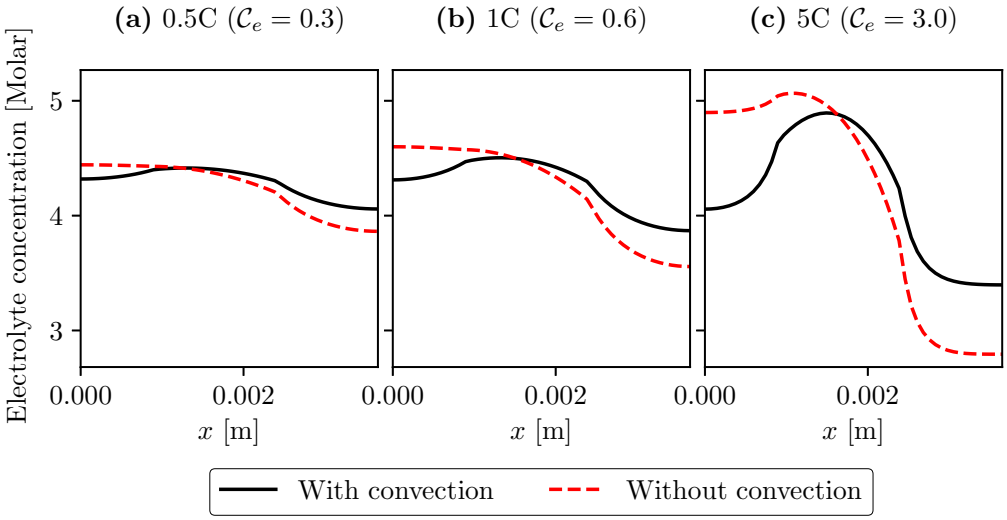

Figure 3.7: Comparing electrolyte concentrations, c_e (in mol/L), at 75% SoC, obtained by solving the system (3.1)-(3.3) with and without convection terms, during a constant-current discharge at a range of C-rates, with volume changes increased by a factor of 5.

3.3 Asymptotic analysis

We now use perturbation methods [52] to produce a hierarchy of simplified but increasingly complex models that are valid in the case where $\mathcal{C}_\mathrm{e}$ is small. At leading order in $\mathcal{C}_\mathrm{e}$ (Section 3.3.2), we reduce the model to a system of ODEs in time that is similar to Newman and Tiedemann's LPM (the system is homogeneous in space). At first order in $\mathcal{C}_\mathrm{e}$ (Section 3.3.3), we account for quasi-static spatial heterogeneity within the cell. As well as improving the fit to the full model, this correction only requires solving a linear system of ODEs. Finally, we improve the first-order solution by accounting for diffusion transients (Section 3.3.4). This requires including just a single linear PDE per species in the liquid (one for each species concentration).

3.3.1 Asymptotic expansions

In this section, we will derive the quasi-static solution of (3.1)-(3.3) in the limit of small $\mathcal{C}_\mathrm{e}$ and small $1/\sigma^\mathrm{eff}$. Since $1/\sigma^\mathrm{eff}$ is much smaller than one for most practical situations (Table 2.1), we only take the leading-order terms in its expansions. In contrast, as shown in Table 2.1, the diffusional C-rate, $\mathcal{C}_\mathrm{e}$, can sometimes be close to one (since the C-rate, $\mathcal{C}$, can be large), so we will consider both the leading-order and first-order terms in $\mathcal{C}_\mathrm{e}$.

To leading order in $1/\sigma^\mathrm{eff}$, (3.1g) becomes

$$\frac{\partial \Phi_\mathrm{s}}{\partial x} = 0 \tag{3.10}$$

in each electrode, and so Φ_s can be approximated as a function of time only. Applying the boundary conditions (3.2), we can now replace (3.1g) with

$$\Phi_\mathrm{s} = \begin{cases} 0 & x \in \Omega_\mathrm{n}, \\ V\left(t\right) & x \in \Omega_\mathrm{p}, \end{cases} \tag{3.11}$$

where $V(t)$ is an unknown function of time, and so we can simplify the system (3.6) to

$$\frac{\partial}{\partial t}\left(\varepsilon c_k\right) + \frac{\partial}{\partial x}\left(c_k v^\square\right) + c_k V_z^\square = \frac{\mathcal{D}_k}{\mathcal{C}_\mathrm{e}} \frac{\partial}{\partial x}\left(D_k^\mathrm{eff} \frac{\partial c_k}{\partial x}\right) - \sum_{r \in \mathcal{R}} s_k^r j^r, \tag{3.12a}$$

$$\frac{\partial \varepsilon}{\partial t} = -\beta^\mathrm{surf} j^\mathrm{S}, \tag{3.12b}$$

$$\mathcal{C}_\mathrm{e}\, i_\mathrm{e} = \kappa^\mathrm{eff}\left(\chi_\mathrm{e} \frac{\partial \ln\left(c_\mathrm{e}\right)}{\partial x} - \frac{\partial \Phi_\mathrm{e}}{\partial x}\right), \tag{3.12c}$$

$$\frac{\partial v^\square}{\partial x} = \sum_{r \in \mathcal{R}} \beta^r j^r - V_z^\square, \tag{3.12d}$$

$$\frac{\partial \phi}{\partial t} = \frac{1}{C^\mathrm{dl}}\left(\frac{\partial i_\mathrm{e}}{\partial x} - \sum_{r \in \mathcal{R}} j^r\right), \tag{3.12e}$$

$$j^r = j^r\left(\{c_k\}, \phi\right), \tag{3.12f}$$

where

$$\phi = \begin{cases} -\Phi_\mathrm{e} & x \in \Omega_\mathrm{n}, \\ V\left(t\right) - \Phi_\mathrm{e} & x \in \Omega_\mathrm{p}. \end{cases} \tag{3.12g}$$

We now consider an asymptotic expansion in the limit $\mathcal{C}_\mathrm{e} \to 0$ and assume that we can expand all variables in (3.12) in powers of $\mathcal{C}_\mathrm{e}$:

$$f(x,t) = f^{(0)}(x,t) + \mathcal{C}_\mathrm{e} f^{(1)}(x,t) + \mathcal{C}_\mathrm{e}^2 f^{(2)}(x,t) + \mathcal{O}(\mathcal{C}_\mathrm{e}^3). \tag{3.13}$$

Hence (3.12) becomes to leading order

$$0 = \frac{\partial}{\partial x}\left(D_k^{\mathrm{eff},(0)}\frac{\partial c_k^{(0)}}{\partial x}\right), \tag{3.14a}$$

$$\frac{\partial \varepsilon^{(0)}}{\partial t} = -\beta^{\mathrm{surf}} j^{\mathrm{S},(0)}, \tag{3.14b}$$

$$0 = \chi_{\mathrm{e}}^{(0)}\frac{\partial \ln\left(c_{\mathrm{e}}^{(0)}\right)}{\partial x} - \frac{\partial \Phi_{\mathrm{e}}^{(0)}}{\partial x}, \tag{3.14c}$$

$$\frac{\partial v^{\square,(0)}}{\partial x} = \sum_{r\in\mathcal{R}} \beta^r j^{r,(0)} - V_z^{\square,(0)}, \tag{3.14d}$$

$$\frac{\partial \phi^{(0)}}{\partial t} = \frac{1}{C^{\mathrm{dl}}}\left(\frac{\partial i_{\mathrm{e}}^{(0)}}{\partial x} - \sum_{r\in\mathcal{R}} j^{r,(0)}\right), \tag{3.14e}$$

$$j^{r,(0)} = j^r\left(\{c_k^{(0)}\}, \phi^{(0)}\right), \tag{3.14f}$$

with boundary conditions

$$\frac{\partial c_k^{(0)}}{\partial x} = i_{\mathrm{e}}^{(0)} = v^{\square,(0)} = 0 \quad \text{at } x = 0, 1, \tag{3.14g}$$

$$i_{\mathrm{e}}^{(0)} = \mathcal{I} \quad \text{at } x = \ell_{\mathrm{n}}, 1-\ell_{\mathrm{p}}, \tag{3.14h}$$

and initial conditions

$$c_k^{(0)}(x,0) = c_k^0, \quad \varepsilon^{(0)}(x,0) = \varepsilon^0, \quad \phi^{(0)}(x,0) = U^{\mathrm{S}}\left(c_{\mathrm{e}}^{(0)}\right). \tag{3.14i}$$

At first order, equating coefficients of $\mathcal{C}_{\mathrm{e}}$ in (3.12) gives

$$\frac{\partial}{\partial t}\left(\varepsilon^{(0)}c_k^{(0)}\right) = \mathcal{D}_k D_k^{\mathrm{eff},(0)}\frac{\partial^2 c_k^{(1)}}{\partial x^2} - c_k^{(0)}\left(\frac{\partial v^{\square,(0)}}{\partial x} + V_z^{\square,(0)}\right) - \sum_{r\in\mathcal{R}} s_k^r j^{r,(0)}, \tag{3.15a}$$

$$\frac{\partial \varepsilon^{(1)}}{\partial t} = -\beta^{\mathrm{surf}} j^{\mathrm{S},(1)}, \tag{3.15b}$$

$$i_{\mathrm{e}}^{(0)} = \kappa^{\mathrm{eff},(0)}\left(\frac{\chi_{\mathrm{e}}^{(0)}}{c_{\mathrm{e}}^{(0)}}\frac{\partial c_{\mathrm{e}}^{(1)}}{\partial x} - \frac{\partial \Phi_{\mathrm{e}}^{(1)}}{\partial x}\right), \tag{3.15c}$$

$$\frac{\partial v^{\square,(1)}}{\partial x} = \sum_{r\in\mathcal{R}} \beta^r j^{r,(1)} - V_z^{\square,(1)}, \tag{3.15d}$$

$$\frac{\partial \phi^{(1)}}{\partial t} = \frac{1}{C^{\mathrm{dl}}}\left(\frac{\partial i_{\mathrm{e}}^{(1)}}{\partial x} - \sum_{r\in\mathcal{R}} j^{r,(1)}\right), \tag{3.15e}$$

$$j^{r,(1)} = \sum_{k\in\mathcal{S}}\left(\frac{\partial j^{r,(0)}}{\partial c_k^{(0)}}c_k^{(1)}\right) + \frac{\partial j^{r,(0)}}{\partial \phi^{(0)}}\phi^{(1)}, \tag{3.15f}$$

with boundary conditions

$$\frac{\partial c_k^{(1)}}{\partial x} = i_{\mathrm{e}}^{(1)} = v^{\square,(1)} = 0 \quad \text{at } x = 0, 1, \tag{3.15g}$$

$$i_{\mathrm{e}}^{(1)} = 0 \quad \text{at } x = \ell_{\mathrm{n}}, 1 - \ell_{\mathrm{p}}, \tag{3.15h}$$

and initial conditions

$$c_k^{(1)}(x, 0) = \varepsilon^{(1)}(x, 0) = \phi^{(1)}(x, 0) = 0. \tag{3.15i}$$

3.3.2 Leading-order quasi-static solution

We now seek the solution to the lowest order problem (3.14). Integrating (3.14a) with boundary conditions (3.14g), then integrating again, gives $c_k^{(0)} = c_k^{(0)}(t)$. We then integrate (3.14c), use boundary conditions (3.14g), and integrate again, to find that $\Phi_{\mathrm{e}}^{(0)} = \Phi_{\mathrm{e}}^{(0)}(t)$. Hence $j_d^{r,(0)}$ are functions of time only, and so, by (3.15c), $\partial i_{\mathrm{e},d}^{(0)}/\partial x$ are functions of time only. Integrating $\partial i_{\mathrm{e},d}^{(0)}/\partial x$ in x over each electrode and applying the boundary conditions (3.14g) and (3.14h) gives

$$\frac{\partial i_{\mathrm{e,n}}^{(0)}}{\partial x} = \frac{\mathcal{I}}{\ell_{\mathrm{n}}}, \qquad \frac{\partial i_{\mathrm{e,p}}^{(0)}}{\partial x} = -\frac{\mathcal{I}}{\ell_{\mathrm{p}}}. \tag{3.16}$$

Finally, by (3.14b), $\varepsilon_d^{(0)}$ are functions of time only (in particular, $\varepsilon_{\mathrm{s}}^{(0)} \equiv \varepsilon_{\mathrm{s}}^{\max}$). Hence to leading order, the whole problem is quasi-static. To determine $c_k^{(0)}$, we need to consider the first-order problem (3.15a) for $c_k^{(1)}$. Integrating (3.15a) from $x = 0$ to $x = 1$ and using the boundary conditions (3.15g) gives a solvability condition that determines $c_k^{(0)}$. We can combine this with the other equations in (3.14), and (3.16), to obtain a nonlinear system of ODEs for $c_k^{(0)}$, $\varepsilon_d^{(0)}$, and $\phi_d^{(0)}$,

$$\frac{\mathrm{d}}{\mathrm{d}t}\left(c_k^{(0)} \sum_{d\in\{\mathrm{n,s,p}\}} \ell_d \varepsilon_d^{(0)}\right) = -\sum_{d\in\{\mathrm{n,p}\}} \sum_{r\in\mathcal{R}} \left(s_{k,d}^r + c_k^{(0)}\beta^r\right) \ell_d j_d^{r,(0)}, \tag{3.17a}$$

$$\frac{\mathrm{d}\varepsilon_d^{(0)}}{\mathrm{d}t} = -\beta_d^{\mathrm{surf}} j_d^{\mathrm{S},(0)}, \tag{3.17b}$$

$$\frac{\mathrm{d}\phi_d^{(0)}}{\mathrm{d}t} = \frac{1}{C_d^{\mathrm{dl}}}\left(\frac{\partial i_{\mathrm{e},d}^{(0)}}{\partial x} - \sum_{r\in\mathcal{R}} j_d^{r,(0)}\right), \tag{3.17c}$$

where

$$j_d^{r,(0)} = j_d^r\left(\{c_k^{(0)}\}, \phi_d^{(0)}\right), \tag{3.17d}$$

and $\partial i_{\mathrm{e},d}^{(0)}/\partial x$ is given by (3.16), with initial conditions (3.14i). The term $\beta^r c_k^{(0)}$ in (3.17a) comes from $V_z^{\square,(0)}$ through (3.1i).

By (3.4) and (3.11), we now know the voltage to leading order since $\Phi_{\mathrm{e}}^{(0)} = -\phi_{\mathrm{n}}^{(0)}$ (uniformly across the whole cell) and

$$V^{(0)}(t) = \phi_{\mathrm{p}}^{(0)} + \Phi_{\mathrm{e}}^{(0)} = \phi_{\mathrm{p}}^{(0)} - \phi_{\mathrm{n}}^{(0)}. \tag{3.18}$$

3.3.3 First-order quasi-static solution

We now solve the first-order system, (3.15), to find the $\mathcal{O}(\mathcal{C}_{\mathrm{e}})$ correction to the voltage. In outline, we solve (3.15) as follows:

(i) find each $c_k^{(1)}$ using (3.15a), up to an arbitrary function of time, $A_k(t)$;

(ii) use the solvability condition on $c_k^{(2)}$, the $\mathcal{O}(\mathcal{C}_{\mathrm{e}}^2)$ correction to c_k, to write an ODE for each $A_k(t)$;

(iii) find $\Phi_{\mathrm{e}}^{(1)}$ given $c_k^{(1)}$, using (3.15c);

(iv) integrate (3.15e) in x across each electrode to find the spatially-averaged potential differences, $\bar{\phi}_d^{(1)}$;

(v) use (3.4) and (3.11) to find $V^{(1)}$, given $\Phi_{\mathrm{e}}^{(1)}$ and $\bar{\phi}_d^{(1)}$.

In detail, following (i), we rearrange (3.15a) to give a second-order ODE in x for each c_k,

$$D_k^{\mathrm{eff},(0)} \frac{\partial^2 c_k^{(1)}}{\partial x^2} = \mathcal{D}_k \left(\frac{\partial}{\partial t} \left(\varepsilon^{(0)} c_k^{(0)} \right) + c_k^{(0)} \left(\frac{\partial v^{\square,(0)}}{\partial x} + V_z^{\square,(0)} \right) + \sum_{r \in \mathcal{R}} s_k^r j^{r,(0)} \right), \tag{3.19}$$

where the right-hand side is a known function of time, and is piecewise constant in space (uniform in each subdomain). We denote the right-hand side of (3.19) by the piecewise constant function $P_k(x,t)$, so that

$$\frac{\partial^2 c_k^{(1)}}{\partial x^2} = \frac{P_k(x,t)}{D_k^{\mathrm{eff},(0)}} = \begin{cases} P_{k,\mathrm{n}}(t)/D_{k,\mathrm{n}}^{\mathrm{eff},(0)}(t), & 0 < x < \ell_{\mathrm{n}}, \\ P_{k,\mathrm{s}}(t)/D_{k,\mathrm{s}}^{\mathrm{eff},(0)}(t), & \ell_{\mathrm{n}} < x < 1 - \ell_{\mathrm{p}}, \\ P_{k,\mathrm{p}}(t)/D_{k,\mathrm{p}}^{\mathrm{eff},(0)}(t), & 1 - \ell_{\mathrm{p}} < x < 1. \end{cases} \tag{3.20}$$

We can then integrate (3.20) analytically, using (3.15g) and continuity of $c_k^{(1)}$ and $D_k^{\mathrm{eff},(0)} \partial c_k^{(1)}/\partial x$ at electrode-separator interfaces, to find an explicit expression for each $c_k^{(1)}$, which we split into two parts

$$c_k^{(1)} = A_k(t) + \tilde{c}_k^{(1)}, \tag{3.21}$$

where A_k is to be determined from the second-order problem. Then $\tilde{c}_k^{(1)}$ are given by

$$\tilde{c}_k^{(1)} = \begin{cases} P_{k,\mathrm{n}} \frac{x^2-\ell_\mathrm{n}^2}{2D_{k,\mathrm{n}}^{\mathrm{eff},(0)}}, & 0 < x < \ell_\mathrm{n}, \\ P_{k,\mathrm{s}} \frac{(x-\ell_\mathrm{n})^2}{2D_{k,\mathrm{s}}^{\mathrm{eff},(0)}} + P_{k,\mathrm{n}} \frac{\ell_\mathrm{n}(x-\ell_\mathrm{n})}{D_{k,\mathrm{s}}^{\mathrm{eff},(0)}}, & \ell_\mathrm{n} < x < 1-\ell_\mathrm{p}, \\ P_{k,\mathrm{p}} \frac{(x-1)^2-\ell_\mathrm{p}^2}{2D_{k,\mathrm{p}}^{\mathrm{eff},(0)}} + P_{k,\mathrm{s}} \frac{\ell_\mathrm{s}^2}{2D_{k,\mathrm{s}}^{\mathrm{eff},(0)}} + P_{k,\mathrm{n}} \frac{\ell_\mathrm{n}\ell_\mathrm{s}}{D_{k,\mathrm{s}}^{\mathrm{eff},(0)}}, & 1-\ell_\mathrm{p} < x < 1. \end{cases} \tag{3.22}$$

We note that $\tilde{c}_k^{(1)}$, and hence c_k, are piecewise quadratic, which justifies the assumption of Knauff [62]. A similar assumption is made in [51] for lithium-ion.

Next, we follow (ii) to find $A_k(t)$ by expanding (3.1a) to second-order in $\mathcal{C}_\mathrm{e}$:

$$\begin{aligned} \frac{\partial}{\partial t}\left(\varepsilon^{(1)}c_k^{(0)} + \varepsilon^{(0)}c_k^{(1)}\right) &= \mathcal{D}_k\left(D_k^{\mathrm{eff},(0)}\frac{\partial^2 c_k^{(2)}}{\partial x^2} + \frac{\partial}{\partial x}\left(D_k^{\mathrm{eff},(1)}\frac{\partial^2 c_k^{(1)}}{\partial x^2}\right)\right) \\ &\quad - \frac{\partial}{\partial x}\left(c_k^{(1)}v^{\square,(0)} + c_k^{(0)}v^{\square,(1)}\right) - c_k^{(0)}V_z^{\square,(1)} - c_k^{(1)}V_z^{\square,(0)} - \sum_{r\in\mathcal{R}} s_k^r j^{r,(1)}. \end{aligned} \tag{3.23}$$

Integrating (3.23) from $x = 0$ to $x = 1$ and using the fact that $\partial c_\mathrm{e}^{(1)}/\partial x = \partial c_\mathrm{e}^{(2)}/\partial x = 0$ at $x = 0, 1$, together with the boundary conditions (3.14g) and (3.15g) for $v^{\square,(0)}$ and $v^{\square,(1)}$, the first four terms on the right-hand side of (3.23) vanish. Hence we obtain an equation relating $A_k(t)$, $\bar{\varepsilon}_d^{(1)}(t)$ and $\bar{j}^{(1)}$ given leading-order terms and $\tilde{c}_k^{(1)}$:

$$\begin{aligned} \frac{\mathrm{d}}{\mathrm{d}t}\left(A_k \sum_{d\in\{\mathrm{n,s,p}\}} \ell_d \varepsilon_d^{(0)}\right) &= -\sum_{d\in\{\mathrm{n,s,p}\}}\left[\ell_d \frac{\mathrm{d}}{\mathrm{d}t}\left(\bar{\varepsilon}_d^{(1)}c_k^{(0)} + \varepsilon_d^{(0)}\bar{\tilde{c}}_{k,d}^{(1)}\right)\right] \\ &\quad - \sum_{d\in\{\mathrm{n,s,p}\}}\left[\ell_d \sum_{r\in\mathcal{R}}\left[\left(s_k^r + \beta^r c_k^{(0)}\right)\bar{j}_d^{r,(1)} + \beta^r\left(\bar{\tilde{c}}_{k,d}^{(1)} + A_k\right)j_d^{r,(0)}\right]\right], \end{aligned} \tag{3.24}$$

where $\bar{\varepsilon}_d^{(1)}$ are found by integrating (3.15b) and we have introduced the averages

$$\bar{\cdot}^{\mathrm{n}} = \frac{1}{\ell_\mathrm{n}}\int_0^{\ell_\mathrm{n}} \cdot\,\mathrm{d}x, \qquad \bar{\cdot}^{\mathrm{s}} = \frac{1}{\ell_\mathrm{s}}\int_{\ell_\mathrm{n}}^{1-\ell_\mathrm{p}} \cdot\,\mathrm{d}x, \qquad \bar{\cdot}^{\mathrm{p}} = \frac{1}{\ell_\mathrm{p}}\int_{1-\ell_\mathrm{p}}^{1} \cdot\,\mathrm{d}x. \tag{3.25}$$

Note that when only one reaction occurs, $\bar{j}_d^{r,(1)}$ is zero in each electrode and so each $\bar{\varepsilon}_d^{r,(1)}$ is zero, whereas if no convection occurs then $V_z^{\square,(0)}$ and $V_z^{\square,(1)}$ are zero. Hence in the case where there is no convection and only one reaction, A_k is given directly by

$$A_k(t) = -\frac{\sum_{d\in\{\mathrm{n,s,p}\}} \ell_d \varepsilon_d^{(0)} \bar{\tilde{c}}_{k,d}^{(1)}}{\sum_{d\in\{\mathrm{n,s,p}\}} \ell_d \varepsilon_d^{(0)}}. \tag{3.26}$$

Having found $c_k^{(1)}$ up to the constants A_k, we proceed to (iii) and integrate (3.15c), using (3.16) and continuity of $\Phi_{\mathrm{e}}^{(1)}$, to find

$$\Phi_{\mathrm{e}}^{(1)} = \frac{\chi_{\mathrm{e}}^{(0)}}{c_{\mathrm{e}}^{(0)}}\left(c_{\mathrm{e}}^{(1)} - \bar{c}_{\mathrm{e,n}}^{(1)}\right) - \bar{\phi}_{\mathrm{n}}^{(1)} - \begin{cases} \mathcal{I}\frac{3x^2-\ell_{\mathrm{n}}^2}{6\ell_{\mathrm{n}}\kappa_{\mathrm{n}}^{\mathrm{eff},(0)}}, & x \in \Omega_{\mathrm{n}}, \\ \mathcal{I}\left(\frac{\ell_{\mathrm{n}}}{3\kappa_{\mathrm{n}}^{\mathrm{eff},(0)}} + \frac{x-\ell_{\mathrm{n}}}{\kappa_{\mathrm{s}}^{\mathrm{eff},(0)}}\right), & x \in \Omega_{\mathrm{s}}, \\ \mathcal{I}\left(\frac{\ell_{\mathrm{n}}}{3\kappa_{\mathrm{n}}^{\mathrm{eff},(0)}} + \frac{\ell_{\mathrm{s}}}{\kappa_{\mathrm{s}}^{\mathrm{eff},(0)}} + \frac{\ell_{\mathrm{p}}^2-(1-x)^2}{2\ell_{\mathrm{p}}\kappa_{\mathrm{p}}^{\mathrm{eff},(0)}}\right), & x \in \Omega_{\mathrm{p}}. \end{cases} \tag{3.27}$$

The constant terms in (3.27) are chosen so that $\bar{\Phi}_{\mathrm{e,n}}^{(1)} = -\bar{\phi}_{\mathrm{n}}^{(1)}$, which must hold by (3.4) and (3.11).

Next, we address (iv) and eliminate $\partial i_{\mathrm{e}}^{(1)}/\partial x$ from (3.15e) by integrating the equation from $x = 0$ to $x = \ell_{\mathrm{n}}$ (for $d = \mathrm{n}$) and from $x = 1 - \ell_{\mathrm{p}}$ to $x = 1$ (for $d = \mathrm{p}$), using (3.15g) and (3.15h) each time. We also integrate (3.15f) across each electrode to give an ODE for each $\bar{\phi}_d^{(1)}$, which we combine with (3.24) and the integrated form of (3.15b) to give a sytem of ODEs for A_k, $\bar{\varepsilon}_d^{(1)}$ and $\bar{\phi}_d^{(1)}$,

$$\begin{aligned} \frac{\mathrm{d}}{\mathrm{d}t}\left(A_k \sum_{d\in\{\mathrm{n,s,p}\}} \ell_d \varepsilon_d^{(0)}\right) = &- \sum_{d\in\{\mathrm{n,s,p}\}} \left[\ell_d \frac{\mathrm{d}}{\mathrm{d}t}\left(\bar{\varepsilon}_d^{(1)} c_k^{(0)} + \varepsilon_d^{(0)} \bar{\tilde{c}}_{k,d}^{(1)}\right)\right] \\ &- \sum_{d\in\{\mathrm{n,s,p}\}} \left[\ell_d \sum_{r\in\mathcal{R}} \left(s_k^r + \beta^r c_k^{(0)}\right) \bar{j}_d^{r,(1)}\right] \\ &- \sum_{d\in\{\mathrm{n,s,p}\}} \left[\ell_d \sum_{r\in\mathcal{R}} \beta^r \left(\bar{\tilde{c}}_{k,d}^{(1)} + A_k\right) j_d^{r,(0)}\right], \end{aligned} \tag{3.28a}$$

$$\frac{\mathrm{d}\bar{\varepsilon}_d^{(1)}}{\mathrm{d}t} = -\beta^{\mathrm{surf}} \bar{j}_d^{\mathrm{S},(1)}, \tag{3.28b}$$

$$\frac{\mathrm{d}\bar{\phi}_d^{(1)}}{\mathrm{d}t} = -\frac{1}{C_d^{\mathrm{dl}}} \sum_{r\in\mathcal{R}} \bar{j}_d^{r,(1)}, \tag{3.28c}$$

where

$$\bar{j}_d^{r,(1)} = \sum_{k\in\mathcal{S}} \left(\frac{\partial j_d^{r,(0)}}{\partial c_k^{(0)}} \bar{c}_k^{(1)}\right) + \frac{\partial j_d^{r,(0)}}{\partial \phi_d^{(0)}} \bar{\phi}_d^{(1)}, \tag{3.28d}$$

with initial conditions (3.15i). In (3.28d), $\bar{c}_k^{(1)}$ depends on A_k through (3.21).

We finally use (v) and, by (3.4), (3.11) and (3.27), the first-order correction to the voltage is

$$\begin{aligned} V^{(1)}(t) &= \bar{\phi}_{\mathrm{p}}^{(1)} + \bar{\Phi}_{\mathrm{e,p}}^{(1)} \\ &= \bar{\phi}_{\mathrm{p}}^{(1)} - \bar{\phi}_{\mathrm{n}}^{(1)} + \frac{\chi_{\mathrm{e}}^{(0)}}{c_{\mathrm{e}}^{(0)}}\left(\bar{c}_{\mathrm{e,p}}^{(1)} - \bar{c}_{\mathrm{e,n}}^{(1)}\right) - \mathcal{I}\left(\frac{\ell_{\mathrm{n}}}{3\kappa_{\mathrm{n}}^{\mathrm{eff},(0)}} + \frac{\ell_{\mathrm{s}}}{\kappa_{\mathrm{s}}^{\mathrm{eff},(0)}} + \frac{\ell_{\mathrm{p}}}{3\kappa_{\mathrm{p}}^{\mathrm{eff},(0)}}\right). \end{aligned} \tag{3.28e}$$

By comparing (3.17) with (3.28), we see that the first-order system has exactly the same complexity as the leading-order system, and further is linear in all its variables.

3.3.4 Composite solution

The quasi-static solution developed in Sections 3.3.2 and 3.3.3 is valid when the current varies slowly, but fails to capture transient behaviour when the current changes more rapidly, such as a jump. To capture such transients, we could consider a boundary layer in time by rescaling time with $\tau = (t - t^*)/\mathcal{C}_\mathrm{e}$, where t^* is the time of the jump in the current, defining $C(\tau) = c_k(t)$ (and likewise for other variables) and expanding in powers of $\mathcal{C}_\mathrm{e}$. We give the details of such an approach in Appendix D.

Such a transient solution would be valid at short times after a jump time t^*, but break down at times long after the jump time. To obtain a solution that is valid both at short times after a jump in current and at long times, without having to repeatedly 'reset' the transient solution, we use a 'composite' solution, which we now develop here. This solution is 'composite' in the sense that it combines terms from the inner (transient) problem with the outer (quasi-static) problem.

We consider the lowest order and first order correction for the concentration by taking $\tilde{c}_k = c_k^{(0)} + \mathcal{C}_\mathrm{e}\, c_k^{(1)}$. We then consider, for each species, the PDE

$$\begin{aligned}\varepsilon^{(0)}\frac{\partial \tilde{c}_k}{\partial t} + c_k^{(0)}\frac{\partial v^{\square,(0)}}{\partial x} = \frac{D^{\mathrm{eff},(0)}}{\mathcal{C}_\mathrm{e}}\frac{\partial^2 \tilde{c}_k}{\partial x^2} - \tilde{c}_k\frac{\partial \varepsilon^{(0)}}{\partial t} - \mathcal{C}_\mathrm{e} c_k^{(0)}\frac{\partial \varepsilon^{(1)}}{\partial t},\\ - \sum_{r\in\mathcal{R}}\left(s_k^r\left(j^{r,(0)} + \mathcal{C}_\mathrm{e} j^{r,(1)}\right) + \beta^r\left(\tilde{c}_k j^{r,(0)} + \mathcal{C}_\mathrm{e} c_k^{(0)} j^{r,(1)}\right)\right), \quad (3.29)\end{aligned}$$

where $c_k^{(0)}$, $\varepsilon^{(0)}$ and $v^{(0)}$ are given by the solution of the leading-order problem. We note that for long times, $\mathcal{C}_\mathrm{e}\,\partial c_k^{(1)}/\partial t$ is a higher-order term and we retrieve the quasi-static problem (3.15a), while for short times, re-scaling $\tau = (t-t^*)/\mathcal{C}_\mathrm{e}$, $c_k^{(0)}$ is constant and terms involving $\mathcal{C}_\mathrm{e}$ are second-order terms, and so we have the transient problem (D.3a) for $c_k^{(1)}$. Hence (3.29) is valid uniformly at both short times and long times.

Deriving the composite solution from the first-order solution would suggest that these first-order terms such as $j^{r,(1)}$ should have been included through their average (as in (3.24)). However, this leads to an integro-differential equation for $\tilde{c}_k$. Instead, we include first-order terms in distributed form, which provides a more accurate solution (since the first-order terms provide better spatial resolution) at lower computational cost (since the equation remains local). Equation (3.29) appears to be approaching a similar level of complexity to the full model, but in reality it is less computationally intensive since (3.29) remains linear in $\tilde{c}$.

The composite solution then consists of solving (3.29) for $\tilde{c}_k$, then computing

$$c_k^{(1)} = \frac{\tilde{c}_k - c_k^{(0)}}{\mathcal{C}_\mathrm{e}}, \quad (3.30)$$

and finally finding $V^{(1)}$ through (3.28) with $c_k^{(1)}$ given by (3.30). Each ODE (3.28a) for A_k (one for each species) has been replaced by a linear PDE for $\tilde{c}_k$.

3.3.5 Comparison with existing models

Leading-order models. Our leading-order model (3.17) is similar to the Lumped Parameter Model (LPM) developed by Newman and Tiedemann [88]. Although their model includes secondary reactions to account for hydrolysis, our model could easily be extended using the framework presented here (as we will show in Chapter 5). Our Leading-Order Quasi-Static (LOQS) model is also very similar to the one developed by Gandhi et al. [42] in the case of a single reaction (in which case (3.17) can be solved explicitly in the limit of $C^{\mathrm{dl}} \to 0$). Finally, our model reinforces the sensitivity analysis performed by van Rensburg [57], which suggests that parameters relating to kinetics (which appear at leading order in our models) are more important than those relating to transport (which appear at first order in our models).

In different chemistries, similar reduced-order models have been derived for discharges at low C-rates. The well-known Single-Particle Model (SPM) for lithium-ion batteries [32, 33, 80, 106, 130] is similar in nature to our leading-order model, with some differences due to the to different underlying chemistries. In lithium-ion batteries, the porosity and average electrolyte concentration are constant, and so our equations (3.17a,b) do not appear in the SPM. However, the SPM includes PDEs for the concentration of lithium in the particles, which is not necessary here as no intercalation occurs. The only comparison that we can make between our model and the SPM is in the kinetic equations. By comparing our (3.17c,d) against (5) in [80], we find agreement in spirit, though we do not in general invert our Butler-Volmer equation to give the voltage explicitly.

By virtue of the different chemistry, our leading-order model is simpler than the SPM as it consists only of ODEs. Hence our model is more directly comparable with the 'Single Particle Model-Electrode Averaged Model' (SPM-EAM) of Moyles et al. [82, 83], which consists of a system of ODEs and is developed by considering the limit of fast lithium diffusion in the particles.

First-order models. Fewer reduced-order models in the literature consider first-order corrections. For lead-acid batteries, Knauff [62] assumes without systematic justification that the electrolyte concentration profile is quadratic in x; this claim is supported by our first-order quasi-static solution (3.22). In different chemistries, our composite model can be compared to the Single Particle Model with electrolyte

(SPMe) for lithium-ion batteries [51, 59, 81, 95, 98, 118]. In the SPMe, corrections to the SPM only appear in the model through the electrolyte, and so can be compared directly with our lead-acid model. The most systematic derivation of the SPMe is performed by Moura et al. [81], who make several assumptions that can be justified by our asymptotic analysis. Our equation for the composite concentration (3.29) agrees exactly with (25-27) in [81] in the case of constant porosity and zero convection, and the first-order forms of the voltage (our (3.28e) versus (32) in [81]) are qualitatively similar, with some quantitative differences.

3.4 Results and discussion: discharge

In Section 3.3, we derived three systems that approximate the full dimensionless system (3.1)-(3.3) with varying degrees of accuracy:

1. Leading-order quasi-static (LOQS) – (3.17)
2. First-order quasi-static (FOQS) – (3.22), (3.27) and (3.28)
3. Composite – (3.27)-(3.29)

Note that to obtain either the FOQS solution or the composite solution, we must first solve the LOQS problem.

In this section, we compare these three reduced-order models with the full one-dimensional system (3.1)-(3.3). We treat the numerical solution of the full system as 'ground truth', and investigate the speed and accuracy of the three other models by comparing them to this full system.

Note that during a discharge the main reactions dominate, so in the results shown here we only include the reactions (1.1). This simplifies the FOQS model by allowing us to use the explicit equation (3.26) for $A_k(t)$ (assuming also that there is no convection), instead of needing to solve the ODE (3.24).

All of the results in this chapter, as well as the rest of this thesis, were obtained using our Python battery modelling software 'PyBaMM' (see Appendix A).

3.4.1 Reduced-order solutions

The most important output from the model is the voltage, since this is the variable that we can compare to experimental data (treating current as a known input). In Figure 3.8, we compare the voltage during a complete constant-current discharge at a range of C-rates. The discharge is deemed to be finished either when the concentration

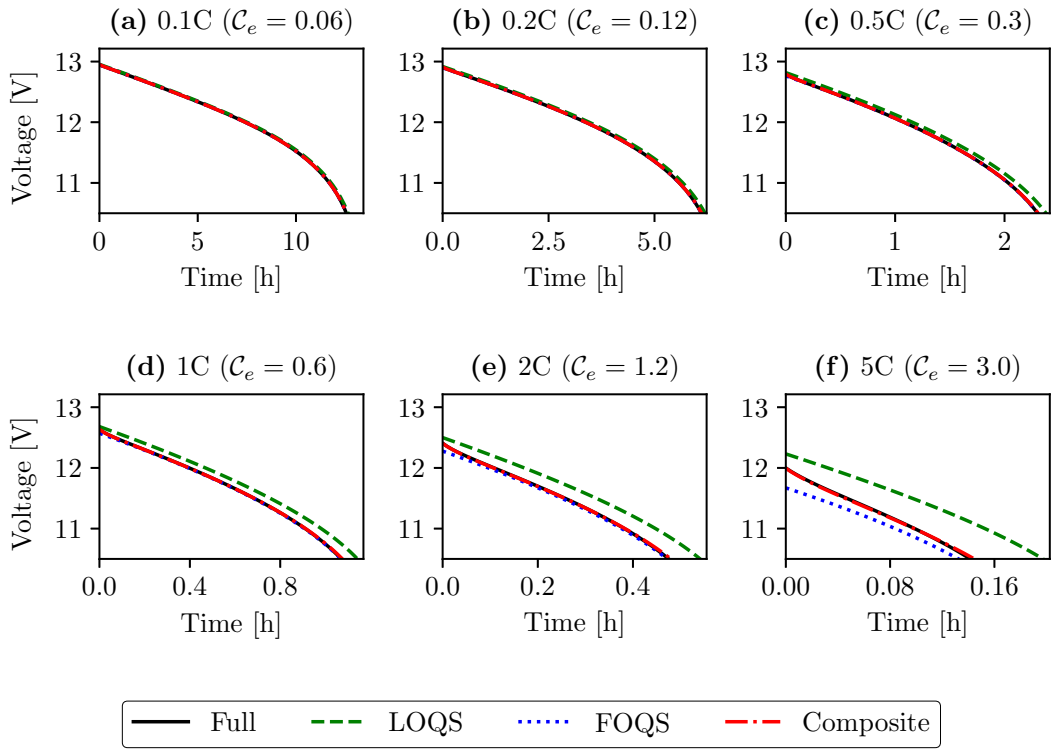

Figure 3.8: Comparing battery voltages for a constant-current discharge at a range of C-rates.

reaches zero anywhere in the cell, or when the voltage reaches a cut-off voltage of 10.5V.

We observe that all three reduced-order solutions agree well with the numerical solution at very low C-rates (Figure 3.8a). As we increase the C-rate (Figures3.8b-d), only the first-order solutions (FOQS and composite) agree with the numerical solution; further, a discrepancy appears between the FOQS solution and the numerical solution at early times. Finally, for very high C-rates (Figures 3.8e-f) the composite solution still agrees very well with the numerical solution, but the FOQS solution does not, since early transients now dominate.

To explain the behaviour observed in the voltages, we investigate internal variables, such as the electrolyte concentration at various states of charge (Figure 3.9). At a very low C-rate of 0.1C (Figure 3.9a), the concentration remains almost uniform throughout the discharge. Hence the LOQS solution, which does not take into account any spatial variations, provides a good fit to the numerical solution. At a higher C-rate of 1C (Figure 3.9b), the concentration in the numerical solution is no longer spatially homogeneous; this is non-uniformity is captured well by the FOQS

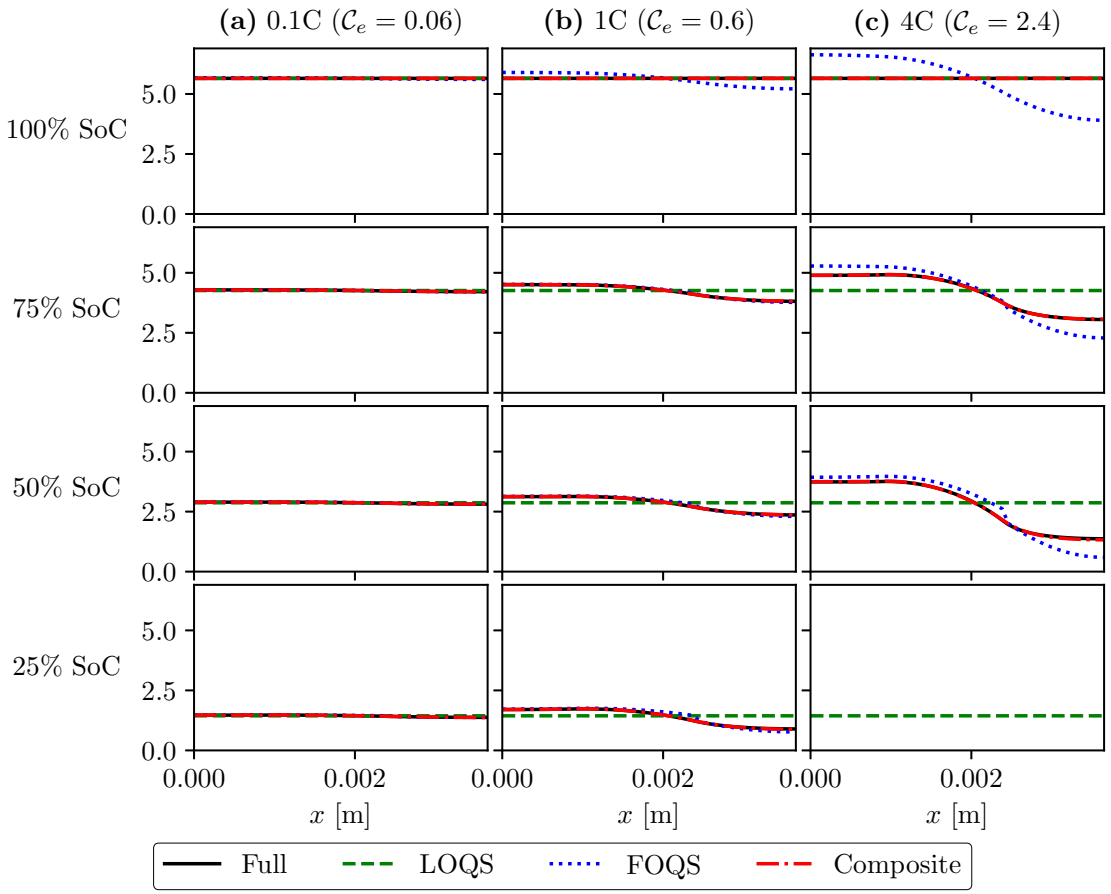

Figure 3.9: Comparing electrolyte concentrations, c_e (in mol/L), at various SoCs for a constant-current discharge at a range of C-rates. Note that, in (c), all solutions except the LOQS solution terminate before 25% SoC.

and composite solutions, but not by the LOQS solution. However, with the FOQS solution, there is a discrepancy in the concentration profiles in the positive electrode (Figures 3.9b,c, right-hand side of the spatial domain). This is because the solutions from the asymptotic methods assume a uniform interfacial current density, but in the numerical solution the interfacial current density is non-uniform. The composite solution captures the concentration profiles very well, due to the inclusion of (linear) first-order terms in (3.29).

Finally, at high C-rates (4C, Figure 3.9c), there is a diffusion transient at the start of the discharge; this is only captured by the composite solution, and not the FOQS solution. This initial diffusion transient also explains the discrepancy between the FOQS and numerical solutions at early times in Figure 3.8d.

The improvement of the composite solution over the LOQS solution can be seen further by comparing electrolyte potentials at various C-rates (Figure 3.10). For the

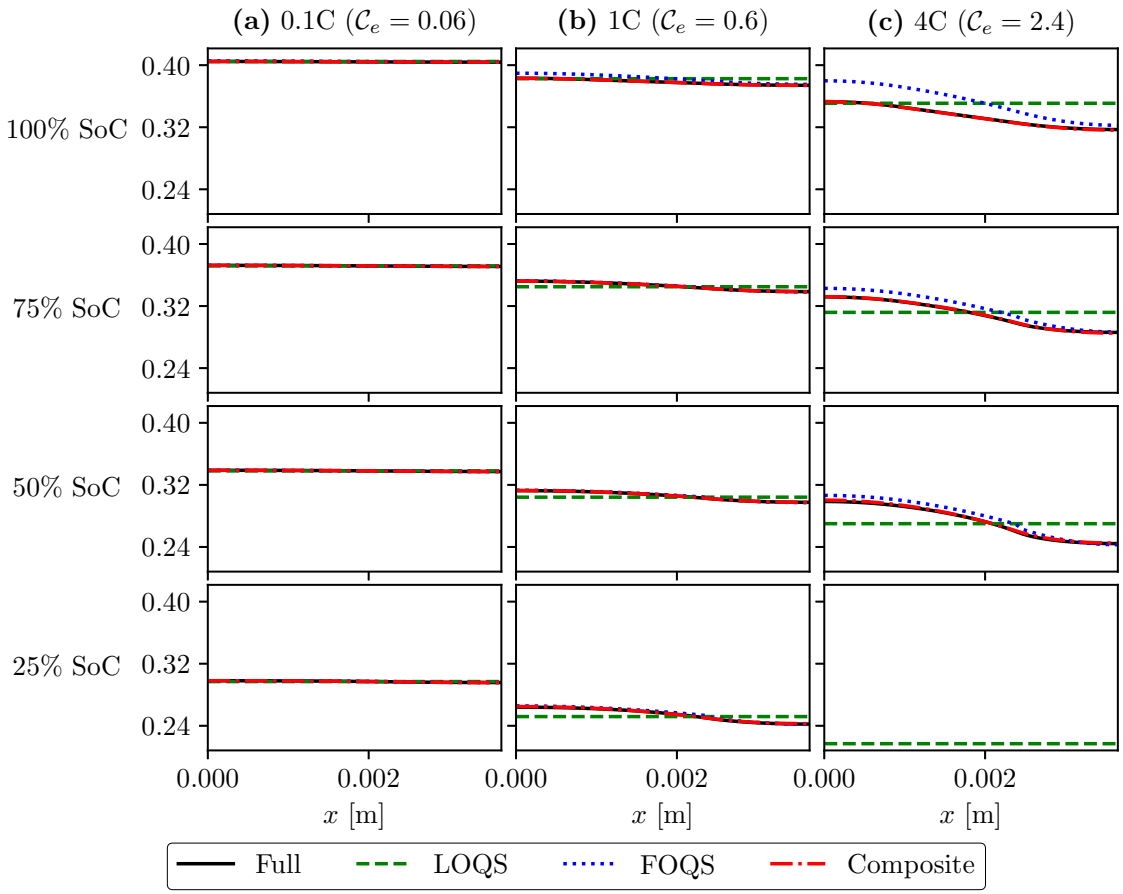

Figure 3.10: Comparing electrolyte potentials, Φ_e (in Volts), across a single cell at various SoCs for a constant-current discharge at a range of C-rates. Note that, in (c), all solutions except the LOQS solution terminate before 25% SoC.

LOQS system, the electrolyte potential is a constant determined by the kinetics in the negative electrode (3.17c). For the FOQS and composite systems, the electrolyte potential is given explicitly by (3.27), with the difference between these two models coming from the different electrolyte concentration. Once again, at low C-rates electrolyte potentials are almost spatially uniform and so all four solutions agree well. As we increase the C-rate, the FOQS solution matches well with the full solution once the quasi-static electrolyte potential is reached, while the composite solution matches well both during early transients and at late times during quasi-static operation, even when the 'small parameter' $\mathcal{C}_e$ is greater than one.

Finally, in Figure 3.11, we compare *dimensionless* interfacial current densities for each of the four models (showing dimensionless results so that the differences between negative and positive electrodes, and different C-rates, can clearly be seen). While all interfacial current densities are almost spatially uniform, and hence agree well,

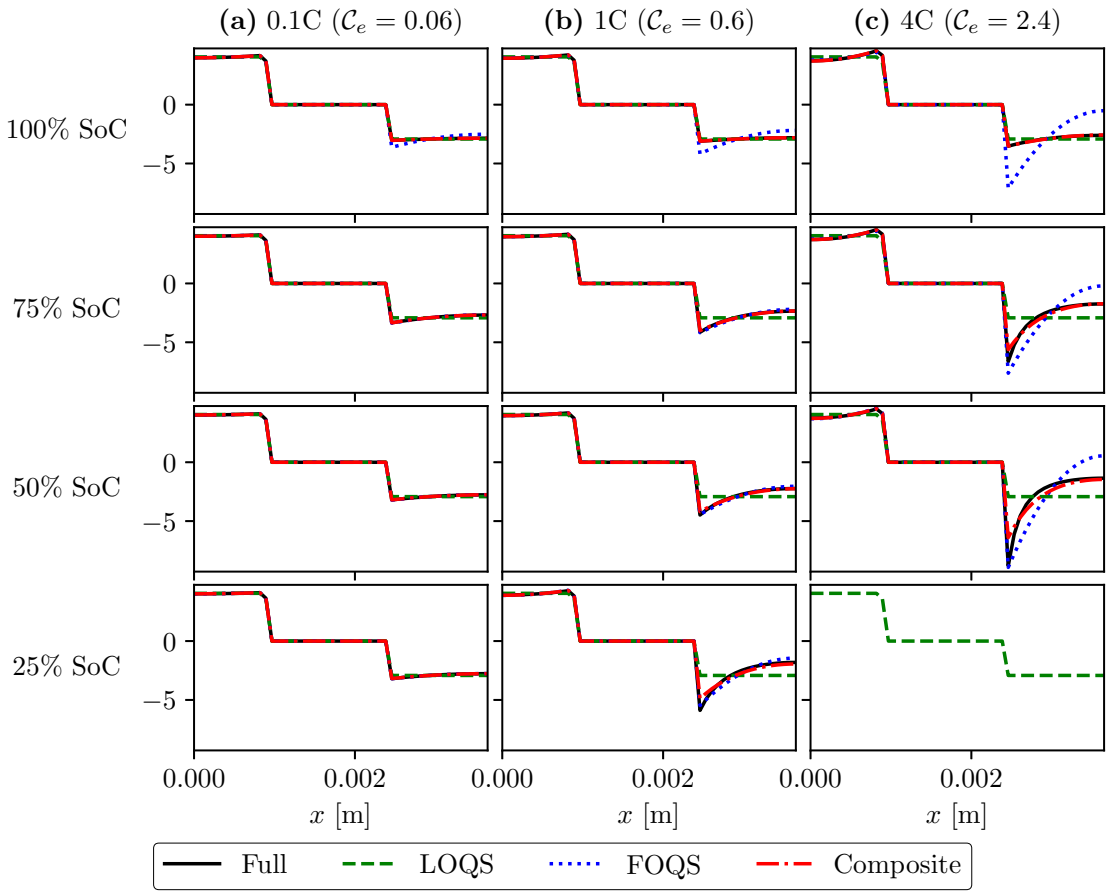

Figure 3.11: Comparing *dimensionless* interfacial current densities, j, at various SoCs for a constant-current discharge at a range of C-rates. Note that, in (c), all solutions except the LOQS solution terminate before 25% SoC.

at low C-rates, at higher C-rates the interfacial current density for the full solution becomes very non-uniform in the positive electrode. The LOQS solution does not capture this non-uniformity well, but the composite solution does. In either case, we expect second-order terms to approximate the interfacial current density with better accuracy if required.

3.4.2 Speed and error comparison

In Figure 3.12a, we show the relative errors of the voltage obtained from reduced-order models relative to the voltage obtained from the full model. Then, in Figure 3.12b, we compare the time taken to solve the various models. We see that the composite solution, LOQS and FOQS solutions are roughly 2, 20 and 100 times faster than the full numerical solution respectively. Coupled with the errors shown in Figure 3.12a, the speeds shown in Figure 3.12b suggest that in order to solve the model accurately

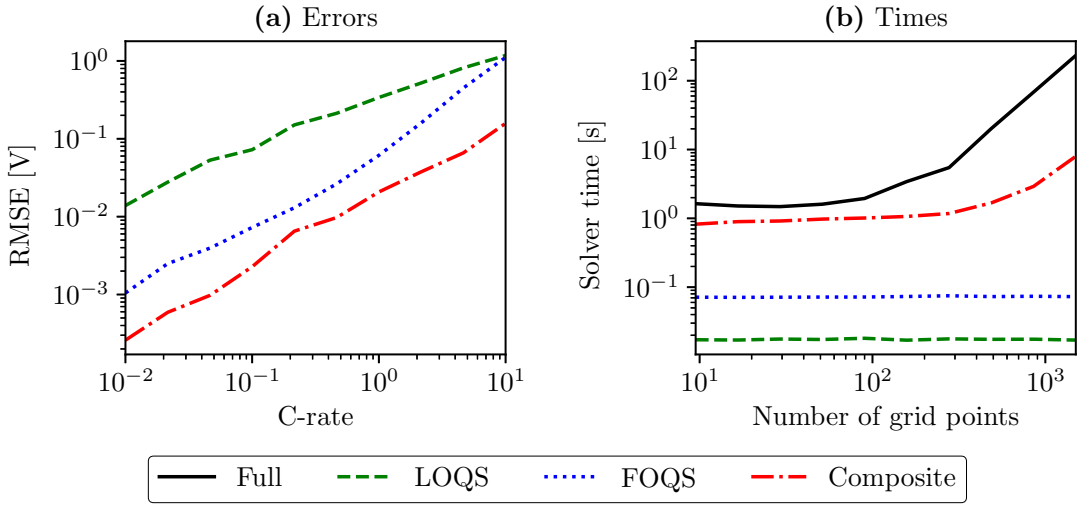

Figure 3.12: Relative RMSE (in Volts) of the reduced-order models compared to the full model, for a constant-current discharge at a range of C-rates. Time is CPU time in seconds, obtained on an Intel(R) Core(TM) i5-8500T CPU.

and as quickly as possible, we should use the LOQS model for C-rates below 0.1C, the FOQS model for C-rates of 0.1-1C, and the composite model for C-rates above 1C. The time taken for the LOQS and FOQS models are independent of grid size, since those models consist only of ODEs. The composite and full models scale exponentially with number of grid points. Efficient numerical methods for large systems was not a focus of this thesis.

3.4.3 Contributing components to the voltage

As well as obtaining a faster solution to the model, the composite solution allows us to easily identify the individual overpotentials that contribute to the total drop in voltage from full charge. Combining (3.18) and (3.28e), we write the total dimensional voltage as the sum of the initial voltage,

$$\hat{V}^0 = U_{\mathrm{p}}^{\mathrm{S},\ominus} - U_{\mathrm{n}}^{\mathrm{S},\ominus} + \frac{RT}{F}\left(\phi_{\mathrm{p}}^0 - \phi_{\mathrm{n}}^0\right), \tag{3.31}$$

and individual voltage drops [30],

$$\hat{V} = \hat{V}^0 + \frac{RT}{F}\left(\bar{\phi}_{\mathrm{p}} - \bar{\phi}_{\mathrm{n}} + V_{\mathrm{c}} + V_{\mathrm{o}}\right), \tag{3.32}$$

where the concentration overpotential, V_{c}, which accounts for losses due to concentration gradients, and the Ohmic overpotential in the electrolyte, V_{o}, which accounts for losses due to the electric resistance of the electrolyte, are given in (3.39). Note

that in (3.32) we have combined the leading-order and average first-order potential differences into a single average potential difference in each electrode,

$$\bar{\phi}_d = \phi_d^{(0)} + \mathcal{C}_\mathrm{e}\bar{\phi}_d^{(1)}. \tag{3.33}$$

Equation (3.32) would usually include a term to account for Ohmic losses in the solid electrodes, but in our reduced-order models this term is zero since σ^eff is large (cf. equation (3.10)).

For further insight, we split each average potential difference $\bar{\phi}_d$ into an open-circuit voltage,

$$V_{\mathrm{U},d} = \bar{U}_d^\mathrm{S}\left(c_\mathrm{e}\right), \tag{3.34}$$

and a kinetic overpotential (which is the same as the average surface overpotential $\bar{\eta}_d$ in each electrode),

$$V_{\mathrm{k},d} = \bar{\phi}_d - \bar{U}_d^\mathrm{S}\left(c_\mathrm{e}\right). \tag{3.35}$$

When considering discharges, in which the only reactions occurring are the main reactions (1.1) and so j^S is the only non-zero interfacial current density, we can find an explicit expression for $V_{\mathrm{k},d}$ as a function of c_e if we make some further simplifications. Taking the limit of small C^dl, so that capacitance effects are negligible, and assuming that the Butler-Volmer equation (2.24) is symmetric ($\alpha^\mathrm{S} = 0.5$), we can invert (3.17c) to give

$$\eta_d^{(0)} = \sinh^{-1}\left(\frac{j_d^{(0)}}{2j_{0,d}^{(0)}}\right). \tag{3.36}$$

Then, we can solve (3.28c) analytically to find

$$V_{\mathrm{k},d} = \eta_d^{(0)} + \frac{\mathcal{C}_\mathrm{e}\bar{j}_{0,\mathrm{n}}^{(1)}}{j_{0,\mathrm{n}}^{(0)}}\tanh\left(\eta_d^{(0)}\right). \tag{3.37}$$

In summary, with the assumptions of no capacitance and symmetric Butler-Volmer, we can write the individual voltage contributions as

$$\hat{V} = \hat{V}^0 + \frac{RT}{F}\left(V_\mathrm{U} + V_\mathrm{k} + V_\mathrm{c} + V_\mathrm{o}\right), \tag{3.38}$$

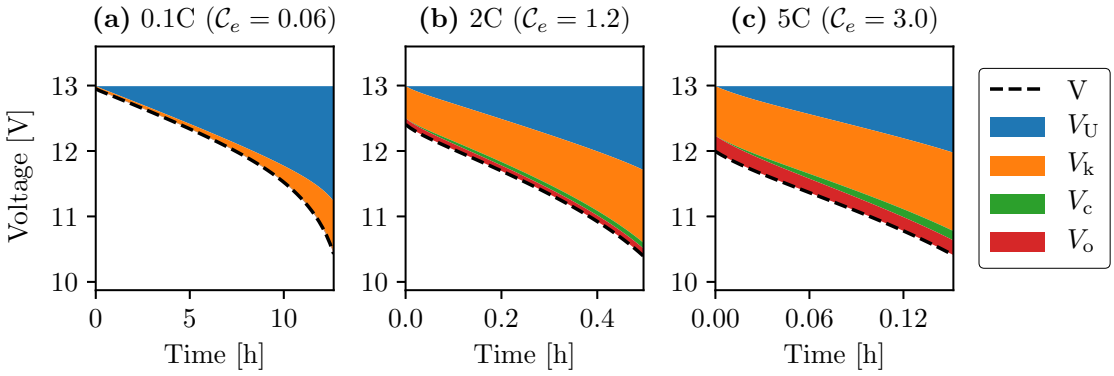

Figure 3.13: Decomposition of voltage drop into dimensional components, as given by (3.38) and (3.39), for a constant-current discharge at a range of C-rates.

where

$$V_U = V_{U,p} - V_{U,n}$$
$$= U_p^S\left(c_e^{(0)}\right) - U_n^S\left(c_e^{(0)}\right) + \mathcal{C}_e\bar{c}_e^{(1)}\left(U_p^S\right)'\left(c_e^{(0)}\right) - \mathcal{C}_e\bar{c}_e^{(1)}\left(U_n^S\right)'\left(c_e^{(0)}\right), \tag{3.39a}$$

$$V_k = V_{k,p} - V_{k,n}$$
$$= -\sinh^{-1}\left(\frac{\mathcal{I}}{2j_{0,p}^{(0)}\ell_p}\right) - \sinh^{-1}\left(\frac{\mathcal{I}}{2j_{0,n}^{(0)}\ell_n}\right)$$
$$- \frac{\mathcal{C}_e\bar{j}_{0,p}^{(1)}}{j_{0,p}^{(0)}}\tanh\left(\sinh^{-1}\left(\frac{\mathcal{I}}{2j_{0,p}^{(0)}\ell_p})\right)\right) - \frac{\mathcal{C}_e\bar{j}_{0,n}^{(1)}}{j_{0,n}^{(0)}}\tanh\left(\sinh^{-1}\left(\frac{\mathcal{I}}{2j_{0,n}^{(0)}\ell_n})\right)\right), \tag{3.39b}$$

$$V_c = \frac{\mathcal{C}_e\,\chi_e^{(0)}}{c_e^{(0)}}\left(\bar{c}_{ep}^{(1)} - \bar{c}_{en}^{(1)}\right), \tag{3.39c}$$

$$V_o = -\mathcal{C}_e\,\mathcal{I}\left(\frac{\ell_n}{3\kappa_n^{\mathrm{eff},(0)}} + \frac{\ell_s}{\kappa_s^{\mathrm{eff},(0)}} + \frac{\ell_p}{3\kappa_p^{\mathrm{eff},(0)}}\right). \tag{3.39d}$$

Combining the leading-order parts of V_U and V_k gives a similar result to equation (5) of [80] and equation [12] of [42]. Together with the quasi-static formulas (3.17a) for $c_e^{(0)}$ and (3.22) and (3.24) for $c_e^{(1)}$, equations (3.38) and (3.39) give an exact formula for the voltage that is valid for most operating C-rates (below 1C). For higher C-rates, we must solve (3.29) and use (3.30), instead of (3.22) and (3.24), to find $c_e^{(1)}$.

In Figure 3.13, we show the relative contribution from each of the terms in (3.39). At low C-rates (Figure 3.13a), the drop in voltage is almost entirely due to the change in the OCP of the two electrodes as the concentration changes, V_U and resistance due to the kinetic potential V_k; this is why the LOQS solution is accurate enough in this regime. As we increase the C-rate (Figure 3.13b), the kinetic overpotential

increases. Finally, at very high C-rates (Figure 3.13c), we see that the sharp initial drop in voltage is due to both kinetic overpotentials and the ohmic overpotential in the electrolyte, V_{o}, in roughly equal measures.

The contributing components to the voltage given by (3.38) could be used to help guide any optimisation of a battery design. For example, the behaviour observed in Figure 3.13b suggests that an effective way to improve the power capacity of the battery (by reducing the voltage drop) might be to target reduction of the kinetic overpotential. Alternatively, this allows us to explore the trade-off between energy capacity and power capacity of the battery, and hence optimise the behaviour of the battery for specific applications. For example, increasing the total thickness, $\hat{L}$, of an cell would increase the total capacity, and hence increase the energy capacity of the battery. However, increasing $\hat{L}$ would also increase the diffusional C-rate (Table 2.1), and so increase the contributions to the voltage drop in (3.39), decreasing the power capacity of the battery. It becomes evident that we need to consider first-order effects in order to fully understand the trade-off between energy capacity and power capacity; the LOQS model would naively suggest that increasing $\hat{L}$ is always the optimal strategy. A third option could be to fix the total thickness $\hat{L}$ (i.e. fix the energy capacity) and optimise the relative thicknesses of the negative electrode, separator and positive electrode in order to minimise the voltage drop given by (3.38), and hence maximise the power capacity of the battery. In all three examples suggested, a quantitative optimisation could be done very efficiently using the formulas given in this chapter.

3.4.4 Parameter fitting

Another potential application for our reduced-order models is in parameter fitting. This is an important challenge when comparing models to experimental data, as many parameters in the model cannot be identified individually *a priori*. To demonstrate how our model can be useful for parameter fitting, we fit each model to six constant-current discharges of a 17 Ah BBOXX Solar Home battery at intervals of 0.5A from 3A to 0.5A. Each constant-current discharge is followed by a two-hour rest period during which the current is zero.

In order to use as few fitting parameters as possible, we take standard values for all parameters (given in Table B.1) except for the following:

(i) the maximum electrode porosities, $\varepsilon_{\mathrm{n}}^{\max}$ and $\varepsilon_{\mathrm{p}}^{\max}$, which we assume to be equal;

(ii) the separator porosity, $\varepsilon_{\mathrm{s}}^{\max}$;

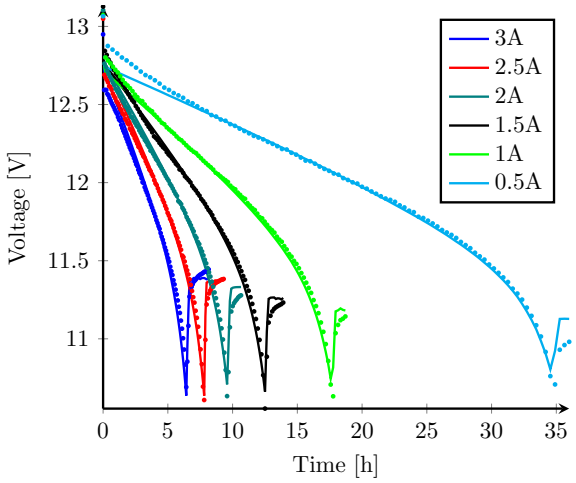

Figure 3.14: Comparing data (dots) with results from full model (lines) for a range of currents, with parameters fitted using DFO-GN (Tables B.1 and 3.2).

(iii) the exchange current-density for the negative electrode, $j_{\mathrm{n}}^{\mathrm{ref}}$ (we do however assume that $j_{\mathrm{p}}^{\mathrm{ref}} = j_{\mathrm{n}}^{\mathrm{ref}}/10$);

(iv) a 'resistance in the wires', R_{circuit}, which accounts for ohmic losses outside the battery within the BBOXX Solar Home (we take away $I_{\mathrm{circuit}}R_{\mathrm{circuit}}$ from the voltage output by the model before fitting to data);

(v) an initial SoC, q^0, for five of the curves (we assume that the first discharge, at 3A, starts from full SoC).

This gives a total of nine fitting parameters for six curves.

To fit our model to the data, we minimise the sum-of-squares of the voltage prediction error. We do this in Python with either a derivative-based (`leastsquares` in SciPy [58]) or derivative-free (DFO-GN [21]) optimisation algorithm.

Since the highest discharge current is quite low (3A corresponds to a C-rate of 0.18C), both the FOQS model and composite model agree well with the full model. These three models give a very good fit to the data except near the start of the discharge, and during the short rest period afterwards, as shown in Figure 3.14. In Table 3.1, we compare the final sum-of-squares error, as well as the time taken to find the minimum when starting from the parameters from literature of Table B.1, for each optimisation algorithm/model combination. As expected, the quasi-static models are faster than the composite model, with the full model being by far the slowest. However, this is compounded by the fact that the derivative-based algorithm from SciPy cannot find the best fit for the composite and full models, and so we must

Algorithm	LOQS		FOQS		Composite		Numerical	
	RMSE	Time	RMSE	Time	RMSE	Time	RMSE	Time
SciPy `leastsquares`	0.051	36	0.050	48	0.245	122	0.253	1443
DFO-GN	0.051	74	0.050	184	0.055	96	0.043	1144

Table 3.1: Performance of fitting algorithms for each model. RMSE is the root-mean-square of voltage prediction errors, in Volts; time is CPU time in seconds, obtained on an Intel(R) Core(TM) i5-8500T CPU.

	$\varepsilon_{\mathrm{n,p}}^{\mathrm{max}}$	$\varepsilon_{\mathrm{sep}}^{\mathrm{max}}$	$j_{\mathrm{n}}^{\mathrm{ref}}$	R_{circuit}	$q_{2.5\mathrm{A}}^{0}$	$q_{2\mathrm{A}}^{0}$	$q_{1.5\mathrm{A}}^{0}$	$q_{1\mathrm{A}}^{0}$	$q_{0.5\mathrm{A}}^{0}$
SciPy + LOQS	0.55	0.81	0.19	0.08	1.00	0.98	0.95	0.90	0.89
SciPy + FOQS	0.55	0.81	0.19	0.08	1.00	0.98	0.95	0.90	0.89
SciPy + Composite	0.60	0.90	0.07	0.13	1.00	1.00	1.00	0.98	1.00
SciPy + Numerical	0.60	0.90	0.08	0.15	1.00	1.00	1.00	1.00	1.00
DFO-GN + LOQS	0.75	0.53	0.19	0.08	1.00	0.98	0.95	0.90	0.89
DFO-GN + FOQS	0.51	0.88	0.32	0.07	1.00	0.98	0.95	0.90	0.89
DFO-GN + Composite	0.60	0.78	0.12	0.06	1.00	0.98	0.96	0.90	0.89
DFO-GN + Numerical	0.55	0.74	0.24	0.07	1.00	0.98	0.95	0.90	0.89

Table 3.2: Parameters obtained from all optimisation algorithms/model combinations. All algorithms were given the values in Table B.1 as initial data for the parameters.

resort to derivative-free optimisation methods. Thus optimising the FOQS model is thirty times faster than optimising the full model.

As shown in Table 3.2, the optimal parameters found by SciPy with the FOQS model are almost the same as those found by DFO-GN with the full model. Hence one could first fit all the parameters using SciPy and the FOQS model to give a good first guess, and then obtain a more accurate fit by using DFO-GN with the full model.

The discrepancy at early times may be due to effects from charging: we assume that the discharge starts from equilibrium, but this might not be the case following a charge. The final relaxation timescale is much longer than the two timescales in our model – the diffusion timescale ($\sim$ 15 minutes) and the capacitance timescale ($\sim$ 2 seconds) – which suggests that there is an extra physical effect that we have not considered. The exact nature of this additional physical effect remains an open question.

3.5 Concluding remarks

In this chapter, we investigated the one-dimensional version of the model developed in Chapter 2. First, we explored the impact of capacitance effects, showing that by

simply reformulating the model into a 'capacitance formulation' we can solve it more efficiently, and by including capacitance terms we obtain an even faster solution since the elliptic equations are replaced by parabolic ones.

Second, we showed the effect of including the Faradaic convection terms in our model. For the parameter values and C-rates considered in this thesis, this effect is small. However, for larger volume changes or higher C-rates, including convection terms can lead to significant differences in the electrolyte concentration, and hence the voltage. Hence it is important to consider such terms in systems where large volume changes occur, such as lithium-ion batteries with silicon anodes, or in fast-charge/fast-discharge applications.

Third, we developed a suite of reduced-order models that approximate the full system. These reduced-order models allow us to simulate a discharge of a lead/acid battery with the low complexity and high speed of equivalent-circuit models, while retaining the accuracy and physical insights of electrochemical models. Further, these models give important physical insight into the structure of the problem that is not obvious from numerical solutions of the full model. In particular, we observe that at low C-rates, the voltage drop from open-circuit potential is mainly due to kinetic effects; ohmic and concentration overpotentials are relatively very small. It is also important to note that our models are tunable: for discharges at low C-rate, we should choose the leading-order quasi-static (LOQS) model, while for high C-rates we can use the composite model, which still provides a significant speed-up compared to the full model.

This could also have been observed using the full model directly with a range of different parameter values. However, given the large number of parameters in the model, it can be time consuming to explore all of the different combinations of parameters to study the behaviour of the full model. In contrast, the reduced-order models allow us to isolate the important physics in the model, and also reduce the number of parameters that need to be varied. Once we have identified the key parameters, the full model can be used to confirm our hypothesis about the dominant physical effects.

To demonstrate the usefulness of our reduced-order models, we have also fitted each model to a set of constant-current discharge curves. The reduced-order models give similar parameter values to the full model, at lower computational cost. We have needed to fit the initial SoC, q_0, individually for each discharge curve as we do not have a good model for recharge. This motivates the work of Chapter 5.

Chapter 4

Small aspect ratio cells

In this chapter, we return to the full three-dimensional model developed in Chapter 2, and exploit the fact that the aspect ratio – the ratio of thickness $\hat{L}$ (~ 1 mm) to height $\hat{H}$ (~ 10 cm) – of most lead-acid cells is very small ($\mathcal{O}(10^{-2})$) to simplify the model. We define the aspect ratio δ by

$$\delta = \hat{L}/\hat{H} = 1/H \ll 1, \tag{4.1}$$

and take the ratio of a cell's width, $\hat{W}$, to its height, $\hat{H}$, to be $\mathcal{O}(1)$.

In the limit of small aspect ratio, we simplify the three-dimensional system (2.65) – (2.68) by decoupling through-cell effects (in the x-direction) from transverse effects (in the y- and z-directions). In Section 4.1, we rescale the y and z dimensions by a factor of $1/\delta$ and expand the solution of (2.65) – (2.68) in powers of δ. In particular, we take the distinguished limit in which the scaled dimensionless conductivity,

$$\sigma' := \sigma^{\text{eff}}\delta^2 = \frac{\hat{\sigma}^{\text{eff}}RT}{F\hat{L}\bar{i}}\frac{\hat{L}^2}{\hat{H}^2}, \tag{4.2}$$

is $\mathcal{O}(1)$, where σ^{eff} is the dimensionless effective electrode conductivity. Then, in Section 4.2, we consider further simplifications to this small-aspect-ratio problem and explore three limits as we vary the size of σ' relative to the diffusional C-rate, $\mathcal{C}_{\text{e}}$.

In the limit of relatively low electrode conductivity, we perform an expansion in $\mathcal{C}_{\text{e}}$ that is similar to that of Chapter 3, but with non-uniformities in the y- and z-directions. As we increase the electrode conductivity, we consider the distinguished limit in which $\mathcal{C}_{\text{e}}$ and $1/\sigma'$ are of similar size, and show that in this limit the electrodes act as series resistors in the transverse directions. Hence we can approximate the full system using a single one-dimensional PDE in the through-cell direction and two decoupled elliptic PDEs in the transverse directions. Finally, in the limit of very large electrode conductivity, we recover the one-dimensional model that was analysed in Chapter 3.

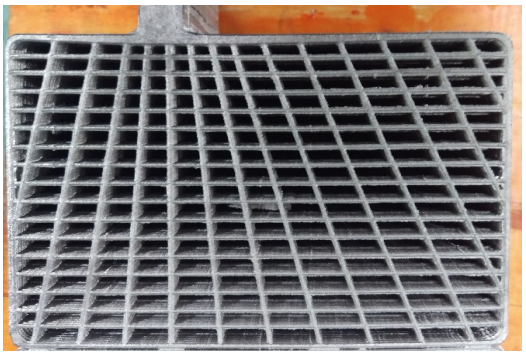

(a) Current collector grids.

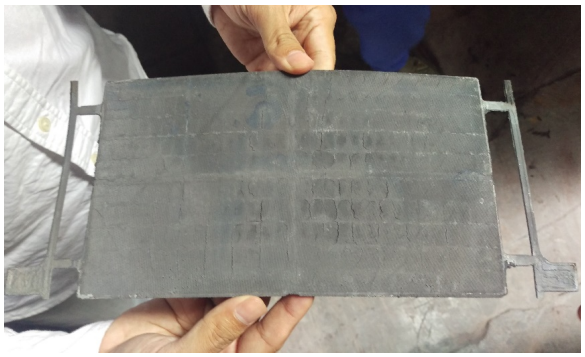

(b) Plated electrodes.

Figure 4.1: Making of an electrode for a lead-acid battery. Photographs by Ashley Grealish (BBOXX).

Current collector geometry. In some battery chemistries, the current collector and electrodes are completely distinct and can be modelled as such. However, in the case of VRLA batteries, the current collector is a grid (Figure 4.1a) onto which the porous electrode material is plated (Figure 4.1b). The current collector is more conductive than the electrodes, but has zero porosity.

To model this properly, we should write a three-dimensional model of the current collector, taking into account its exact geometry. We could then systematically homogenise this system in the current collector plane to obtain a single 'current collector/electrode' domain with an effective conductivity, porosity and permeability. For the purpose of this thesis, we do not perform this homogenisation systematically, but do consider the current collector and electrode as a single entity. Henceforth, we refer to the homogenised current collector/electrode domain simply as the 'electrode domain'.

As shown Table B.1, the positive electrode is much less conductive than the negative electrode, and hence is the limiting one. In the results of this chapter, we will consider cases where the conductivity of the homogenised positive current collector/-electrode is equal to or 5 times, 10 times or 100 times greater than the conductivity of lead dioxide (8×10^3 S/m).

4.1 Asymptotic analysis – small aspect ratio

Since the cell is tall and thin, we rescale in the y- and z-directions. With the aspect ratio δ defined by (4.1), we rescale

$$(y, z) = (Y, Z)H = (Y, Z)/\delta, \tag{4.3}$$

so that the side and top of the cell are at $Y = W' := W/H$ and $Z = 1$ respectively. Thus, the gradient and divergence operators become

$$\nabla A = \left(\frac{\partial A}{\partial x}, \delta \nabla_\perp A\right) \quad \text{and} \quad \nabla \cdot \mathbf{f} = \frac{\partial f^x}{\partial x} + \delta \nabla_\perp \cdot \mathbf{f}^\perp, \tag{4.4}$$

respectively, where $\mathbf{f} = (f^x, \mathbf{f}^\perp)$ and $\mathbf{f}^\perp = (f^y, f^z)$ and

$$\nabla_\perp A = \left(\frac{\partial A}{\partial Y}, \frac{\partial A}{\partial Z}\right) \quad \text{and} \quad \nabla_\perp \cdot \mathbf{f}^\perp = \frac{\partial f^y}{\partial Y} + \frac{\partial f^z}{\partial Z}. \tag{4.5}$$

We will expand all variables in powers of δ as

$$f(\mathbf{x}, \tau) = f^{(0)}(\mathbf{x}, \tau) + \delta f^{(1)}(\mathbf{x}, \tau) + \mathcal{O}(\delta^2), \tag{4.6}$$

and equate coefficients at different orders of δ as we take the limit of small δ.

4.1.1 Current and potential in the solid

The current density in the y- and z-directions is much larger than the current density in the through-cell directions. Hence we rescale the transverse current by defining $\mathbf{i}_\mathrm{s} = \left(i_\mathrm{s}^x, \mathbf{I}_\mathrm{s}^\perp/\delta\right)$ in component form, where both i_s^x and $\mathbf{I}_\mathrm{s}^\perp$ are order one. This is similar to the scaling of velocities for lubrication theory. Then (2.65i) becomes

$$\frac{\partial i_\mathrm{s}^x}{\partial x} + \nabla_\perp \cdot \mathbf{I}_\mathrm{s}^\perp = -\sum_{r \in \mathcal{R}} j^r - C^\mathrm{dl} \frac{\partial}{\partial t} \left(\Phi_\mathrm{s} - \Phi_\mathrm{e}\right). \tag{4.7}$$

In component form, Ohm's law (2.65j) becomes

$$i_\mathrm{s}^x = -\sigma^\mathrm{eff} \frac{\partial \Phi_\mathrm{s}}{\partial x}, \tag{4.8a}$$

$$\mathbf{I}_\mathrm{s}^\perp = -\sigma^\mathrm{eff} \delta^2 \nabla_\perp \Phi_\mathrm{s}. \tag{4.8b}$$

We now expand all variables in powers of δ, assuming the limit in which $\sigma^\mathrm{eff} = \mathcal{O}\left(1/\delta^2\right) \gg 1$ ($\sigma' = \mathcal{O}(1)$), use (4.2) and keep only leading-order terms:

$$\frac{\partial i_\mathrm{s}^{x,(0)}}{\partial x} + \nabla_\perp \cdot \mathbf{I}_\mathrm{s}^{\perp,(0)} = -\sum_{r \in \mathcal{R}} j^{r,(0)} - C^\mathrm{dl} \frac{\partial}{\partial t} \left(\Phi_\mathrm{s}^{(0)} - \Phi_\mathrm{e}^{(0)}\right), \tag{4.9a}$$

$$0 = -\frac{\partial \Phi_\mathrm{s}^{(0)}}{\partial x}, \tag{4.9b}$$

$$\mathbf{I}_\mathrm{s}^{\perp,(0)} = -\sigma' \nabla_\perp \Phi_\mathrm{s}^{(0)}. \tag{4.9c}$$

We see that $\Phi_\mathrm{s}^{(0)}$ is independent of x by (4.9b), and hence (4.9c) gives that $\mathbf{I}_\mathrm{s}^{\perp,(0)}$ is independent of x in each of the three subdomains (negative electrode, separator,

positive electrode). Note that $\mathbf{I}_{\mathrm{s}}^{\perp,(0)}$ can be discontinuous across interfaces between subdomains, and hence is not equal in the three subdomains. Integrating (4.9a) across each electrode and using the fact that $i_{\mathrm{s}}^{x,(0)} = 0$ at $x = 0, 1$ (external boundary condition (2.66b)) and $x = \ell_{\mathrm{n}}, 1 - \ell_{\mathrm{p}}$ (no current in the separator), we find

$$\nabla_{\perp} \cdot \mathbf{I}_{\mathrm{s}}^{\perp,(0)} = \begin{cases} -\sum_{r\in\mathcal{R}} \bar{j}_{\mathrm{n}}^{r,(0)} - C_{\mathrm{n}}^{\mathrm{dl}} \frac{\partial}{\partial t}\left(\bar{\Phi}_{\mathrm{s,n}}^{(0)} - \bar{\Phi}_{\mathrm{e,n}}^{(0)}\right), & \mathbf{x} \in \Omega_{\mathrm{n}}, \\ 0, & \mathbf{x} \in \Omega_{\mathrm{s}}, \\ -\sum_{r\in\mathcal{R}} \bar{j}_{\mathrm{p}}^{r,(0)} - C_{\mathrm{p}}^{\mathrm{dl}} \frac{\partial}{\partial t}\left(\bar{\Phi}_{\mathrm{s,p}}^{(0)} - \bar{\Phi}_{\mathrm{e,p}}^{(0)}\right), & \mathbf{x} \in \Omega_{\mathrm{p}}, \end{cases} \tag{4.10}$$

where $\bar{\cdot}$ indicates subdomain-averaged variables as defined in (3.25).

4.1.2 Current and potential in the liquid

As before, we let $\mathbf{i}_{\mathrm{e}} = \left(i_{\mathrm{e}}^{x}, \mathbf{I}_{\mathrm{e}}^{\perp}/\delta\right)$ in component form so that (2.65d) becomes

$$\frac{\partial i_{\mathrm{e}}^{x}}{\partial x} + \nabla_{\perp} \cdot \mathbf{I}_{\mathrm{e}}^{\perp} = \sum_{r\in\mathcal{R}} j^{r} + C^{\mathrm{dl}} \frac{\partial}{\partial t}\left(\Phi_{\mathrm{s}} - \Phi_{\mathrm{e}}\right), \tag{4.11}$$

and the MacInnes equation (2.65e) becomes

$$\mathcal{C}_{\mathrm{e}}\, i_{\mathrm{e}}^{x} = \frac{\partial}{\partial x}\left[\kappa^{\mathrm{eff}}\left(\chi \frac{\partial \ln\left(c_{\mathrm{e}}\right)}{\partial x} - \frac{\partial \Phi_{\mathrm{e}}}{\partial x}\right)\right], \tag{4.12a}$$

$$\mathcal{C}_{\mathrm{e}}\, \mathbf{I}_{\mathrm{e}}^{\perp} = \delta^{2} \nabla_{\perp}\left[\kappa^{\mathrm{eff}}\left(\chi \nabla_{\perp}\left(\ln\left(c_{\mathrm{e}}\right)\right) - \nabla_{\perp}\Phi_{\mathrm{e}}\right)\right]. \tag{4.12b}$$

Then, to leading order in δ,

$$\mathcal{C}_{\mathrm{e}}\, i_{\mathrm{e}}^{x,(0)} = \frac{\partial}{\partial x}\left[\kappa^{\mathrm{eff},(0)}\left(\chi^{(0)} \frac{\partial \ln\left(c_{\mathrm{e}}^{(0)}\right)}{\partial x} - \frac{\partial \Phi_{\mathrm{e}}^{(0)}}{\partial x}\right)\right], \tag{4.13a}$$

$$\mathcal{C}_{\mathrm{e}}\, \mathbf{I}_{\mathrm{e}}^{\perp,(0)} = \mathbf{0} \tag{4.13b}$$

and so (4.11) gives, to leading order in δ,

$$\frac{\partial i_{\mathrm{e}}^{x,(0)}}{\partial x} = \sum_{r\in\mathcal{R}} j^{r,(0)} + C^{\mathrm{dl}} \frac{\partial}{\partial t}\left(\Phi_{\mathrm{s}}^{(0)} - \Phi_{\mathrm{e}}^{(0)}\right). \tag{4.14}$$

By integrating (4.14) and using (4.10) together with the boundary conditions (2.66a) at $x = 0$ and $x = 1$, we can find how much current crosses into the separator at the

electrode interfaces,

$$\begin{aligned} i_{\mathrm{e}}^{x,(0)}\big|_{x=\ell_{\mathrm{n}}} &= \int_0^{\ell_{\mathrm{n}}} \left[\sum_{r\in\mathcal{R}} j^{r,(0)} + C^{\mathrm{dl}} \frac{\partial}{\partial t} \left(\Phi_{\mathrm{s}}^{(0)} - \Phi_{\mathrm{e}}^{(0)} \right) \right] \mathrm{d}x \\ &= -\ell_{\mathrm{n}} \nabla_\perp \cdot \mathbf{I}_{\mathrm{s,n}}^{\perp,(0)}, \end{aligned} \tag{4.15a}$$

$$\begin{aligned} i_{\mathrm{e}}^{x,(0)}\big|_{x=1-\ell_{\mathrm{p}}} &= -\int_{1-\ell_{\mathrm{p}}}^{1} \left[\sum_{r\in\mathcal{R}} j^{r,(0)} + C^{\mathrm{dl}} \frac{\partial}{\partial t} \left(\Phi_{\mathrm{s}}^{(0)} - \Phi_{\mathrm{e}}^{(0)} \right) \right] \mathrm{d}x \\ &= \ell_{\mathrm{p}} \nabla_\perp \cdot \mathbf{I}_{\mathrm{s,p}}^{\perp,(0)}. \end{aligned} \tag{4.15b}$$

Further, since $j^{r,(0)} = 0$ in the separator for all r and there are no capacitance effects there, $i_{\mathrm{e}}^{x,(0)}$ is constant in the separator and hence the leading-order current density in the separator in the x-direction is independent of x and is given by

$$i_{\mathrm{e,s}}^{x,(0)}(Y,Z,t) = i_{\mathrm{e}}^{x,(0)}\big|_{x=\ell_{\mathrm{n}}} = i_{\mathrm{e}}^{x,(0)}\big|_{x=1-\ell_{\mathrm{p}}} = -\ell_{\mathrm{n}} \nabla_\perp \cdot \mathbf{I}_{\mathrm{s,n}}^{\perp,(0)} = \ell_{\mathrm{p}} \nabla_\perp \cdot \mathbf{I}_{\mathrm{s,p}}^{\perp,(0)}. \tag{4.16}$$

4.1.3 Velocity and pressure

Similarly to the current densities, we expand mass-averaged and volume-average velocities component-wise as $\mathbf{v} = \left(v^x, \mathbf{V}^\perp/\delta\right)$ and $\mathbf{v}^\square = \left(v^{\square,x}, \mathbf{V}^{\square,\perp}/\delta\right)$ respectively. We now take leading order in δ, but do not drop higher-order terms for now. Then the volume-conservation equation (2.65f) becomes

$$\frac{\partial v^{\square,x,(0)}}{\partial x} + \nabla_\perp \cdot \mathbf{V}^{\square,\perp,(0)} = \sum_{r\in\mathcal{R}} \beta^r j^{r,(0)}, \tag{4.17}$$

Darcy's law (2.65g) becomes

$$v^{x,(0)} = -\frac{\mathcal{K}^{(0)}}{\mu^{(0)}} \frac{\partial p^{(0)}}{\partial x}, \tag{4.18a}$$

$$\mathbf{V}^{\perp,(0)} = -\frac{\mathcal{K}^{(0)}\delta^2}{\mu^{(0)}} \nabla_\perp p^{(0)}, \tag{4.18b}$$

and finally the kinematic relation (2.65h) becomes, in the limit of small π_{os},

$$\rho^{(0)} \left(v^{x,(0)} - v^{\square,x,(0)} \right) = \frac{\omega_c D_{\mathrm{e}}^{\mathrm{eff},(0)}}{\mathcal{C}_{\mathrm{e}}} \frac{\partial c_{\mathrm{e}}^{(0)}}{\partial x} + \omega_i i_{\mathrm{e}}^{x,(0)} \tag{4.19a}$$

$$\rho^{(0)} \left(\mathbf{V}^{\perp,(0)} - \mathbf{V}^{\square,\perp,(0)} \right) = \frac{\omega_c D_{\mathrm{e}}^{\mathrm{eff},(0)} \delta^2}{\mathcal{C}_{\mathrm{e}}} \nabla_\perp c_{\mathrm{e}}^{(0)} + \omega_i \delta^2 \mathbf{I}_{\mathrm{e}}^{\perp,(0)}. \tag{4.19b}$$

The naive approach at this stage would be to take $\mathcal{K}^{(0)}$ and $\mu^{(0)}$ to be order one everywhere, in which case both the transverse mass-averaged velocity, by (4.18b), and

the transverse volume-averaged velocity, by (4.19b) are zero everywhere. However, this causes an inconsistency at leading order: integrating (4.17), with $\mathbf{V}^{\square,\perp,(0)} = \mathbf{0}$, from $x = 0$ to $x = 1$, we find

$$\sum_{r\in\mathcal{R}} \int_0^1 \beta^r j^r \,\mathrm{d}x = \left[v^{\square,x,(0)}\right]_{x=0}^{x=1}. \tag{4.20}$$

The right-hand side of (4.20) should be zero, by the boundary condition (2.66a), but the left-hand side integral is in general non-zero since β^r take different values in each electrode (Table 2.1).

Physically, this inconsistency is caused by the fact that the incompressible fluid changes volume by different amounts in each electrode, and so by conservation of volume flow must occur in the transverse directions. Hence we allow the transverse velocities to be non-zero at leading order. To resolve this inconsistency, we note that, with the Kozeny-Carman form (2.60) for $\mathcal{K}^{(0)}$, the permeability of the separator can be several orders of magnitude larger than the permeability of the electrodes, since both the pore size and porosity are larger in the separator (Table B.1). Hence we take the distinguished limit in which

$$\mathcal{K}'_{\mathrm{s}} := \mathcal{K}_{\mathrm{s}}\delta^2 = \mathcal{O}(1), \tag{4.21}$$

while $\mathcal{K}_{\mathrm{n}}$ and $\mathcal{K}_{\mathrm{p}}$ remain order one. Then the transverse velocities are zero in each electrode,

$$\mathbf{V}^{\square,\perp,(0)} = \mathbf{V}^{\perp,(0)} = \mathbf{0}, \quad \mathbf{x} \in \Omega_{\mathrm{n}} \cup \Omega_{\mathrm{p}}, \tag{4.22}$$

and so (4.17) gives

$$\frac{\partial v^{\square,x,(0)}}{\partial x} = \sum_{r\in\mathcal{R}} \beta^r j^{r,(0)}. \tag{4.23}$$

In the separator, the transverse velocities are non-zero. Since $\mathcal{K}_{\mathrm{s}}^{(0)} = \mathcal{O}(1/\delta^2) \gg 1$ in the separator, (4.18a) gives that $p_{\mathrm{s}}^{(0)}$ is independent of x, and hence (4.18b) gives that $\mathbf{V}_{\mathrm{s}}^{\perp,(0)}$ is independent of x. Further, (4.19b) gives $\mathbf{V}_{\mathrm{s}}^{\square,\perp,(0)} = \mathbf{V}_{\mathrm{s}}^{\perp,(0)}$ and so $\mathbf{V}_{\mathrm{s}}^{\square,\perp,(0)}$ is independent of x. Integrating (4.17) from $x = 0$ to $x = 1$ with $\mathbf{V}_{\mathrm{n}}^{\square,\perp,(0)} = \mathbf{V}_{\mathrm{p}}^{\square,\perp,(0)} = \mathbf{0}$ and the boundary conditions $v^{\square,x,(0)} = 0$ at $x = 0, 1$ gives

$$\nabla_\perp \cdot \mathbf{V}_{\mathrm{s}}^{\square,\perp,(0)} = -\frac{1}{\ell_{\mathrm{s}}} \sum_{r\in\mathcal{R}} \int_0^1 \beta^r j^r \,\mathrm{d}x. \tag{4.24}$$

Using Darcy's equation (4.18b), we can write this as a Poisson's equation for the separator pressure $p_{\mathrm{s}}^{(0)}$,

$$\nabla_\perp^2 p_{\mathrm{s}}^{(0)} = \frac{\mu^{(0)}}{\mathcal{K}_{\mathrm{s}}'^{(0)}\ell_{\mathrm{s}}} \sum_{r\in\mathcal{R}} \int_0^1 \beta^r j^{r,(0)} \,\mathrm{d}x. \tag{4.25}$$

In summary, the separator acts as an escape channel for the extra fluid that is produced in the electrodes. An alternative resolution for the inconsistency could have been to rescale pressure with $1/\delta^2$, in which case transverse velocities would have been non-zero everywhere in the cell (separator *and* electrodes).

4.1.4 Other variables

To leading-order in δ, equation (2.65a) for the concentrations becomes

$$\frac{\partial}{\partial t}\left(\varepsilon^{(0)}c_k^{(0)}\right) + \frac{\partial}{\partial x}\left(c_k^{(0)}v^{\square,x,(0)}\right) + \nabla_\perp \cdot \left(c_k^{(0)}\mathbf{V}^{\square,\perp,(0)}\right) = \frac{\mathcal{D}_k}{\mathcal{C}_\mathrm{e}}\frac{\partial}{\partial x}\left(D_k^{\mathrm{eff},(0)}\frac{\partial c_k^{(0)}}{\partial x}\right) - \sum_{r\in\mathcal{R}} s_k^r j^{r,(0)}. \quad (4.26)$$

The equations (2.65c) for porosity and (2.65k) for interfacial current density have no spatial derivatives and thus are unchanged. In keeping with Chapter 3, we assume constant surface area and neglect (2.65l).

4.1.5 Boundary conditions for the transverse problem

We close the problem by deriving boundary conditions for the transverse problem from (2.66), some of which will be affected by the small aspect ratio rescaling.

The no-flux boundary conditions (2.66a) and (2.66b), and reference potential conditions (2.66d), are unchanged. Expanding in powers of δ, the boundary conditions (2.66c) for concentration, electrolyte current density and pressure at the top of the cell become

$$c_k^{(0)} = c_k^{\mathrm{head},(0)}, \quad \mathbf{i}_\mathrm{e}^{(0)}\cdot\mathbf{n} = 0, \quad p^{(0)} = \delta h^{(0)}(t) \quad \text{on } Z = 1, \quad (4.27)$$

with $c_k^{\mathrm{head},(0)}$ and $h^{(0)}$ given by (2.67) (which is unchanged by the small aspect ratio rescaling since factors of δ cancel out). The first equation in (4.27) is a boundary condition for the advective term in (4.26). The second equation is identically satisfied by (4.13b) – the transverse electrolyte current is always zero to leading order in δ. The third equation implies that, to leading order in δ, the pressure at $Z = 1$ is zero.

Finally, for the current condition (2.66e), rescaling the $z-$derivative gives

$$A_{\mathrm{tab,p}}\sigma_\mathrm{p}^{\mathrm{eff}}\delta\frac{\partial\Phi_{\mathrm{s,p}}^{(0)}}{\partial Z} = A_{\mathrm{cs}}\mathcal{I}(t) = HW\mathcal{I}(t) \quad \text{on } \partial\Omega_{\mathrm{tab,p}}, \quad (4.28)$$

and so, substituting $\sigma' = \sigma^{\mathrm{eff}}\delta^2 = \sigma^{\mathrm{eff}}/H^2$,

$$A'_{\mathrm{tab,p}}\sigma'_\mathrm{p}\frac{\partial\Phi_{\mathrm{s,p}}^{(0)}}{\partial Z} = \frac{W}{H}\mathcal{I}(t) = W'\mathcal{I}(t) \quad \text{on } \partial\Omega_{\mathrm{tab,p}}, \quad (4.29)$$

where $A'_{\mathrm{tab,p}} = A_{\mathrm{tab,p}}/H = \delta A_{\mathrm{tab,p}}$ is the rescaled tab area and $W' = W/H$ is the rescaled cell depth.

4.1.6 Summary of leading-order model

Dropping the superscripts (0), the simplified system, to leading-order in δ, consists of a through-cell problem,

$$\frac{\partial}{\partial t}\left(\varepsilon c_k\right) = \frac{\mathcal{D}_k}{\mathcal{C}_\mathrm{e}}\frac{\partial}{\partial x}\left(D_k^\mathrm{eff}\frac{\partial c_k}{\partial x}\right) - \sum_{r\in\mathcal{R}} s_k^r j^r - \frac{\partial}{\partial x}\left(c_k v^{\square,x}\right) - \nabla_\perp\cdot\left(c_k\mathbf{V}^{\square,\perp}\right), \tag{4.30a}$$

$$\frac{\partial \varepsilon}{\partial t} = -\beta^\mathrm{surf} j^\mathrm{S}, \tag{4.30b}$$

$$\frac{\partial i_\mathrm{e}^x}{\partial x} = \sum_{r\in\mathcal{R}} j^r + C^\mathrm{dl}\frac{\partial}{\partial t}\left(\Phi_\mathrm{s}-\Phi_\mathrm{e}\right), \tag{4.30c}$$

$$\mathcal{C}_\mathrm{e}\, i_\mathrm{e}^x = \kappa^\mathrm{eff}\left(\chi_\mathrm{e}\frac{\partial \ln\left(c_\mathrm{e}\right)}{\partial x} - \frac{\partial \Phi_\mathrm{e}}{\partial x}\right), \tag{4.30d}$$

$$j^r = j^r\left(\{c_k\}, \Phi_\mathrm{s}-\Phi_\mathrm{e}\right), \tag{4.30e}$$

$$\frac{\partial v^{\square,x}}{\partial x} = \sum_{r\in\mathcal{R}}\beta^r j^r - \nabla_\perp\cdot\mathbf{V}^{\square,\perp}, \tag{4.30f}$$

$$v^{\square,x} = -\frac{\mathcal{K}}{\mu}\frac{\partial p}{\partial x} - \frac{\omega_c D_\mathrm{e}^\mathrm{eff}}{\rho\mathcal{C}_\mathrm{e}}\frac{\partial c_\mathrm{e}}{\partial x} - \frac{\omega_i}{\rho} i_\mathrm{e}^x, \quad \mathbf{x}\in\Omega_\mathrm{n}\cup\Omega_\mathrm{p}, \tag{4.30g}$$

coupled with a transverse problem,

$$\mathbf{V}^{\square,\perp} = \begin{cases} \mathbf{V}_\mathrm{s}^{\square,\perp} = -\frac{\mathcal{K}'_\mathrm{s}}{\mu_\mathrm{s}}\nabla_\perp p_\mathrm{s}, & \mathbf{x}\in\Omega_\mathrm{s}, \\ \mathbf{0}, & \mathbf{x}\in\Omega_\mathrm{n}\cup\Omega_\mathrm{p}, \end{cases} \tag{4.31a}$$

$$\nabla\cdot\mathbf{V}_\mathrm{s}^{\square,\perp} = -\frac{1}{\ell_\mathrm{s}}\sum_{r\in\mathcal{R}}\int_0^1 \beta^r j^r\,\mathrm{d}x, \tag{4.31b}$$

$$\nabla_\perp\cdot\mathbf{I}_\mathrm{s,n}^\perp = -i_\mathrm{e,s}^x/\ell_\mathrm{n}, \tag{4.31c}$$

$$\nabla_\perp\cdot\mathbf{I}_\mathrm{s,n}^\perp = i_\mathrm{e,s}^x/\ell_\mathrm{p}, \tag{4.31d}$$

$$\mathbf{I}_\mathrm{s,n}^\perp = -\sigma'_\mathrm{n}\nabla_\perp\Phi_\mathrm{s,n}, \tag{4.31e}$$

$$\mathbf{I}_\mathrm{s,p}^\perp = -\sigma'_\mathrm{p}\nabla_\perp\Phi_\mathrm{s,p}. \tag{4.31f}$$

For the through-cell problem, the boundary conditions are

$$\frac{\partial c_k}{\partial x} = \frac{\partial \Phi_\mathrm{e}}{\partial x} = \frac{\partial p}{\partial x} = 0 \quad \text{on } x = 0, 1, \tag{4.32a}$$

$$i_\mathrm{e}^x = i_\mathrm{e,s}^x, \quad p = p_\mathrm{s} \quad \text{on } x = \ell_\mathrm{n}, 1-\ell_\mathrm{p}, \tag{4.32b}$$

$$c_k = c_k^\mathrm{head} \quad \text{on } \mathrm{Z} = 1, \tag{4.32c}$$

with c_k^{head} given by (2.67), and continuity of c_k and Φ_e and their fluxes at $x = \ell_\text{n}, 1-\ell_\text{p}$. For the transverse problem, the boundary conditions are

$$\frac{\partial p_\text{s}}{\partial \text{n}} = 0 \quad \text{on } Y = 0, W' \text{ and on } Z = 0, \tag{4.33a}$$

$$\frac{\partial \Phi_{\text{s},d}}{\partial \text{n}} = 0 \quad \text{on } \partial\Omega_\text{ext} / \partial\Omega_{\text{tab},d}\ , \tag{4.33b}$$

$$p_\text{s} = 0 \quad \text{on } Z = 1, \tag{4.33c}$$

$$\Phi_{\text{s,n}} = 0 \quad \text{on } \partial\Omega_{\text{tab,n}}, \tag{4.33d}$$

$$A'_{\text{tab,p}}\sigma'_\text{p}\frac{\partial \Phi_{\text{s,p}}}{\partial Z} = W'\mathcal{I}(t) \quad \text{on } \partial\Omega_{\text{tab,p}}. \tag{4.33e}$$

The initial conditions follow from (2.68):

$$\begin{aligned} &c_k(\mathbf{x}, 0) = c_k^{\text{head}}(0) = c_k^0, \quad \varepsilon(\mathbf{x}, 0) = \varepsilon^0, \\ &\Phi_\text{s}(\mathbf{x}, 0) - \Phi_\text{e}(\mathbf{x}, 0) = U^\text{S}\left(c_\text{e}^0\right), \quad h(0) = h^0. \end{aligned} \tag{4.34}$$

In summary, by taking the small aspect ratio limit, we have transformed the system (2.65)-(2.68), which consisted of coupled three-dimensional PDEs, into the system (4.30)-(4.34), in which the through-cell and transverse directions are decomposed. At each point in (y, z)-space, the through-cell dynamics are modelled by (4.30). This through-cell system alone is not closed, since the value of the transverse velocity $\mathbf{V}^{\square,\perp}$, and the boundary conditions for i_e^x and p, are unknown. We close the system with the transverse equations (4.31), which are equations for the x-independent variables $\mathbf{V}_\text{s}^{\square,\perp}$, p_s, $\mathbf{I}_{\text{s,n}}^\perp$, $\mathbf{I}_{\text{s,p}}^\perp$, $\Phi_{\text{s,n}}$ and $\Phi_{\text{s,p}}$, and couple the through-cell problem to the transverse problem via (4.31c) and (4.31d).

Note that, if we are only interested in the voltage, we do not need to solve (4.30g) for the pressure in the electrodes since (4.30f) can be integrated in x to find $v^{\square,x}$. However, we do need to solve both (4.31a) and (4.31b) to find the separator pressure, $p_\text{s}(Y, Z, t)$, and transverse velocity, $\mathbf{V}_\text{s}^{\square,\perp}(Y, Z, t)$.

The 3D through-cell problem (4.30) is quite similar to the one-dimensional system (3.1). The differences are in the equations for solid potential Φ_s and concentrations c_k, and in the boundary conditions for electrolyte current i_e. Firstly, there is no through-cell equation for Φ_s in 3D, since we have taken the limit in which Φ_s is independent of x. Secondly, the concentration equation (4.30a) is slightly different to (2.65a) as $\mathbf{V}^{\square,\perp}$ is not uniform in Y and Z. Finally, further non-uniformity in the transverse directions is introduced by the boundary conditions (4.32b). In Section 4.2.3, we show how the 3D through-cell problem (4.30) reduces to the 1D system (3.1) in the limit of very conductive electrodes.

4.1.7 Capacitance formulation in the small aspect ratio

The system (4.30)-(4.34) is a closed system of PDEs, and could now be solved numerically. However, we note that Φ_s appears in both the through-cell sytem (4.30), via (4.30c) and (4.30e), and the transverse system (4.31). We would like to simplify the systems so that variables appear in either the through-cell system or the transverse system, with the two systems only coupled by boundary conditions for the through-cell system. To do this, we use observations from Section 3.2.1 and reformulate our system into the capacitance formulation.

As before, we introduce the potential difference

$$\phi = \Phi_\mathrm{s} - \Phi_\mathrm{e} \tag{4.35}$$

in each electrode. We note that Φ_e only appears in (4.30) either within a potential difference pair, or via its x-derivative $\partial\Phi_\mathrm{e}/\partial x$. Therefore we can easily eliminate Φ_e from (4.30): since Φ_s is independent of x in each electrode, we can write $\partial\phi/\partial x = -\partial\Phi_\mathrm{e}/\partial x$ and replace (4.30c)-(4.30e) with

$$\frac{\partial i_\mathrm{e}^x}{\partial x} = \sum_{r\in\mathcal{R}} j^r + C^\mathrm{dl}\frac{\partial\phi}{\partial t}, \tag{4.36a}$$

$$\mathcal{C}_\mathrm{e}\, i_\mathrm{e}^x = \kappa^\mathrm{eff}\left(\chi_\mathrm{e}\frac{\partial \ln(c_\mathrm{e})}{\partial x} + \frac{\partial\phi}{\partial x}\right), \tag{4.36b}$$

$$j^r = j^r\left(\{c_k\},\phi\right). \tag{4.36c}$$

The electrolyte potential Φ_e can then be found through

$$\Phi_\mathrm{e} = \int_0^x \left(\chi\frac{\partial \ln(c_\mathrm{e})}{\partial x} - \mathcal{C}_\mathrm{e}\frac{i_\mathrm{e}^x}{\kappa^{\mathrm{eff},(0)}}\right)\mathrm{d}x + \Phi_{\mathrm{s,n}}|_{x=0} - \phi|_{x=0}\,, \tag{4.37}$$

where the last two terms are chosen so that (4.35) is satisfied, and $\Phi_\mathrm{s,p}$ is given as a function of ϕ and Φ_e by

$$\Phi_\mathrm{s,p} = (\phi+\Phi_\mathrm{e})|_{x=1} = (\phi+\Phi_\mathrm{e})|_{\mathbf{x}\in\Omega_\mathrm{p}}\,, \tag{4.38}$$

since Φ_s is uniform in x in Ω_p. Finally, we find the voltage across the cell using

$$V = \Phi_\mathrm{s,p}|_{\mathbf{x}\in\partial\Omega_\mathrm{tab,p}} - \Phi_\mathrm{s,n}|_{\mathbf{x}\in\partial\Omega_\mathrm{tab,n}}\,. \tag{4.39}$$

4.1.8 Results

We compare the solution of our model in the small-aspect-ratio limit, (4.30)-(4.34), to the solution of the full three-dimensional system obtained in COMSOL [56]. In

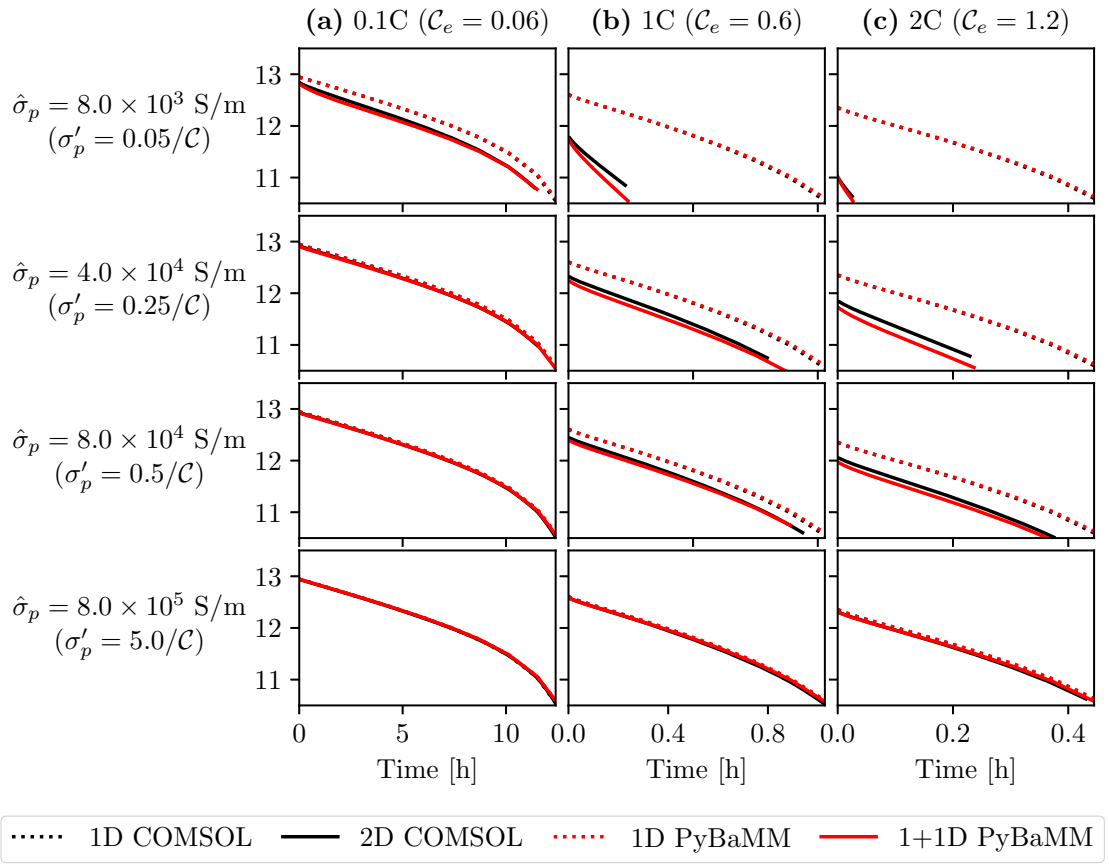

Figure 4.2: Comparing voltages given by our small-aspect-ratio model (1+1D PyBaMM) with those given by the full 2D model solved in COMSOL, for a range of C-rates and positive electrode conductivities. The voltages from 1D models from both COMSOL and PyBaMM are also shown for reference.

this thesis, we only show two-dimensional results in the x- and z-directions, with the behaviour assumed to be uniform in the y-direction. This is equivalent to assuming that the tabs cover the whole electrode (the tab width is the same as the electrode width). These results are sufficient to demonstrate the effect of non-uniformities in transverse directions. In addition to this, since we have shown in Chapter 3 that the effect of convection is small, we do not include it in the results that we show in this chapter.

In Figure 4.2, we compare the voltages from the full 2D model in COMSOL and our 1+1D model, which was solved using our Python battery modelling software 'PyBaMM' (see Appendix A). We also include the voltages from the 1D models for reference. We observe that at low C-rates (left column) or at high conductivities (bottom row), the 2D and 1D models all agree well, since non-uniformities in the

transverse directions are small. As we either decrease the conductivity or increase the C-rate, differences appears between the 1D solutions and the 2D solutions, due to non-uniformities in the transverse directions. In all cases, our 1+1D model captures the voltage response quite accurately. We will show the internal states of the battery in detail later in this chapter.

4.2 Further asymptotics

We now explore three limits as we vary the size of σ' relative to $\mathcal{C}_\mathrm{e}$. Firstly, in Section 4.2.1, we consider relatively poorly conducting electrodes ($\mathcal{C}_\mathrm{e} \to 0$, $1/\sigma' = \mathcal{O}(1)$). In this case, we take a perturbation expansion in small $\mathcal{C}_\mathrm{e}$ with $1/\sigma'$ being $\mathcal{O}(1)$, which simplifies the model to a system of PDEs in the planar directions only. Secondly, in Section 4.2.2, we consider quite conductive electrodes ($\mathcal{C}_\mathrm{e} \to 0, 1/\sigma' = \mathcal{O}(\mathcal{C}_\mathrm{e})$), and take a perturbation expansion in small $1/\sigma'$ and $\mathcal{C}_\mathrm{e}$. Here, the leading-order problem is identical to the one-dimensional leading-order problem, but the first-order problem has an extra term due to resistance in the electrodes in the planar directions. Finally, in Section 4.2.3, we consider very conductive electrodes ($1/\sigma' \to 0, \mathcal{C}_\mathrm{e} = \mathcal{O}(1)$). In this case, we take a perturbation expansion in large σ' with $\mathcal{C}_\mathrm{e}$ being $\mathcal{O}(1)$, and obtain the one-dimensional model analysed in Chapter 3.

4.2.1 Poorly conducting electrodes

We begin by considering the case of a small discharge rate in which the electrodes are relatively poor conductors of electricity, and so $\mathcal{C}_\mathrm{e} \to 0$ and $\sigma' = \mathcal{O}(1)$. In this case, we expand the system (4.30)-(4.34) in powers of $\mathcal{C}_\mathrm{e}$, as by (3.13). The resulting analysis is very similar to the one-dimensional case developed in Section 3.3.

4.2.1.1 Asymptotic expansions

The leading-order and first-order expansions of the through-cell problem are almost identical to (3.14) and (3.15) respectively, so we do not reproduce them here[1]. The boundary conditions for the leading-order through-cell problem are

$$\frac{\partial c_k^{(0)}}{\partial x} = i_\mathrm{e}^{(0)} = v^{\square,(0)} = 0 \quad \text{on } x = 0, 1, \tag{4.40a}$$

$$i_\mathrm{e}^{(0)} = i_\mathrm{e,s}^{x,(0)}, \quad p^{(0)} = p_\mathrm{s}^{(0)}, \quad \text{on } x = \ell_\mathrm{n}, 1 - \ell_\mathrm{p}, \tag{4.40b}$$

$$c_k^{(0)} = c_k^{\mathrm{head},(0)} \quad \text{on } \mathrm{Z} = 1, \tag{4.40c}$$

[1]The only difference between the expansions in 1D and 3D are that, in 3D, the terms $c_k V_z^\square$ are replaced by $\nabla_\perp \cdot \left(c_k \mathbf{V}_\mathrm{s}^{\square,\perp}\right)$.

and the initial conditions are

$$c_k^{(0)}(x,0) = c_k^{\mathrm{head},(0)} = c_k^0, \quad \varepsilon^{(0)}(x,0) = \varepsilon^0, \quad \phi^{(0)}(x,0) = U^{\mathrm{S}}\left(c_{\mathrm{e}}^{(0)}\right), \quad h^{(0)} = h^0. \tag{4.40d}$$

For the first-order through-cell problem, the boundary conditions are

$$\frac{\partial c_k^{(1)}}{\partial x} = i_{\mathrm{e}}^{(1)} = v^{\square,(1)} = 0 \quad \text{on } x = 0, 1, \tag{4.41a}$$

$$i_{\mathrm{e}}^{(1)} = i_{\mathrm{e,s}}^{x,(1)}, \quad p^{(1)} = p_{\mathrm{s}}^{(1)}, \quad \text{on } x = \ell_{\mathrm{n}}, 1 - \ell_{\mathrm{p}}, \tag{4.41b}$$

$$c_k^{(1)} = c_k^{\mathrm{head},(1)} \quad \text{on } \mathrm{Z} = 1, \tag{4.41c}$$

and the initial conditions are

$$c_k^{(1)}(x,0) = \varepsilon^{(1)}(x,0) = \phi^{(1)}(x,0) = c_k^{\mathrm{head},(1)}(0) = h^{(1)}(0) = 0. \tag{4.41d}$$

The key difference between the three-dimensional and one-dimensional boundary conditions is that i_{e} is a function of Y and Z (as well as t) at the electrode-separator interfaces. In particular, $i_{\mathrm{e}}^{(1)}$ is not zero at those interfaces.

At leading order in $\mathcal{C}_{\mathrm{e}}$, the transverse problem (4.31) becomes

$$\mathbf{V}_{\mathrm{s}}^{\square,\perp,(0)} = -\frac{\mathcal{K}_{\mathrm{s}}'^{(0)}}{\mu_{\mathrm{s}}^{(0)}} \nabla_\perp p_{\mathrm{s}}^{(0)}, \tag{4.42a}$$

$$\nabla \cdot \mathbf{V}_{\mathrm{s}}^{\square,\perp,(0)} = -\frac{1}{\ell_{\mathrm{s}}} \sum_{r \in \mathcal{R}} \int_0^1 \beta^r j^{r,(0)} \, \mathrm{d}x, \tag{4.42b}$$

$$i_{\mathrm{e,s}}^{x,(0)} = \sigma_{\mathrm{n}}' \ell_{\mathrm{n}} \nabla_\perp^2 \Phi_{\mathrm{s,n}}^{(0)}, \tag{4.42c}$$

$$i_{\mathrm{e,s}}^{x,(0)} = -\sigma_{\mathrm{p}}' \ell_{\mathrm{p}} \nabla_\perp^2 \Phi_{\mathrm{s,p}}^{(0)}, \tag{4.42d}$$

with boundary conditions

$$\frac{\partial p_{\mathrm{s}}^{(0)}}{\partial \mathrm{n}} = 0 \quad \text{on } Y = 0, W' \text{ and on } Z = 0, \tag{4.43a}$$

$$\frac{\partial \Phi_{\mathrm{s,n}}^{(0)}}{\partial \mathrm{n}} = 0 \quad \text{on } \partial\Omega_{\mathrm{ext}} / \partial\Omega_{\mathrm{tab,n}}, \tag{4.43b}$$

$$\frac{\partial \Phi_{\mathrm{s,p}}^{(0)}}{\partial \mathrm{n}} = 0 \quad \text{on } \partial\Omega_{\mathrm{ext}} / \partial\Omega_{\mathrm{tab,p}}, \tag{4.43c}$$

$$p_{\mathrm{s}}^{(0)} = 0 \quad \text{on } Z = 1, \tag{4.43d}$$

$$\Phi_{\mathrm{s,n}}^{(0)} = 0 \quad \text{on } \partial\Omega_{\mathrm{tab,n}}, \tag{4.43e}$$

$$\frac{\partial \Phi_{\mathrm{s,p}}^{(0)}}{\partial Z} = \frac{W' \mathcal{I}(t)}{A_{\mathrm{tab,p}}' \sigma_{\mathrm{p}}'} \quad \text{on } \partial\Omega_{\mathrm{tab,p}}. \tag{4.43f}$$

At first order, equating coefficients of $\mathcal{C}_\mathrm{e}$ in (4.31) gives

$$\mathbf{V}_\mathrm{s}^{\square,\perp,(1)} = -\frac{\mathcal{K}_\mathrm{s}^{\prime(0)}}{\mu_\mathrm{s}^{(0)}}\nabla_\perp p_\mathrm{s}^{(1)} - \left(\frac{\mathcal{K}_\mathrm{s}^{\prime(1)}}{\mu_\mathrm{s}^{(0)}} - \frac{\mathcal{K}_\mathrm{s}^{\prime(0)}\mu_\mathrm{s}^{(1)}}{\left(\mu_\mathrm{s}^{(0)}\right)^2}\right)\nabla_\perp p_\mathrm{s}^{(0)}, \tag{4.44a}$$

$$\nabla\cdot\mathbf{V}_\mathrm{s}^{\square,\perp,(1)} = -\frac{1}{\ell_\mathrm{s}}\sum_{r\in\mathcal{R}}\int_0^1 \beta^r j^{r,(1)}\,\mathrm{d}x, \tag{4.44b}$$

$$i_{\mathrm{e,s}}^{x,(1)} = \sigma_\mathrm{n}'\ell_\mathrm{n}\nabla_\perp^2\Phi_{\mathrm{s,n}}^{(1)}, \tag{4.44c}$$

$$i_{\mathrm{e,s}}^{x,(1)} = -\sigma_\mathrm{p}'\ell_\mathrm{p}\nabla_\perp^2\Phi_{\mathrm{s,p}}^{(1)}, \tag{4.44d}$$

with boundary conditions

$$\frac{\partial p_\mathrm{s}^{(1)}}{\partial \mathrm{n}} = 0 \quad \text{on } Y=0, W' \text{ and on } Z=0, \tag{4.45a}$$

$$\frac{\partial \Phi_{\mathrm{s,n}}^{(1)}}{\partial \mathrm{n}} = 0 \quad \text{on } \partial\Omega_\mathrm{ext}/\partial\Omega_{\mathrm{tab,n}}\,, \tag{4.45b}$$

$$\frac{\partial \Phi_{\mathrm{s,p}}^{(1)}}{\partial \mathrm{n}} = 0 \quad \text{on } \partial\Omega_\mathrm{ext}/\partial\Omega_{\mathrm{tab,p}}\,, \tag{4.45c}$$

$$p_\mathrm{s}^{(1)} = 0 \quad \text{on } Z=1, \tag{4.45d}$$

$$\Phi_{\mathrm{s,n}}^{(1)} = 0 \quad \text{on } \partial\Omega_{\mathrm{tab,n}}, \tag{4.45e}$$

$$\frac{\partial \Phi_{\mathrm{s,p}}^{(1)}}{\partial Z} = 0 \quad \text{on } \partial\Omega_{\mathrm{tab,p}}. \tag{4.45f}$$

4.2.1.2 Leading-order quasi-static solution

We now seek the solution to the lowest order problem consisting of (3.14) with boundary conditions (4.40) and (4.42) with boundary conditions (4.43).

The analysis is very similar to that of Section 3.3.2, but with variation in the Y- and Z-directions. First, integrating (3.14a) with boundary conditions (4.40a), then integrating again, gives $c_k^{(0)} = c_k^{(0)}(Y,Z,t)$. We then integrate (3.14c), use boundary conditions (4.40a), and integrate again, to find that $\Phi_\mathrm{e}^{(0)} = \Phi_\mathrm{e}^{(0)}(Y,Z,t)$. Hence $j_d^{r,(0)}$ are independent of x, and so, by (3.15c), $\partial i_{\mathrm{e},d}^{(0)}/\partial x$ are independent of x; the boundary conditions (4.40a) and (4.40b) give

$$\frac{\partial i_{\mathrm{e,n}}^{(0)}}{\partial x} = \frac{i_{\mathrm{e,s}}^{x,(0)}(Y,Z,t)}{\ell_\mathrm{n}}, \qquad \frac{\partial i_{\mathrm{e,p}}^{(0)}}{\partial x} = -\frac{i_{\mathrm{e,s}}^{x,(0)}(Y,Z,t)}{\ell_\mathrm{p}}. \tag{4.46}$$

Finally, by (3.14b), $\varepsilon_d^{(0)}$ are independent of x. Hence to leading order, the whole problem is a system of equations in Y, Z and t only. To determine $c_k^{(0)}$, we need to consider the first-order problem (3.15a) for $c_k^{(1)}$. Integrating (3.15a) from $x=0$ to

$x = 1$ and using the boundary conditions (4.41a) gives a solvability condition that determines $c_k^{(0)}$. We can combine this with the other equations in (3.14), and (4.46), to obtain a nonlinear system of PDEs for the $c_k^{(0)}$, $\varepsilon_d^{(0)}$, $\phi_{\mathrm{n}}^{(0)}$ and $\phi_{\mathrm{p}}^{(0)}$,

$$\frac{\partial}{\partial t}\left(c_k^{(0)} \sum_{d\in\{\mathrm{n,s,p}\}} \ell_d \varepsilon_d^{(0)}\right) = -\sum_{d\in\{\mathrm{n,p}\}} \sum_{r\in\mathcal{R}} s_{k,d}^r \ell_d j_d^{r,(0)} - \nabla_\perp \left(c_k^{(0)} \mathbf{V}_{\mathrm{s}}^{\square,\perp,(0)}\right), \tag{4.47a}$$

$$\frac{\partial \varepsilon_d^{(0)}}{\partial t} = -\beta_d^{\mathrm{surf}} j_d^{\mathrm{S},(0)}, \tag{4.47b}$$

$$\frac{\partial \phi_{\mathrm{n}}^{(0)}}{\partial t} = \frac{1}{C_{\mathrm{n}}^{\mathrm{dl}}}\left(\frac{i_{\mathrm{e,s}}^{x,(0)}}{\ell_{\mathrm{n}}} - \sum_{r\in\mathcal{R}} j_{\mathrm{n}}^{r,(0)}\right), \tag{4.47c}$$

$$\frac{\partial \phi_{\mathrm{p}}^{(0)}}{\partial t} = \frac{1}{C_{\mathrm{p}}^{\mathrm{dl}}}\left(-\frac{i_{\mathrm{e,s}}^{x,(0)}}{\ell_{\mathrm{p}}} - \sum_{r\in\mathcal{R}} j_{\mathrm{p}}^{r,(0)}\right), \tag{4.47d}$$

where

$$j_d^{r,(0)} = j_d^r\left(\{c_k^{(0)}\}, \phi_d^{(0)}\right), \tag{4.47e}$$

and $i_{\mathrm{e,s}}^{x,(0)}$ and $\mathbf{V}_{\mathrm{s}}^{\square,\perp,(0)}$ satisfy (4.42). Since $\Phi_{\mathrm{e}}^{(0)}$ is uniform in x, equation (4.35) couples $\Phi_{\mathrm{s,p}}^{(0)}$ to the rest of the system by

$$\Phi_{\mathrm{s,p}}^{(0)} = \phi_{\mathrm{p}}^{(0)} + \Phi_{\mathrm{e,p}}^{(0)} = \phi_{\mathrm{p}}^{(0)} - \phi_{\mathrm{n}}^{(0)} + \Phi_{\mathrm{s,n}}^{(0)}. \tag{4.48}$$

Equations (4.42c), (4.42d) and (4.48) are three equations for $i_{\mathrm{e,s}}^{x,(0)}$, $\Phi_{\mathrm{s,n}}^{(0)}$ and $\Phi_{\mathrm{s,p}}^{(0)}$ given the solution of the through-cell system, and so the whole system is closed. The transverse boundary conditions are given by (4.43), and the initial conditions by (4.40d).

The leading-order voltage is then given by

$$V^{(0)}(t) = \Phi_{\mathrm{s,p}}^{(0)}\big|_{\mathbf{x}\in\partial\Omega_{\mathrm{tab,p}}} - \Phi_{\mathrm{s,n}}^{(0)}\big|_{\mathbf{x}\in\partial\Omega_{\mathrm{tab,n}}}. \tag{4.49}$$

Note that this is not exactly equal to $\left(\phi_{\mathrm{p}}^{(0)} - \phi_{\mathrm{n}}^{(0)}\right)\Big|_{\mathbf{x}\in\partial\Omega_{\mathrm{tab,p}}}$ if the tabs are not at the same place in each electrode.

Finally, the through-cell velocity, and pressure in the electrodes, are decoupled from the other variables at leading order. We solve for these using

$$\frac{\partial v^{\square,x,(0)}}{\partial x} = \sum_{r\in\mathcal{R}} \beta^r j^{r,(0)} - \nabla_\perp \cdot \mathbf{V}_{\mathrm{s}}^{\square,\perp,(0)}, \tag{4.50a}$$

$$v^{\square,x,(0)} = -\frac{\mathcal{K}^{(0)}}{\mu^{(0)}}\frac{\partial p^{(0)}}{\partial x} - \frac{\omega_c D_{\mathrm{e}}^{\mathrm{eff},(0)}}{\rho \mathcal{C}_{\mathrm{e}}}\frac{\partial c_{\mathrm{e}}^{(0)}}{\partial x} - \frac{\omega_i}{\rho^{(0)}} i_{\mathrm{e}}^{x,(0)}, \quad \mathbf{x}\in\Omega_{\mathrm{n}}\cup\Omega_{\mathrm{p}}, \tag{4.50b}$$

with boundary conditions

$$\frac{\partial p^{(0)}}{\partial x} = 0 \quad \text{on } x = 0, 1, \tag{4.51a}$$

$$p^{(0)} = p_{\mathrm{s}}^{(0)} \quad \text{on } x = \ell_{\mathrm{n}}, 1 - \ell_{\mathrm{p}}. \tag{4.51b}$$

We will need the solutions for the leading-order velocity in order to find the first-order concentration.

4.2.1.3 First-order quasi-static and composite solutions

The first-order quasi-static solution is also similar to the one-dimensional case. The first-order concentrations are given by $c_k^{(1)} = \tilde{c}_k^{(1)} + A_k(Y, Z, t)$, where $\tilde{c}_k^{(1)}$ is given by (3.22) and A_k is given by a similar equation to (3.24). Both A_k and $\tilde{c}_k^{(1)}$ are now functions of Y, Z and t, since the leading-order variables are.

The first-order electrolyte potential, found by integrating (3.15c), is given by an equation that is very similar to (3.27). For consistency, we write this in the form

$$\Phi_{\mathrm{e}}^{(1)} = \frac{\chi_{\mathrm{e}}^{(0)}}{c_{\mathrm{e}}^{(0)}} \left(c_{\mathrm{e}}^{(1)} - \bar{c}_{\mathrm{e,n}}^{(1)}\right) + \Phi_{\mathrm{s,n}}^{(1)} - \bar{\phi}_{\mathrm{n}}^{(1)} - \begin{cases} i_{\mathrm{e,s}}^{x,(0)} \frac{3x^2 - \ell_{\mathrm{n}}^2}{6\ell_{\mathrm{n}} \kappa_{\mathrm{n}}^{\mathrm{eff},(0)}}, & x \in \Omega_{\mathrm{n}}, \\ i_{\mathrm{e,s}}^{x,(0)} \left(\frac{\ell_{\mathrm{n}}}{3\kappa_{\mathrm{n}}^{\mathrm{eff},(0)}} + \frac{x - \ell_{\mathrm{n}}}{\kappa_{\mathrm{s}}^{\mathrm{eff},(0)}} \right), & x \in \Omega_{\mathrm{s}}, \\ i_{\mathrm{e,s}}^{x,(0)} \left(\frac{\ell_{\mathrm{n}}}{3\kappa_{\mathrm{n}}^{\mathrm{eff},(0)}} + \frac{\ell_{\mathrm{s}}}{\kappa_{\mathrm{s}}^{\mathrm{eff},(0)}} + \frac{\ell_{\mathrm{p}}^2 - (1-x)^2}{2\ell_{\mathrm{p}} \kappa_{\mathrm{p}}^{\mathrm{eff},(0)}} \right), & x \in \Omega_{\mathrm{p}}. \end{cases} \tag{4.52}$$

The main difference between (3.27) and (4.52) is the term '$\Phi_{\mathrm{s,n}}^{(1)}$' in (4.52), which is not in (3.27) since $\Phi_{\mathrm{s,n}}^{(1)} = 0$ in 1D. Averaging (4.52) in x over the negative electrode gives $\bar{\Phi}_{\mathrm{e,n}}^{(1)} = \Phi_{\mathrm{s,n}}^{(1)} - \bar{\phi}_{\mathrm{n}}^{(1)}$, which satisfies (4.35). At this stage, both $\Phi_{\mathrm{s,n}}^{(1)}$ and $\bar{\phi}_{\mathrm{n}}^{(1)}$ are unknown functions of Y, Z and t.

To find $\bar{\phi}_{\mathrm{n}}^{(1)}$ (and $\bar{\phi}_{\mathrm{p}}^{(1)}$), we eliminate $\partial i_{\mathrm{e}}^{(1)}/\partial x$ from (3.15e) by integrating in x across each electrode and applying the boundary conditions (4.41). This introduces the first-order separator current $i_{\mathrm{e,s}}^{x,(1)}$ (which was zero in 1D). Also integrating (3.15f) across each electrode gives PDEs for $\bar{\phi}_{\mathrm{n}}^{(1)}$, $\bar{\phi}_{\mathrm{p}}^{(1)}$, which we couple with (3.24) and (3.28b)

to give a linear system of PDEs for A_k, $\bar{\varepsilon}_d^{(1)}$, $\bar{\phi}_{\mathrm{n}}^{(1)}$ and $\bar{\phi}_{\mathrm{p}}^{(1)}$,

$$\begin{aligned}\frac{\partial}{\partial t}\left(A_k \sum_{d\in\{\mathrm{n,s,p}\}} \ell_d \varepsilon_d^{(0)}\right) = &- \sum_{d\in\{\mathrm{n,s,p}\}} \left[\ell_d \frac{\partial}{\partial t}\left(\bar{\varepsilon}_d^{(1)} c_k^{(0)} + \varepsilon_d^{(0)} \bar{c}_{k,d}^{(1)}\right)\right] \\ &- \sum_{d\in\{\mathrm{n,s,p}\}} \left[\ell_d \sum_{r\in\mathcal{R}} s_k^r \bar{j}_d^{r,(1)}\right] \\ &- \ell_{\mathrm{s}} \nabla_\perp \cdot \left[c_k^{(0)} \mathbf{V}_{\mathrm{s}}^{\square,\perp,(1)} + \bar{c}_{k,d}^{(1)} \mathbf{V}_{\mathrm{s}}^{\square,\perp,(0)}\right],\end{aligned} \tag{4.53a}$$

$$\frac{\partial \bar{\varepsilon}_d^{(1)}}{\partial t} = -\beta^{\mathrm{surf}} \bar{j}_d^{\mathrm{S},(1)}, \tag{4.53b}$$

$$\frac{\partial \bar{\phi}_{\mathrm{n}}^{(1)}}{\partial t} = \frac{1}{C_{\mathrm{n}}^{\mathrm{dl}}}\left(\frac{i_{\mathrm{e,s}}^{x,(1)}}{\ell_{\mathrm{n}}} - \sum_{r\in\mathcal{R}} \bar{j}_{\mathrm{n}}^{r,(1)}\right), \tag{4.53c}$$

$$\frac{\partial \bar{\phi}_{\mathrm{p}}^{(1)}}{\partial t} = \frac{1}{C_{\mathrm{p}}^{\mathrm{dl}}}\left(-\frac{i_{\mathrm{e,s}}^{x,(1)}}{\ell_{\mathrm{p}}} - \sum_{r\in\mathcal{R}} \bar{j}_{\mathrm{p}}^{r,(1)}\right), \tag{4.53d}$$

where

$$\bar{j}_d^{r,(1)} = \sum_{k\in\mathcal{S}}\left(\frac{\partial j_d^{r,(0)}}{\partial c_k^{(0)}} \bar{c}_k^{(1)}\right) + \frac{\partial j_d^{r,(0)}}{\partial \phi_d^{(0)}} \bar{\phi}_d^{(1)}, \tag{4.53e}$$

and $i_{\mathrm{e,s}}^{x,(1)}$ and $\mathbf{V}_{\mathrm{s}}^{\square,\perp,(1)}$ satisfy (4.44), with initial conditions (4.41d).

The system (4.53) is not yet closed since we must define $\Phi_{\mathrm{s,p}}^{(1)}$ in terms of other variables, as we did in the leading-order case (equation (4.48)). To do this, we first integrate (4.52) from $x = 1 - \ell_{\mathrm{p}}$ to $x = 1$, which gives

$$\bar{\Phi}_{\mathrm{e,p}}^{(1)} = \Phi_{\mathrm{s,n}}^{(1)} - \bar{\phi}_{\mathrm{n}}^{(1)} + \frac{\chi_{\mathrm{e}}^{(0)}}{c_{\mathrm{e}}^{(0)}}\left(\bar{c}_{\mathrm{e,p}}^{(1)} - \bar{c}_{\mathrm{e,n}}^{(1)}\right) - i_{\mathrm{e,s}}^{x,(0)}\left(\frac{\ell_{\mathrm{n}}}{3\kappa_{\mathrm{n}}^{\mathrm{eff},(0)}} + \frac{\ell_{\mathrm{s}}}{\kappa_{\mathrm{s}}^{\mathrm{eff},(0)}} + \frac{\ell_{\mathrm{p}}}{3\kappa_{\mathrm{p}}^{\mathrm{eff},(0)}}\right). \tag{4.54}$$

Then, by (4.35), $\Phi_{\mathrm{s,p}}^{(1)}$ is given by

$$\begin{aligned}\Phi_{\mathrm{s,p}}^{(1)} &= \bar{\phi}_{\mathrm{p}}^{(1)} + \bar{\Phi}_{\mathrm{e,p}}^{(1)} \\ &= \Phi_{\mathrm{s,n}}^{(1)} + \bar{\phi}_{\mathrm{p}}^{(1)} - \bar{\phi}_{\mathrm{n}}^{(1)} + \frac{\chi_{\mathrm{e}}^{(0)}}{c_{\mathrm{e}}^{(0)}}\left(\bar{c}_{\mathrm{e,p}}^{(1)} - \bar{c}_{\mathrm{e,n}}^{(1)}\right) - i_{\mathrm{e,s}}^{x,(0)}\left(\frac{\ell_{\mathrm{n}}}{3\kappa_{\mathrm{n}}^{\mathrm{eff},(0)}} + \frac{\ell_{\mathrm{s}}}{\kappa_{\mathrm{s}}^{\mathrm{eff},(0)}} + \frac{\ell_{\mathrm{p}}}{3\kappa_{\mathrm{p}}^{\mathrm{eff},(0)}}\right),\end{aligned} \tag{4.55}$$

which is a generalisation of the one-dimensional voltage (3.28e) to the three-dimensional case. Substituting (4.55) into (4.44d) closes the system, and the first-order voltage is given by

$$V^{(1)}(t) = \Phi_{\mathrm{s,p}}^{(1)}\big|_{\mathbf{x}\in\partial\Omega_{\mathrm{tab,p}}} - \Phi_{\mathrm{s,n}}^{(1)}\big|_{\mathbf{x}\in\partial\Omega_{\mathrm{tab,n}}}. \tag{4.56}$$

Finally, we can calculate the through-cell velocity, and pressure in the electrodes, by an analogous approach to that of Section 4.2.1.2.

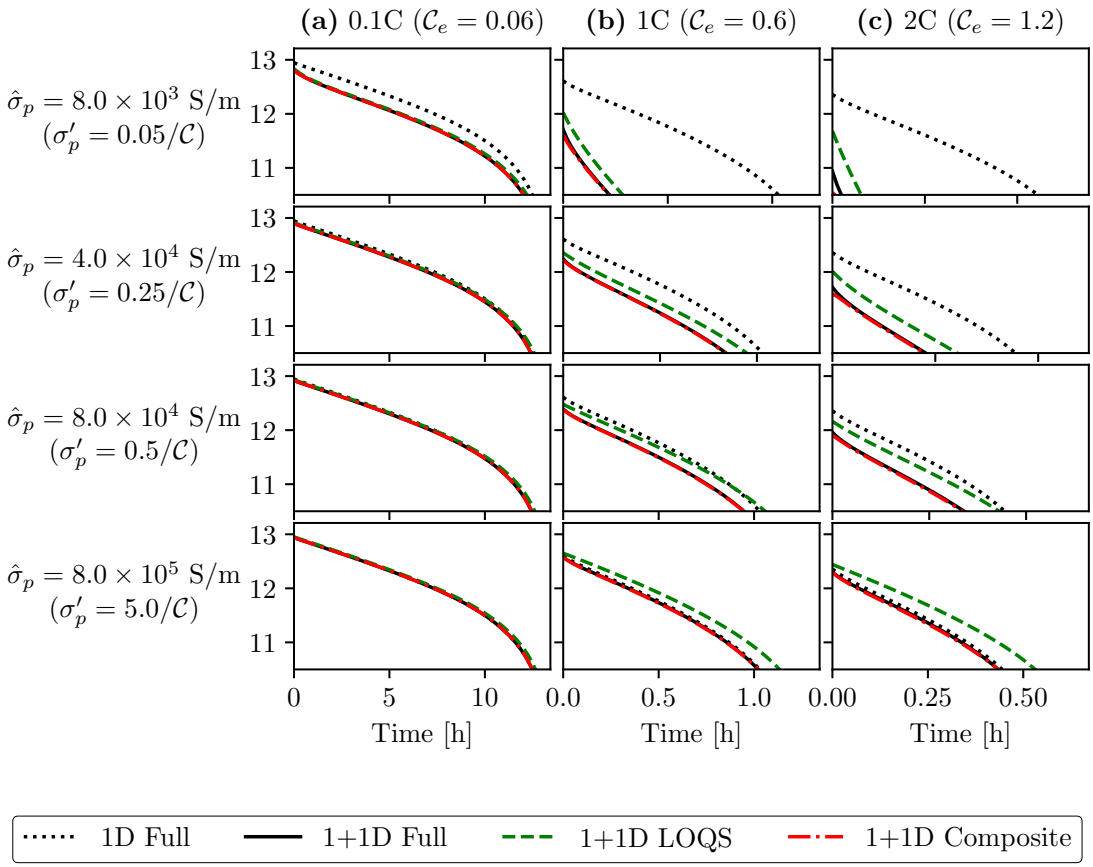

Figure 4.3: Comparison of battery voltages for a constant-current discharge at a range of C-rates and with a range of positive electrode conductivities.

Composite solution. The composite solution is found by solving the composite PDEs (3.29) and applying (3.30) to find $c_k^{(1)}$, instead of using the quasi-static solutions (3.22). The rest of the three-dimensional analysis follows unchanged.

4.2.1.4 Results

We now compare the results the 'full' small-aspect-ratio model (4.30)-(4.34) to the reduced-order models. In order to keep the results clear, we only show results from the 1+1D LOQS model and the 1+1D Composite model. The 1+1D FOQS model would provide an intermediate solution between these two.

In Figure 4.3, we compare the three models (1+1D LOQS, 1+1D Composite and 1+1D Full), showing also the 1D Full model (from Chapter 3) for reference. The 1D Full model and 1+1D Full models are the same as the corresponding PyBaMM models in Figure 4.2.

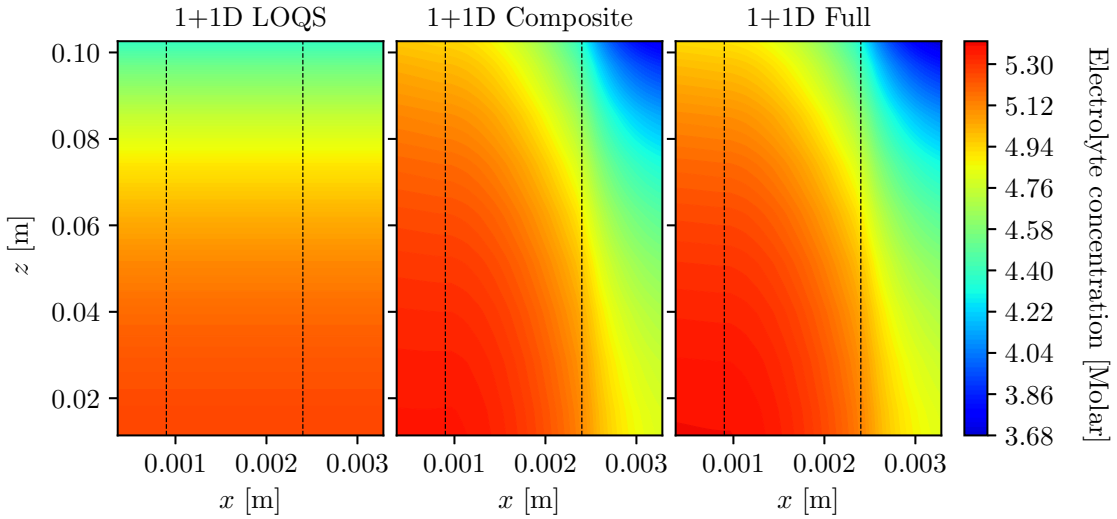

Figure 4.4: Comparison of electrolyte concentrations, c_e, in mol/L, at 90% SoC for a 1C discharge with $\hat{\sigma}_p = 4 \times 10^5$ S/m. Dashed lines indicate the position of the electrode/separator interfaces.

The accuracy of the 1+1D LOQS model decreases as we increase the C-rate, but is independent of conductivity. At a low value of the C-rate and conductivity (first plot in Figure 4.3a), the 1+1D LOQS model is actually more accurate than the 1D Full model, since only the 1+1D LOQS model captures transverse non-uniformities, and through-cell non-uniformities are small. The 1+1D Composite model is accurate in all cases except the very high C-rate/very low conductivity regime. Hence the conclusions from Chapter 3 carry forward to this chapter: if σ_p' is relatively small, then the 1+1D model should be used for discharge rates up to 0.1C, the 1+1D Composite model for discharge rates up to 5C, and the 1+1D full model for higher discharge rates.

To better understand the relationship between variations in the through-cell direction (controlled by $\mathcal{C}_e$) and variations in the transverse direction (controlled by σ_p'), in Figure 4.4 we show electrolyte concentrations at 90% SoC for a 1C discharge with $\hat{\sigma}_p = 4 \times 10^5$ S/m. The concentration is lower near the top of the cell than near the bottom. This is because more current goes through the top of the battery, so the battery discharges faster there. In the through-cell direction, there is a concentration gradient from the negative electrode to the positive electrode as seen in 1D (Figure 3.9).

For the 1+1D Composite and 1+1D Full solutions, the concentration varies in both the x- and z-directions, and the composite solution captures all of the behaviour from the full solution. For the 1+1D LOQS solution, the concentration varies only in the

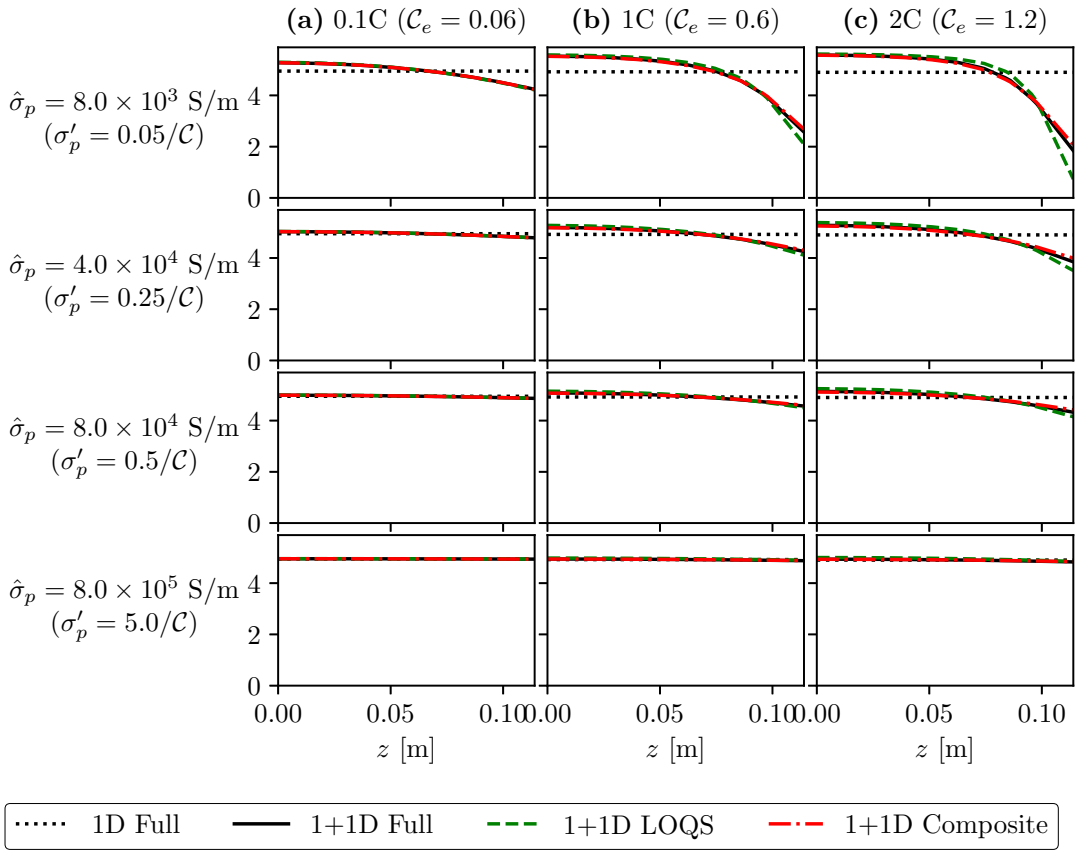

Figure 4.5: Comparison of electrolyte concentration profiles (averaged in the through-cell direction), in mol/L, at 90% SoC for discharges at a range of C-rates and conductivities.

z-direction, but the LOQS solution seems to capture most of the variation in that direction compared to the full solution.

We can quantitatively compare electrolyte concentrations from the 1+1D LOQS and 1+1D Composite solutions with the 1+1D Full solution by comparing the x-averaged concentration profiles, as functions of z, at different conductivies and C-rates (Figure 4.5). Figure 4.5 shows that concentration gradients in the z-direction increase with decreasing conductivity and increasing C-rate, as is expected. This is what causes the decreased voltage in Figure 4.3 at lower conductivities and higher C-rates. We also see that the 1+1D Composite solution captures all of the non-uniformity of electrolyte concentration in z, at all values of σ_{p}' and $\mathcal{C}_{\mathrm{e}}$ considered. The 1+1D LOQS solution captures most of the non-uniformity, except at very low conductivity and high C-rate. The z-averaged electrolyte concentration profiles would give an identical picture to Figure 3.9.

4.2.2 Quite conductive electrodes

Next, we consider the case of a small discharge rate, $\mathcal{C}_\mathrm{e} \to 0$, where the electrodes are quite conductive with $1/\sigma' = \mathcal{O}(\mathcal{C}_\mathrm{e})$. We define

$$\sigma'' = \mathcal{C}_\mathrm{e}\sigma', \tag{4.57}$$

and take σ'' to be $\mathcal{O}(1)$. We then expand the system (4.30)-(4.34) in powers of $\mathcal{C}_\mathrm{e}$, as by (3.13), and consider the leading-order and first-order problems.

4.2.2.1 Leading-order quasi-static solution

The leading-order through-cell system is identical to the leading-order through-cell system for poorly conducting electrodes derived in Section 4.2.1.2. However, the transverse problem for $\Phi_{\mathrm{s,n}}^{(0)}$ and $\Phi_{\mathrm{s,p}}^{(0)}$ becomes

$$i_{\mathrm{e,s}}^{x,(0)} = -\ell_\mathrm{n}\nabla_\perp \cdot \mathbf{I}_{\mathrm{s,n}}^{\perp,(0)}, \tag{4.58a}$$

$$\mathbf{0} = -\sigma_\mathrm{n}''\nabla_\perp \Phi_{\mathrm{s,n}}^{(0)}, \tag{4.58b}$$

$$i_{\mathrm{e,s}}^{x,(0)} = \ell_\mathrm{p}\nabla_\perp \cdot \mathbf{I}_{\mathrm{s,p}}^{\perp,(0)}, \tag{4.58c}$$

$$\mathbf{0} = -\sigma_\mathrm{p}''\nabla_\perp \Phi_{\mathrm{s,p}}^{(0)}, \tag{4.58d}$$

with boundary conditions

$$\frac{\partial \Phi_{\mathrm{s,n}}^{(0)}}{\partial \mathrm{n}} = 0 \quad \text{on } \partial\Omega_\mathrm{ext}\,/\partial\Omega_\mathrm{tab,n}\,, \tag{4.59a}$$

$$\frac{\partial \Phi_{\mathrm{s,p}}^{(0)}}{\partial \mathrm{n}} = 0 \quad \text{on } \partial\Omega_\mathrm{ext}\,/\partial\Omega_\mathrm{tab,p}\,, \tag{4.59b}$$

$$\Phi_{\mathrm{s,n}}^{(0)} = 0 \quad \text{on } \partial\Omega_\mathrm{tab,n}, \tag{4.59c}$$

$$\frac{\partial \Phi_{\mathrm{s,p}}^{(0)}}{\partial Z} = 0 \quad \text{on } \partial\Omega_\mathrm{tab,p}. \tag{4.59d}$$

Hence $\Phi_{\mathrm{s,n}}^{(0)}$ and $\Phi_{\mathrm{s,p}}^{(0)}$ are independent of Y and Z, and the solid potential is uniform in each electrode.

The leading-order separator current density $i_{\mathrm{e,s}}^{x,(0)}$ cannot be determined from the leading-order problem. However, the local voltage $\Phi_{\mathrm{s,p}}^{(0)} - \Phi_{\mathrm{s,n}}^{(0)}$ is a function of time only, and since the initial states are uniform, all through-cell systems at each point in Y and Z must behave the same. Hence $i_{\mathrm{e,s}}^{x,(0)}$ is uniform in Y and Z. Integrating (4.58c) in Y and Z and applying the Divergence Theorem and boundary conditions

$$\mathbf{I}_{\mathrm{s,p}}^{\perp,(0)} \cdot \mathbf{n} = 0 \quad \text{on } \partial\Omega_\mathrm{ext}\,/\partial\Omega_\mathrm{tab,p}\,, \tag{4.60}$$

$$\mathbf{I}_{\mathrm{s,p}}^{\perp,(0)} \cdot \mathbf{n} = \frac{W'\mathcal{I}(t)}{A'_\mathrm{tab,p}} \quad \text{on } \partial\Omega_\mathrm{tab,p}, \tag{4.61}$$

we find a solvability condition for $i_{\mathrm{e,s}}^{x,(0)}$,

$$\int_0^1 \int_0^{W'} i_{\mathrm{e,s}}^{x,(0)} \,\mathrm{d}Y \,\mathrm{d}Z = W'\mathcal{I}(t). \tag{4.62}$$

Therefore $i_{\mathrm{e,s}}^{x,(0)} = \mathcal{I}(t)$. Most other variables must also remain uniform in Y and Z and so to leading-order we recover exactly the leading-order problem analysed in Section 3.3.2. We only need to solve a one-dimensional problem to find the through-cell behaviour, and there is no additional resistance from the transverse directions at leading order.

Note that the transverse velocity is not uniform in Y and Z (but this does not impact the leading-order). We discuss this further in Section 4.2.2.4.

4.2.2.2 First-order quasi-static and composite solutions

In the limit of quite conductive electrodes, the first-order through-cell system is identical to the first-order through-cell system for poorly conducting electrodes derived in Section 4.2.1.2. However, the transverse problem for $\Phi_{\mathrm{s,n}}^{(0)}$ and $\Phi_{\mathrm{s,p}}^{(0)}$ becomes

$$i_{\mathrm{e,s}}^{x,(1)} = -\ell_{\mathrm{n}} \nabla_\perp \cdot \mathbf{I}_{\mathrm{s,n}}^{\perp,(1)}, \tag{4.63a}$$
$$\mathbf{I}_{\mathrm{s,n}}^{\perp,(0)} = -\sigma_{\mathrm{n}}'' \nabla_\perp \Phi_{\mathrm{s,n}}^{(1)}, \tag{4.63b}$$
$$i_{\mathrm{e,s}}^{x,(1)} = \ell_{\mathrm{p}} \nabla_\perp \cdot \mathbf{I}_{\mathrm{s,p}}^{\perp,(1)}, \tag{4.63c}$$
$$\mathbf{I}_{\mathrm{s,p}}^{\perp,(0)} = -\sigma_{\mathrm{p}}'' \nabla_\perp \Phi_{\mathrm{s,p}}^{(1)}, \tag{4.63d}$$

with boundary conditions

$$\frac{\partial \Phi_{\mathrm{s,n}}^{(1)}}{\partial \mathrm{n}} = 0 \quad \text{on } \partial\Omega_{\mathrm{ext}} / \partial\Omega_{\mathrm{tab,n}}\,, \tag{4.64a}$$
$$\frac{\partial \Phi_{\mathrm{s,p}}^{(1)}}{\partial \mathrm{n}} = 0 \quad \text{on } \partial\Omega_{\mathrm{ext}} / \partial\Omega_{\mathrm{tab,p}}\,, \tag{4.64b}$$
$$\Phi_{\mathrm{s,n}}^{(1)} = 0 \quad \text{on } \partial\Omega_{\mathrm{tab,n}}, \tag{4.64c}$$
$$\frac{\partial \Phi_{\mathrm{s,p}}^{(1)}}{\partial Z} = \frac{W'\mathcal{I}}{A'_{\mathrm{tab,p}}\sigma_{\mathrm{p}}''} \quad \text{on } \partial\Omega_{\mathrm{tab,p}}. \tag{4.64d}$$

Combining (4.63b) and (4.58a) gives a Poisson equation in Y and Z for $\Phi_{\mathrm{s,n}}^{(1)}$,

$$-\sigma_{\mathrm{n}}'' \ell_{\mathrm{n}} \nabla_\perp^2 \Phi_{\mathrm{s,n}}^{(1)} = \mathcal{I}(t), \tag{4.65a}$$
$$\frac{\partial \Phi_{\mathrm{s,n}}^{(1)}}{\partial \mathrm{n}} = 0 \quad \text{on } \partial\Omega_{\mathrm{ext}} / \partial\Omega_{\mathrm{tab,n}}\,, \tag{4.65b}$$
$$\Phi_{\mathrm{s,n}}^{(1)} = 0 \quad \text{on } \partial\Omega_{\mathrm{tab,n}}, \tag{4.65c}$$

where $\mathcal{I}(t)$ is a known function of time. Hence we can directly find $\Phi_{\mathrm{s,n}}^{(1)}$ using only information from the leading-order problem. We could write a similar system for $\Phi_{\mathrm{s,p}}^{(1)}$, but the boundary condition at the tab is a Neumann condition and so we could only find $\Phi_{\mathrm{s,p}}^{(1)}$ up to an additive function of t.

The first-order corrections to the concentrations can again be found by solving the first-order quasi-static reaction-diffusion equation to give $c_k^{(1)} = \tilde{c}_k^{(1)} + A_k(Y, Z, t)$, with $\tilde{c}_k^{(1)}$ given by (3.22) and A_k by (3.24). Note that the first-order concentrations are not uniform in Y and Z since A_k depends on Y and Z.

With known first-order concentration, the first-order electrolyte potential satisfies (4.52), with $\Phi_{\mathrm{s,n}}^{(1)}$ known from solving (4.65) and $\bar{\phi}_{\mathrm{n}}^{(1)}$ to be determined.

The concentration constant(s) A_k, average porosities $\bar{\varepsilon}_d^{(1)}$ and average potential differences $\bar{\phi}_d^{(1)}$ are found by solving (4.53), together with

$$-\sigma_{\mathrm{p}}''\ell_{\mathrm{p}}\nabla_{\perp}^2\Phi_{\mathrm{s,p}}^{(1)} = \mathcal{I}(t), \tag{4.66a}$$

$$\frac{\partial\Phi_{\mathrm{s,p}}^{(1)}}{\partial \mathrm{n}} = 0 \quad \text{on } \partial\Omega_{\mathrm{ext}}\,/\partial\Omega_{\mathrm{tab,p}}\,, \tag{4.66b}$$

$$\frac{\partial\Phi_{\mathrm{s,p}}^{(1)}}{\partial Z} = \frac{W'\mathcal{I}}{A'_{\mathrm{tab,p}}\sigma_{\mathrm{p}}''} \quad \text{on } \partial\Omega_{\mathrm{tab,p}}, \tag{4.66c}$$

where $\Phi_{\mathrm{s,p}}^{(1)}$ is coupled to through-cell variables via (4.55). This only determines $\Phi_{\mathrm{s,p}}^{(1)}$ up to a function of t, so we also need to impose the integral condition

$$\int_0^1\int_0^{W'} i_{\mathrm{e,s}}^{x,(1)}\,\mathrm{d}Y\,\mathrm{d}Z = 0, \tag{4.67}$$

which comes from integrating (4.63c) across the whole electrode and applying the Divergence Theorem with homogeneous Neumann conditions on $\mathbf{I}_{\mathrm{s,p}}^{\perp,(1)}$. Finally, the voltage is given by (4.56).

Composite solution. The composite solution is identical to the FOQS solution, but with the first-order concentrations given by (3.29) instead of (3.22).

4.2.2.3 Simplified expression for the voltage

The system derived in Section 4.2.2.2 can be simplified further by performing the appropriate rescalings. Since $\mathcal{I}$ is a function of time only, we can rescale

$$\Phi_{\mathrm{s},d}^{(1)} = \frac{\mathcal{I}(t)}{\sigma_d''\ell_d}\hat{\Phi}_{\mathrm{s},d}, \quad d \in \{\mathrm{n}, \mathrm{p}\}, \tag{4.68}$$

so that $\hat{\Phi}_{\mathrm{s,n}}$ satisfies

$$-\nabla_\perp^2 \hat{\Phi}_{\mathrm{s,n}} = 1, \tag{4.69a}$$

$$\frac{\partial \hat{\Phi}_{\mathrm{s,n}}}{\partial \mathrm{n}} = 0 \quad \text{on } \partial\Omega_{\mathrm{ext}} / \partial\Omega_{\mathrm{tab,n}}\,, \tag{4.69b}$$

$$\hat{\Phi}_{\mathrm{s,n}} = 0 \quad \text{on } \partial\Omega_{\mathrm{tab,n}}, \tag{4.69c}$$

and $\hat{\Phi}_{\mathrm{s,p}}$ satisfies

$$-\nabla_\perp^2 \hat{\Phi}_{\mathrm{s,p}} = 1, \tag{4.70a}$$

$$\frac{\partial \hat{\Phi}_{\mathrm{s,p}}}{\partial \mathrm{n}} = 0 \quad \text{on } \partial\Omega_{\mathrm{ext}} / \partial\Omega_{\mathrm{tab,p}}\,, \tag{4.70b}$$

$$\frac{\partial \hat{\Phi}_{\mathrm{s,p}}}{\partial Z} = \frac{W' \ell_{\mathrm{p}}}{A'_{\mathrm{tab,p}}} \quad \text{on } \partial\Omega_{\mathrm{tab,n}}. \tag{4.70c}$$

Hence $\hat{\Phi}_{\mathrm{s,n}}$ and $\hat{\Phi}_{\mathrm{s,p}}$ depend only on the geometry of the cell (including tab placement), and can be determined 'offline' for any particular cell geometry. The rescaled positive electrode potential, $\hat{\Phi}_{\mathrm{s,p}}$, is still only determined up to a function of t, which can be found using the integral condition (4.67).

If the aim is only to find the voltage, rather than the profiles of internal variables in the transverse directions, then we can further simplify the system. To do this, we observe that the first-order correction to the voltage is given by

$$V^{(1)} = \Phi^{(1)}_{\mathrm{s,p}}\big|_{\mathbf{x}\in\partial\Omega_{\mathrm{tab,p}}} - \Phi^{(1)}_{\mathrm{s,n}}\big|_{\mathbf{x}\in\partial\Omega_{\mathrm{tab,n}}} = \Delta\Phi_{\mathrm{s,p}} - \Delta\Phi_{\mathrm{s,n}} + \breve{\Phi}^{(1)}_{\mathrm{s,p}} - \breve{\Phi}^{(1)}_{\mathrm{s,n}}, \tag{4.71}$$

where we have defined

$$\Delta\Phi_{\mathrm{s},d} = \Phi^{(1)}_{\mathrm{s},d}\Big|_{\mathbf{x}\in\partial\Omega_{\mathrm{tab},d}} - \breve{\Phi}^{(1)}_{\mathrm{s},d}, \quad d \in \{\mathrm{n},\mathrm{p}\}, \tag{4.72}$$

and the transverse-direction average is given by

$$\breve{\cdot} = \frac{1}{W'} \int_0^1 \int_0^{W'} \cdot \,\mathrm{d}Y\,\mathrm{d}Z. \tag{4.73}$$

We can find each $\Delta\Phi_{\mathrm{s},d}$ by defining $\hat{\Phi}_{\mathrm{s},d}$ as in (4.68) and $\Delta\hat{\Phi}_{\mathrm{s},d}$ analogously, and solving the system

$$-\nabla_\perp^2 \hat{\Phi}_{\mathrm{s},d} = 1, \tag{4.74a}$$

$$\frac{\partial \hat{\Phi}_{\mathrm{s},d}}{\partial \mathrm{n}} = 0 \quad \text{on } \partial\Omega_{\mathrm{ext}} / \partial\Omega_{\mathrm{tab},d}\,, \tag{4.74b}$$

$$\hat{\Phi}_{\mathrm{s},d} = 0 \quad \text{on } \partial\Omega_{\mathrm{tab},d}. \tag{4.74c}$$

This is exactly the same system as (4.69) for $\hat{\Phi}_{\mathrm{s,n}}$, and differs only from the true system (4.70) for $\hat{\Phi}_{\mathrm{s,p}}$ in using the Dirichlet condition (4.74c) instead of the Neumann condition (4.64d). The value of the Dirichlet condition does not matter, since we only care about the difference $\Delta\hat{\Phi}_{\mathrm{s},d}$ between average and boundary value. Since $\mathcal{I}$ is found from the solvability condition for $\hat{\Phi}^{(1)}_{\mathrm{s,p}}$, the Neumann condition is automatically satisfied.

As with (4.69) and (4.70), the system (4.74) depends only on electrode geometry (tab placement), and so we can solve it offline to pre-compute a representative $\Delta\hat{\Phi}_{\mathrm{s},d}$ in each electrode. We denote the (scaled) difference of these offline solutions by $\Delta\Phi_{\mathrm{cc}}$:

$$\Delta\Phi_{\mathrm{cc}} = \left(\frac{\Delta\hat{\Phi}_{\mathrm{s,p}}}{\sigma''_{\mathrm{p}}\ell_{\mathrm{p}}} - \frac{\Delta\hat{\Phi}_{\mathrm{s,n}}}{\sigma''_{\mathrm{n}}\ell_{\mathrm{n}}}\right) = \frac{1}{\mathcal{I}}\left(\Delta\Phi_{\mathrm{s,p}} - \Delta\Phi_{\mathrm{s,n}}\right), \tag{4.75}$$

which, for fixed geometry and conductivities, is a constant scalar. We can now write the voltage (4.76) as

$$V^{(1)} = \mathcal{I}\Delta\Phi_{\mathrm{cc}} + \breve{\Phi}^{(1)}_{\mathrm{s,p}} - \breve{\Phi}^{(1)}_{\mathrm{s,n}}, \tag{4.76}$$

and we only need to find the *average* solid potentials $\breve{\Phi}^{(1)}_{\mathrm{s,n}}$ and $\breve{\Phi}^{(1)}_{\mathrm{s,p}}$.

This is easier than finding the full potentials, since now, integrating (4.52) from $x = 1 - \ell_{\mathrm{p}}$ to $x = 1$ and $Y = 0$ to $Y = W'$ and $Z = 0$ to $Z = 1$, $\breve{\Phi}^{(1)}_{\mathrm{s,p}}$ is given by

$$\begin{aligned}\breve{\Phi}^{(1)}_{\mathrm{s,p}} &= \breve{\bar{\phi}}^{(1)}_{\mathrm{p}} + \breve{\bar{\Phi}}^{(1)}_{\mathrm{e,p}} \\ &= \breve{\Phi}^{(1)}_{\mathrm{s,n}} + \breve{\bar{\phi}}^{(1)}_{\mathrm{p}} - \breve{\bar{\phi}}^{(1)}_{\mathrm{n}} + \frac{\chi^{(0)}_{\mathrm{e}}}{c^{(0)}_{\mathrm{e}}}\left(\breve{\bar{c}}^{(1)}_{\mathrm{e,p}} - \breve{\bar{c}}^{(1)}_{\mathrm{e,n}}\right) - \mathcal{I}\left(\frac{\ell_{\mathrm{n}}}{3\kappa^{\mathrm{eff},(0)}_{\mathrm{n}}} + \frac{\ell_{\mathrm{s}}}{\kappa^{\mathrm{eff},(0)}_{\mathrm{s}}} + \frac{\ell_{\mathrm{p}}}{3\kappa^{\mathrm{eff},(0)}_{\mathrm{p}}}\right),\end{aligned} \tag{4.77}$$

and the only remaining unknowns are functions of time only. We integrate (4.53)

across the whole current collector to find these:

$$\frac{\mathrm{d}}{\mathrm{d}t}\left(\breve{A}_k \sum_{d\in\{\mathrm{n,s,p}\}} \ell_d \varepsilon_d^{(0)}\right) = -\sum_{d\in\{\mathrm{n,s,p}\}} \left[\ell_d \frac{\mathrm{d}}{\mathrm{d}t}\left(\breve{\bar{\varepsilon}}_d^{(1)} c_k^{(0)} + \varepsilon_d^{(0)} \breve{\bar{c}}_{k,d}^{(1)}\right)\right] \tag{4.78a}$$

$$- \sum_{d\in\{\mathrm{n,s,p}\}} \left[\ell_d \sum_{r\in\mathcal{R}} s_k^r \breve{\bar{j}}_d^{r,(1)}\right]$$

$$- \ell_{\mathrm{s}} \left[c_k^{(0)} \mathbf{V}_{\mathrm{s}}^{\square,\perp,(1)} + \bar{c}_{k,d}^{(1)} \mathbf{V}_{\mathrm{s}}^{\square,\perp,(0)}\right]\Big|_{Z=1},$$

$$\frac{\mathrm{d}\breve{\bar{\varepsilon}}_d^{(1)}}{\mathrm{d}t} = -\beta^{\mathrm{surf}} \breve{\bar{j}}_d^{\mathrm{S},(1)}, \tag{4.78b}$$

$$\frac{\mathrm{d}\breve{\bar{\phi}}_{\mathrm{n}}^{(1)}}{\mathrm{d}t} = -\frac{1}{C_{\mathrm{n}}^{\mathrm{dl}}} \sum_{r\in\mathcal{R}} \breve{\bar{j}}_{\mathrm{n}}^{r,(1)}, \tag{4.78c}$$

$$\frac{\mathrm{d}\breve{\bar{\phi}}_{\mathrm{p}}^{(1)}}{\mathrm{d}t} = -\frac{1}{C_{\mathrm{p}}^{\mathrm{dl}}} \sum_{r\in\mathcal{R}} \breve{\bar{j}}_{\mathrm{p}}^{r,(1)}, \tag{4.78d}$$

where

$$\breve{\bar{j}}_d^{r,(1)} = \sum_{k\in\mathcal{S}} \left(\frac{\mathrm{d}j_d^{r,(0)}}{\mathrm{d}c_k^{(0)}} \breve{\bar{c}}_k^{(1)}\right) + \frac{\mathrm{d}j_d^{r,(0)}}{\mathrm{d}\phi_d^{(0)}} \breve{\bar{\phi}}_d^{(1)}, \tag{4.78e}$$

where in (4.78c) and (4.78d) we have applied the integral condition (4.67). This is exactly the same set of equations as (3.28), but for Y-Z-averaged variables, and so in this limit the system has (almost) the same complexity as the one-dimensional system.

In summary, in this limit, the voltage is given by

$$V^{(1)}(t) = \breve{\bar{\phi}}_{\mathrm{p}}^{(1)} - \breve{\bar{\phi}}_{\mathrm{n}}^{(1)} + \frac{\chi_{\mathrm{e}}^{(0)}}{c_{\mathrm{e}}^{(0)}} \left(\breve{\bar{c}}_{\mathrm{e,p}}^{(1)} - \breve{\bar{c}}_{\mathrm{e,n}}^{(1)}\right) - \mathcal{I}\left(\frac{\ell_{\mathrm{n}}}{3\kappa_{\mathrm{n}}^{\mathrm{eff},(0)}} + \frac{\ell_{\mathrm{s}}}{\kappa_{\mathrm{s}}^{\mathrm{eff},(0)}} + \frac{\ell_{\mathrm{p}}}{3\kappa_{\mathrm{p}}^{\mathrm{eff},(0)}}\right) + \mathcal{I}\Delta\Phi_{\mathrm{cc}}. \tag{4.79}$$

Comparing (4.79) with the one-dimensional voltage expression (3.28e) allows us to isolate the voltage losses due to variations in the transverse directions to the final term in (4.79), which is a function of electrode geometry and conductivity only. Therefore the electrodes act as series resistors.

4.2.2.4 Effect of permeability

In the limit considered so far, the convection problem at leading-order is non-uniform in Y and Z. This introduces further non-uniformity in the first-order concentrations, via the leading-order through-cell velocity $v^{\square,x,(0)}$, in addition to the non-uniformity from the solid potentials.

We can instead take the further limit of $\mathcal{K}' = \mathcal{O}(1/\mathcal{C}_\mathrm{e})$, setting $\mathcal{K}'' = \mathcal{K}'\mathcal{C}_\mathrm{e}$ to be $\mathcal{O}(1)$. Then the separator pressure p_s and transverse velocity $\mathbf{V}_\mathrm{s}^{\square,\perp}$ satisfy, to leading order in $\mathcal{C}_\mathrm{e}$,

$$\mathbf{0} = -\frac{\mathcal{K}_\mathrm{s}''^{(0)}}{\mu_\mathrm{s}^{(0)}} \nabla_\perp p_\mathrm{s}^{(0)}, \tag{4.80a}$$

$$\nabla \cdot \mathbf{V}_\mathrm{s}^{\square,\perp,(0)} = -\frac{1}{\ell_\mathrm{s}} \sum_{r \in \mathcal{R}} \int_0^1 \beta^r j^{r,(0)} \,\mathrm{d}x, \tag{4.80b}$$

$$\frac{\partial p_\mathrm{s}^{(0)}}{\partial \mathrm{n}} = 0 \quad \text{on } Y = 0, W' \text{ and on } Z = 0, \tag{4.80c}$$

$$p_\mathrm{s}^{(0)} = 0 \quad \text{on } Z = 1. \tag{4.80d}$$

Hence the separator pressure is uniform in Y and Z to leading order in $\mathcal{C}_\mathrm{e}$, and so no further non-uniformity is introduced by the boundary condition (4.51b), and the through-cell velocity $v^{\square,x,(0)}$ is also uniform in Y and Z. The transverse velocity $\mathbf{V}_\mathrm{s}^{\square,\perp,(0)}$ is then also uniform in Y and Z, since the right-hand side of (4.80b) is. In this case, the only non-uniformities in transverse directions are caused by the solid potentials and currents, and so, in the limit studied in Section 4.2.2.3, the final system has exactly the same complexity as the one-dimensional system, with just the extra term $\Delta\Phi_\mathrm{cc}$ causing a voltage drop due to series resistance in transverse directions.

4.2.2.5 Results

In Figure 4.6, we compare voltages from the 'full' small-aspect-ratio model against reduced-order models in the 'quite conductive' limit. Note that the voltage from the '1+1D Composite' model immediately drops below the cut-off voltage of 10.5V in the top row of Figure 4.6b,c, and hence is not shown. There are a few differences between Figures 4.3 and 4.6. The 1+1D LOQS solution in the quite conductive limit (Figure 4.6) is less accurate than the 1+1D LOQS solution in the poorly conducting limit (Figure 4.3), since the former does not capture any of the vertical non-uniformities (it is identical to the 1D LOQS solution). Similarly, the 1+1D Composite solution performs slightly worse in the quite conductive limit than in the poorly conducting limit. In particular, this solution fails to capture the early transients. However, the composite solution in the quite conductive limit is still very accurate at all but the lowest conductivities and highest C-rates.

Since this composite solution consists only of a one-dimensional time-dependent system, with the current collector acting as a series resistor which can be modelled independently by two elliptic PDEs, it can be solved with almost the same complexity

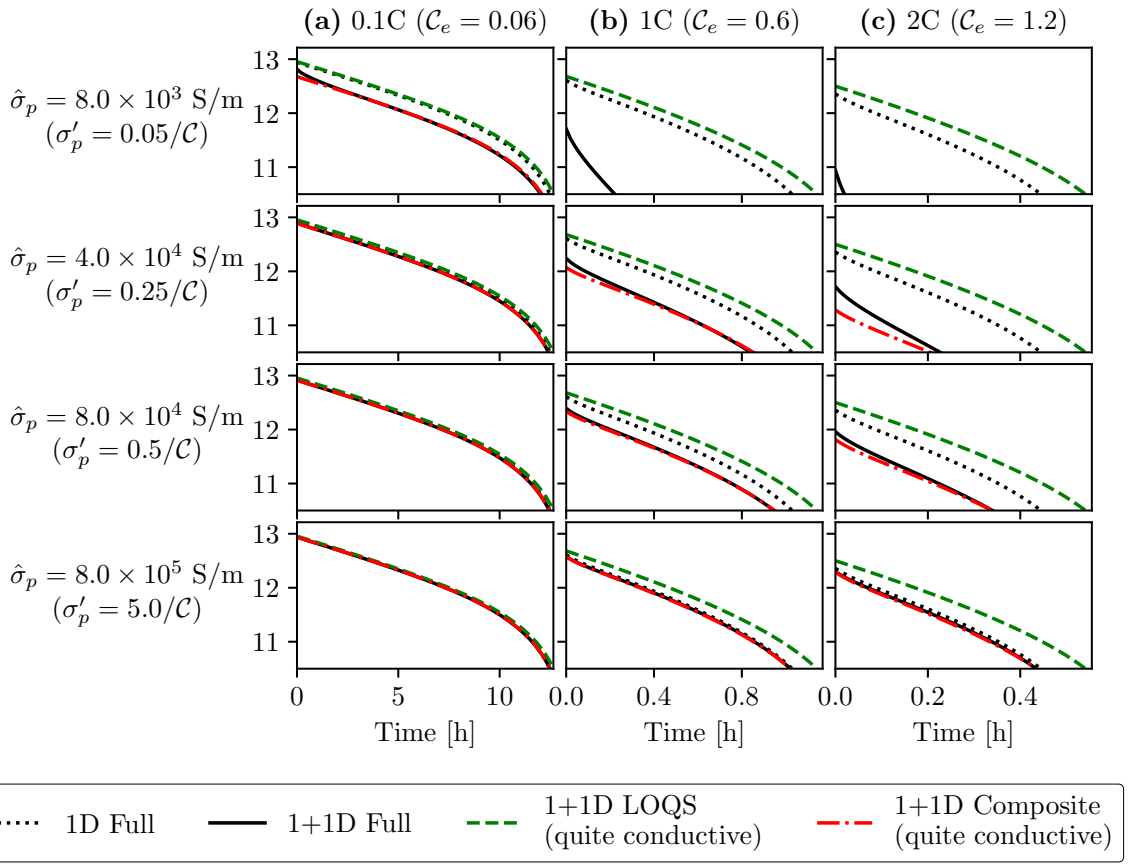

Figure 4.6: Comparison of battery voltages from the 'quite conductive' 1+1D LOQS and Composite models, for a constant-current discharge at a range of C-rates and with a range of positive electrode conductivities.

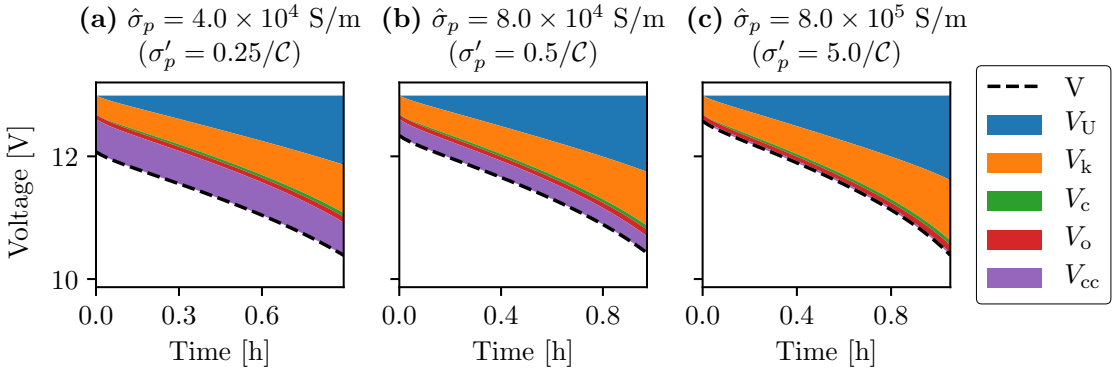

Figure 4.7: Decomposition of voltage drop into dimensional components, as given by (4.81), for a 1C discharge with a range of positive electrode conductivities.

as the one-dimensional composite model of Chapter 3. Hence the quite conductive composite solution can be very useful for capturing transverse non-uniformities at low computational cost. We will compare all of the reduced-order solutions quantitatively in Section 4.3.

In Figure 4.7, we extend the decomposition of the voltage into components, discussed in Section 3.4.3, to include the additional term accounting for transverse non-uniformity:

$$\hat{V} = \hat{V}^0 + \frac{RT}{F}\left(V_{\mathrm{U}} + V_{\mathrm{k}} + V_{\mathrm{c}} + V_{\mathrm{o}} + V_{\mathrm{cc}}\right), \tag{4.81}$$

where

$$V_{\mathrm{cc}} = \mathcal{I}\Delta\Phi_{\mathrm{cc}}, \tag{4.82}$$

and $\Delta\Phi_{\mathrm{cc}}$ is found using (4.72), (4.74) and (4.75). Equation (4.81) shows that, in this limit, the current collector acts as a series resistor, whose resistance is inversely proportional to the positive electrode conductivity. This is clearly seen in Figure 4.7, with a much higher contribution from V_{cc} at lower conductivities.

4.2.3 Very conductive electrodes

Finally, we consider the limit of very conductive electrodes with $1/\sigma' \to 0$ and $\mathcal{C}_{\mathrm{e}} = \mathcal{O}(1)$. To leading order in $1/\sigma'$, Ohm's law (4.31e) and (4.31f) gives $\nabla_\perp \Phi_{\mathrm{s}} = \mathbf{0}$ in each electrode, and so Φ_{s} is a function of time only in each electrode:

$$\Phi_{\mathrm{s}} = \begin{cases} 0 & x \in \Omega_{\mathrm{n}}, \\ V(t) & x \in \Omega_{\mathrm{p}}. \end{cases} \tag{4.83}$$

By a similar argument to that of Section 4.2.2.1, the separator current density $i^x_{\mathrm{e,s}}$ must now also be independent of Y and Z, to leading order in $1/\sigma'$. For large enough

values of σ', this is true at both leading-order and first-order in $\mathcal{C}_\mathrm{e}$. Hence, by assuming that $1/\sigma'$ is smaller than every order of $\mathcal{C}_\mathrm{e}$ that we consider, we recover (almost) the one-dimensional system (3.1)-(3.3).

The only difference between the system that is derived systematically from the three-dimensional model and the system that we wrote down in Chapter 3 is the Ohm's law in the through-cell direction for the solid potential, Φ_s. According to our reduction from 3D, the solid potential should be uniform in x, instead of being governed by (3.1g). In (3.1), we have left Ohm's law in the model to stay in line with the literature. Note that it would be possible to perform the small-aspect-ratio asymptotics and still have Φ_s obeying Ohm's law in the through-cell directions if the cell has a very conductive current collector, which allows fast electron transport in the transverse directions but not in the through-cell ones. However, this is not the case for lead-acid, where the current collector is not separate from the electrode but the whole electrode can be treated as a homogeneous current collector/electrode domain, as discussed at the start of this chapter.

Note also that, since our aim is to recover the one-dimensional system (3.1)-(3.3), we must also take the limit $1/\mathcal{K}' \to 0$ so that the transverse velocity and pressure, and hence through-cell concentrations, are uniform in the separator, as discussed in Section 4.2.2.4.

The results in the very conductive limit are identical to the results for the one-dimensional models of Chapter 3, so we do not reproduce them here.

4.3 Comparison of reduced-order models

To compare the reduced-order models, we calculate the RMSE of the voltage (relative to the full 1+1D model) at different values of positive electrode conductivity $\hat{\sigma}_\mathrm{p}$ and C-rate $\mathcal{C}$. In particular, we consider the following models:

1. 1D Full – Section 3.1
2. 1D LOQS – Section 3.3.2
3. 1D Composite – Section 3.3.4
4. 1+1D LOQS – Section 4.2.1.2
5. 1+1D Composite – Section 4.2.1.3
6. 1+1D Composite Averaged – Section 4.2.2.3

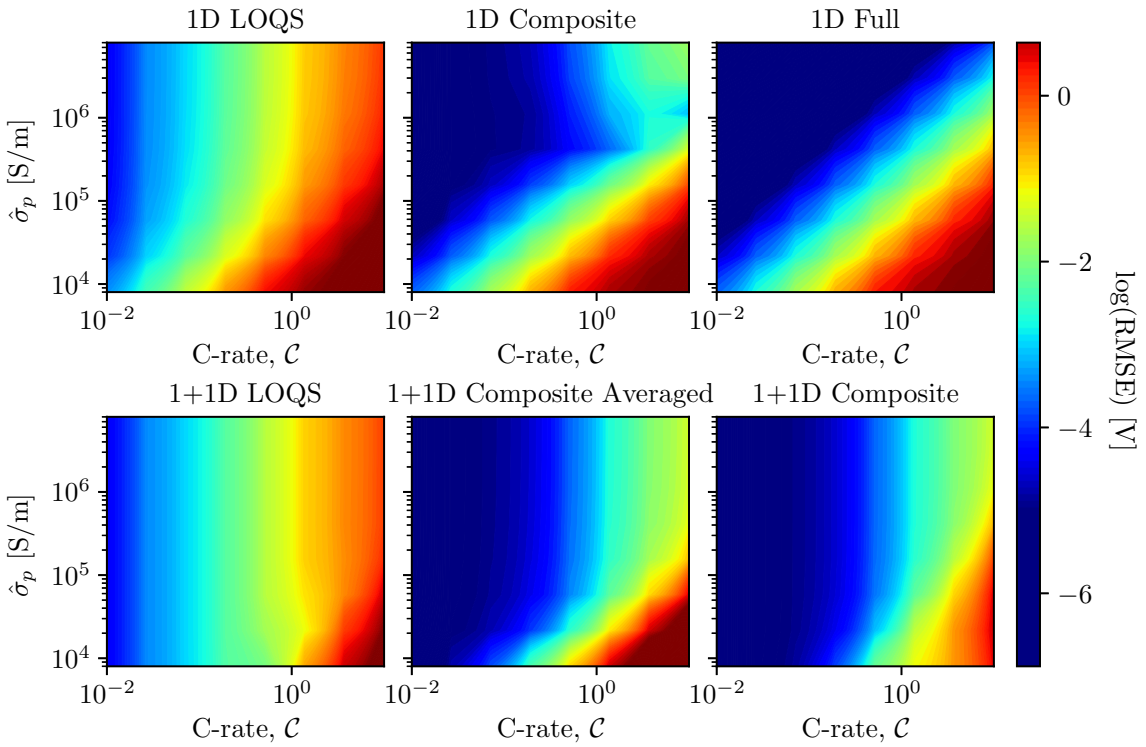

Figure 4.8: Log(RMSE) in Volts, relative to the 1+1D Full model, for a full discharge curve at a range of positive electrode conductivities and C-rates.

We do not consider the 1+1D LOQS Averaged model (Section 4.2.2.1), since it is equivalent to the 1D LOQS model.

In Figure 4.8, we show the log(RMSE) error for a full discharge voltage curve for each model, relative to the full 1+1D model, as we vary $\mathcal{C}$ and $\hat{\sigma}_\mathrm{p}$.

The first feature that we can observe is that the error for the 1+1D LOQS and 1+1D Composite models varies with C-rate but is independent of conductivity (except at very high C-rates). This is to be expected since we have made no simplifications in σ' to obtain these models. For the 1D models, the lines of constant error are diagonal (most clearly in the 1D Full plot), which is consistent with the fact that σ' is inversely proportional to C-rate.

In the top-left corner of each plot, at high conductivities and low C-rates, all of the models are accurate to a few millivolts or less, and so the 1D LOQS model should be used as it is the least complex. As we decrease $\hat{\sigma}_\mathrm{p}$, staying at low C-rate (bottom left corner of each plot), each 1+1D model outperforms its corresponding 1D model (note that the error from the full 1+1D model is zero, by definition), since the 1+1D models all capture non-uniformities in the vertical direction, and the 1+1D LOQS

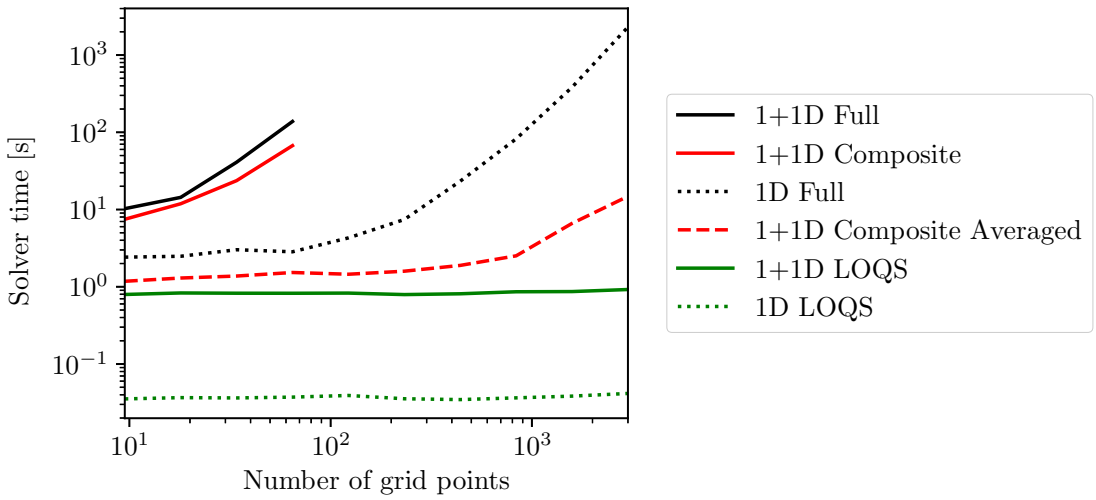

Figure 4.9: Time taken by each model to simulate a full discharge at 1C with $\hat{\sigma}_\mathrm{p} = 8 \times 10^4$ S/m. Solver time is CPU time in seconds, obtained on an Intel(R) Core(TM) i5-8500T CPU.

model is the least complex of the accurate models in this region.

Meanwhile, as we increase the C-rate (either at low conductivity or at high conductivity), we gain in accuracy (at the cost of higher complexity) from LOQS to Composite to Full. At high conductivity and high C-rate (top right corners), the 1D full model is most accurate since variations in the vertical direction are small. At low conductivities and quite high C-rates (bottom right corners), the 1+1D Composite model should be used. At intermediate values of the C-rate, the 1D Composite or 1+1D Composite Averaged models capture most of the behaviour. Finally, at the lowest conductivities and highest C-rates considered, one should return to the full 1+1D model to obtain an accurate estimate of the voltage. Even the 1+1D Composite model is inaccurate in this region, due to discrepancies in the interfacial current density (as can be seen, for example, in Figure 3.11c).

In Figure 4.9, we show the time taken to solve each model as we increase the grid size. Together, Figures 4.8 and 4.9 inform which is the 'best' (accurate and with the lowest complexity) model to use in each region of the $\mathcal{C}$-$\hat{\sigma}_\mathrm{p}$ plane. This is summarised schematically in Figure 4.10.

4.4 Concluding remarks

In this chapter, we started with the full three-dimensional model developed in Chapter 2 and exploited the small aspect ratio of the cells to derive a simplified '2+1D'

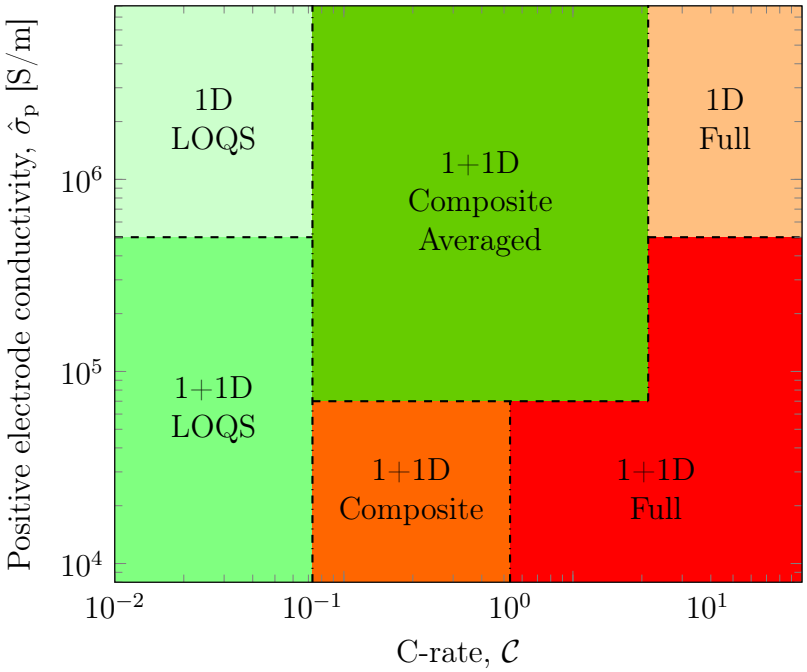

Figure 4.10: Best model (i.e. model that is accurate and has the lowest complexity of the accurate models) to use at each conductivity and C-rate. Each model is accurate, relative to the 1+1D Full model, in its own region and above and to the left, as shown in Figure 4.8. Colours indicates the relative time taken to solve the model, as shown in Figure 4.9 (lighter green means less time, darker red means more time).

model in which the through-cell and transverse directions are decomposed. We found good agreement between the simplified small-aspect-ratio model and the solution of the full model in COMSOL. The battery discharges faster near the top of the electrodes, near the tabs, since more current is going through the top than the bottom.

We then developed a hierarchy of further reduced-order models in the limits of low C-rate and high conductivity. The reduced-order models show good agreement with the full small-aspect-ratio model, with leading-order models agreeing well at low C-rates and composite models at higher C-rates. We compared the RMSE for all of the reduced-order models quantitatively, and indicated which model was most appropriate in each region of the C-rate/conductivity plane. The 1+1D Composite Averaged model was found to be accurate for a large range of C-rates and conductivities, while remaining computationally simple since the electrodes act as series resistors and all of the behaviour in transverse directions can be captured by two elliptic PDEs.

Our reduced-order models allow us to greatly reduce the computational cost of three-dimensional modelling. Usually, three-dimensional models are computationally expensive to solve. For example, COMSOL requires the same grid spacing in the

through-cell direction and the transverse direction, and so solving a two-dimensional system for a single discharge with 17 points in the through-cell direction requires on the order of 1000 points in the transverse direction, and takes a few minutes on a standard desktop. In contrast, with our small-aspect-ratio, the through-cell and transverse directions are decomposed and so we can decrease the grid size in the through-cell direction without needing to decrease it in the transverse direction. For example, we can solve the same problem with 17 points in the through-cell direction and only take 20 points in the transverse direction, and obtain the solution in 2 seconds. Further reduced-order models have even lower computational cost. It would therefore be much easier to use the reduced-order models to simulate several charge-discharge cycles and hence simulate the transverse degradation effects that occur over several hundred such cycles. Since any model involves making simplifying assumptions (for example, regarding the physics, chemistry or geometry), the small loss of accuracy from using reduced-order models is an acceptable offset for reduced computational time; there is no point in trying to make the solution more accurate than the model.

The models developed in this chapter can be extended to study such degradation effects. Several studies [10, 17, 20] demonstrate non-uniform degradation of batteries in the transverse directions, highlighting the importance of three-dimensional modelling. In particular, Birkl et al. [10] show that a lithium-ion pouch cell can be non-uniformly lithiated, with higher lithiation near the tabs. Our models show that the battery discharges faster near the tabs, so it is plausible that more degradation would occur there.

An important extension of this work would be to include thermal effects in order to analyse the distribution of temperature in the electrodes. Due to the small aspect ratio of the cells, it can be shown that the temperature is almost uniform in the through-cell direction. However, there can be significant temperature gradient in the transverse directions [103], leading to further non-uniformities and degradation.

Chapter 5

Preliminary model for recharge

The models, both full and reduced-order, that we have developed so far have assumed a general form with an arbitrary number of (dilute) species in the liquid, and an arbitrary number of side reactions following some concentration- and potential-dependent kinetics. However, we have only solved them for discharge conditions, in which the main reactions dominate.

In this chapter, we now consider the behaviour of the battery during charge. This is electrochemically more complex than the discharge reaction, with several side reactions occurring as the State-of-Charge, and hence open-circuit potential, increases. For the purpose of this thesis, we will focus on a toy model in which the only additional species, other than the electrolyte cations and anions and solvent, is oxygen dissolved in liquid, and the only side reaction is oxygen evolution and recombination, (1.2).

In practice, this toy model contains several electrochemical inconsistencies and is not an accurate model for recharge of a lead-acid battery – we discuss this further in Section 5.5. However, the intent of this chapter is to investigate the behaviour of our reduced-order models in the case where there is more than one diffusing species in the model, and more importantly more than one reaction taking place in each electrode. As we discover below, our toy model including only oxygen side reactions provides an interesting basis to study additional side reactions, since the reaction in the negative electrode is limited by diffusion rather than kinetics.

Before solving the reduced-order models developed in Section 3.3 for charging of a lead-acid battery, we need to modify the kinetic equations. In Section 5.1, we show that the oxygen reaction (1.2) follows Tafel kinetics in the positive electrode (evolution of oxygen only), and is diffusion-limited in the negative electrode (recombination of oxygen only). As a consequence of the diffusion-limited oxygen reaction, we must adapt our reduced-order models in Section 5.3, so that the oxygen reaction is

localised at the negative electrode/separator interface (see Figure 5.1). We compare the modified reduced-order models in Section 5.4.

5.1 Tafel and diffusion-limited oxygen kinetics during charge

We have so far assumed a general form of Butler-Volmer kinetics (2.24) for the relationship between the interfacial current density for the oxygen reaction, j^{O} and the potential difference ϕ,

$$j^{\mathrm{O}} = j_{0\mathrm{a}}^{\mathrm{O}} \exp\left[n_{\mathrm{e}^-}^{\mathrm{O}} \alpha^{\mathrm{O}} \left(\phi - U^{\mathrm{O}}\right)\right] - j_{0\mathrm{c}}^{\mathrm{O}} \exp\left[-n_{\mathrm{e}^-}^{\mathrm{O}} \left(1 - \alpha^{\mathrm{O}}\right) \left(\phi - U^{\mathrm{O}}\right)\right], \tag{5.1}$$

with the open-circuit potentials U^{O} and reference exchange-current densities $j_{0\mathrm{a,c}}^{\mathrm{O}}$ given in dimensional form in Tables B.2 and B.3 respectively. However, since the potential ϕ deviates significantly from the open-circuit potentials for oxygen, the surface overpotential for the oxygen reaction is always either large and positive or large and negative, and either the forward or backward reaction dominates.

Positive electrode. Following (2.45a), we centre potentials in the positive electrode around $\hat{U}_{\mathrm{p}}^{\mathrm{S},\ominus}$ and rescale relative to the thermal voltage, $RT/F \approx 25$ mV. Hence the dimensionless open-circuit potential for the oxygen reaction is large and negative (approximately -16), and so the forward reaction in (5.1) dominates. It is therefore appropriate to model the oxygen side reaction in the positive electrode with Tafel kinetics,

$$j_{\mathrm{p}}^{\mathrm{O}} = j_{0\mathrm{a,p}}^{\mathrm{O}} \exp\left[n_{\mathrm{e}^-}^{\mathrm{O}} \alpha_{\mathrm{p}}^{\mathrm{O}} \left(\phi_{\mathrm{p}} - U_{\mathrm{p}}^{\mathrm{O}}\right)\right]. \tag{5.2}$$

Values of $n_{\mathrm{e}^-}^{\mathrm{O}} = 4$ and $\alpha_{\mathrm{p}}^{\mathrm{O}} = 0.5$ give an exponent of approximately 32, and so the exponential is approximately of order 10^{14}. Since the dimensionless reference exchange-current density is much smaller than this, of order 10^{-21}, the oxygen reaction does not happen at most SoCs. During discharge, the only reaction taking place in the positive electrode is the main reaction (1.1b). However, ϕ_{p} can increase by several thermal voltages as the SoC increases (or if the charging current is large), and so the oxygen reaction starts to dominate at higher SoCs during charge.

Negative electrode. Similarly to the positive electrode, following (2.45a), we centre potentials in the negative electrode around $\hat{U}_{\mathrm{n}}^{\mathrm{S},\ominus}$ and rescale relative to the thermal voltage, $RT/F \approx 25$ mV. Hence the dimensionless open-circuit potentials for the oxygen reaction is large and positive (approximately 60), and so the backward reaction

in (5.1) dominates. Hence it seems appropriate to model the oxygen side reaction in the negative electrode with Tafel kinetics,

$$j_{\mathrm{n}}^{\mathrm{O}} = -j_{0\mathrm{c,p}}^{\mathrm{O}} \exp\left[-n_{\mathrm{e^-}}^{\mathrm{O}} \left(1-\alpha_{\mathrm{n}}^{\mathrm{O}}\right)\left(\phi_{\mathrm{n}} - U_{\mathrm{n}}^{\mathrm{O}}\right)\right]. \tag{5.3}$$

Values of $n_{\mathrm{e^-}}^{\mathrm{O}} = 4$ and $\alpha_{\mathrm{n}}^{\mathrm{O}} = 0.5$ give an exponent of approximately 120, and so the exponential is approximately of order 10^{52}. The dimensionless reference exchange-current density $j_{\mathrm{n}}^{\mathrm{O,ref}}$ is only of order 10^{-31}, but the exchange-current density $j_{0\mathrm{c,p}}^{\mathrm{O}}$ depends on the oxygen concentration (Table B.3). Hence the oxygen concentration in the negative electrode must be extremely small, with all of the oxygen reaction occurring at the interface between the negative electrode and the separator. The reaction rate is limited by how quickly oxygen can diffuse from the positive electrode to this interface.

The diffusion-limited behaviour would be captured by a numerical solution of our exisiting model, but the problem would be very stiff due to the extremely small oxygen concentrations in the negative electrode. Hence we adapt our model by enforcing that c_{o} be identically zero in the negative electrode, while in the separator and positive electrode c_{o} satisfies (noting also that $s_{\mathrm{o}}^{\mathrm{O}}$ is the only non-zero stoichiometry for oxygen molecules)

$$\frac{\partial}{\partial t}\left(\varepsilon c_{\mathrm{o}}\right) + \frac{\partial}{\partial x}\left(c_{\mathrm{o}} v^{\square}\right) = \frac{\mathcal{D}_{\mathrm{o}}}{\mathcal{C}_{\mathrm{e}}}\frac{\partial}{\partial x}\left(D_{\mathrm{o}}^{\mathrm{eff}}\frac{\partial c_{\mathrm{o}}}{\partial x}\right) - s_{\mathrm{o}}^{\mathrm{O}} j^{\mathrm{O}}, \quad \ell_{\mathrm{n}} < x < 1. \tag{5.4a}$$

Note that, in keeping with previous chapters, we assume a constant reactive surface area. Our assumption about c_{o} in the negative electrode gives us a homogeneous Dirichlet boundary condition for c_{o} at $x = \ell_{\mathrm{n}}$, while the boundary condition at $x = 1$ and initial condition are unchanged from (2.66a) and (2.68):

$$c_{\mathrm{o}} = 0 \quad \text{at } x = \ell_{\mathrm{n}}, \tag{5.4ba}$$

$$\frac{\partial c_{\mathrm{o}}}{\partial x} = 0 \quad \text{at } x = 1, \tag{5.4bb}$$

$$c_{\mathrm{o}} = 0 \quad \text{at } t = 0. \tag{5.4bc}$$

By Faraday's law of electrolysis, the interfacial current density for the oxygen reaction at $x = \ell_{\mathrm{n}}$ is now given by the flux of oxygen at that interface:

$$s_{\mathrm{o}}^{\mathrm{O}} j^{\mathrm{O}}\big|_{x\searrow\ell_{\mathrm{n}}} = -\frac{N_{\mathrm{o}}}{\mathcal{C}_{\mathrm{e}}}\bigg|_{x=\ell_{\mathrm{n}}} = \left(\frac{\mathcal{D}_{\mathrm{o}} D_{\mathrm{o}}^{\mathrm{eff}}}{\mathcal{C}_{\mathrm{e}}}\frac{\partial c_{\mathrm{o}}}{\partial x} - c_{\mathrm{o}} v^{\square}\right)\bigg|_{x=\ell_{\mathrm{n}}}. \tag{5.4c}$$

We schematise the diffusion-limited system (5.4), and compare with the previous reaction-limited system, in Figure 5.1.

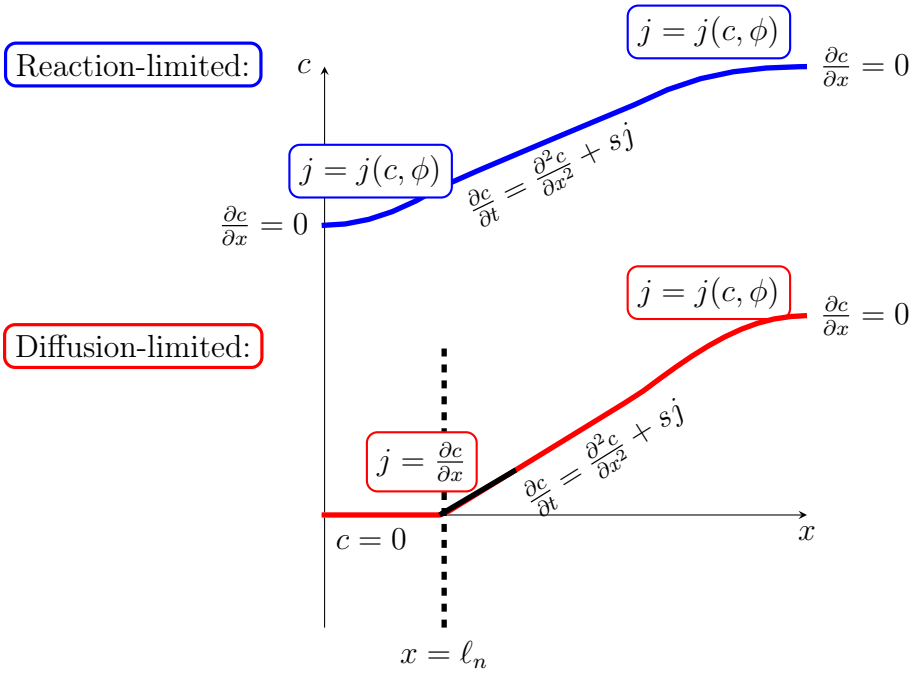

Figure 5.1: Schematic of concentration profiles, comparing a reaction-limited system with a diffusion-limited system. In the reaction-limited system, the interfacial current density, j, in each electrode depends on the kinetics (e.g. Butler-Volmer), with reaction-diffusion for the electrolyte concentration across the whole system (negative electrode, separator, positive electrode) and no-flux conditions at each end. In the diffusion-limited system, the interfacial current density in the positive electrode still depends on kinetics, but now the interfacial current density in the negative electrode is localised at the electrode-separator interface ($x = \ell_\mathrm{n}$), and depends only on the flux of electrolyte arriving at that interface. The electrolyte concentration is zero in the negative electrode, and is governed by reaction-diffusion in the separator and positive electrode, with zero concentration at the left boundary and no-flux at the right boundary.

Finally, since the oxygen reaction in the negative electrode occurs entirely at the interface with the separator, the solid current in the negative electrode is no longer given by (3.1f) with $i_{\mathrm{s}} = 0$ at $x = \ell_{\mathrm{n}}$, but instead by

$$\frac{\partial i_{\mathrm{s}}}{\partial x} = j^{\mathrm{S}} + C^{\mathrm{dl}} \frac{\partial}{\partial t} \left(\Phi_{\mathrm{s}} - \Phi_{\mathrm{e}} \right), \tag{5.3}$$

with boundary condition

$$i_{\mathrm{s}} = j^{\mathrm{O}} \quad \text{on } x = \ell_{\mathrm{n}}. \tag{5.4}$$

For the boundary condition at $x = 0$, we still set a reference potential $\Phi_{\mathrm{s}} = 0$, but conservation of current implies that $i_{\mathrm{s}} = \mathcal{I}$ there. Since i_{s} is zero in the separator, there is a jump in the solid current of size $-j^{\mathrm{O}}$ at $x = \ell_{\mathrm{n}}$. The remainder of the equations are unchanged from (3.1), except j^{O} is now given by

$$j^{\mathrm{O}} = \begin{cases} \frac{1}{s_{\mathrm{o}}^{\mathrm{O}}} \left(\frac{\mathcal{D}_{\mathrm{o}} D_{\mathrm{o}}^{\mathrm{eff}}}{\mathcal{C}_{\mathrm{e}}} \frac{\partial c_{\mathrm{o}}}{\partial x} - c_{\mathrm{o}} v^{\square} \right) \Big|_{x=\ell_{\mathrm{n}}} \delta(x - \ell_{\mathrm{n}}), & 0 < x < 1 - \ell_{\mathrm{p}}, \\ j^{\mathrm{O}} \left(\{c_k\}, \Phi_{\mathrm{s}} - \Phi_{\mathrm{e}} \right), & 1 - \ell_{\mathrm{p}} < x < 1, \end{cases} \tag{5.5}$$

where δ is the Dirac delta function. As a result, there is a jump in the electrolyte current of size j^{O} at $x = \ell_{\mathrm{n}}$, with $i_{\mathrm{e}} = \mathcal{I} - j^{\mathrm{O}}$ on the negative electrode side, and $i_{\mathrm{e}} = \mathcal{I}$ in the separator as before. Similarly, there is a jump in the electrolyte flux of size $t_+^{\mathrm{w}} j^{\mathrm{O}}$ at $x = \ell_{\mathrm{n}}$.

5.2 Effect of side reactions

We compare our toy model, with oxygen evolution and recombination, with a model in which no side reactions occur (and hence the oxygen concentration is always zero).

In Figure 5.2, we investigate the effect of oxygen side reactions on the voltage. As expected, in the case with no side reactions the voltage continues to increase as the battery is charged. However, when the oxygen reactions are included, the system reaches a steady state in which the voltage is constant. At low C-rates (Figure 5.2a), this steady state is reached monotonically (Figure 5.2a). As we increase the C-rate, we observe a peak in the voltage before the steady state is reached (Figures 5.2b,c).

The steady state behaviour can be understood by observing the average interfacial current densities in each electrode associated with each reaction (Figure 5.3). In the case without oxygen, all of the current goes towards the main reactions in each electrode. However, once we include oxygen, there is a switchover from the main reactions to the oxygen reactions. This occurs first in the positive electrode, and then in the negative electrode, with a time delay on the order of the diffusion timescale for oxygen ($\sim$20 minutes). At low C-rates (Figures 5.2a and 5.3a), the switchover is almost

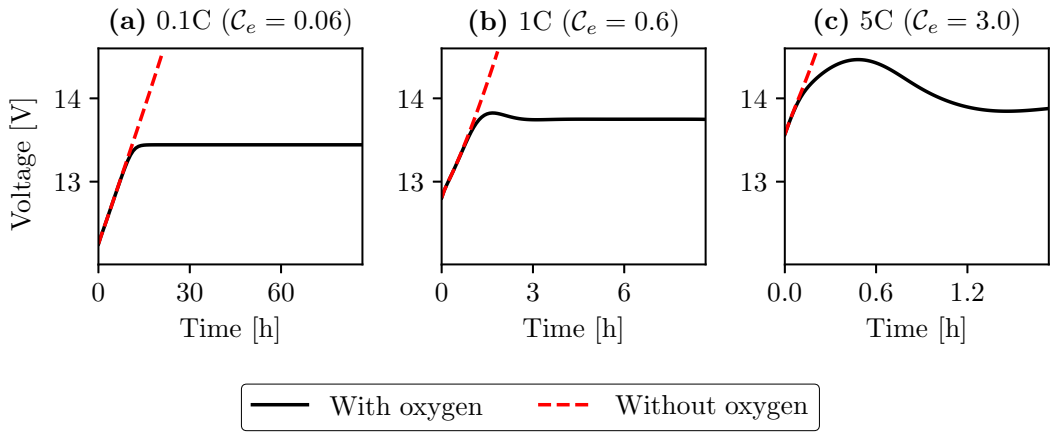

Figure 5.2: Effect of including oxygen side reactions on the battery voltage, for a constant current charge at a range of C-rates.

instantaneous since the system is dominated by kinetics and the exponent in (5.2) is large. At higher C-rates, the switchover is less sharp (Figure 5.2b,c), and average interfacial current densities display non-monotonic behaviour (Figure 5.3b,c). Since the interfacial current densities for the main reactions become negative, the battery is in fact briefly *discharging*, which explains the peak in voltage. This non-monotonicity may be attributable to the diffusion delay for oxygen to reach the negative electrode.

5.3 Asymptotic analysis for the diffusion-limited reaction

We now adapt our three reduced-order models (LOQS, FOQS and Composite) to capture the diffusion-limited kinetics in the negative electrode. We expand all variables in powers of $\mathcal{C}_\mathrm{e}$ as in (3.13), and then equate coefficients at leading order, and then at first order.

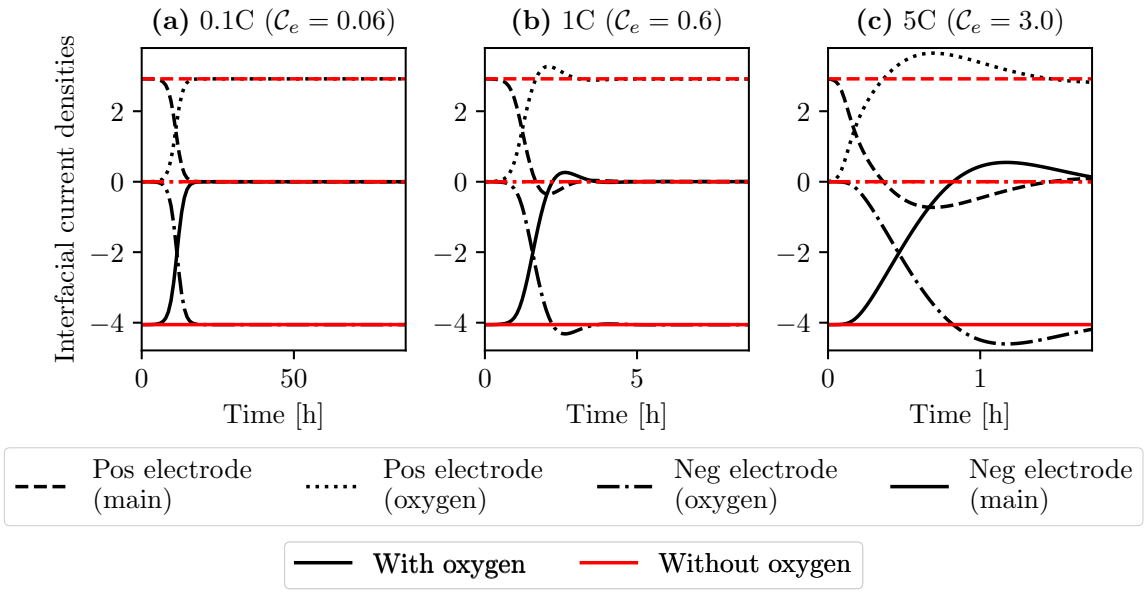

Figure 5.3: Effect of including oxygen side reactions on the average (dimensionless) interfacial current densities, $\bar{j}$, for a constant current charge at a range of C-rates.

5.3.1 Leading-order quasi-static solution

To leading order in $\mathcal{C}_\mathrm{e}$, the system (5.4) becomes

$$\frac{\partial}{\partial x}\left(D_\mathrm{o}^{\mathrm{eff},(0)}\frac{\partial c_\mathrm{o}^{(0)}}{\partial x}\right) = 0, \tag{5.6a}$$

$$c_\mathrm{o}^{(0)} = 0 \quad \text{at } x = \ell_\mathrm{n}, \tag{5.6b}$$

$$\frac{\partial c_\mathrm{o}^{(0)}}{\partial x} = 0 \quad \text{at } x = 1, \tag{5.6c}$$

$$D_\mathrm{o}^{\mathrm{eff},(0)}\frac{\partial c_\mathrm{o}^{(0)}}{\partial x} = 0 \quad \text{at } x = \ell_\mathrm{n}. \tag{5.6d}$$

By (5.6a), $c_\mathrm{o}^{(0)}$ is identically zero: on the discharge timescale, any oxygen evolved in the positive electrode immediately diffuses to, and recombines at, the negative electrode.

Recall that the oxygen reaction in the positive electrode is dominated by the forward reaction (Tafel kinetics) and the exchange-current density for the forward oxygen reaction is independent of oxygen concentration (Table B.3). Hence the forward reaction can occur even if the oxygen concentration is zero, at a rate that depends only on the electrolyte concentration, c_e, and the potential difference, ϕ. Since the LOQS solution developed in Section 3.3.2 has uniform $c_\mathrm{e}^{(0)}$ and $\phi_\mathrm{p}^{(0)}$, the leading-order oxygen current in the positive electrode, $j_\mathrm{p}^{\mathrm{O},(0)}$, must also be uniform in space. For the same

reason, the solid current density, and interfacial current densities from the main and hydrogen reactions, are also uniform in space in the negative electrode. Integrating (5.3) and applying the boundary conditions (5.4) and $i_{\mathrm{s}}|_{x=0} = \mathcal{I}$, we find

$$-\ell_{\mathrm{n}}\left(j_{\mathrm{n}}^{\mathrm{S},(0)} + C^{\mathrm{dl}}\frac{\mathrm{d}\phi_{\mathrm{n}}^{(0)}}{\mathrm{d}t}\right) = j^{\mathrm{O},(0)}\big|_{x\searrow\ell_{\mathrm{n}}} - \mathcal{I}. \tag{5.7}$$

This is the same result as (3.17c), but with $j_{\mathrm{n}}^{\mathrm{O},(0)}$ replaced by $j^{\mathrm{O},(0)}\big|_{x\searrow\ell_{\mathrm{n}}}/\ell_{\mathrm{n}}$. The factor of $1/\ell_{\mathrm{n}}$ appears with $j^{\mathrm{O},(0)}\big|_{x\searrow\ell_{\mathrm{n}}}$ when integrating because $j_{\mathrm{n}}^{\mathrm{O},(0)}$ acts on the whole electrode in (3.17c) but $j^{\mathrm{O},(0)}\big|_{x\searrow\ell_{\mathrm{n}}}$ acts on the boundary in (5.7). For the positive electrode, (3.17c) is unchanged.

To find $j^{\mathrm{O},(0)}\big|_{x\searrow\ell_{\mathrm{n}}}$, we must use the first-order problem in $\mathcal{C}_{\mathrm{e}}$. At first order, equating coefficients of $\mathcal{C}_{\mathrm{e}}$ in (5.4) gives, with $c_{\mathrm{o}}^{(0)} = 0$,

$$0 = \mathcal{D}_{\mathrm{o}}D_{\mathrm{o}}^{\mathrm{eff},(0)}\frac{\partial^2 c_{\mathrm{o}}^{(1)}}{\partial x^2} - s_{\mathrm{o}}^{\mathrm{O}}j^{\mathrm{O},(0)}, \tag{5.8a}$$

$$c_{\mathrm{o}}^{(1)} = 0 \quad \text{at } x = \ell_{\mathrm{n}}, \tag{5.8b}$$

$$\frac{\partial c_{\mathrm{o}}^{(1)}}{\partial x} = 0 \quad \text{at } x = 1, \tag{5.8c}$$

$$s_{\mathrm{o}}^{\mathrm{O}}j^{\mathrm{O},(0)} = \mathcal{D}_{\mathrm{o}}D_{\mathrm{o}}^{\mathrm{eff},(0)}\frac{\partial c_{\mathrm{o}}^{(1)}}{\partial x} \quad \text{at } x = \ell_{\mathrm{n}}. \tag{5.8d}$$

Integrating (5.8a) from $x = \ell_{\mathrm{n}}$ to $x = 1$ and applying the boundary conditions (5.8b)-(5.8d), we find that

$$j^{\mathrm{O},(0)}\big|_{x\searrow\ell_{\mathrm{n}}} = -\ell_{\mathrm{p}}j_{\mathrm{p}}^{\mathrm{O},(0)}. \tag{5.9}$$

Hence at leading order the oxygen current density at the negative electrode/separator interface is determined entirely by the leading-order oxygen interfacial current density in the positive electrode.

5.3.2 First-order quasi-static solution

Solving (5.8a) with the boundary conditions (5.4ba) gives a quasi-static profile for $c_{\mathrm{o}}^{(1)}$,

$$c_{\mathrm{o}}^{(1)} = \begin{cases} -\frac{s^{\mathrm{O}}\ell_{\mathrm{p}}j_{\mathrm{p}}^{\mathrm{O},(0)}(x-\ell_{\mathrm{n}})}{\mathcal{D}_{\mathrm{o}}D_{\mathrm{o,s}}^{\mathrm{eff},(0)}}, & \ell_{\mathrm{n}} < x < 1-\ell_{\mathrm{p}}, \\ s^{\mathrm{O}}j_{\mathrm{p}}^{\mathrm{O},(0)}\left(\frac{(x-1)^2-\ell_{\mathrm{p}}^2}{2\mathcal{D}_{\mathrm{o}}D_{\mathrm{o,p}}^{\mathrm{eff},(0)}} - \frac{\ell_{\mathrm{s}}\ell_{\mathrm{p}}}{\mathcal{D}_{\mathrm{o}}D_{\mathrm{o,s}}^{\mathrm{eff},(0)}}\right), & 1-\ell_{\mathrm{p}} < x < 1. \end{cases} \tag{5.10}$$

Evaluating $\partial c_{\mathrm{o}}^{(1)}/\partial x$ at $x = \ell_{\mathrm{n}}$ confirms (5.9). By a similar analysis to (5.7), we can recover an equation similar to (3.28c) for the negative electrode,

$$\frac{\mathrm{d}\bar{\phi}_{\mathrm{n}}^{(1)}}{\mathrm{d}t} = -\frac{1}{C_{\mathrm{n}}^{\mathrm{dl}}}\left(\bar{j}_{\mathrm{n}}^{\mathrm{S},(1)} + j^{\mathrm{O},(1)}\big|_{x\searrow\ell_{\mathrm{n}}}\right), \tag{5.11}$$

while (3.28c) is unchanged for the positive electrode.

To find $j^{\mathrm{O},(1)}\big|_{x\searrow\ell_\mathrm{n}}$, we use the second-order problem in $\mathcal{C}_\mathrm{e}$. At second order, equating coefficients of $\mathcal{C}_\mathrm{e}$ in (5.4) gives

$$\frac{\partial}{\partial t}\left(\varepsilon^{(0)}c_\mathrm{o}^{(1)}\right) = \mathcal{D}_\mathrm{o}\left(D_\mathrm{o}^{\mathrm{eff},(1)}\frac{\partial c_\mathrm{o}^{(1)}}{\partial x} + D_\mathrm{o}^{\mathrm{eff},(0)}\frac{\partial c_\mathrm{o}^{(2)}}{\partial x}\right) - s_\mathrm{o}^\mathrm{O} j^{\mathrm{O},(1)}, \tag{5.12a}$$

$$c_\mathrm{o}^{(2)} = 0 \quad \text{at } x = \ell_\mathrm{n}, \tag{5.12b}$$

$$\frac{\partial c_\mathrm{o}^{(2)}}{\partial x} = 0 \quad \text{at } x = 1, \tag{5.12c}$$

$$s_\mathrm{o}^\mathrm{O} j^{\mathrm{O},(1)} = \mathcal{D}_\mathrm{o}\left(D_\mathrm{o}^{\mathrm{eff},(1)}\frac{\partial c_\mathrm{o}^{(1)}}{\partial x} + D_\mathrm{o}^{\mathrm{eff},(0)}\frac{\partial c_\mathrm{o}^{(2)}}{\partial x}\right) \quad \text{at } x = \ell_\mathrm{n}. \tag{5.12d}$$

Integrating (5.12a) from $x = \ell_\mathrm{n}$ to $x = 1$ and applying the boundary conditions (5.12b)-(5.12d), we obtain the first-order correction to the oxygen current at the negative electrode/separator interface:

$$s_\mathrm{o}^\mathrm{O} j^{\mathrm{O},(1)}\big|_{x\searrow\ell_\mathrm{n}} = \int_{\ell_\mathrm{n}}^1 \frac{\partial}{\partial t}\left(\varepsilon^{(0)}c_\mathrm{o}^{(1)}\right) + s_\mathrm{o}^\mathrm{O} j^{\mathrm{O},(1)}\,\mathrm{d}x, \tag{5.13}$$

where we find $\partial c_\mathrm{o}^{(1)}/\partial t$ by applying the chain rule to (5.10).

5.3.3 Composite model

By analogy with Section 3.3.4, we can also derive a composite solution that captures both diffusion transients following jumps in the current, and quasi-static behaviour after long periods of constant current. The electrolyte concentration is governed by the PDE (3.29), but with $j^{\mathrm{O},(0)}$ being the leading-order equivalent of the delta function (5.5). Since the leading-order oxygen concentration is zero, the first-order correction to the oxygen concentration, $c_\mathrm{o}^{(1)}$, is directly given by

$$\frac{\partial}{\partial t}\left(\varepsilon^{(0)}c_\mathrm{o}^{(1)}\right) = \frac{\mathcal{D}_\mathrm{o}D_\mathrm{o}^{\mathrm{eff},(0)}}{\mathcal{C}_\mathrm{e}}\frac{\partial^2 c_\mathrm{o}^{(1)}}{\partial x^2} - s_\mathrm{o}^\mathrm{O}\left(j^{\mathrm{O},(0)} + \mathcal{C}_\mathrm{e}\bar{j}^{\mathrm{O},(1)}\right), \tag{5.14}$$

with boundary conditions (5.8b) and (5.8c). Then $j^{\mathrm{O},(0)}\big|_{x\searrow\ell_\mathrm{n}}$ is given by (5.8d).

5.4 Results

We now compare reduced-order models with the full system, once again treating the full system as 'ground truth'. The FOQS solution is difficult to implement when there are multiple side reactions, since we must solve the ODE (3.24) instead of using

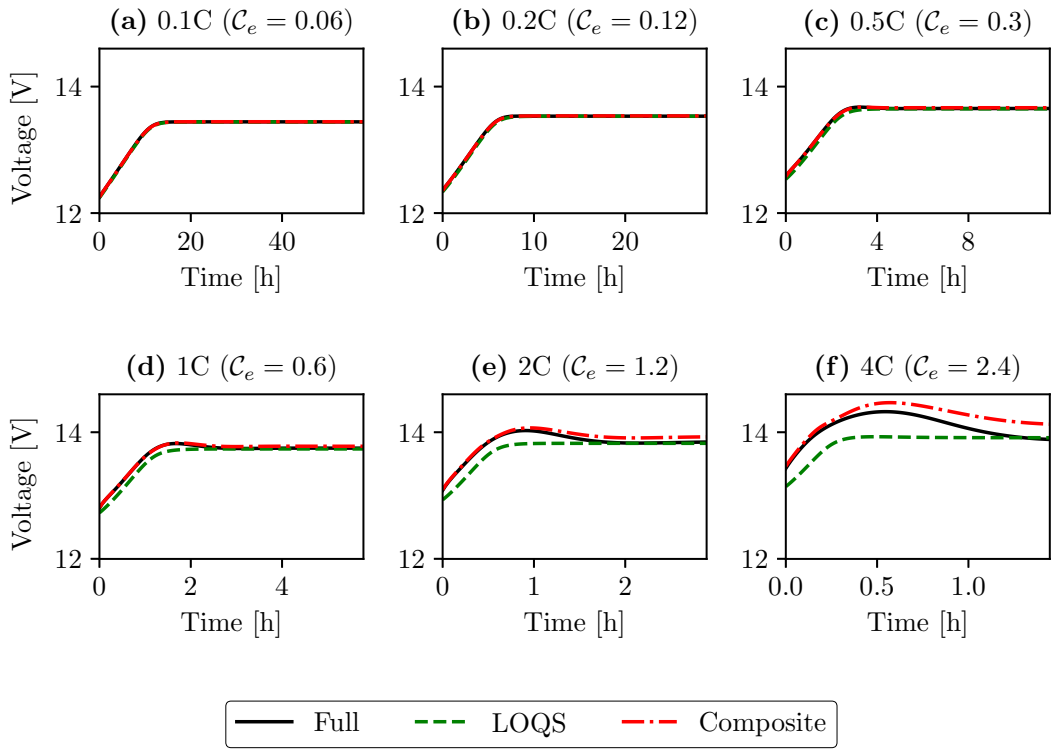

Figure 5.4: Comparing battery voltages for a constant-current discharge at a range of C-rates.

the explicit equation (3.26), which requires multiple applications of the chain rule. Therefore, we only show results for the LOQS and composite models. Together, these two models give good physical insight, and approximate the full model well at different degrees of accuracy and complexity.

In Figure 5.4, we compare voltages for constant-current recharge at a range of C-rates. At low C-rates, both the LOQS model and composite model give a good approximation to the full model. As we increase the C-rate, the composite model captures the non-monotonic voltage response, but the LOQS does not. In all cases, the full and composite solutions eventually tend towards the LOQS solution, even at higher C-rates. The fact that the LOQS does not capture the voltage peak confirms our assertion that this peak is due to the diffusion delay for oxygen that is evolved at the positive electrode to reach the negative electrode, since to leading order diffusion from the positive electrode to the negative electrode is instantaneous.

To understand these effects, we turn to the comparison of electrolyte concentrations (Figure 5.5). As was the case for a discharge, the electrolyte concentration is uniform at a low C-rate (Figure 5.5a), with all solutions showing good agreement.

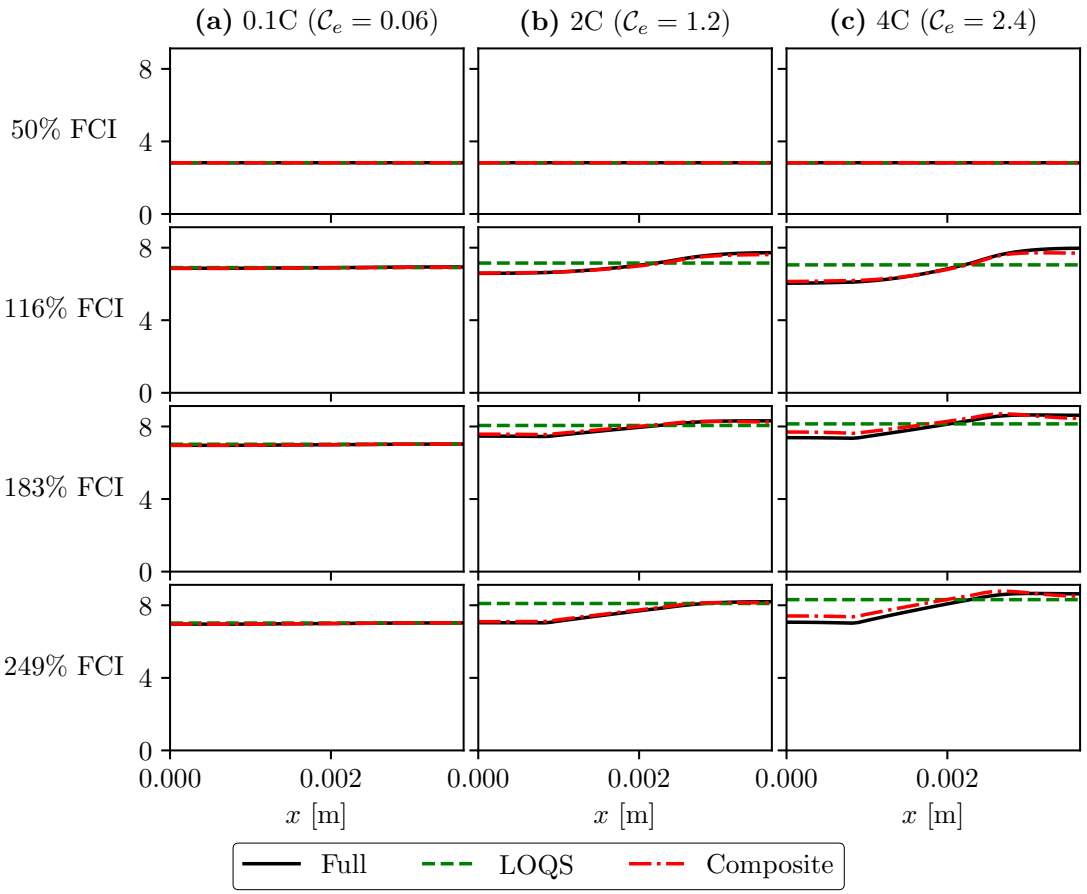

Figure 5.5: Comparing electrolyte concentrations, c_e (in mol/L), at various SoCs, for a constant-current charge at a range of C-rates. Fractional Charge Input (FCI) is defined as the amount of charge put into the battery relative to the amount of charge required for a full charge, and in dimensionless units is given by (5.15).

However, a key difference with the discharge results is that, as we increase C-rate, the average electrolyte concentration is no longer perfectly predicted by the LOQS solution. This is because the average interfacial current density in each electrode (which directly determines the average electrolyte concentration through (3.17a)) is no longer known in advance, since the main reaction competes with the oxygen reaction: first-order corrections to the average interfacial current densities, $\bar{j}^{r,(1)}$, are non-zero, and there are corrections to the average electrolyte concentration at first order. At later times during charge, the electrolyte concentration in the positive electrode has a similar value for all three models. Since the rate of oxygen evolution in the positive electrode, and hence oxygen recombination in the negative electrode, and hence overall voltage, depend mainly on the electrolyte concentration in the positive electrode, this explains why the final voltages observed are similar for all three

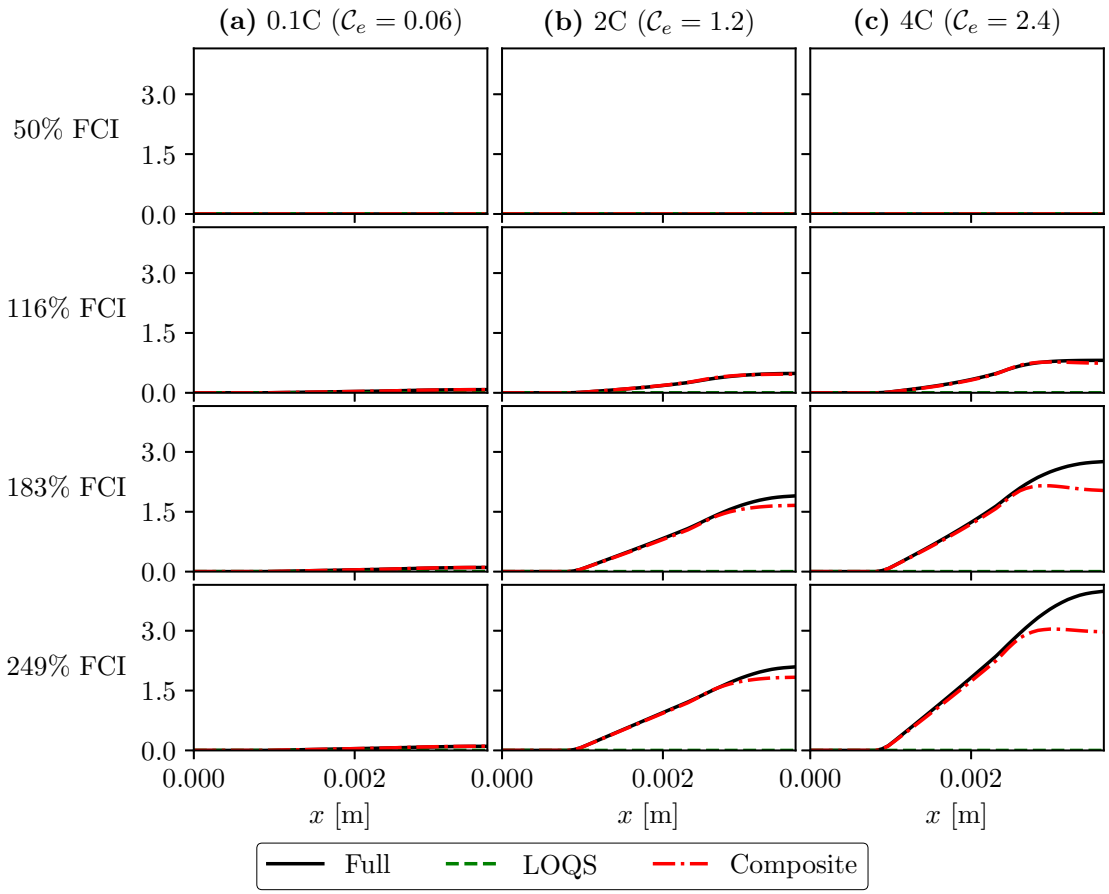

Figure 5.6: Comparing oxygen concentrations, c_o (in mol/L), at various SoCs, for a constant-current charge at a range of C-rates.

models.

In Figure 5.6, we compare oxygen concentrations during recharge. Both the full solution and the composite solution display the oxygen concentration profile shown in Figure 5.1, with some discrepancies in the composite solution in the positive electrode at high C-rate. These discrepancies appear because the interfacial current density for the oxygen reaction in the positive electrode is not approximated accurately by the composite solution at high C-rates. The oxygen concentration in the LOQS solution is always exactly zero.

Note that in Figures 5.5 and 5.6, we have followed [6] and used Fractional Charge Input (FCI) as the indication of how much the charge has progressed, since the SoC reaches a steady state, as shown (the steady-state SoC is different at different C-rates). FCI is defined as the amount of charge put into the battery relative to the

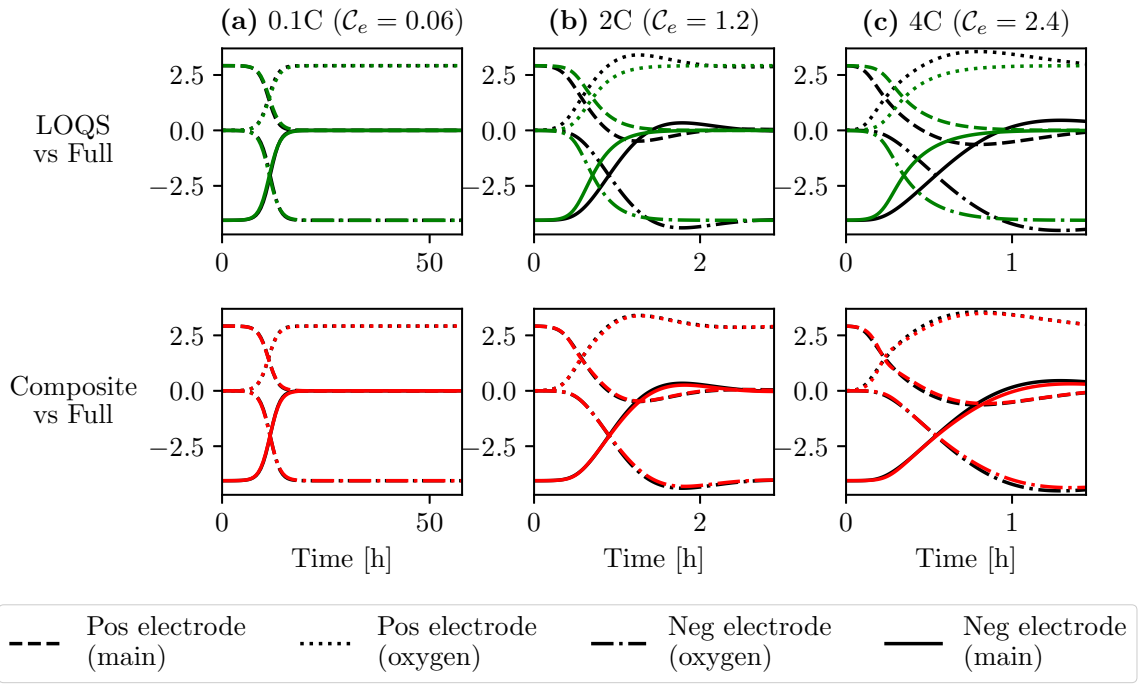

Figure 5.7: Comparing dimensionless average interfacial current densities, $\bar{j}$, for a constant-current charge at a range of C-rates. In all cases, the solution from the full system is shown in black, and the colours for other solutions match those from previous plots.

amount of charge required for a full charge, and in dimensionless units is given by

$$\frac{\mathrm{d}}{\mathrm{d}t}\left(FCI\right) = -\mathcal{I}(t), \tag{5.15a}$$

$$FCI(0) = q^0, \tag{5.15b}$$

with a minus sign in (5.15a) since $\mathcal{I}$ is positive for a discharge.

We also compare averaged interfacial current densities, in Figure 5.7. The composite solution approximates all interfacial current densities very accurately for all C-rates shown. At high C-rates, there are significant differences between the LOQS and full solutions. In particular, the cross-over point from main reaction to oxygen reaction happens simultaneously in both electrodes for the LOQS solution, without the delay that is observed in the full and composite solutions. This can again be attributed to the instantaneous diffusion at leading order, and adds weight to the theory that diffusion-limited effects are important during recharge.

Finally, we again consider the decomposition of the voltage into contributing parts (Figure 5.8). We observe that this decomposition is qualitatively quite different to the decomposition of the voltage during discharge (Figure 3.13), even when taking

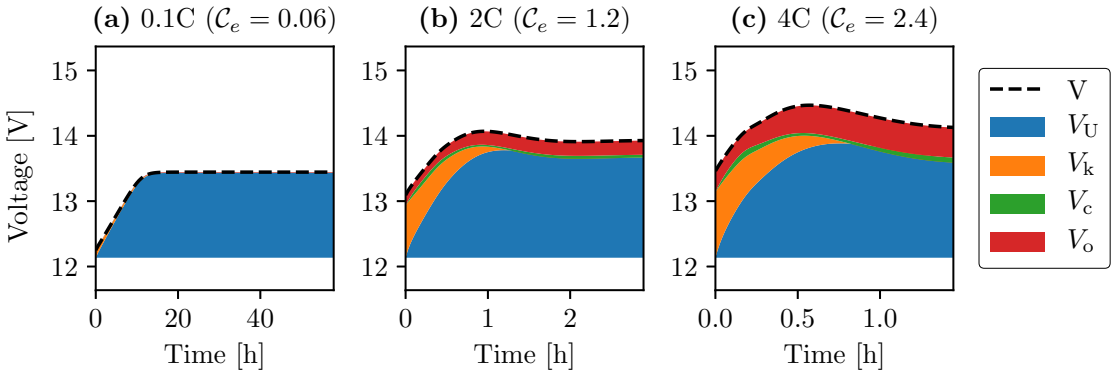

Figure 5.8: Decomposition of voltage change into dimensional components, for a constant-current charge at a range of C-rates.

account for the non-monotonicity of the voltage. As the voltage progresses towards steady state, the kinetic overpotential V_k decreases before becoming zero at steady state. This shows that, at steady state, the main reaction is in equilibrium in each electrode, with only the oxygen reaction taking place: oxygen is evolved in the positive electrode and recombines in the negative electrode at an equal rate.

5.5 Concluding remarks

In this chapter, we considered a toy model for recharge of a lead-acid battery by incorporating oxygen evolution and recombination as a side reaction to the one-dimensional model studied in Chapter 3.

Qualitatively, this toy model behaves similarly to existing models in the literature during constant-current charging [6, 49, 88, 115], capturing the voltage peak and then steady state, which is also observed experimentally by Bernardi and Carpenter [6]. In contrast with existing models in the literature, we explicitly write a full diffusion-limited equation for the oxygen concentration. It has been shown experimentally that the oxygen reaction must be diffusion-limited in the negative electrode [8, 74], and we have confirmed this via a simple analysis of the exponents in the Butler-Volmer kinetics. This is only addressed via a lumped parameter model by Newman and Tiedemann [88], while other authors assume standard kinetics [6, 49, 115] and do not address the resulting stiffness in the model. As a result of the diffusion-limited kinetics, our model can capture a sharp voltage peak without needing to include additional side reactions.

We then developed a suite of reduced-order models and again showed good agreement with the full system by choosing the appropriate model and different discharge rates. From the solutions of the reduced-order models, it becomes clear that the voltage peak is due to diffusion-limited effects, since the peak is not present at leading order. This once again demonstrates the insight that the reduced-order models can provide, beyond simply reproducing voltage curves with lower computational effort.

An inconsistency in our toy model is that we have assumed that the oxygen is always dissolved in the liquid, but the concentrations that we observe are superior to the saturation concentration of oxygen (a few millimolar [131]). We could artificially fix this by increasing the diffusion coefficient of oxygen, but this too would then imply that oxygen exists in the gaseous phase. In reality, a more physically consistent model of oxygen should include oxygen in both the liquid and gas phases. This then requires including an additional volume fraction for the gas phase, and a model for oxygen transport in the gas phase, which may not be driven by diffusion but rather by convection of bubbles.

In additions to this, our toy model does not perfectly reproduce the behaviour of lead-acid batteries during charge, since in reality several additional reactions occur such as hydrogen evolution/recombination and limited rate of transport of Pb^{2+} ions [88], or sulfate crystal growth and hardening [121], that we have not considered in this thesis.

Chapter 6

Conclusions

The work on mathematical modelling of lead-acid batteries in this thesis has led to several novel contributions. In this chapter, we summarise the contributions of this thesis and explore future perspectives.

6.1 Summary of thesis and contributions

Three-dimensional model with solute-volume effects. In Chapter 2, we presented a well-known macroscopic model for lead-acid batteries, but highlighted some additional physical effects that are not usually taken into account. First, we generalised the results of Liu and Monroe [71] to include solute-volume changes due to additional species in the liquid. Second, we considered the non-isobaric case, in order to allow pressure-driven flow, and investigate pressure-diffusion effects, though we found that these were very small for lead-acid batteries. Finally, we included Faradaic convection, the flow induced by volume changes due to the reactions at the electrode/electrolyte interface.

In Chapter 3, we solved a one-dimensional reduction of this model and investigated the effect of the additional terms relating to Faradaic convection. Faradaic convection was investigated by Liu and Monroe [71] in a planar electrode system, but to our knowledge this is the first implementation of these terms in a porous-electrode battery model. Although the effect of Faradaic convection was found to be quite small for lead-acid batteries at typical discharge rates, numerical experiments suggested that it would be greater at higher discharge rates or for other systems in which larger volume changes occur.

Non-dimensionalisation of the 3D model. In Chapter 2, we then nondimensionalised the full three-dimensional model. The choice of scales is similar to Richard-

son et al. [100], but the resulting dimensionless model is new. Using our dimensionless model, we were able to identify three key dimensionless parameters that control the response of the battery, either individually or in combination. Firstly, the *diffusional C-rate*, $\mathcal{C}_{\mathrm{e}}$, which is the ratio of the electrolyte diffusion timescale to the discharge timescale (equation (2.48)), controls variations in the through-cell direction (perpendicular to the electrode plane). Secondly, the cell aspect ratio, δ (ratio of cell thickness to height) is usually small, which allows us to decompose the problem in the through-cell direction from that in the transverse direction (parallel to the electrode plane). Thirdly, the dimensionless electrode conductivity, σ', which is the ratio of electrode conductivity to electrolyte conductivity scaled with the cell aspect ratio (equation (4.2)), controls variations in the transverse directions. For lead-acid batteries, the positive electrode is much less conductive than the negative electrode, and so the key conductivity is σ'_{p}, the dimensionless scaled conductivity of the positive electrode.

Both $\mathcal{C}_{\mathrm{e}}$ and σ' depend on the C-rate, with non-uniformities growing as the C-rate increases. The remainder of this thesis mainly consisted of deriving approximate models by systematic use of asymptotic expansions in powers of $\mathcal{C}_{\mathrm{e}}$ (Chapter 3 and 5) and δ and σ' (Chapter 4).

Systematic asymptotics in the slow-discharge limit. The first major contribution of this thesis, in Chapter 3, was to develop a framework for the systematic derivation of reduced-order models, in the case of slow discharge (small $\mathcal{C}_{\mathrm{e}}$). By performing a perturbation expansion in $\mathcal{C}_{\mathrm{e}}$, we obtained a series of reduced-order models of increasing complexity and accuracy. The simplest, LOQS, model gave an algebraic expression for the voltage, and was found to be accurate up to C-rates of 0.1C. Quasi-static corrections to the LOQS model were given by the first-order quasi-static (FOQS) model, which has the same complexity but gives increased accuracy up to 1C. A further more complex, composite, model required solving an additional linear PDE, and was found to be accurate up to 5C. In addition to accurate voltage predictions for less computational complexity, the reduced-order models gave physical insight into the problem by allowing us to more easily decompose the voltage into its constituent parts. Further, we have demonstrated that reduced-order models can allow accurate parameter fitting with reduced computational cost.

The reduced-order models are extensions of well-known models: the LOQS model is similar to Newman and Tiedemann's LPM or the SPM for lithium-ion batteries, while the composite model is similar to the SPMe for lithium-ion batteries. However,

the systematic derivation of these from the full one-dimensional model is new, and gives a framework for including additional physical effects.

Asymptotics in the small-aspect-ratio limit. The second major contribution was to use the fact that the aspect ratio of the batteries is small to allow systematic simplifications that decompose the transverse direction from the planar directions, and hence obtain a reduced-order model of a three-dimensional battery, in Chapter 4. We found good agreement between our decomposed model and the solution of the full three-dimensional model, obtained using COMSOL [56]. Our model showed that more current crosses the separator near the top of the battery than near the bottom, and so the battery discharges more quickly at the top. The uniformity of discharge rate in the vertical direction is mainly controlled by the conductivity of the positive electrode: the battery discharges more uniformly if the current collector is more conductive.

We then explored three further limits as we varied the electrode conductivity. First, in the limit of poorly conducting electrodes, we showed that the reduced-order models from Chapter 3 can be adapted to capture the non-uniformities in transverse directions. Second, in the limit of quite conductive electrodes, we derived a simplified model that is uniform in both through-cell and transverse directions at leading order in $\mathcal{C}_{\mathrm{e}}$, with variations in both directions appearing at first order in $\mathcal{C}_{\mathrm{e}}$. By averaging the first-order model over the transverse directions, we only need to solve a one-dimensional 'averaged' through-cell problem, and the current collector overpotential is given by two decoupled elliptic PDEs. These two elliptic PDEs can be solved offline in advance and give a series resistance due to the electrodes. Hence, in this limit, all of the three-dimensional effects are captured at only the cost of a one-dimensional model. Finally, in the case where the conductivity of the electrodes was very large, we showed that the three-dimensional model reduces to the one-dimensional through-cell model that is usually studied. By comparing of all the different limits as we varied electrode conductivity and C-rate, we suggested which model was most appropriate in each parameter regime.

In addition to the reduced-order models, our analysis of the three-dimensional model provided a mechanism to allow different volume changes in the two electrodes. In the limit in which the separator is much more permeable than the electrodes, we showed that, in the separator, flow must occur in the transverse directions, to balance the flow in the through-cell direction.

Toy model for charge, and asymptotic analysis. In Chapter 5, we extended our model to specifically include oxygen evolution and recombination. The resulting model displayed the known behaviour that oxygen recombination in the negative electrode must be diffusion-limited. Hence we adapted the standard equations for oxygen kinetics and transport to model the diffusion-limited system. To our knowledge, this is the first one-dimensional model of side reactions that takes into account diffusion-limited effects and resolves the oxygen concentration profile (a zero-dimensional 'lumped-parameter model' was studied by Newman and Tiedemann [88]). We showed that the framework developed for discharge in Chapter 3 can easily be extended to the case of recharge with an additional reaction, and the reduced-order models agreed well with the full-order model in the appropriate parameter regimes. Further physical insight was provided by the reduced-order models as they showed that the non-monotonicity of the voltage increase that was observed during charge must be due to diffusion-limited effects.

PyBaMM software. Finally, we developed the open-source Python package 'PyBaMM' (Python Battery Mathematical Modelling, Appendix A) in order to implement the numerical results (both full- and reduced-order) in this thesis, as well as similar results for lithium-ion batteries. This software has been designed as the Common Modelling Framework for the Faraday Institution and is currently being expanded to include new battery models by other UK researchers. PyBaMM offers greater flexibility and robustness than existing open-source battery modelling softwares, and thus provides a strong platform for the investigation of new models and numerical methods.

6.2 Future work and perspectives

The models developed in this thesis allow us to simulate a single charge or discharge of a lead-acid battery with the accuracy of mechanistic models but at a computational cost similar to equivalent-circuit models. There are many exciting applications for the reduced-order models resulting from our asymptotic methods.

One possible application for the reduced-order models is for estimating parameters and states (SoC and SoH) in the model using data. In this area, having fast forward models is crucial, especially for estimating SoH since one must simulate several years of data with frequencies on the order of minutes. Our physics-based reduced-order models improve on equivalent-circuit models as the physical parameters in our models

are much more robust to different SoCs and SoHs than the resistances and capacitances in equivalent-circuit models. In cases where the reduced-order models are not as accurate as the full model, one could use ideas from multi-fidelity optimisation [92] to combine the speed of the reduced-order models with the accuracy of the full model. In addition to this, our battery modelling software PyBaMM could allow us to algorithmically compute adjoints with respect to any parameter in the model, which can greatly improve the efficiency of parameter-estimation algorithms.

A second possible area for applying these models is in optimisation of battery design and operation. By considering an additional reaction of oxygen evolution and recombination, we have shown that our reduced-order modelling framework can be applied to models with multiple side reactions, including some that are diffusion-limited. In this area, a significant amount of additional modelling work is still required in order to properly account for the many different side reactions that occur during recharge. This additional physics can the be incorporated into the existing framework in order to create an accurate and fast model for recharge. This could then be used to construct optimal charging strategies that minimise both charge time and degradation. Reniers et al. [99] have shown that using physically-based models instead of equivalent-circuit ones can drastically improve the effectiveness of such optimal control strategies.

For battery design, we have decomposed the voltage into constituent parts in order to explicitly show the effect of the relevant parameters on the voltage. This could be used to optimise battery design for specific applications, for example trading off between power and capacity. In addition to this, the results of Chapter 4 could be used to design better current collectors. In particular, in Section 4.2.2, we isolate the effect of the current collector/electrode design on the voltage by showing that all of the transverse effects can be captured by two elliptic PDEs (one in each electrode). Further, we have shown in order to minimise the voltage loss due to transverse effects, one must minimise the difference between the average potential in the electrodes and the potential at the tabs. This could be used together with systematic homogenisation of the electrode/current collector domain to reveal the optimal geometry and tab placement.

The framework that we create in this thesis can be applied to different battery chemistries in which electrolyte diffusion occurs on a faster timescale than a typical discharge, or the cell aspect ratio is small. For the former case, the framework has already been adapted to the case of lithium-ion batteries by Marquis et al. [77].

Finally, all of the models considered so far are valid only at the individual cell level: we have assumed that all cells in a battery pack discharge uniformly. In practice, there can be non-uniformities between cells in a battery pack. For example, cells at the edges of the battery pack are cooled more than cells in the middle. Understanding this effect would require the inclusion of thermal effects into the model. With thermal effects included, the reduced-order models can be extended to the battery level, and thus give physical insight into macroscopic effects without needing to solve a complete porous-electrode model in each cell.

Appendix A

Python Battery Mathematical Modelling (PyBaMM) Software

All of the results in this thesis have been obtained using the open-source Python package 'PyBaMM' (**Py**thon **Ba**ttery **M**athematical **M**odelling), of which I was the main developer. This chapter contains an overview of PyBaMM. Comprehensive documentation and examples are available online[1].

A.1 Introduction

With the battery modelling research community growing rapidly in the UK in the last few years, it is crucial to develop tools that facilitate cross-institutional collaboration. One such tool is battery modelling software that allows new discoveries to be used with minimal effort by the rest of the community. Such software would also allow quantitative comparison of different models and numerical methods. Existing open-source battery modelling software, such as M-PET [112] and LIONSIMBA [123], were found to lack the flexibility and test-driven structure required for cross-institutional development.

PyBaMM allows improved collaboration and research impact in battery modelling by providing a modular framework through which either existing or new tools can be combined in order to solve continuum models for batteries. From its inception, PyBaMM has followed software best practices with a full set of unit and integration tests and comprehensive documentation, providing confidence in the validity of solutions as well as robustness when extensions are added.

Using the modular framework, PyBaMM can easily be adapted to incorporate alternative spatial discretisations or time-stepping algorithms. Any such additions

[1] https://github.com/pybamm-team/PyBaMM

can then immediately be used on the existing suite of models already implemented. Thus, different discretisations and solvers can be directly compared, without needing to account for different hardware, software or model implementations.

Similarly, additional physics can be incorporated into the existing models, without needing to start from scratch to study each new effect. This facilitates the simultaneous study of a range of extensions to the standard battery models, for example by coupling together several degradation mechanisms.

Alongside the results contained in this thesis, PyBaMM is currently being used to develop results for reduced-order models for lithium-ion batteries, both in 1D and 3D. We are working with other researchers from the Faraday Institution to extend this software into a 'Common Modelling Framework', which would act as a central repository for UK battery modelling research. In particular, several additional models for lithium-ion batteries are starting to be added, such as models that include thermal or degradation effects.

A.2 The PyBaMM pipeline

We now present a very simple example in order to demonstrate the PyBaMM pipeline. We implement the simple diffusion model

$$\frac{\partial c}{\partial t} = \frac{\partial}{\partial x}\left(D(c)\frac{\partial c}{\partial x}\right) \qquad \text{in } 0 < x < 1, \quad t > 0, \tag{A.1a}$$

$$c = 1 \qquad \text{at } x = 0, \tag{A.1b}$$

$$\frac{\partial c}{\partial x} = -1 \qquad \text{at } x = 1, \tag{A.1c}$$

$$c = x + 1 \qquad \text{at } t = 0, \tag{A.1d}$$

where $D(c) = k(1 + c)$.

First, we create a model using the PyBaMM expression tree. Variables are represented by `Variable` objects, to which `grad` and `div` operators can be applied, while parameters are represented by `Parameter` objects. The model is created by assigning a right-hand side, boundary conditions and initial conditions to a `BaseModel` object. The resulting model is represented by an expression tree, which is shown in Figure A.2a. As shown in Listing A.1, implementing a model in this way is very straightforward and directly relatable to the mathematical form (A.1), requiring no thought about how to subsequently solve it numerically. Hence new physics can be added and explored with minimal effort.

Listing A.1: Defining a model in PyBaMM

```
# 1. Initialise model
model = pybamm.BaseModel()

# 2. Define parameters and variables
c = pybamm.Variable("c", domain="unit line")
k = pybamm.Parameter("Diffusion parameter")

# 3. State governing equations
D = k * (1 + c)
dcdt = pybamm.div(D * pybamm.grad(c))
model.rhs = {c: dcdt}

# 4. State boundary conditions
model.boundary_conditions = {
  c: {"left": (1, "Dirichlet"), "right": (-1, "Neumann")}
}

# 5. State initial conditions
x = pybamm.SpatialVariable("x", domain="unit line")
model.initial_conditions = {c: x + 1}
```

The second step before solving the model is to set the parameter '`k`', which transforms the expression tree to the one shown in Figure A.2b. Although the example here is very basic, this flexible way of setting parameters is very useful as it allows us to easily use different sets of parameters (for example, by reading in a csv file of parameters). Since parameters are defined as their own objects, they can easily be changed, creating opportunities for parameter estimation.

We then solve the model numerically using the Method of Lines. First, we discretise the model spatially, using any spatial discretisation method (such as Finite Volumes). The resulting model is shown in Figure A.2c. The variable `c` has been transformed into a state vector `y[0:50]`, while the gradient and divergence operators have both been transformed into matrix-vector products that act on this vector. The discretised model can now receive a time `t` and state `y` and return the time derivative at that time and state. Hence the discretised model can now be solved using a time-stepping algorithm (such as SciPy [58] or SUNDIALS [53, 54, 75]), giving the solution shown in Figure A.1. Much more complicated models than the one shown in detail here are possible, as demonstrated in this thesis.

Another useful feature of PyBaMM is the use of Algorithmic Differentiation to

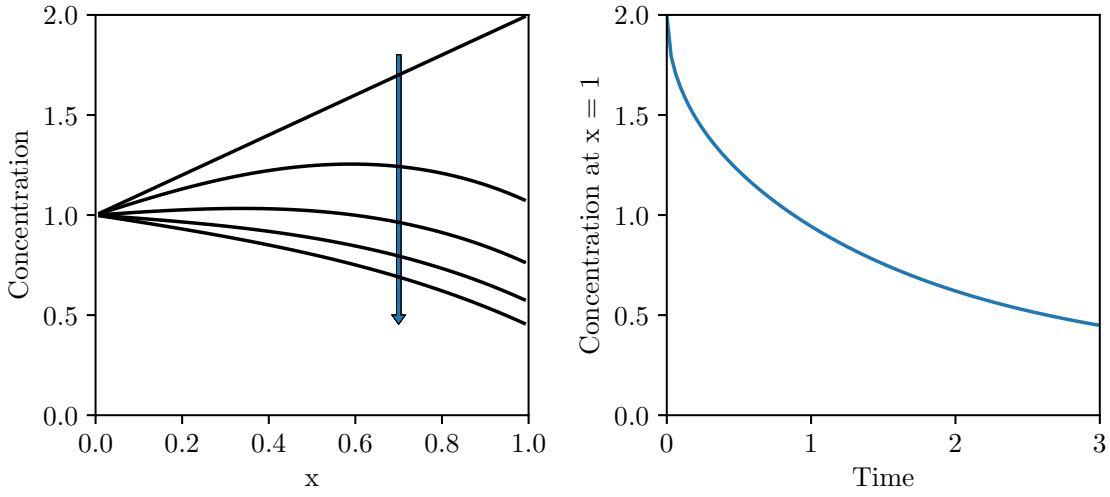

Figure A.1: Solution of the model (A.1).

calculate the Jacobian matrix from the expression tree, which is done by default by the solver. Supplying accurate Jacobian matrices to solvers is critical to speed up the solution of the DAE systems investigated in this thesis. Automatic differentiation could also be used to calculate adjoints relative to parameters in the model, and hence greatly enhance the efficiency of parameter estimation and optimisation algorithms. For example, as shown in Section 3.4.4, standard derivative-based parameter fitting algorithms are prone to failure when applied to numerical solutions of complex models, since the Jacobian matrices obtained with finite differences are inaccurate due to inherent noise in the numerical simulation. Providing the Jacobian explicitly would help to circumvent this problem.

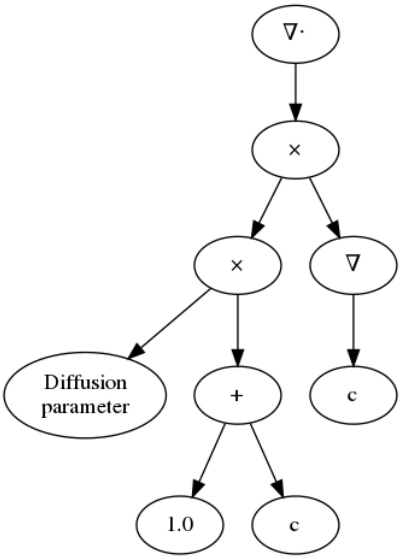

(a) Initial model.

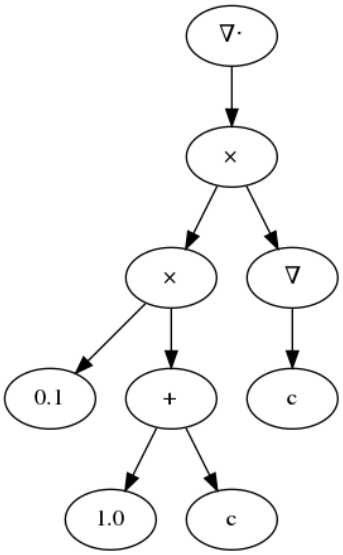

(b) Parametrised model.

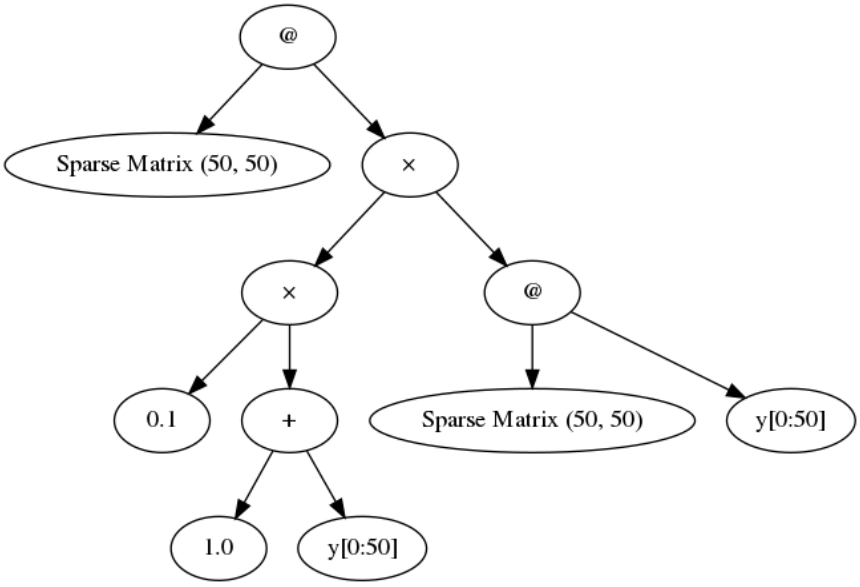

(c) Discretised model.

Figure A.2: Representative model (A.1), defined in Listing A.1, at various stages in the PyBaMM pipeline.

Appendix B

Parameters

The dimensional parameters are given in Table B.1, and the concentration-dependence of coefficients in Table B.2. The formulae for open-circuit potentials are obtained empirically by Bode [13]. Note that these could be written as

$$\hat{U}_{\mathrm{n}}^{\mathrm{S}}\left(\hat{c}_{\mathrm{e}}\right) = U_{\mathrm{n}}^{\mathrm{S},\ominus} + \frac{RT}{F} U_{\mathrm{n}}^{\mathrm{S}}(c), \tag{B.1a}$$

$$\hat{U}_{\mathrm{p}}^{\mathrm{S}}\left(\hat{c}_{\mathrm{e}}\right) = U_{\mathrm{p}}^{\mathrm{S},\ominus} + \frac{RT}{F} U_{\mathrm{p}}^{\mathrm{S}}(c), \tag{B.1b}$$

to reflect their relation to the Nernst equation (e.g. [126]), with $U_{\mathrm{n}}^{\mathrm{S},\ominus} = -0.295$ and $U_{\mathrm{p}}^{\mathrm{S},\ominus} = 1.628$.

Consistent initial conditions For consistent initial conditions, we would like starting at $x\%$ SoC to be equivalent to having started with a full battery and then discharged the battery uniformly (i.e. at a very low C-rate) and without side reactions (j^S being the only non-zero interfacial current density) until it is at $x\%$ SoC. We now choose initial conditions for c_{e}, ε and $\mathcal{U}$ so that this holds. During this period of uniform discharge, assuming that capacitance effects are negligible, we can integrate (2.65i) and apply the Divergence Theorem and boundary conditions (2.66) to find that j^{S} is given by

$$j^{\mathrm{S}} = \begin{cases} \mathcal{I}/\ell_{\mathrm{n}}, & 0 < x < \ell_{\mathrm{n}}, \\ 0, & \ell_{\mathrm{n}} < x < 1 - \ell_{\mathrm{p}}, \\ -\mathcal{I}/\ell_{\mathrm{p}}, & 1 - \ell_{\mathrm{p}} < x < 1. \end{cases} \tag{B.2}$$

Nondimensionalising time and current in (2.35), we obtain

$$q = q^0 - \frac{1}{\mathcal{Q}_{\mathrm{e}}^{\max}} \int_0^t \mathcal{I}(s)\,\mathrm{d}s, \tag{B.3}$$

where $\mathcal{Q}_{\mathrm{e}}^{\max} = \hat{\mathcal{Q}}_{\mathrm{e}}^{\max}/c_{\mathrm{e}}^{\max}F$. Inverting (B.3) gives the time-integral of current in terms of the SoC, q:

$$\int_0^t \mathcal{I}(s)\,\mathrm{d}s = \mathcal{Q}_{\mathrm{e}}^{\max}\left(q^0 - q\right). \tag{B.4}$$

Now, integrating (2.65a) (for $k = \mathrm{e}$) in x across the whole cell and using the no-flux conditions (2.26), the relationship (B.2), and (B.4) with $q^0 = 1$,

$$\frac{1}{A_{\mathrm{cs}}}\int_0^H\int_0^W\int_0^{\ell_{\mathrm{n}}} \varepsilon c_{\mathrm{e}}\,\mathrm{d}x\,\mathrm{d}y\,\mathrm{d}z = \left(\ell_{\mathrm{n}}\varepsilon_{\mathrm{n}}^{\max} + \ell_{\mathrm{s}}\varepsilon_{\mathrm{s}}^{\max} + \ell_{\mathrm{p}}\varepsilon_{\mathrm{p}}^{\max}\right) + (s_{\mathrm{n}} - s_{\mathrm{p}})\mathcal{Q}_{\mathrm{e}}^{\max}(1-q). \tag{B.5}$$

Both sides of (B.5) should be zero when $q = 0$; hence we choose

$$\mathcal{Q}_{\mathrm{e}}^{\max} = \frac{\ell_{\mathrm{n}}\varepsilon_{\mathrm{n}}^{\max} + \ell_{\mathrm{s}}\varepsilon_{\mathrm{s}}^{\max} + \ell_{\mathrm{p}}\varepsilon_{\mathrm{p}}^{\max}}{s_{\mathrm{p}} - s_{\mathrm{n}}}, \tag{B.6}$$

which, with the parameter values in Table B.1, gives a dimensional maximum capacity of 22.4 Ah for the whole battery (eight cells in parallel with a capacity of 2.82 Ah each). This compares favourably to the stated battery capacity of 17 Ah.

Now, integrating (2.56) in x across the whole negative electrode and using (B.2) and the SoC-current relationship (B.4),

$$\frac{1}{A_{\mathrm{cs}}}\int_0^H\int_0^W\int_0^{\ell_{\mathrm{n}}} \varepsilon_{\mathrm{n}}\,\mathrm{d}x\,\mathrm{d}y\,\mathrm{d}z = \ell_{\mathrm{n}}\varepsilon_{\mathrm{n}}^{\max} - \beta_{\mathrm{n}}^{\mathrm{surf}}\mathcal{Q}_{\mathrm{e}}^{\max}(1-q). \tag{B.7}$$

Hence, assuming that $\varepsilon_{\mathrm{n}}^0$ is spatially uniform,

$$\varepsilon_{\mathrm{n}}^0 = \varepsilon_{\mathrm{n}}^{\max} - \frac{\beta_{\mathrm{n}}^{\mathrm{surf}}\mathcal{Q}_{\mathrm{e}}^{\max}(1-q^0)}{\ell_{\mathrm{n}}}. \tag{B.8}$$

Similarly,

$$\varepsilon_{\mathrm{p}}^0 = \varepsilon_{\mathrm{p}}^{\max} + \frac{\beta_{\mathrm{p}}^{\mathrm{surf}}\mathcal{Q}_{\mathrm{e}}^{\max}(1-q^0)}{\ell_{\mathrm{p}}}. \tag{B.9}$$

A similar analysis gives a consistent initial electrode utilisation. Integrating (2.61) in x across the whole negative electrode and using (B.2) and the SoC-current relationship (B.4),

$$\frac{1}{A_{\mathrm{cs}}}\int_0^H\int_0^W\int_0^{\ell_{\mathrm{n}}} \mathcal{U}_{\mathrm{n}}\,\mathrm{d}x\,\mathrm{d}y\,\mathrm{d}z = \frac{\mathcal{Q}_{\mathrm{e}}^{\max}(1-q)}{\mathcal{Q}_{\mathrm{n}}^{\max}}. \tag{B.10}$$

Hence, assuming that $\mathcal{U}_{\mathrm{n}}^0$ is spatially uniform,

$$\mathcal{U}_{\mathrm{n}}^0 = \frac{\mathcal{Q}_{\mathrm{e}}^{\max}(1-q^0)}{\mathcal{Q}_{\mathrm{n}}^{\max}\ell_{\mathrm{n}}}, \tag{B.11}$$

and similarly

$$\mathcal{U}_{\mathrm{p}}^0 = \frac{\mathcal{Q}_{\mathrm{e}}^{\max}(1-q^0)}{\mathcal{Q}_{\mathrm{p}}^{\max}\ell_{\mathrm{p}}}. \tag{B.12}$$

Parameter [units]	Value			Reference
	n	sep	p	
$\hat{\ell}$ [m]	0.9×10^{-3}	1.5×10^{-3}	1.25×10^{-3}	Private communication
$\varepsilon^{\max}$ [-]	0.53	0.92	0.57	[115]
$\hat{H}$ [m]		11.4×10^{-2}		Measured
$\hat{W}$ [m]		6.5×10^{-2}		Measured
$\bar{V}_+$ [m^3/mol]		1.35×10^{-5}		[14]
$\bar{V}_-$ [m^3/mol]		3.15×10^{-5}		[14]
$\bar{V}_{\mathrm{w}}$ [m^3/mol]		1.75×10^{-5}		[6]
$\bar{V}_{\mathrm{o}}$ [m^3/mol]		3.21×10^{-5}		[132]
$\bar{V}_{\mathrm{Pb}}$ [m^3/mol]		1.83×10^{-5}		[69]
$\bar{V}_{\mathrm{PbO_2}}$ [m^3/mol]		2.55×10^{-5}		[69]
$\bar{V}_{\mathrm{PbSO_4}}$ [m^3/mol]		4.82×10^{-5}		[69]
M_{w} [kg/mol]		1.8×10^{-2}		[69]
M_+ [kg/mol]		0.1×10^{-2}		[69]
M_- [kg/mol]		9.7×10^{-2}		[69]
M_{o} [kg/mol]		3.2×10^{-2}		[69]
T [K]		298.15		Room temperature
t_+^{w} [-]		0.72		[22, 47]
$\hat{\sigma}$ [S/m]	4.8×10^{6}	-	8×10^{3}	[48]
$\hat{j}_0^{\mathrm{S,ref}}$ [A/m^3]	4.96×10^{-2}	-	4×10^{-3}	[115]
$\hat{j}_0^{\mathrm{O,ref}}$ [A/m^3]	2.5×10^{-32}	-	2.5×10^{-23}	[115]
$\hat{j}_0^{\mathrm{H,ref}}$ [A/m^3]	1.56×10^{-11}	-	0	[115]
$\mathcal{A}$ [m^2/m^3]	2.3×10^{6}	-	2.3×10^{7}	[122] (reported by [48])
d [m]	10^{-7}	10^{-6}	10^{-7}	[48], [64]
$\hat{C}^{\mathrm{dl}}$ [F/m^2]	0.2	-	0.2	[115]
q^0 [-]		1		Full initial SOC
Q [Ah]		17		Manufacturer-specified
α^{S} [-]	0.775	-	0.605	[115]
α^{O} [-]	0.5	-	0.5	[115]
γ^{S} [-]	0	-	0.3	[115]
γ^{O} [-]	1	-	2	[115]
δ^{O} [-]	1	-	0.5	[115]
$\hat{\mathcal{Q}}^{\max}$ [C/m^3]	3.473×10^{9}	-	2.745×10^{9}	[6]
$c_{\mathrm{e}}^{\max}$ [mol/m^3]		5.6×10^{3}		Private communication
$c_{\mathrm{o}}^{\mathrm{ref}}$ [mol/m^3]		1.0×10^{3}		[115]

Table B.1: Dimensional parameters from the literature. Parameters with several values indicate different values in negative electrode (n), separator (s) and positive electrode (p).

Function [units]	Formula	Value at $\hat{c}_\mathrm{e} = c_\mathrm{e}^\mathrm{max}$	Reference
$\hat{D}_\mathrm{e}$ [m^2/s]	$(1.75 + 2.6 \times 10^{-4}\hat{c}_\mathrm{e}) \times 10^{-9}$	3.02×10^{-9}	(†)
$\hat{D}_\mathrm{o}$ [m^2/s]	2.1×10^{-9}	2.1×10^{-9}	[29]
$\hat{\chi}$ [-]	$0.49 + 4.1 \times 10^{-4}\hat{c}_\mathrm{e}$	2.8	[22, 94] (*)
$\hat{\kappa}$ [S/m]	$\hat{c}_\mathrm{e} \exp(6.23 - 1.34 \times 10^{-4}\hat{c}_\mathrm{e} - 1.61 \times 10^{-8}\hat{c}_\mathrm{e}^2) \times 10^{-4}$	77	(†)
$\hat{\mu}$ [Pa s]	$0.89 \times 10^{-3} + 1.11 \times 10^{-7}\hat{c}_\mathrm{e} + 3.29 \times 10^{-11}\hat{c}_\mathrm{e}^2$	2.5×10^{-3}	[22] (*)
$\hat{U}_\mathrm{n}^\mathrm{S}$ [V]	$-0.295 - 0.074 \log m - 0.030 \log^2 m$ $-0.031 \log^3 m - 0.012 \log^4 m$ (‡)	-0.41	[13]
$\hat{U}_\mathrm{p}^\mathrm{S}$ [V]	$1.628 + 0.074 \log m + 0.033 \log^2 m$ $+0.043 \log^3 m + 0.022 \log^4 m$ (‡)	1.76	[13]
$\hat{U}^\mathrm{O}$ [V]	1.229	1.229	[115]

Table B.2: Dimensional functions of concentration, $\hat{c}_\mathrm{e}$ (measured in mol/m^3) and $\hat{\varepsilon}$ (dimensionless). (†) Empirical formulae are given by [48], citing [122], and agree with data of [22]. (*) Our fit to data of given reference(s). (‡) $m\,(\hat{c}_\mathrm{e}) = \hat{c}_\mathrm{e}\bar{V}_\mathrm{w}/[(1-\hat{c}_\mathrm{e}\bar{V}_\mathrm{e})M_\mathrm{w}]$.

Function	[6]	[88]	[49]	[115]
$\hat{j}_{0\mathrm{a}}^\mathrm{S} \Big/ \hat{j}_0^\mathrm{S,ref}$ $\hat{j}_{0\mathrm{c}}^\mathrm{S} \Big/ \hat{j}_0^\mathrm{S,ref}$	$\left(\frac{\hat{c}_\mathrm{e}}{c_\mathrm{e}^\mathrm{ref}}\right)^{\gamma^\mathrm{S}}$			
$\hat{j}_{0\mathrm{a}}^\mathrm{O} \Big/ \hat{j}_0^\mathrm{O,ref}$	$\left(\frac{\hat{c}_\mathrm{e}}{c_\mathrm{e}^\mathrm{ref}}\right)^{\gamma^\mathrm{O}} \left(\frac{\hat{p}_\mathrm{o}}{p_\mathrm{o}^\mathrm{ref}}\right)^{\delta^\mathrm{O}}$		$\left(\frac{\hat{c}_\mathrm{e}}{c_\mathrm{e}^\mathrm{ref}}\right)^{\gamma^\mathrm{O}}$	
$\hat{j}_{0\mathrm{c}}^\mathrm{O} \Big/ \hat{j}_0^\mathrm{O,ref}$	$\left(\frac{\hat{c}_\mathrm{e}}{c_\mathrm{e}^\mathrm{ref}}\right)^{\gamma^\mathrm{O}} \left(\frac{\hat{p}_\mathrm{o}}{p_\mathrm{o}^\mathrm{ref}}\right)^{\delta^\mathrm{O}}$		$\left(\frac{\hat{c}_\mathrm{e}}{c_\mathrm{e}^\mathrm{ref}}\right)^{\gamma^\mathrm{O}} \left(\frac{\hat{c}_\mathrm{o}}{c_\mathrm{o}^\mathrm{ref}}\right)^{\delta^\mathrm{O}}$	

Table B.3: Summary of functions relating to the interfacial reactions (1.1) and (1.2). All exchange-current densities $\hat{j}$ have units A/m^2. Oxygen pressure, $\hat{p}_\mathrm{o}$, is a function of oxygen concentration, $\hat{c}_\mathrm{o}$. Exponents are left in general form here for qualitative comparison, and given in Table B.1 where available.

Appendix C

Homogenisation

We follow the method presented by Richardson et al. [100] to systematically derive a macroscale, averaged, model based on the microscale model

$$k\frac{\partial f}{\partial t} + \nabla \cdot \mathbf{q} = 0 \qquad \text{in } \tilde{\Omega}_\mathrm{e}, \tag{C.1a}$$

$$\mathbf{q} = -D\nabla f \qquad \text{in } \tilde{\Omega}_\mathrm{e}, \tag{C.1b}$$

$$\mathbf{q}\cdot\mathbf{n} = \delta_\mathrm{p}\left(k\beta^\mathrm{surf} f + Q\right) j \qquad \text{on } \partial\tilde{\Omega}. \tag{C.1c}$$

The results of [100] are augmented by considering a moving interface $\partial\tilde{\Omega}$, with the interface velocity proportional to β^surf. We begin by introducing a microscale variable,

$$\mathbf{x} = \delta_\mathrm{p}\tilde{\mathbf{x}}, \tag{C.2}$$

where $\tilde{\mathbf{x}}$ is the microscale variable and $\mathbf{x}$ is the macroscale variable, and look for a solution which is a function of both $\tilde{\mathbf{x}}$ and $\mathbf{x}$, and periodic in $\tilde{\mathbf{x}}$ for uniqueness. Then the gradient operator transforms according to $\nabla \to \nabla + \tilde{\nabla}/\delta_\mathrm{p}$, and the ansatz for the expansions of the variables is

$$f = f^{(0)}(\tilde{\mathbf{x}},\mathbf{x},t) + \delta_\mathrm{p} f^{(1)}(\tilde{\mathbf{x}},\mathbf{x},t) + \delta_\mathrm{p}^2 f^{(2)}(\tilde{\mathbf{x}},\mathbf{x},t) + \ldots, \tag{C.3}$$

$$\mathbf{q} = \mathbf{q}^{(0)}(\tilde{\mathbf{x}},\mathbf{x},t) + \delta_\mathrm{p}\mathbf{q}^{(1)}(\tilde{\mathbf{x}},\mathbf{x},t) + \delta_\mathrm{p}^2\mathbf{q}^{(2)}(\tilde{\mathbf{x}},\mathbf{x},t) + \ldots, \tag{C.4}$$

$$j = j^{(0)}(\tilde{\mathbf{x}},\mathbf{x},t) + \delta_\mathrm{p} j^{(1)}(\tilde{\mathbf{x}},\mathbf{x},t) + \delta_\mathrm{p}^2 j^{(2)}(\tilde{\mathbf{x}},\mathbf{x},t) + \ldots. \tag{C.5}$$

We define the interface $\partial\tilde{\Omega}$ by the zero level set of the function θ, i.e. $\theta(\tilde{\mathbf{x}},\mathbf{x},t) = 0$. Further, we define θ so that $\mathbf{n}$, the outward unit normal to $\tilde{\Omega}_\mathrm{s}$ into $\tilde{\Omega}_\mathrm{e}$, is given by

$$\mathbf{n} = -\frac{\tilde{\nabla}\theta + \delta_\mathrm{p}\nabla\theta}{|\tilde{\nabla}\theta + \delta_\mathrm{p}\nabla\theta|}. \tag{C.6}$$

From [100] we have the identities

$$\frac{\partial}{\partial x_i}\int_{\tilde{\Omega}_\mathrm{e}} f(\tilde{\mathbf{x}},\mathbf{x},t)\,\mathrm{d}\tilde{V} \sim \int_{\tilde{\Omega}_\mathrm{e}} \frac{\partial f}{\partial x_i}\,\mathrm{d}\tilde{V} - \int_{\partial\tilde{\Omega}} \frac{f}{|\tilde{\nabla}\theta|}\frac{\partial\theta}{\partial x_i}\,\mathrm{d}\tilde{S}, \tag{C.7a}$$

$$\nabla\cdot\int_{\tilde{\Omega}_\mathrm{e}} \mathbf{q}(\tilde{\mathbf{x}},\mathbf{x},t)\,\mathrm{d}\tilde{V} \sim \int_{\tilde{\Omega}_\mathrm{e}} \nabla\cdot\mathbf{q}\,\mathrm{d}\tilde{V} - \int_{\partial\tilde{\Omega}} \frac{\mathbf{q}\cdot\nabla\theta}{|\tilde{\nabla}\theta|}\,\mathrm{d}\tilde{S}. \tag{C.7b}$$

The identities (C.7) are valid to leading order in δ_p. We can also derive the Reynolds Transport Theorem [65] in dimensionless form,

$$\frac{\partial}{\partial t}\int_{\tilde{\Omega}_\mathrm{e}} f(\tilde{\mathbf{x}},\mathbf{x},t)\,\mathrm{d}V = \int_{\tilde{\Omega}_\mathrm{e}} \frac{\partial f}{\partial t}\,\mathrm{d}V - \int_{\partial\tilde{\Omega}} \beta^{\mathrm{surf}} j f\,\mathrm{d}S, \tag{C.8}$$

where f may be a scalar or a vector and β^{surf} is the dimensionless surface velocity in the normal direction. The sign of the second term on the right-hand side is a minus sign, since here $\mathbf{n}$ is the unit *inward* normal to $\tilde{\Omega}_\mathrm{e}$.

Performing the multiple-scales expansion for the gradient operator, (C.1a) and (C.1b) become

$$k\frac{\partial f}{\partial t} + \left(\frac{1}{\delta_\mathrm{p}}\tilde{\nabla}\cdot\mathbf{q} + \nabla\cdot\mathbf{q}\right) = 0, \tag{C.9a}$$

$$\mathbf{q} = -D\left(\frac{1}{\delta_\mathrm{p}}\tilde{\nabla}f + \nabla f\right). \tag{C.9b}$$

The interface condition for (C.9) is

$$\mathbf{q}\cdot\mathbf{n} = \delta_\mathrm{p}\left(k\beta^{\mathrm{surf}} f + Q\right) j, \quad \text{at } \partial\tilde{\Omega}, \tag{C.10}$$

and f, $\mathbf{q}$ and Q are periodic in $\tilde{\Omega}_\mathrm{e}$. After expanding variables in powers of δ_p, as per (C.3), the $\mathcal{O}(1)$ problem for the material balance equation (C.9a) is

$$\tilde{\nabla}\cdot\mathbf{q}^{(0)} = 0, \quad \mathbf{q}^{(0)}\cdot\mathbf{n}\big|_{\partial\tilde{\Omega}} = 0, \quad \mathbf{q}^{(0)} \text{ periodic on } \tilde{\Omega}_\mathrm{e}, \tag{C.11}$$

and the $\mathcal{O}(\delta_\mathrm{p})$ problem is

$$k\frac{\partial f^{(0)}}{\partial t} + \left(\tilde{\nabla}\cdot\mathbf{q}^{(1)} + \nabla\cdot\mathbf{q}^{(0)}\right) = 0, \quad \mathbf{q}^{(1)} \text{ periodic in } \tilde{\Omega}_\mathrm{e}, \tag{C.12a}$$

$$\mathbf{q}^{(1)}\cdot\mathbf{n}\big|_{\partial\tilde{\Omega}} = \delta_\mathrm{p}\left(k\beta^{\mathrm{surf}} f^{(0)} + Q\right) j^{(0)}. \tag{C.12b}$$

For the flux law (C.9b), the $\mathcal{O}(1)$ problem is

$$\tilde{\nabla} f^{(0)} = 0, \tag{C.13a}$$

and the $\mathcal{O}(\delta_{\mathrm{p}})$ problem is

$$\mathbf{q}^{(0)} = -D^{(0)}\left(\tilde{\nabla} f^{(1)} + \nabla f^{(0)}\right), \tag{C.13b}$$

where $D^{(0)} = D(f^{(0)})$.

Rewriting the boundary condition (C.12b) in terms of the surface function $\theta(\tilde{\mathbf{x}}, \mathbf{x})$ gives

$$\mathbf{q}^{(1)} \cdot \tilde{\nabla}\theta + \mathbf{q}^{(0)} \cdot \nabla\theta = -|\tilde{\nabla}\theta|\left(k\beta^{\mathrm{surf}} f^{(0)} + Q\right) j^{(0)}. \tag{C.14}$$

Integrating (C.12a) over $\tilde{\Omega}_{\mathrm{e}}$ and using the Divergence Theorem and the fact that the outward unit normal to $\tilde{\Omega}_{\mathrm{e}}$ is $-\mathbf{n}$, and so to leading order in δ_{p} is $\tilde{\nabla}\theta/|\tilde{\nabla}\theta|$ (by (C.6)), gives

$$\int_{\tilde{\Omega}_{\mathrm{e}}} k\frac{\partial f^{(0)}}{\partial t} + \nabla \cdot \mathbf{q}^{(0)}\,\mathrm{d}V + \int_{\partial\tilde{\Omega}} \mathbf{q}^{(1)} \cdot \frac{\tilde{\nabla}\theta}{|\tilde{\nabla}\theta|}\,\mathrm{d}S = 0. \tag{C.15}$$

Substituting the boundary condition in the form (C.14), (C.15) becomes

$$\int_{\tilde{\Omega}_{\mathrm{e}}} k\frac{\partial f^{(0)}}{\partial t} + \nabla \cdot \mathbf{q}^{(0)}\,\mathrm{d}V - \int_{\partial\tilde{\Omega}} \mathbf{q}^{(0)} \cdot \frac{\nabla\theta}{|\tilde{\nabla}\theta|}\,\mathrm{d}S = \int_{\partial\tilde{\Omega}} \left(k\beta^{\mathrm{surf}} f^{(0)} + Q\right) j^{(0)}\,\mathrm{d}S. \tag{C.16}$$

Applying the identity (C.7b) gives

$$\int_{\tilde{\Omega}_{\mathrm{e}}} k\frac{\partial f^{(0)}}{\partial t}\,\mathrm{d}V + \nabla \cdot \int_{\tilde{\Omega}_{\mathrm{e}}} \mathbf{q}^{(0)}\,\mathrm{d}V = \int_{\partial\tilde{\Omega}} \left(k\beta^{\mathrm{surf}} f^{(0)} + Q\right) j^{(0)}\,\mathrm{d}S. \tag{C.17}$$

Finally, we apply the Reynolds Transport Theorem (C.8). Then (C.17) becomes

$$k\frac{\partial}{\partial t}\int_{\tilde{\Omega}_{\mathrm{e}}} f^{(0)}\,\mathrm{d}V + \nabla \cdot \int_{\tilde{\Omega}_{\mathrm{e}}} \mathbf{q}^{(0)}\,\mathrm{d}V = Q\int_{\partial\tilde{\Omega}} j^{(0)}\,\mathrm{d}S. \tag{C.18}$$

Since $f^{(0)}$ is independent of the microscale, and assuming that $j^{(0)}$ is also independent of the microscale, we can write this as

$$k\frac{\partial}{\partial t}(\varepsilon f^{(0)}) = -\nabla \cdot \left\langle \mathbf{q}^{(0)} \right\rangle_V + Qaj^{(0)}, \tag{C.19}$$

where we have defined the liquid average, $\langle\cdot\rangle_V$, porosity, ε, and reactive surface area per unit volume, a, as

$$\langle\cdot\rangle_V = \frac{1}{|V|}\int_{\tilde{\Omega}_{\mathrm{e}}} \cdot\,\mathrm{d}V, \quad \varepsilon(\mathbf{x}, t) = \langle 1\rangle_V \quad \text{and} \quad a(\mathbf{x}, t) = \int_{\partial\tilde{\Omega}} 1\,\mathrm{d}S, \tag{C.20}$$

where $|V| = \int_{\tilde{\Omega}_\mathrm{e}} 1 \, \mathrm{d}V + \int_{\tilde{\Omega}_\mathrm{s}} 1 \, \mathrm{d}V$ is assumed to be constant. The porosity and reactive surface area per unit volume can vary over the macroscale $\mathbf{x}$, or with time t, as $\tilde{\Omega}_\mathrm{e}$ and $\partial\tilde{\Omega}$ vary.

The next step is to investigate the expansion of the flux $\mathbf{q}^{(0)}$. Substituting the first-order problem, (C.13b), into (C.11) gives

$$0 = \tilde{\nabla} \cdot \left(-D^{(0)} \left[\tilde{\nabla} f^{(1)} + \nabla f^{(0)} \right] \right). \tag{C.21}$$

The leading-order diffusivity, $D^{(0)}$, is independent of the microscale, by (C.13a), as it is a function of $f^{(0)}$ only. Hence (C.21) becomes

$$\tilde{\nabla}^2 f^{(1)} = 0. \tag{C.22}$$

Substituting (C.13b) into the boundary condition (C.11) gives

$$\mathbf{n} \cdot \tilde{\nabla} f^{(1)} \Big|_{\partial\tilde{\Omega}} = - \, \mathbf{n} \cdot \nabla f^{(0)} \big|_{\partial\tilde{\Omega}} \, . \tag{C.23}$$

Since $\mathbf{q}^{(0)}$ and $f^{(0)}$ are periodic on $\tilde{\Omega}_\mathrm{e}$, $f^{(1)}$ must also be periodic on $\tilde{\Omega}_\mathrm{e}$.

We make use of the linearity of (C.23) to write its solution in the form

$$f^{(1)} = -B_j(\tilde{\mathbf{x}}, \mathbf{x}) \frac{\partial f^{(0)}}{\partial x_j}, \tag{C.24}$$

where B_j are independent and satisfy

$$\tilde{\nabla}^2 B_j = 0 \qquad \text{in } \tilde{\Omega}_\mathrm{e}, \tag{C.25a}$$

$$\tilde{\nabla} B_j \cdot \mathbf{n} = \mathbf{e}_j \cdot \mathbf{n} \qquad \text{on } \partial\tilde{\Omega}, \tag{C.25b}$$

$$B_j \text{ periodic in } \tilde{\mathbf{x}} \qquad \text{in } \tilde{\Omega}_\mathrm{e}, \tag{C.25c}$$

$$\int_{\tilde{\Omega}_\mathrm{e}} B_j \, \mathrm{d}V = 0, \tag{C.25d}$$

for $i = 1, 2, 3$. Substituting $f^{(1)}$, from (C.24) back into (C.13b), we have

$$\mathbf{q}^{(0)} = -D^{(0)} \left(\delta_{ij} - \frac{\partial B_j}{\partial \tilde{x}_i} \right) \frac{\partial f^{(0)}}{\partial x_j}. \tag{C.26}$$

Finally, we integrate (C.26) over $\tilde{\Omega}_\mathrm{e}$ to find

$$\left\langle \mathbf{q}^{(0)} \right\rangle_V = -D^{(0)} \mathcal{B} \cdot \nabla f^{(0)}, \tag{C.27}$$

where $\mathcal{B}$ is the diffusivity tensor, defined by

$$\mathcal{B}_{ij} = \left\langle \delta_{ij} - \frac{\partial B_j}{\partial \tilde{x}_i} \right\rangle_V . \tag{C.28}$$

In summary, the microscale system (C.1) is homogenised to (C.19) and (C.27). In this thesis, we implicitly consider only integrated leading-order terms, and drop the superscript (0) and brackets $\langle\rangle_V$.

When homogenising the equations in the electrodes, we switch the sign of the unit normal in the derivation, and introduce the solid average, porosity and diffusivity tensor:

$$\langle\cdot\rangle_\Omega = \frac{1}{|V|}\int_{\tilde{\Omega}_\mathrm{s}} \cdot \,\mathrm{d}V, \quad \varepsilon_\mathrm{s} = \langle 1\rangle_\Omega \quad \text{and} \quad \mathcal{B}_{\mathrm{s},ij} = \left\langle \delta_{ij} - \frac{\partial B_{\mathrm{s},j}}{\partial \tilde{x}_i} \right\rangle_\Omega, \tag{C.29}$$

where B_s satisfies the same cell problem as in (C.25a) but in $\tilde{\Omega}_\mathrm{s}$ instead of $\tilde{\Omega}_\mathrm{e}$.

Appendix D

Transient one-dimensional solution

In this appendix, we consider the model introduced in Section 3.3.4 for the transient response following jumps in the applied current.

Denoting the time of the jump by t^*, we rescale time with $\tau = (t - t^*)/\mathcal{C}_\mathrm{e}$. Then (3.12) becomes

$$\frac{\partial}{\partial \tau}\left(\varepsilon c_k\right) + \mathcal{C}_\mathrm{e}\left(\frac{\partial}{\partial x}\left(c_k v^{\square}\right) + c_k V_z^{\square}\right) = \mathcal{D}_k \frac{\partial}{\partial x}\left(D_k^{\mathrm{eff}} \frac{\partial c_k}{\partial x}\right) - \mathcal{C}_\mathrm{e} \sum_{r \in \mathcal{R}} s_k^r j^r, \tag{D.1a}$$

$$\frac{\partial \varepsilon}{\partial \tau} = -\mathcal{C}_\mathrm{e} \beta^{\mathrm{surf}} j^{\mathrm{S}}, \tag{D.1b}$$

$$\mathcal{C}_\mathrm{e}\, i_\mathrm{e} = \kappa^{\mathrm{eff}}\left(\chi_\mathrm{e} \frac{\partial \ln\left(c_\mathrm{e}\right)}{\partial x} - \frac{\partial \Phi_\mathrm{e}}{\partial x}\right), \tag{D.1c}$$

$$\frac{\partial v^{\square}}{\partial x} = \sum_{r \in \mathcal{R}} \beta^r j^r - V_z^{\square}, \tag{D.1d}$$

$$\frac{\partial \phi}{\partial \tau} = \frac{\mathcal{C}_\mathrm{e}}{C^{\mathrm{dl}}}\left(\frac{\partial i_\mathrm{e}}{\partial x} - \sum_{r \in \mathcal{R}} j^r\right), \tag{D.1e}$$

$$j^r = j^r\left(\{c_k\}, \phi\right). \tag{D.1f}$$

We now expand the variables in powers of $\mathcal{C}_\mathrm{e}$, as done in (3.13). Then (D.1) becomes,

to leading order in $\mathcal{C}_\mathrm{e}$,

$$\frac{\partial}{\partial\tau}\left(\varepsilon^{(0)}c_k^{(0)}\right) = \frac{\partial}{\partial x}\left(D_k^{\mathrm{eff},(0)}\frac{\partial c_k^{(0)}}{\partial x}\right), \tag{D.2a}$$

$$\frac{\partial\varepsilon^{(0)}}{\partial\tau} = 0, \tag{D.2b}$$

$$0 = \chi_\mathrm{e}^{(0)}\frac{\partial\ln\left(c_\mathrm{e}^{(0)}\right)}{\partial x} - \frac{\partial\Phi_\mathrm{e}^{(0)}}{\partial x}, \tag{D.2c}$$

$$\frac{\partial v^{\square,(0)}}{\partial x} = \sum_{r\in\mathcal{R}}\beta^r j^{r,(0)} - V_z^{\square,(0)}, \tag{D.2d}$$

$$\frac{\partial\phi^{(0)}}{\partial\tau} = \frac{\mathcal{C}_\mathrm{e}}{C^\mathrm{dl}}\left(\frac{\partial i_\mathrm{e}^{(0)}}{\partial x} - \sum_{r\in\mathcal{R}} j^{r,(0)}\right), \tag{D.2e}$$

$$j^{r,(0)} = j^r\left(\{c_k^{(0)}\},\phi^{(0)}\right), \tag{D.2f}$$

and to first order in $\mathcal{C}_\mathrm{e}$,

$$\begin{aligned}\frac{\partial}{\partial\tau}\left(\varepsilon^{(0)}c_k^{(1)}\right) = \mathcal{D}_k\frac{\partial}{\partial x}\left(D_k^{\mathrm{eff},(0)}\frac{\partial c_k^{(1)}}{\partial x}\right) - c_k^{(0)}\left(\frac{\partial v^{\square,(0)}}{\partial x} + V_z^{\square,(0)}\right)\\ - \sum_{r\in\mathcal{R}} s_k^r j^{r,(0)} - \frac{\partial}{\partial\tau}\left(\varepsilon^{(1)}c_k^{(0)}\right),\end{aligned} \tag{D.3a}$$

$$\frac{\partial\varepsilon^{(1)}}{\partial\tau} = -\beta^\mathrm{surf}j^{\mathrm{S},(0)}, \tag{D.3b}$$

$$i_\mathrm{e}^{(0)} = \kappa^{\mathrm{eff},(0)}\left(\frac{\chi_\mathrm{e}^{(0)}}{c_\mathrm{e}^{(0)}}\frac{\partial c_\mathrm{e}^{(1)}}{\partial x} - \frac{\partial\Phi_\mathrm{e}^{(1)}}{\partial x}\right), \tag{D.3c}$$

$$\frac{\partial v^{\square,(1)}}{\partial x} = \sum_{r\in\mathcal{R}}\beta^r j^{r,(1)} - V_z^{\square,(1)}, \tag{D.3d}$$

$$\frac{\partial\phi^{(1)}}{\partial\tau} = \frac{\mathcal{C}_\mathrm{e}}{C^\mathrm{dl}}\left(\frac{\partial i_\mathrm{e}^{(1)}}{\partial x} - \sum_{r\in\mathcal{R}} j^{r,(1)}\right), \tag{D.3e}$$

$$j^{r,(1)} = \sum_{k\in\mathcal{S}}\left(\frac{\partial j^{r,(0)}}{\partial c_k^{(0)}}c_k^{(1)}\right) + \frac{\partial j^{r,(0)}}{\partial\phi^{(0)}}\phi^{(1)}. \tag{D.3f}$$

The boundary conditions follow from (3.2) and the initial conditions are given by the states at the jump time t^*.

Equations (D.2) decouple: we first solve (D.2b) for $\varepsilon^{(0)}$then (D.2a) for $c_k^{(0)}$, then (D.2e) and (D.3f) for $\phi^{(0)}$, and (D.2c) for $\Phi_\mathrm{e}^{(0)}$. Finally, we can find $V^{(0)}$ using (2.70) and (3.11). Similarly, having found the leading-order solution, equations (D.3) decouple and can be solved in the same order as (D.2). Hence we solve (D.2) and (D.3) more easily than the full system (D.1).

However, we note that (D.2), (D.3) and the boundary conditions (3.2) imply that $\int_0^1 c_k^{(0)}\,\mathrm{d}x$ is constant, but $|c_k^{(1)}|$ grows with time. Hence the asymptotic expansion breaks down for long times since, when $\tau \sim \mathcal{O}(1/\mathcal{C}_\mathrm{e})$, $|\mathcal{C}_\mathrm{e}\, c_k^{(1)}| \sim |c_k^{(0)}|$.

Bibliography

[1] F Alavyoon et al. "Theoretical and experimental studies of free convection and stratification of electrolyte in a lead-acid cell during recharge". In: *Electrochimica Acta* 36.14 (1991), pp. 2153–2164.

[2] AB Ansari, V Esfahanian, and F Torabi. "Discharge, rest and charge simulation of lead-acid batteries using an efficient reduced order model based on proper orthogonal decomposition". In: *Applied Energy* 173 (2016), pp. 152–167.

[3] H Arunachalam, S Onori, and I Battiato. "Temperature-dependent multiscale-dynamics in lithium-ion battery electrochemical models". In: *2015 American Control Conference (ACC)*. IEEE. 2015, pp. 305–310.

[4] H Arunachalam et al. "Multiscale modeling approach to determine effective lithium-ion transport properties". In: *2017 American Control Conference (ACC)*. IEEE. 2017, pp. 92–97.

[5] B Bensmann et al. "Model simulation and analysis of proton incorporation into the positive active mass of a lead/acid battery". In: *Journal of the Electrochemical Society* 157.3 (2010), A243–A253.

[6] DM Bernardi and MK Carpenter. "A mathematical model of the oxygen-recombination lead-acid Cell". In: *Journal of The Electrochemical Society* 142.8 (1995), pp. 2631–2642.

[7] DM Bernardi, H Gu, and AY Schoene. "Two-dimensional mathematical model of a lead-acid Cell". In: *Journal of The Electrochemical Society* 140.8 (1993), pp. 2250–2258.

[8] D Berndt. "Valve-regulated lead-acid batteries". In: *Journal of Power Sources* 100.1 (2001), pp. 29–46.

[9] H Bindner et al. *Lifetime modelling of lead acid batteries*. Tech. rep. 2005.

[10] CR Birkl et al. "Degradation diagnostics for lithium ion cells". In: *Journal of Power Sources* 341 (2017), pp. 373–386.

[11] AM Bizeray, DA Howey, and CW Monroe. "Resolving a discrepancy in diffusion potentials, with a case study for li-ion batteries". In: *Journal of The Electrochemical Society* 163.8 (2016), E223–E229.

[12] AM Bizeray et al. "Lithium-ion battery thermal-electrochemical model-based state estimation using orthogonal collocation and a modified extended Kalman filter". In: *Journal of Power Sources* 296 (2015), pp. 400–412.

[13] H Bode. *Lead-acid batteries.* John Wiley and Sons, Inc., New York, NY, 1977.

[14] V Boovaragavan et al. "A mathematical model of the lead-acid battery to address the effect of corrosion". In: *Journal of The Electrochemical Society* 156.11 (2009), A854–A862.

[15] AF Bower, PR Guduru, and VA Sethuraman. "A finite strain model of stress, diffusion, plastic flow, and electrochemical reactions in a lithium-ion half-cell". In: *Journal of the Mechanics and Physics of Solids* 59.4 (2011), pp. 804–828.

[16] M Bruna and SJ Chapman. "Diffusion in spatially varying porous media". In: *SIAM Journal on Applied Mathematics* 75.4 (2015), pp. 1648–1674.

[17] D Burow et al. "Inhomogeneous degradation of graphite anodes in automotive lithium ion batteries under low-temperature pulse cycling conditions". In: *Journal of Power Sources* 307 (2016), pp. 806–814.

[18] L Cai and RE White. "An efficient electrochemical–thermal model for a lithium-ion cell by using the proper orthogonal decomposition method". In: *Journal of the Electrochemical Society* 157.11 (2010), A1188–A1195.

[19] L Cai and RE White. "Reduction of model order based on proper orthogonal decomposition for lithium-ion battery simulations". In: *Journal of The Electrochemical Society* 156.3 (2009), A154–A161.

[20] L Cai et al. "In-situ observation of inhomogeneous degradation in large format Li-ion cells by neutron diffraction". In: *Journal of Power Sources* 236 (2013), pp. 163–168.

[21] C Cartis and L Roberts. "A derivative-free Gauss-Newton method". In: *arXiv preprint arXiv:1710.11005* (2017).

[22] TW Chapman and J Newman. *Compilation of selected thermodynamic and transport properties of binary electrolytes in aqueous solution.* Tech. rep. California Univ., Berkeley. Lawrence Radiation Lab., 1968.

[23] MJ Chon et al. "Real-time measurement of stress and damage evolution during initial lithiation of crystalline silicon". In: *Physical Review Letters* 107.4 (2011), p. 045503.

[24] D-W Chung et al. "Validity of the Bruggeman relation for porous electrodes". In: *Modelling and Simulation in Materials Science and Engineering* 21.7 (2013), p. 074009.

[25] A Costa. "Permeability-porosity relationship: A reexamination of the Kozeny-Carman equation based on a fractal pore-space geometry assumption". In: *Geophysical Research Letters* 33.2 (2006).

[26] M Cugnet and BY Liaw. "Effect of discharge rate on charging a lead-acid battery simulated by mathematical model". In: *Journal of Power Sources* 196.7 (2011), pp. 3414–3419.

[27] M Cugnet et al. "A mathematical model for the simulation of new and aged automotive lead-acid batteries". In: *Journal of The Electrochemical Society* 156.12 (2009), A974–A985.

[28] B Culpin. "Thermal runaway in valve-regulated lead-acid cells and the effect of separator structure". In: *Journal of Power Sources* 133.1 (2004), pp. 79–86.

[29] EL Cussler. *Diffusion: mass transfer in fluid systems*. Cambridge University Press, 2009.

[30] MJ Daigle and CS Kulkarni. "Electrochemistry-based battery modeling for prognostics". In: (2013).

[31] LS Darken. "Diffusion, mobility and their interrelation through free energy in binary metallic systems". In: *Trans. Aime* 175.1 (1948), pp. 184–201.

[32] S Dey and B Ayalew. "Nonlinear observer designs for state-of-charge estimation of lithium-ion batteries". In: *American Control Conference (ACC), 2014*. IEEE. 2014, pp. 248–253.

[33] D Di Domenico, A Stefanopoulou, and G Fiengo. "Lithium-ion battery state of charge and critical surface charge estimation using an electrochemical model-based extended Kalman filter". In: *Journal of dynamic systems, measurement, and control* 132.6 (2010), p. 061302.

[34] V Esfahanian, AB Ansari, and F Torabi. "Simulation of lead-acid battery using model order reduction". In: *Journal of Power Sources* 279 (2015), pp. 294–305.

[35] V Esfahanian and F Torabi. "Numerical simulation of lead-acid batteries using Keller–Box method". In: *Journal of Power Sources* 158.2 (2006), pp. 949–952.

[36] V Esfahanian, F Torabi, and A Mosahebi. "An innovative computational algorithm for simulation of lead-acid batteries". In: *Journal of Power Sources* 176.1 (2008), pp. 373–380.

[37] G Fan, K Pan, and M Canova. "A comparison of model order reduction techniques for electrochemical characterization of lithium-ion batteries". In: *2015 54th IEEE Conference on Decision and Control (CDC)*. IEEE. 2015, pp. 3922–3931.

[38] JC Forman et al. "Reduction of an electrochemistry-based li-ion battery model via quasi-linearization and pade approximation". In: *Journal of the Electrochemical Society* 158.2 (2011), A93–A101.

[39] AC Fowler. *Mathematical models in the applied sciences*. Vol. 17. Cambridge University Press, 1997.

[40] KS Gandhi. "Modeling of effect of double-layer capacitance and failure of lead-acid batteries in HRPSoC application". In: *Journal of The Electrochemical Society* 164.11 (2017), E3092–E3101.

[41] KS Gandhi. "Role of electrical resistance of electrodes in modeling of discharging and charging of flooded lead-acid batteries". In: *Journal of Power Sources* 277 (2015), pp. 124–130.

[42] KS Gandhi et al. "Simplified mathematical model for effects of freezing on the low-temperature performance of the lead-acid battery". In: *Journal of the Electrochemical Society* 156.3 (2009), A238–A245.

[43] RE Gerver and JP Meyers. "Three-dimensional modeling of electrochemical performance and heat generation of lithium-ion batteries in tabbed planar configurations". In: *Journal of The Electrochemical Society* 158.7 (2011), A835–A843.

[44] P Goyal and CW Monroe. "Exploring the impedance signatures of electrochemical/mechanical transport coupling in concentrated liquid electrolytes". In: *Meeting Abstracts*. 22. The Electrochemical Society. 2017, pp. 1137–1137.

[45] P Goyal and CW Monroe. "Models to couple mechanics and electrochemical transport in solid electrolytes". In: *ECS Transactions* 75.14 (2016), pp. 659–670.

[46] P Goyal and CW Monroe. "New foundations of Newman's theory for solid electrolytes: thermodynamics and transient balances". In: *Journal of The Electrochemical Society* 164.11 (2017), E3647–E3660.

[47] H Gu, TV Nguyen, and RE White. "A mathematical model of a lead-acid cell: discharge, rest, and charge". In: *Journal of The Electrochemical Society* 134.12 (1987), pp. 2953–2960.

[48] WB Gu, C-Y Wang, and BY Liaw. "Numerical modeling of coupled electrochemical and transport processes in lead-acid batteries". In: *Journal of The Electrochemical Society* 144.6 (1997), pp. 2053–2061.

[49] WB Gu, GQ Wang, and C-Y Wang. "Modeling the overcharge process of VRLA batteries". In: *Journal of Power Sources* 108.1 (2002), pp. 174–184.

[50] Y Guo et al. "The behavior of oxygen transport in valve-regulated lead-acid batteries with absorptive glass mat separator". In: *Journal of The Electrochemical Society* 148.12 (2001), A1287–A1293.

[51] X Han et al. "Simplification of physics-based electrochemical model for lithium ion battery on electric vehicle. Part I: Diffusion simplification and single particle model". In: *Journal of Power Sources* 278 (2015), pp. 802–813.

[52] EJ Hinch. *Perturbation methods*. Cambridge University Press, 1991.

[53] AC Hindmarsh. *The PVODE and IDA algorithms*. Tech. rep. Lawrence Livermore National Lab., CA (US), 2000.

[54] AC Hindmarsh et al. "SUNDIALS: Suite of nonlinear and differential/algebraic equation solvers". In: *ACM Transactions on Mathematical Software (TOMS)* 31.3 (2005), pp. 363–396.

[55] JO Hirschfelder, CF Curtis, and RB Bird. *Molecular theory of gases and liquids*. John Wiley & Sons, 1964.

[56] COMSOL Inc. *COMSOL Multiphysics reference manual, version 5.4*. URL: `https://www.comsol.com`.

[57] A Janse Van Rensburg. "Multi-scale model of a valve-regulated lead-acid battery with electromotive force characterization to investigate irreversible sulphation". PhD thesis. North-West University (South Africa), Potchefstroom Campus, 2016.

[58] E Jones, T Oliphant, P Peterson, et al. *SciPy: Open source scientific tools for Python*. 2001–. URL: `http://www.scipy.org/`.

[59] P Kemper and D Kum. "Extended single particle model of Li-ion batteries towards high current applications". In: *Vehicle Power and Propulsion Conference (VPPC), 2013 IEEE*. IEEE. 2013, pp. 1–6.

[60] G-H Kim et al. "Multi-domain modeling of lithium-ion batteries encompassing multi-physics in varied length scales". In: *Journal of The Electrochemical Society* 158.8 (2011), A955–A969.

[61] SU Kim and CW Monroe. "Increasing the rate capability of batteries with electrolyte flow". In: *Applied energy* 103 (2013), pp. 207–211.

[62] MC Knauff. "Kalman filter based State of Charge estimation for valve regulated lead acid batteries in wind power smoothing applications". PhD thesis. Drexel University, 2013.

[63] S Kosch et al. "A computationally efficient multi-scale model for lithium-ion cells". In: *Journal of The Electrochemical Society* 165.10 (2018), A2374–A2388.

[64] A Krishnamoorthy and DR Alexander. *Absorbent glass mat separators, VRLA batteries, and related methods of manufacture and use*. US Patent App. 10/056,592. 2018.

[65] LG Leal. *Advanced transport phenomena: fluid mechanics and convective transport processes*. Cambridge University Press, 2007.

[66] CK Lee, C-C Sun, and CC Mei. "Computation of permeability and dispersivities of solute or heat in periodic porous media". In: *International journal of heat and mass transfer* 39.4 (1996), pp. 661–676.

[67] K-J Lee et al. "Three dimensional thermal-, electrical-, and electrochemical-coupled model for cylindrical wound large format lithium-ion batteries". In: *Journal of Power Sources* 241 (2013), pp. 20 –32. ISSN: 0378-7753.

[68] Z Li et al. "Factors influencing oxygen recombination at the negative plate in valve-regulated lead-acid batteries". In: *Journal of The Electrochemical Society* 149.7 (2002), A934–A938.

[69] DR Lide and HPR Frederikse. *CRC handbook of chemistry and physics: a ready-reference book of chemical and physical data*. Vol. 83. Boca Raton: CRC Press LLC, 1992.

[70] D Linden and TB Reddy. *Handbook of Batteries*. 2002.

[71] J Liu and CW Monroe. "Solute-volume effects in electrolyte transport". In: *Electrochimica Acta* 135 (2014), pp. 447–460.

[72] J Liu, SK Rahimian, and CW Monroe. "Capacity-limiting mechanisms in Li/O2 batteries". In: *Physical Chemistry Chemical Physics* (2016).

[73] Z Liu and H-X Li. "Extreme learning machine based spatiotemporal modeling of lithium-ion battery thermal dynamics". In: *Journal of Power Sources* 277 (2015), pp. 228–238.

[74] BK Mahato, EY Weissman, and EC Laird. "Some aspects of gas recombination in lead-acid Systems". In: *Journal of The Electrochemical Society* 121.1 (1974), pp. 13–16.

[75] B Malengier et al. "ODES: a high level interface to ODE and DAE solvers". In: *The Journal of Open Source Software* 3.22 (2018), p. 165. URL: `https://doi.org/10.21105/joss.00165`.

[76] J Marcicki et al. "Design and parametrization analysis of a reduced-order electrochemical model of graphite/LiFePO4 cells for SOC/SOH estimation". In: *Journal of Power Sources* 237 (2013), pp. 310–324.

[77] SG Marquis et al. "An asymptotic derivation of a single particle model with electrolyte". In: *arXiv preprint arXiv:1905.12553* (2019).

[78] CW Monroe. "Does oxygen transport affect the cell voltages of metal/air batteries?" In: *Journal of The Electrochemical Society* 164.11 (2017), E3547–E3551.

[79] CW Monroe and C Delacourt. "Continuum transport laws for locally non-neutral concentrated electrolytes". In: *Electrochimica Acta* 114 (2013), pp. 649–657.

[80] SJ Moura, M Krstic, and NA Chaturvedi. "Adaptive PDE observer for battery SOC/SOH estimation". In: *ASME 2012 5th Annual Dynamic Systems and Control Conference joint with the JSME 2012 11th Motion and Vibration Conference*. American Society of Mechanical Engineers. 2012, pp. 101–110.

[81] SJ Moura et al. "Battery state estimation for a single particle model with electrolyte dynamics". In: *IEEE Transactions on Control Systems Technology* 25.2 (2017), pp. 453–468.

[82] IR Moyles et al. "An experimentally validated equivalent circuit model for lithium-ion batteries systematically derived from porous electrode theory". In: (2018).

[83] IR Moyles et al. "Asymptotic reduction of a porous electrode model for lithium-ion batteries". In: *arXiv preprint arXiv:1805.07093* (2018).

[84] M Muratori et al. "A model order reduction method for the temperature estimation in a cylindrical li-ion battery cell". In: *ASME 2010 Dynamic Systems and Control Conference*. American Society of Mechanical Engineers Digital Collection. 2011, pp. 633–640.

[85] J Newman and TW Chapman. "Restricted diffusion in binary solutions". In: *AIChE Journal* 19.2 (1973), pp. 343–348.

[86] J Newman and KE Thomas-Alyea. *Electrochemical systems*. John Wiley & Sons, 2012.

[87] J Newman and W Tiedemann. "Porous-electrode theory with battery applications". In: *AIChE Journal* 21.1 (1975), pp. 25–41.

[88] J Newman and W Tiedemann. "Simulation of recombinant lead-acid batteries". In: *Journal of The Electrochemical Society* 144.9 (1997), pp. 3081–3091.

[89] M Ohlberger, S Rave, and F Schindler. "Model reduction for multiscale lithium-ion battery simulation". In: *Numerical Mathematics and Advanced Applications ENUMATH 2015*. Springer, 2016, pp. 317–331.

[90] IJ Ong and J Newman. "Double-layer capacitance in a dual lithium ion insertion cell". In: *Journal of The Electrochemical Society* 146.12 (1999), pp. 4360–4365.

[91] D Pavlov, A Kirchev, and B Monahov. "Mechanism of the oxygen cycle reactions proceeding at the negative plates of VRLA batteries". In: *Journal of Power Sources* 144.2 (2005), pp. 521–527.

[92] B Peherstorfer, K Willcox, and M Gunzburger. "Survey of multifidelity methods in uncertainty propagation, inference, and optimization". In: *SIAM Review* 60.3 (2018), pp. 550–591.

[93] JG Pharoah, K Karan, and W Sun. "On effective transport coefficients in PEM fuel cell electrodes: Anisotropy of the porous transport layers". In: *Journal of Power Sources* 161.1 (2006), pp. 214–224.

[94] KS Pitzer, RN Roy, and LF Silvester. "Thermodynamics of electrolytes. 7. Sulfuric acid". In: *Journal of the American Chemical Society* 99.15 (1977), pp. 4930–4936.

[95] E Prada et al. "Simplified electrochemical and thermal model of LiFePO4-graphite Li-ion batteries for fast charge applications". In: *Journal of The Electrochemical Society* 159.9 (2012), A1508–A1519.

[96] M Ptashnyk and T Roose. "Derivation of a macroscopic model for transport of strongly sorbed solutes in the soil using homogenization theory". In: *SIAM Journal on Applied Mathematics* 70.7 (2010), pp. 2097–2118.

[97] M Ptashnyk, T Roose, and GJD Kirk. "Diffusion of strongly sorbed solutes in soil: a dual-porosity model allowing for slow access to sorption sites and time-dependent sorption reactions". In: *European Journal of Soil Science* 61.1 (2010), pp. 108–119.

[98] SK Rahimian, S Rayman, and RE White. "Extension of physics-based single particle model for higher charge–discharge rates". In: *Journal of Power Sources* 224 (2013), pp. 180–194.

[99] JM Reniers et al. "Improving optimal control of grid-connected lithium-ion batteries through more accurate battery and degradation modelling". In: *Journal of Power Sources* 379 (2018), pp. 91–102.

[100] G Richardson, G Denuault, and CP Please. "Multiscale modelling and analysis of lithium-ion battery charge and discharge". In: *Journal of Engineering Mathematics* 72.1 (2012), pp. 41–72.

[101] G Richardson and JR King. "Time-dependent modelling and asymptotic analysis of electrochemical cells". In: *Journal of Engineering Mathematics* 59.3 (2007), pp. 239–275.

[102] G Richardson et al. "Generalised single particle models for high-rate operation of graded lithium-ion electrodes: systematic derivation and validation". In: *arXiv preprint arXiv:1907.09410* (2019).

[103] B Rieger et al. "Multi-dimensional modeling of the influence of cell design on temperature, displacement and stress inhomogeneity in large-format lithium-ion cells". In: *Journal of The Electrochemical Society* 163.14 (2016), A3099–A3110.

[104] ZM Salameh, MA Casacca, and WA Lynch. "A mathematical model for lead-acid batteries". In: *IEEE Transactions on Energy Conversion* 7.1 (1992), pp. 93–98.

[105] H Sanderson. "Aqua Metals sees future for lead-acid batteries in green energy". In: *Financial Times* (2016). [Online; accessed 8-August-2016]. URL: `http://on.ft.com/2aoFWQX`.

[106] S Santhanagopalan and RE White. "Online estimation of the state of charge of a lithium ion cell". In: *Journal of power sources* 161.2 (2006), pp. 1346–1355.

[107] VA Sethuraman, Kristin Kowolik, and V Srinivasan. "Increased cycling efficiency and rate capability of copper-coated silicon anodes in lithium-ion batteries". In: *Journal of Power Sources* 196.1 (2011), pp. 393–398.

[108] VA Sethuraman et al. "In situ measurement of biaxial modulus of Si anode for Li-ion batteries". In: *arXiv preprint arXiv:1108.0567* (2011).

[109] VA Sethuraman et al. "In situ measurements of stress evolution in silicon thin films during electrochemical lithiation and delithiation". In: *Journal of Power Sources* 195.15 (2010), pp. 5062–5066.

[110] VA Sethuraman et al. "In situ measurements of stress-potential coupling in lithiated silicon". In: *Journal of The Electrochemical Society* 157.11 (2010), A1253–A1261.

[111] Y Shi. "Modeling, real-time degradation identification, and remediation of pb-acid batteries". PhD thesis. The Pennsylvania State University, 2013.

[112] RB Smith and MZ Bazant. "Multiphase porous electrode theory". In: *Journal of The Electrochemical Society* 164.11 (2017), E3291–E3310.

[113] I Snihir et al. "Battery open-circuit voltage estimation by a method of statistical analysis". In: *Journal of Power Sources* 159.2 (2006), pp. 1484–1487.

[114] V Srinivasan and C-Y Wang. "Analysis of electrochemical and thermal behavior of Li-ion cells". In: *Journal of The Electrochemical Society* 150.1 (2003), A98–A106.

[115] V Srinivasan, GQ Wang, and C-Y Wang. "Mathematical modeling of current-interrupt and pulse operation of valve-regulated lead acid cells". In: *Journal of The Electrochemical Society* 150.3 (2003), A316–A325.

[116] V Sulzer et al. "Faster lead-acid battery simulations from porous-electrode theory: Part I. Physical model". In: *Journal of The Electrochemical Society* 166.12 (2019), A2363–A2371.

[117] V Sulzer et al. "Faster lead-acid battery simulations from porous-electrode theory: Part II. Asymptotic analysis". In: *Journal of The Electrochemical Society* 166.12 (2019), A2372–A2382.

[118] TR Tanim, CD Rahn, and C-Y Wang. "A temperature dependent, single particle, lithium ion cell model including electrolyte diffusion". In: *Journal of Dynamic Systems, Measurement, and Control* 137.1 (2015), p. 011005.

[119] A Tenno. *Modelling and evaluation of valve-regulated lead-acid batteries*. Helsinki University of Technology, 2004.

[120] A Tenno, R Tenno, and T Suntio. "Charge–discharge behaviour of VRLA batteries: model calibration and application for state estimation and failure detection". In: *Journal of Power Sources* 103.1 (2001), pp. 42–53.

[121] M Thele et al. "Modeling of the charge acceptance of lead-acid batteries". In: *Journal of Power Sources* 168.1 (2007), pp. 31–39.

[122] WH Tiedemann and J Newman. "Battery design and optimization". In: *Journal of Electrochemical Society, Softbound Proceeding Series, Princeton, New York* 79.1 (1979), p. 23.

[123] M Torchio et al. "Lionsimba: A matlab framework based on a finite volume model suitable for li-ion battery design, simulation, and control". In: *Journal of The Electrochemical Society* 163.7 (2016), A1192–A1205.

[124] JA Trainham III. "Flow-through porous electrodes". In: *Lawrence Berkeley National Laboratory* (2011).

[125] NT Tran et al. "A Padé approximate model of lithium ion batteries". In: *Journal of The Electrochemical Society* 165.7 (2018), A1409–A1421.

[126] RS Treptow. "The lead-acid battery: its voltage in theory and in practice". In: *Journal of Chemical Education* 79.3 (2002), p. 334.

[127] FJ Vaccaro and RE Landwehrle. "Experiments on thermal run-a-way and its management for electrolyte immobilized lead-acid batteries". In: *Telecommunications Energy Conference, 1991. INTELEC'91., 13th International*. IEEE. 1991, pp. 20–25.

[128] J Van Brakel and PM Heertjes. "Analysis of diffusion in macroporous media in terms of a porosity, a tortuosity and a constrictivity factor". In: *International Journal of Heat and Mass Transfer* 17.9 (1974), pp. 1093–1103.

[129] C-Y Wang, WB Gu, and BY Liaw. "Micro-macroscopic coupled modeling of batteries and fuel cells I. Model development". In: *Journal of the Electrochemical Society* 145.10 (1998), pp. 3407–3417.

[130] Y Wang et al. "Adaptive estimation of the state of charge for lithium-ion batteries: Nonlinear geometric observer approach". In: *IEEE Transactions on Control Systems Technology* 23.3 (2015), pp. 948–962.

[131] RF Weiss. "The solubility of nitrogen, oxygen and argon in water and seawater". In: *Deep Sea Research and Oceanographic Abstracts*. Vol. 17. 4. Elsevier. 1970, pp. 721–735.

[132] T Zhou and R Battino. "Partial molar volumes of 13 gases in water at 298.15 K and 303.15 K". In: *Journal of Chemical & Engineering Data* 46.2 (2001), pp. 331–332.